Large scale simulations of conduction in carbon nanotube networks

A dissertation submitted for the degree of

Doctor of Philosophy

at the University of Cambridge

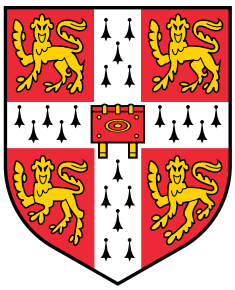

Robert Andrew Bell

Pembroke College, Cambridge

November, 2014

For my family.

SUMMARY

Macroscopic wires fabricated from carbon nanotubes (CNTs) are an exciting new material that aims to replicate the exceptional electric properties of microscopic individual CNTs in a macroscopic scale material. Recently there have been significant experimental advances that allow these wires to be synthesised reliably and on an industrial scale. Their electrical conductance, however, is orders of magnitude lower than expected and the origin of this poor performance is not well understood. In these wires, the CNTs form a conducting network whereby current flows along individual CNTs and also between the CNTs. This dissertation presents theoretical investigations of mechanisms that affect conduction in these networks.

First, the factors that affect tunnelling rates between axially-aligned CNTs are investigated. Using scattering theory and tight-binding calculations, a novel mechanism is identified whereby momentum scattering induced by weak perturbations can greatly improve conductances between CNTs with a large chirality mismatch. It is suggested that the disorder found in realistic networks is vital to the conductance of the network as a whole and, unintuitively, that purifying these networks by removing disorder will decrease rather than increase the overall network conductivity.

This mechanism is then investigated using first-principles calculations for the specific structural perturbations of terminations and bends in CNTs. An optimised methodology is described that couples density functional theory with the Landauer-Büttiker transport formalism and allows for the unbiased study of the quantum conductance of systems containing thousands of atoms. Using this methodology, it is found that small, physically realistic bends can improve the conductance between CNTs by an order of magnitude, confirming the relevance of the momentum-scattering mechanism to realistic CNT networks. A comparison is made between improvements to the conductance and the induced backscattering due to bends and a range of termination geometries.

Finally, the evidence for charge doping of CNTs by adsorbed water molecules is investigated. The conclusion of earlier calculations from the literature that water dopes carbon nanotubes is suggested to be unreliable due to the difficulty in isolating charge doping from charge polarisation effects due to the permanent electric dipole moment of water. Using large-scale first-principles simulations, novel semi-classical models and an analysis of the local electronic structures it is shown that the residual charge transfer between water and carbon nanotubes, once charge polarisation have been accounted for, is negligible.

PREFACE

This dissertation describes work carried out between October 2011 and November 2014 in the Theory of Condensed Matter group at the Cavendish Laboratory, Cambridge, under the supervision of Prof. M. C. Payne.

Except where stated otherwise in the text, this dissertation is a result of my own work and contains nothing which is the outcome of work done in collaboration. This dissertation has not been submitted in whole or in part for any degree of diploma at this or any other university. Parts of this thesis have been published or prepared for publication as follows:

1. Chapter 5: R. A. Bell, S. M.-M. Dubois, M. C. Payne, and A. A. Mostofi, "Electronic transport calculations in the ONETEP code: implementation and applications," *submitted*, 2014.

2. Chapter 6: R. A. Bell, M. C. Payne, and A. A. Mostofi, "Improving the conductance of carbon nanotube networks through resonant momentum exchange," *Phys. Rev. B*, vol. 89, p. 245426, Jun 2014.

3. Chapter 7: R. A. Bell, M. C. Payne, and A. A. Mostofi, *In preparation*, 2014.

4. Chapter 8: R. A. Bell, M. C. Payne, and A. A. Mostofi, "Does water dope carbon nanotubes?," *The Journal of Chemical Physics*, vol. 141, no. 16, p. 164703, 2014.

This dissertation does not exceed 60,000 works in length.

Robert Bell
Cambridge, November 2014

ACKNOWLEDGEMENTS

It is a great pleasure to be able to thank the people who have helped along the way with the research described in this dissertation. Firstly, I wish to thank my supervisor, Mike Payne, who has been a faithful source of wisdom, fine coffee, opportunities and encouragement. I am indebted to Arash Mostofi for his kindness and support in acting as my second supervisor. He has been endless supply of advice, hospitality and patience. I also thank both Mike and Arash for their critical reading of drafts of this dissertation and for their suggestions and corrections.

I thank Helen Verrechia, David Taylor and Alan Clarke for hiding administrative inner-workings from me and for ensuring the smooth-running of TCM, and Michael Rutter and Daniel Corbett for ensuring the TCM computers worked, despite my best efforts. Michael has also been an excellent educator of the finer points of computing, the many colours of politics and the art of humour.

I am grateful for funding from the Engineering and Physical Research Council and a scholarship from British Telecommunications.

It has been a pleasure to share an office with James Mayoh (and his cubes) for the duration of my time in TCM. He has put up with my bad sense of humour and my ramblings and rantings with good humour and great kindness. I thank also my other colleagues within TCM, in particular Gareth Conduit, Sebastian John, Michal Kwasigroch, Jonathan Lloyd-Williams, Tomeu Monserrat, Emma Towlson and Nick Worth, who have not only encouraged and challenged me to be a better physicist but who have also made TCM a far more interesting place to work.

I am particularly grateful to Natalie who has been a constant source of much needed love and support. I'm sorry that I've been a bit grumpy the last few years. Finally I thank my family who have always encouraged me throughout my studies. I am incredibly grateful to you for giving me the values and aspirations that I hold, without which I would never have got here in the first place.

CONTENTS

1 Introduction **1**

1.1 Carbon nanotubes 1

1.2 The experimental theorist: computational modelling 2

1.3 Outline of this thesis 3

2 The structural and electronic properties of carbon nanotubes **5**

2.1 The structure of carbon nanotubes 6

2.1.1 Carbon nanotube wires, fibres and networks 6

2.2 The geometry of individual carbon nanotubes 9

2.3 The electronic properties of carbon nanotubes 11

2.3.1 Tight-binding model of graphene 11

2.3.2 Zone-folding approximation 16

2.3.3 Beyond the π/π^* zone-folding model 18

2.3.4 Electronic structure of carbon nanotube bundles 19

2.4 Summary 20

3 Mesoscopic current and ballistic conductance **21**

3.1 Introduction 21

3.2 Scattering lengths in carbon nanotubes 23

3.3 The Landauer-Büttiker formalism 24

3.3.1 Current from transmission 26

3.3.2 Ballistic conductance 29

3.3.3 Conduction at low bias and linear-response 29

3.3.4 Transmission from Green's functions 31

3.3.5 Limitations of the Landauer-Büttiker formalism 32

3.4 Summary 32

4 First-principles methods **35**
4.1 Quasi-particles . . . 36
4.2 The exact solution to the Schrödinger equation . . . 37
4.2.1 The variational principle . . . 37
4.2.2 Exponential scaling . . . 38
4.3 Density functional theory . . . 39
4.3.1 The Hohenberg-Kohn theorems . . . 39
4.3.2 The Kohn-Sham mapping . . . 42
4.3.3 The exchange-correlation functional . . . 44
4.3.4 Quasi-particles from density functional theory . . . 46
4.3.5 Limitations of density functional theory . . . 47
4.4 Practical implementations . . . 49
4.4.1 Basis sets . . . 49
4.4.2 The pseudopotential approximation . . . 52
4.4.3 Periodic and aperiodic systems . . . 54
4.5 Summary . . . 55

5 First-principles electronic transport **57**
5.1 Introduction . . . 57
5.1.1 Preliminaries and definitions . . . 59
5.1.2 Non-orthogonal basis . . . 60
5.2 Constructing the device matrices . . . 60
5.2.1 Lead self energies . . . 61
5.2.2 The auxiliary simulation geometry . . . 61
5.3 Optimisation strategies . . . 63
5.4 Properties beyond the transmission coefficients . . . 66
5.4.1 Properties of the leads . . . 66
5.4.2 Eigenchannels for multi-lead devices . . . 66
5.5 Applications . . . 69
5.5.1 Poly-acetylene wire . . . 70
5.5.2 Conduction between terminated carbon nanotubes . . . 73
5.6 Outstanding issues . . . 77
5.7 Summary . . . 80

6 Momentum-resonant tunnelling between carbon nanotubes **83**
6.1 Introduction . . . 84

6.2 Linear-response from perturbation theory . . . 85
6.3 Tight-binding model . . . 87
6.4 Resonant tunnelling between CNTs . . . 90
6.4.1 Scaling relations of the momentum-resonant scattering mechanism 92
6.5 Momentum resonances in compositionally disordered networks . . . 95
6.6 Momentum resonances in doped nanotubes . . . 98
6.7 Resonant back-scattering . . . 99
6.8 Summary . . . 102

7 First-principles conductance between carbon nanotubes 105
7.1 Introduction . . . 105
7.2 Methods . . . 106
7.2.1 Generating the structure . . . 108
7.3 The role of bend angle . . . 110
7.3.1 The effect of chirality mismatch . . . 112
7.4 The role of end termination . . . 115
7.4.1 The effect of chirality mismatch . . . 123
7.5 Conductance between terminated nanotubes at finite bias . . . 125
7.5.1 Methods . . . 125
7.5.2 Bias drop . . . 126
7.5.3 Non-equilibrium forces . . . 126
7.6 Conclusions . . . 130

8 Charge doping in water-adsorbed carbon nanotubes 133
8.1 Introduction . . . 133
8.2 Methods . . . 135
8.3 Computing the charge polarisation . . . 136
8.4 Thermal effects . . . 141
8.5 Estimating the residual charge transfer . . . 144
8.6 Considerations of the electronic energy level alignment . . . 145
8.7 Summary . . . 148

9 Conclusions 149
9.1 Summary . . . 149
9.2 Further work . . . 150

A Transmission from Green's functions **153**
A.1 Preliminaries 153
A.1.1 State normalisation 155
A.2 Scattering states from the leads 156
A.3 Device spectral function 157
A.4 Current operator 158
A.5 The transmission amplitude matrix and the Fisher-Lee relation 159
A.6 Computing the transmission matrix and eigenchannels 160

B Block tri-diagonal matrix inversion **163**

C Classical electrostatic charge polarisation model **165**

D Local density of states **169**

LIST OF FIGURES

2.1 Bundles of double walled CNTs imaged under transmission electron microscopy. 7
2.2 The hierarchical structure of carbon nanotubes 8
2.3 The relationship between the hexagonal graphene lattice and CNT structure 10
2.4 A $|\sigma\rangle$ bond and $|p_z\rangle$ orbital of the graphene sheet. 11
2.5 The band structure of graphene. 12
2.6 The basis vectors and hexagonal lattice of graphene 14
2.7 The π/π^* band structure of graphene 15
2.8 The band structures and densities of states of the achiral $(9,0)$ and $(5,5)$ CNTs 17
2.9 The band structure of the $(10,0)$ CNT 18

3.1 Ballistic conductance measured in metallic CNTs 24
3.2 The schematic geometry used in the Landauer formalism 28
3.3 The quantum conductance observed in conductance through a point-contact 30
3.4 The temperature dependence of the conductance of a micrometer-length single-walled metallic CNT. 30

4.1 The optimisation of a single NGWF 52
4.2 An illustration of the pseudopotential approximation 54
4.3 An illustration of the supercell approximation 56

5.1 Comparison of the transmission and auxiliary simulation geometries . . . 62
5.2 Geometry of the poly-acetylene wire 70
5.3 The lead band structure for the poly-acetylene structure 72
5.4 The transmission through the poly-acetylene chain 72
5.5 The eigenchannels for a poly-acetylene chain with probe 74

5.6 The auxiliary simulation geometry for computing transmission between two terminated CNTs . . . 75
5.7 The lead band structure for, and transmission between two terminated CNTs 75
5.8 The dependence of transmission on NGWF radius . . . 76
5.9 Comparison of transmission using the valence and joint NGWF bases . . 79

6.1 The inter-tube geometry . . . 88
6.2 Diagrammatic second-order scattering processes . . . 88
6.3 The momentum resonances between two metallic CNTs . . . 91
6.4 Comparison of the handedness dependence of the momentum resonant mechanism . . . 92
6.5 The momentum resonances between two semiconductor CNTs . . . 93
6.6 The scaling relations of the momentum resonance . . . 94
6.7 The improvement in inter-tube conductance between metallic CNTs with a range of diameters . . . 96
6.8 The improvement in inter-tube conductance between semiconductor CNTs with a range of diameters . . . 97
6.9 The dependence of the resonant momenta on chirality difference . . . 98
6.10 The energy dependence of conductance, leads 1 to 4 . . . 100
6.11 The energy dependence of conductance, leads 1 to 3 . . . 101
6.12 Resonant back-scattering in metallic CNTs . . . 103

7.1 The schematic geometries of the CNTs in the end-scattering and bend-scattering configurations . . . 107
7.2 The different termination schemes . . . 109
7.3 The auxiliary simulation geometries . . . 110
7.4 The dependence of inter-tube conductance on bend angle . . . 112
7.5 Eigenchannels in the bend-scattering geometry . . . 113
7.6 The dependence of inter-tube conductance on chiral angle . . . 114
7.7 The conductance spectra between $(9, 0)$ and $(5, 5)$ terminated CNTs . . . 115
7.8 The conductance spectra between two $(5, 5)$ terminated CNTs . . . 116
7.9 Eigenchannels in the end-scattering geometry . . . 118
7.10 Comparison of the conductance energy dependence using first principles and an interference model . . . 120
7.11 Comparison of the conductance overlap length dependence using first principles and an interference model . . . 121

7.12 The mean and range of the characteristic conductance as a function of chirality mismatch 124
7.13 The difference between the electrostatic local potentials at $0.5\ \mathrm{V}$ bias . . . 127
7.14 Non-equilibrium inter-tube forces at finite bias 128
7.15 The electron density difference induced at $0.5\ \mathrm{V}$ bias 129

8.1 The density perturbation induced by an adsorbed water molecule 137
8.2 The geometry of the water-adsorbed CNT 138
8.3 Comparison of electrostatic potentials 140
8.4 Comparison of different water molecules, metallic CNT 141
8.5 Comparison of different water molecules, semiconductor CNT 142
8.6 Water-CNT binding energy curve 143
8.7 The dependence of the induced density difference on binding distance . . 143
8.8 Comparison of water/CNT (local) densities of states, single water molecule 146
8.9 Comparison of water/CNT (local) densities of states, water cluster 147

A.1 The complex contour to calculate the non-equilibrium density matrix . . . 158

C.1 The difference in induced charge density between the cylindrical and planar models 167

LIST OF TABLES

3.1 Experimentally-determined scattering lengths in CNTs 25

7.1 The *rms* and maximum bond strains (in $\%$) within the bend region for the different CNT pairs and bend angles. The bends are introduced to the $(5, 5)$ CNT. 111

CHAPTER

ONE

INTRODUCTION

1.1 Carbon nanotubes

Since the time of Benjamin Franklin's early investigations into electricity, conventional metals, such as iron or copper, have remained more-or-less unchallenged as the material of choice for making electrical wires. The excellent conductivity that these materials posses, coupled with the ease with which wires can be made, has led to their dominant use for the transport of electrical signals.

Whilst these conventional wires currently remain the *de facto* standard, there have recently been concerted efforts to search for new materials that out-perform this standard. There are various motivators for this search, including superior electrical performance (lower resistivities, higher sustainable band widths); greater endurance (stable performances at high temperatures, or under chemically harsh conditions); or economic reasons (material costs, wire weight). In particular, the weight of conventional wires can be especially significant in weight-sensitive applications due to the typically-high densities of conventional metals. For instance, copper wiring can account for over a third of the weight of a satellite; similarly, the 135 miles of copper wiring in commercial aircraft weighs more than two tonnes.

One material that has emerged as a potential candidate for novel electrical wiring is carbon nanotubes.[1] The properties of individual carbon nanotubes have been found to

[1]The discovery by Iijima in 1991[1] of hollow nanometre-sized graphitic tubules in the soot from electric arc-discharge between graphite electrodes can certainly be identified as the discovery that prompted significant research into carbon nanotubes. Naturally, however, a number of studies prior to this date identified carbon nanotube-like structures[2, 3, 4, 5]. The earliest of these discoveries, from 1952, went mostly unnoticed in Western science as it was printed in Russian at a time when Western access to Soviet journals was limited. Implicit discovery can also be traced back to far earlier dates: recent analyses have found carbon nanotubes in

be quite remarkable with measurements determining that conductivities and maximum current densities can be exceptionally high whilst having a density much lower than that of conventional metals. (See chapter 2 for a more detailed exposition of the properties of carbon nanotubes.)

Recently, there has been significant focus on fabricating carbon nanotube-based materials that reproduce the exceptional properties of individual carbon nanotubes on the macroscopic scale, meters or even kilometers in length. Synthesising individual nanotubes that are this large remains unfeasible, with typical rapid-production methods producing nanotubes of the order microns or millimetres in length.[2] Instead approaches have been developed that combine many individual microscopic nanotubes into fibres and threads.[8, 9, 10] The results are similar to conventional fibres such as cotton, with the addition that these nanotube fibres offer good conductance.

The measured conductance is, however, orders of magnitude lower than that expected based on the maximum conductance of the individual constituent nanotubes,[8, 9, 10] and the origin of this poor conductance is currently not well understood. In addition to the conductance of the individual nanotubes within the fibre, the *intra*-tube conductance, the conductance of the fibre network as a whole is dependent on how the current flows between the nanotubes within that network, the *inter*-tube conductance. The highlighted terminology introduced here will be used throughout this dissertation.

The aim of the work described in this dissertation is to study the factors that affect conduction in these carbon nanotube networks. The goal of these studies, which are based on theory and simulation, is to identify optimisations and improvements to improve the electrical performance of this material.

1.2 The experimental theorist: computational modelling

Whilst experiment remains the only method for confirming the laws of nature that govern the properties of materials, the study of materials through computer simulation can offer significant insights that are difficult if not impossible to achieve through experiment alone. For instance, in simulation individual atoms may be manipulated and moved with a level of control inaccessible to the experimentalist, and the resulting consequences calculated without ever donning a lab coat. Further, through simulation, mechanisms can be identified on a microscopic scale directly and strategies for developing or exploiting such mechanisms

Damascus steel dating from the seventeenth century[6].

[2] Whilst synthesis of carbon nanotubes that are over half a meter in length has been reported[7], practical use of this approach is limited by long synthesis times of over an hour.

can be screened using a single piece of apparatus — the computer. In the experimental study of carbon nanotubes, controlling all the factors that may affect conductivity is challenging, whereas in simulation one does have this degree of control. Computer simulation is therefore invaluable as a tool to identify and understand the mechanisms that affect the properties of carbon nanotubes.

1.3 Outline of this thesis

In chapter 2 we outline some of the fundamental properties of carbon nanotubes, focusing on the structural and electronic properties from a theoretical perspective. The fundamental concepts, and associated notation, introduced within this chapter will be used throughout this dissertation.

In chapter 3 we turn to the theoretical problem of calculating conductances using quantum mechanics. We first discuss the mechanisms of conductance in carbon nanotubes and explain that the observation of large electron scattering lengths justifies treating conductance as ballistic. We introduce the theoretical methodology due to Landauer for computing conductance from a quantum-mechanical description of electronic structure and discuss its limitations.

In chapter 4 we explain the theoretical methodology for computing electronic structures from first principles. We outline the difficulty associated with dealing with the many-body electronic structure in an exact fashion, even numerically, and introduce the formalism of density functional theory as a practical alternative. We outline the approximations and limitations associated with this method and discuss several practical implementations that are used within this thesis.

In chapter 5 we describe a practical method, implemented within the ONETEP project, for computing the Landauer conductance using electronic structures derived from the first-principles methods described in chapter 4. This implementation, which builds on previous similar implementations, benefits from use of a series of optimisations that allows for the study of conductance through systems containing thousands of atoms whilst achieving systematically improvable accuracy.

In chapter 6 we investigate the factors that affect conductance between carbon nanotubes. Using scattering theory within a perturbative framework, and confirmed by tight-binding calculations, we identify a novel mechanism for improving the inter-tube conductance using momentum scattering mediated by weak interactions between the nanotubes and the environment or from defects. This mechanism leads to the wholly unintuitive conclusion

that increasing the purity of carbon nanotube networks by removing local disorder will decrease the conductivity of the network.

In chapter 7 we investigate this mechanism further using the first-principles techniques developed in chapter 5. We focus on two sources of momentum scattering, arising from terminations and from strain fields due to bends in nanotubes, confirming that weak momentum scattering is vital to the conduction of carbon nanotube networks. A number of related effects are also investigated.

In chapter 8 we look at the problem of charge doping in water adsorbed carbon nanotubes. We discuss the contradictions found in earlier experimental and theoretical works over the effect of water on the conductivity of carbon nanotubes, and suggest that previous calculations that predict that water *n*-dopes carbon nanotubes are unreliable due to the difficulty in isolating charge doping from charge polarisation effects due to the dipole moment of water. Using large-scale first-principles simulations, novel semi-classical models and an analysis of the local electronic structures we show that the residual charge transfer between water and carbon nanotubes, once charge polarisation have been accounted for, is negligible.

Finally, in chapter 9 we summarise the overall conclusions from this thesis and outline some suggestions for future work in this field.

CHAPTER

TWO

THE STRUCTURAL AND ELECTRONIC PROPERTIES OF CARBON NANOTUBES

Carbon has a rich and varied chemistry, forming compounds with almost every other known element of the periodic table. It is also the compounds that it forms with itself, however, that are of great technological interest. Bulk carbon materials, such as diamond and graphite, have been known for centuries; more recently, quasi-low-dimensional allotropes of carbon have been discovered: the two-dimensional graphene[11, 12], zero-dimensional fullerenes[13], and one-dimensional nanotubes[14]. The excitement that arises from these newly discovered materials comes from their physical properties which offer unparalleled improvements over conventional materials. For instance, many remarkable properties of carbon nanotubes have been identified including a mechanical strength greater than most other materials [15] and thermal conductivity an order of magnitude greater than that of copper[16].

It is the electronic properties of carbon nanotubes that form the focus of this thesis. Very high conductivities have been observed in CNTs, with ballistic conductance occurring over very large length-scales or order microns (see section 3.2). The maximum current densities obtainable in carbon nanotubes is found to be very high, up to $10^9 - 10^{10}\ \mathrm{A/cm^2}$, which considerably exceeds the $10^6\ \mathrm{A/cm^2}$ current found to destroy copper nanowires[17], and even exceeds the critical current densities of superconductors ($10^8 - 10^9\ \mathrm{A/cm^2}$)[18]. Applications for high-frequency electronics may also prove fruitful as the impact of the skin effect is reduced.[19] In a wire made from a conventional material, the skin effect makes high frequency current flow at the surface of a wire reducing the effective cross-sectional area of a wire and increasing the resistance; in carbon nanotubes, the tubular structure already makes the current flow at the nanotube surface minimising the impact of the skin

effect. Coupled with the low mass density of carbon nanotubes, $1.3 - 2.1\ \mathrm{g/cm^3}$[20, 21] compared to $9\ \mathrm{g/cm^3}$ for copper, carbon nanotubes are promising candidates for light-weight high-performance electrical wires.

In this chapter, we introduce the fundamental structural and electronic properties of carbon nanotubes (CNTs). The theoretical electronic structure is derived within a tight-binding framework, and a discussion is made on how these results are modified by more sophisticated calculations. The aim of this chapter is to introduce this background and define relevant quantities in sufficient detail that are then used throughout the remainder of this dissertation. For a comprehensive review of the electronic and structural properties of carbon nanotubes see [14, 22].

2.1 The structure of carbon nanotubes

Carbon nanotubes (CNTs) are tubules of carbon with walls made from a single layer of carbon atoms arranged in a hexagonal structure. As structures, they can have remarkably high aspect ratios, defined as the ratio of the tube diameter to the length of the tube, on the order of $1 : 10^6$ — typical diameters are on the order of nanometres, and maximum length on the order of microns up to centimetres[7] — and can therefore be considered as a realisation of ideal atomic wires of carbon.

Along with individual single-walled CNTs, multiple CNTs can be combined to form composite structures. A CNT inside another CNT with larger diameter forms a double-walled CNT, shown in Fig. 2.1; further CNTs contained within this double-walled CNT forms multi-walled CNTs[1] with a spacing between the concentric shells of individual CNTs around 3.4 Å as in graphite.

These single- or multi-walled CNTs may also conglomerate together to form bundles. The axes of the constituent CNTs are aligned and the individual CNTs have a hexagonal packing arrangement as shown in Fig. 2.1, with a similar inter-tube separation.

2.1.1 Carbon nanotube wires, fibres and networks

As a result of the impressive electronic properties of individual CNTs on the atomic scale, considerable effort has been made to construct macroscopic materials that reproduce these desirable quantities. It is currently impractical to grow perfect CNTs that are macroscopic in length, and so alternative approaches have been investigated. One approach is to spin the

[1] Note that double-walled CNTs are often referred to as multi-walled CNTs.

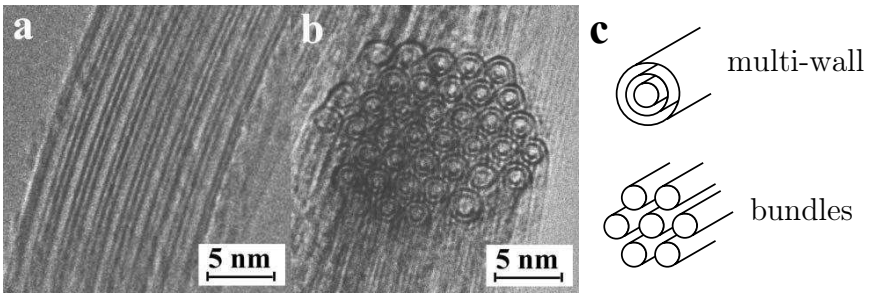

Figure 2.1: Bundles of double walled CNTs imaged under transmission electron microscopy. a) bulk-like region; b) a cross-sectional view demonstrating the hexagonal packing within the bundle and the double walls of the CNTs; c) the schematic geometry of multi-walled CNTs and CNT bundles. Adapted from Ref. [23] with permission from The Royal Society of Chemistry.

individual CNTs into bundles and then into fibres and wires.[8, 9, 10] Fig. 2.2a shows such a CNT fibre.

In this material, a conducting network of CNTs is formed and, as no individual CNT traverses the length of the wire, electrons must percolate through paths involving many CNTs. The conductivities of these wires is orders of magnitude lower than expected based on the conductances of the individual CNTs. To date, the highest specific conductivity[2] obtained for a CNT fibre is $20\ \mathrm{S\ m^{-1}/(g\ cm^{-3})}$[25] which is somewhat better than the same quantity for copper ($6.5\ \mathrm{S\ m^{-1}/(g\ cm^{-3})}$) and aluminium ($14\ \mathrm{S\ m^{-1}/(g\ cm^{-3})}$). The theoretical maximum specific conductivity for CNTs can be estimated to be of order $10^3 - 10^4\ \mathrm{S\ m^{-1}/(g\ cm^{-3})}$, however, indicating that significant improvement could still be made.[3] The additional resistance found in experiment is attributed to a range of factors,

[2]Specific conductivity, defined as the conductivity normalised by the density, is used to allow comparison of CNT networks with different morphologies and densities.

[3]This estimate is obtained by assuming that conductance within a CNT can be considered ballistic over the electron mean free path of carbon nanotubes $\ell_{\mathrm{m.f.p.}} \sim 1\ \mu\mathrm{m}$ (see chapter 3 for a discussion of ballistic conductance and mean free paths). This defines a conductivity of $\sigma \sim G\ell_{\mathrm{m.f.p.}}/A$ where the conductance G is of order the quantum conductance $G_0 = 7.75 \times 10^{-5}$ S and A is the CNT cross-sectional area. Assuming that each CNT within the network contributes independently to the conductivity, the specific conductivity of the network as a whole is equal to the specific conductivity of an individual CNT. The mass density of an individual CNT is obtained as $\rho = Nm_C/Ad$ where d is the unit length of the tube, $m_C \sim 10^{-26}$ kg is the atomic mass of a carbon atom and $N = 2\pi Dd/3\sqrt{3}a_{CC}^2$ is the number of carbon atoms per unit length d with $D \sim 1$ nm the CNT diameter and $a_{CC} = 1.4$ Å the carbon-carbon bond length. The resulting expression for the specific conductivity is

$$\sigma' = \frac{\sigma}{\rho} = \frac{3\sqrt{3}G_0\ell_{\mathrm{m.f.p.}}a_{CC}^2}{2\pi Dm_C}. \tag{2.1}$$

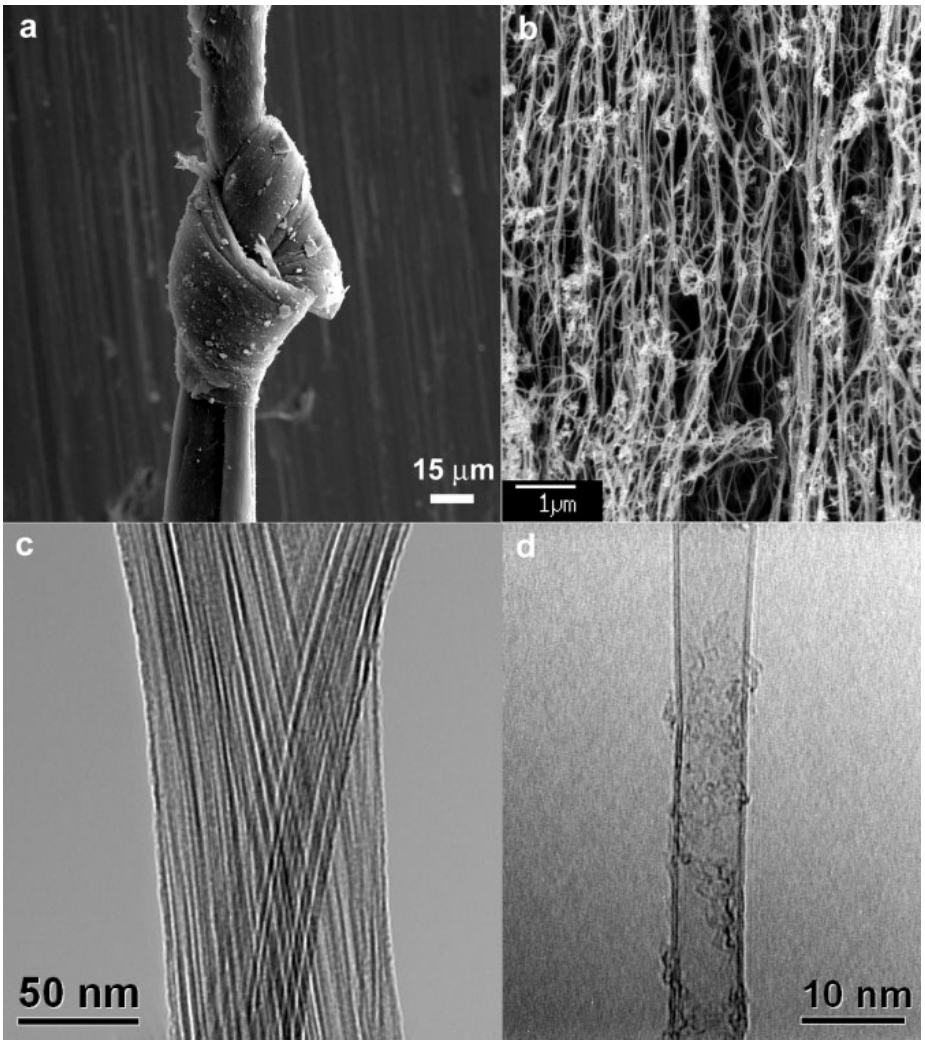

Figure 2.2: The hierarchical structure of carbon nanotubes: (a) a macroscopic nanotube fibre with knot; (b) a disordered nanotube bundle network; (c) bundles of single and multiwall carbon nanotubes; (d) an individual (double wall) nanotube. From [24], copyright © 2007 WILEY-VCH Verlag GmbH & Co. KGaA, Weinheim.

including the relative contributions from metallic/semiconducting CNTs (see section 2.3), the morphology of the network and the presence of defects and impurities. An additional significant contribution to the resistance is believed to come from poor tunnelling between CNTs in the network. Understanding the factors that affect this *inter-tube* tunnelling rate and how it may be improved forms a significant focus of this thesis. To achieve this goal, however, an understanding of the electronic structure of individual CNTs is required.

2.2 The geometry of individual carbon nanotubes

The structure of an individual CNT can be considered to be derived from the graphene lattice, an infinite hexagonal planar network of carbon atoms, which is rolled up to form a cylinder. Depending on how this rolling performed, CNTs of different structure, diameter and indeed electronic properties (see section 2.3) can be made.

To uniquely determine the type of CNT, it is sufficient to specify the circumferential vector ($\mathbf{C}_h$) that defines the chiral vector (AA' in Fig. 2.3) between two sites of the graphene lattice (A and A') that are equivalent once the sheet is rolled. This chiral vector can be defined simply in terms of a pair of indices (n, m) which define the vector in terms of the graphene lattice vectors ($\mathbf{a}_1$, $\mathbf{a}_2$):

$$\mathbf{C}_h = n\mathbf{a}_1 + m\mathbf{a}_2. \tag{2.2}$$

A vector within the graphene plane that is perpendicular to $\mathbf{C}_h$ defines the direction of the CNT axis. In addition to $\mathbf{C}_h$, a chiral angle θ can be defined as the angle between the chiral vector and the $\mathbf{a}_1$ graphene lattice vector

$$\cos\theta = \frac{\mathbf{C}_h \cdot \mathbf{a}_1}{|\mathbf{C}_h||\mathbf{a}_1|} = \frac{2n+m}{2\sqrt{n^2+nm+m^2}}. \tag{2.3}$$

Due to the hexagonal symmetry of the graphene lattice, the chiral angle can always be defined within the range $0° \leq \theta \leq 30°$. In general, CNTs are chiral and have a left- or right-handed screw direction (Fig. 2.3 bottom right). There are two exceptions, however, where the CNTs are achiral: for either $n = 0$ or $m = 0$, $\theta = 0°$ and the CNT is said to be *zig-zag*; for $n = m$, $\theta = 30°$, the CNT is said to be armchair. These names arise from the profile of the CNT cross-sections as shown in Fig. 2.3. The diameter of the CNT can also be defined from the chiral vector ($a = |\mathbf{a}_1|$)

$$d = \frac{|\mathbf{C}_h|}{\pi} = \frac{a}{\pi}\sqrt{n^2+nm+m^2}. \tag{2.4}$$

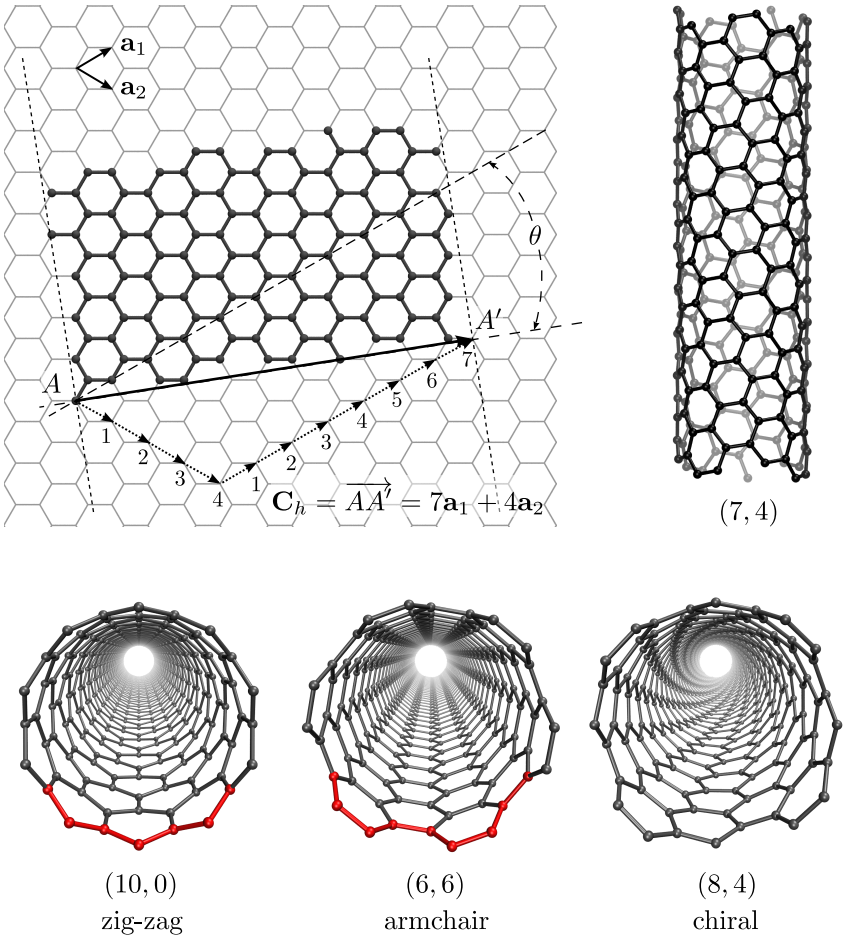

Figure 2.3: Top panel: the graphene hexagonal lattice with lattice vectors $\mathbf{a}_1$, $\mathbf{a}_2$. The chiral vector $\mathbf{C}_h = 7\mathbf{a}_1 + 4\mathbf{a}_2$ represents one wrapping of the graphene lattice to form the $(7, 4)$ CNT which is shown on the right; rolling into a tube joins the two dashed lines. The shaded atoms represent the periodic repeating unit of this CNT. The chiral angle θ is defined as the angle between $\mathbf{C}_h$ and the $\mathbf{a}_1$ vector defining the zig-zag $(n, 0)$ direction. Bottom panel: the atomic structures of the zig-zag $(10, 0)$, armchair $(6, 6)$, and chiral $(8, 4)$ CNTs; the zig-zag and armchair edges are indicated in red. Adapted from [22].

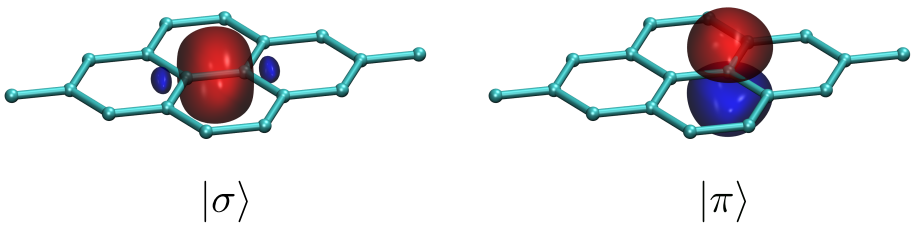

Figure 2.4: A $|\sigma\rangle$ bond and $|p_z\rangle$ orbital of the graphene sheet.

2.3 The electronic properties of carbon nanotubes

As a result of the relationship between the structure of CNTs and graphene, it is useful to describe the CNT bonding structure in terms of the electronic structure of graphene. In the following discussion, we follow the review of Ref. [22].

The electronic structure within graphene can be described using hybridisation theory. Of the four valence orbitals of the carbon atom ($2s$, $2p_x$, $2p_y$ and $2p_z$ with the z-axis perpendicular to the atomic-plane), the s, p_x and p_y orbitals are combined together into a planar sp^2 hybridisation scheme. These sp^2 orbitals are symmetric with respect to the planar symmetry and hybridise with equivalent orbitals on adjacent carbon atoms producing strong, covalent σ/σ^* bonds that are responsible for the majority of the binding energy and elastic properties of the graphene sheet. The remaining p_z orbitals are out-of-plane and, for a flat graphene lattice, cannot couple with the σ/σ^* bonds due to symmetry. Interactions between neighbouring p_z orbitals, however, are strong creating a manifold of delocalised π/π^* orbitals which exist in the planes above and below the atomic sheet. In Fig. 2.4 we show the relative shapes of the σ bonds and p_z orbitals.

The energy of the σ/σ^* bonds lie far from the Fermi energy (see Fig. 2.5), and therefore contribute little to conduction. In contrast, the Fermi energy is located within the π/π^* bands making these states the dominant contributor to conduction within the material.

2.3.1 Tight-binding model of graphene

A simple but efficient description of the electronic band structure of graphene can be obtained using a straightforward tight-binding model which we now describe. The primitive unit cell of graphene is hexagonal and contains two carbon atoms, each of which form hexagonal sublattices which are conventionally denoted the A and B sublattices. Each atom contributes four electrons for a total of eight electrons per unit cell. The interactions between the six sp^2 hybrid orbitals within the primitive unit cell (three per carbon atom) produce three bonding σ bands and three anti-bonding σ^* bands. The three bonding σ bands

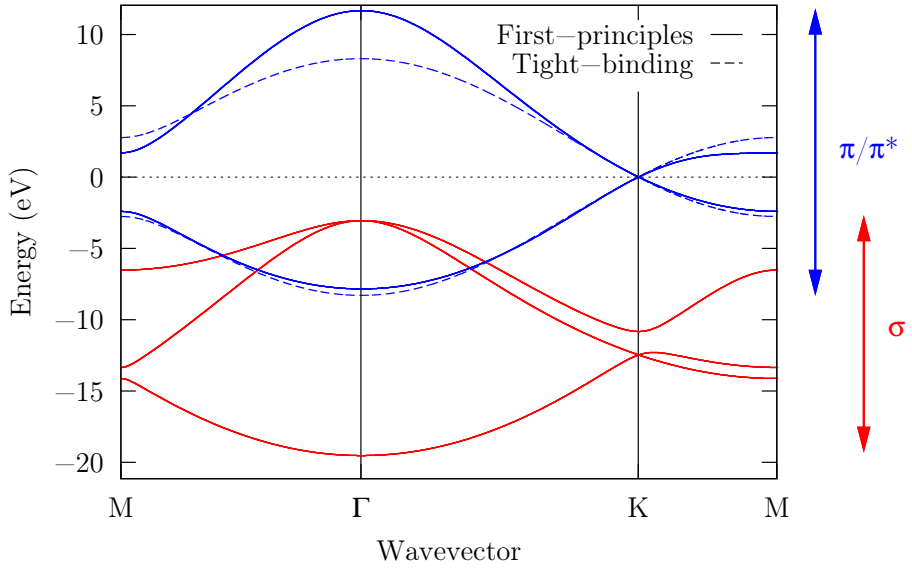

Figure 2.5: The band structure of graphene. The solid lines are calculated from first-principles calculations (see chapter 4), and coloured by the symmetry of the orbitals: σ in red, π in blue. The dashed line gives band structure calculated using the π/π^* tight-binding model (section 2.3.1).

are occupied by six of the eight electrons per unit cell, but as these bands lie far below the Fermi energy their contribution to the transport properties is negligible. The anti-bonding σ^* bands lie high in energy and are unoccupied. The remaining two electrons per unit cell are placed within the π/π^* bands which are formed from the interactions between the p_z orbitals only. The Fermi energy is found to lie within these bands and therefore a tight-binding model that describes only this band is sufficient to describe the electronic transport properties of graphene. A suitable basis for this tight-binding calculation is therefore a single $p_z(\mathbf{r} - \mathbf{r}_{A,B})$ orbital located on each atom site $\mathbf{r}_{A,B}$ of the A/B sublattice.

To solve the Schrödinger equation for graphene, we apply Bloch's theorem[26] and write the wavefunctions[4] as

$$\psi_{\mathbf{k}}(\mathbf{r}) = c_A(\mathbf{k})\tilde{p}_z^A(\mathbf{k},\mathbf{r}) + c_B(\mathbf{k})\tilde{p}_z^B(\mathbf{k},\mathbf{r}), \tag{2.5}$$

where

$$\tilde{p}_z^{A,B}(\mathbf{k},\mathbf{r}) = \sum_{\mathbf{R}} e^{i\mathbf{k}\cdot\mathbf{R}} p_z(\mathbf{r} - \mathbf{r}_{A,B} - \mathbf{R}), \tag{2.6}$$

$\mathbf{k}$ is the electron momentum within the plane and $\mathbf{R}$ is a lattice vector. In the basis of $\tilde{p}_z^{A,B}$,

[4]For clarity, we omit the normalisation of the wavefunction.

the Schrödinger equation is solved by the solutions to the secular equation

$$\begin{vmatrix} H_{AA} - E(\mathbf{k}) & H_{AB} \\ H_{BA} & H_{BB} - E(\mathbf{k}) \end{vmatrix} = 0, \tag{2.7}$$

with the matrix elements defined as

$$H_{AA}(\mathbf{k}) = \sum_{\mathbf{R},\mathbf{R}'} e^{i\mathbf{k}\cdot(\mathbf{R}-\mathbf{R}')} \langle p_z^A(\mathbf{R}')|\hat{H}|p_z^A(\mathbf{R})\rangle, \tag{2.8}$$

$$H_{AB}(\mathbf{k}) = \sum_{\mathbf{R},\mathbf{R}'} e^{i\mathbf{k}\cdot(\mathbf{R}-\mathbf{R}')} \langle p_z^A(\mathbf{R}')|\hat{H}|p_z^B(\mathbf{R})\rangle, \tag{2.9}$$

where $\hat{H}$ is the Hamiltonian operator. The state

$$\langle \mathbf{r}|p_z^{A/B}(\mathbf{R})\rangle = p_z(\mathbf{r} - \mathbf{r}_{A,B} - \mathbf{R}) \tag{2.10}$$

denotes a p_z orbital at position $\mathbf{r}_{A,B} + \mathbf{R}$ and we have assumed that the orbitals are orthogonal.

Under a nearest-neighbour approximation, shown schematically in Fig. 2.6, $H_{AA} = H_{BB}$ are independent of $\mathbf{k}$ and can be set to zero as an energy reference, and H_{AB} simplifies to

$$\begin{aligned} H_{AB} = & \\ & \Big[\langle p_z^A(\mathbf{0})|\hat{H}|p_z^B(\mathbf{0})\rangle + e^{i\mathbf{k}\cdot\mathbf{a}_1}\langle p_z^A(\mathbf{0})|\hat{H}|p_z^B(\mathbf{a}_1)\rangle + e^{i\mathbf{k}\cdot\mathbf{a}_2}\langle p_z^A(\mathbf{0})|\hat{H}|p_z^B(\mathbf{a}_2)\rangle\Big] && (2.11)\\ & = -t_0\alpha(\mathbf{k}), && (2.12) \end{aligned}$$

where t_0 defines the transfer integral between first-nearest neighbours, typically of order 2.9 eV[27], and $\alpha(\mathbf{k}) = (1 + e^{i\mathbf{k}\cdot\mathbf{a}_1} + e^{i\mathbf{k}\cdot\mathbf{a}_2})$.

Upon solving Eqn. (2.7) the dispersion relations become ($\mathbf{k} = (k_x, k_y)$, $a = |\mathbf{a}_1|$)[5]

$$\begin{aligned} E(\mathbf{k}) &= |H_{AA}|^2 \pm |H_{AB}|^2 && (2.13)\\ &= \pm t_0|\alpha(\mathbf{k})| && (2.14)\\ &= \pm t_0\sqrt{1 + 4\cos\frac{\sqrt{3}k_x a}{2}\cos\frac{k_y a}{2} + 4\cos^2\frac{k_y a}{2}}. && (2.15) \end{aligned}$$

From the plot shown in Fig. 2.7a, this dispersion relation is seen to consist of two sheets that touch at $E = 0$. These contacts occur at the corners of the first Brillouin zone and are

[5]We assume the graphene lattice vectors to be

$$\mathbf{a}_1 = (a_{1,x}, a_{1,y}) = \left(\frac{\sqrt{3}}{2}, \frac{1}{2}\right)a, \qquad \mathbf{a}_2 = \left(\frac{\sqrt{3}}{2}, -\frac{1}{2}\right)a.$$

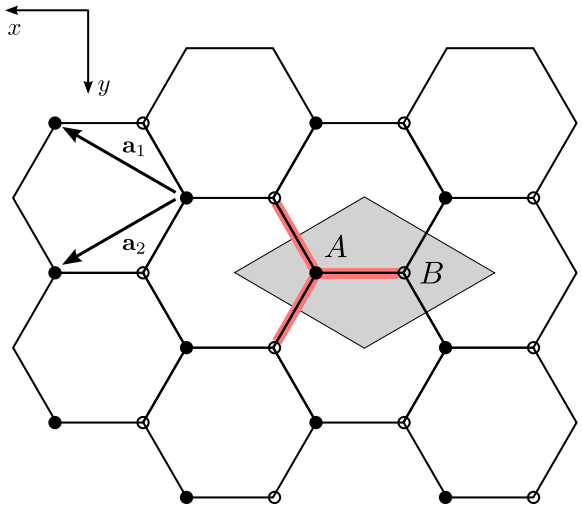

Figure 2.6: The basis vectors and hexagonal lattice of graphene. The red bars indicate interactions between the three nearest-neighbour p_z orbitals. The shaded region indicates the graphene unit cell.

denoted as the K and K' points. As the π/π^* manifold is to contain two electrons, both[6] are placed within the lower sheet (the negative energy branch of Eqn. (2.15)) which is fully occupied, the upper sheet is unoccupied and therefore the Fermi energy is the energy at which the two sheets touch which can be verified to be $E_F = H_{AA} = 0$ by our choice energy reference. As there are unoccupied states within the upper sheet that lie at infinitesimal energy away from the Fermi energy, graphene therefore displays metallic characteristics, although it is found that there is a low density of states in the vicinity of the Fermi energy and the term semi-metal is often used.

The low energy excitations can be obtained by expanding the dispersion relation about either the K or K' point[7] resulting in linear dispersion relations

$$E(\mathbf{K} + \delta\mathbf{k}) = \pm\frac{\sqrt{3}a}{2}t_0|\delta\mathbf{k}|, \tag{2.16}$$

where $\mathbf{K}$ is the co-ordinate vector of the K point with respect to the origin of the Brillouin zone.

[6]Placed in each spin channel.

[7]These points are equivalent under time-reversal symmetry.

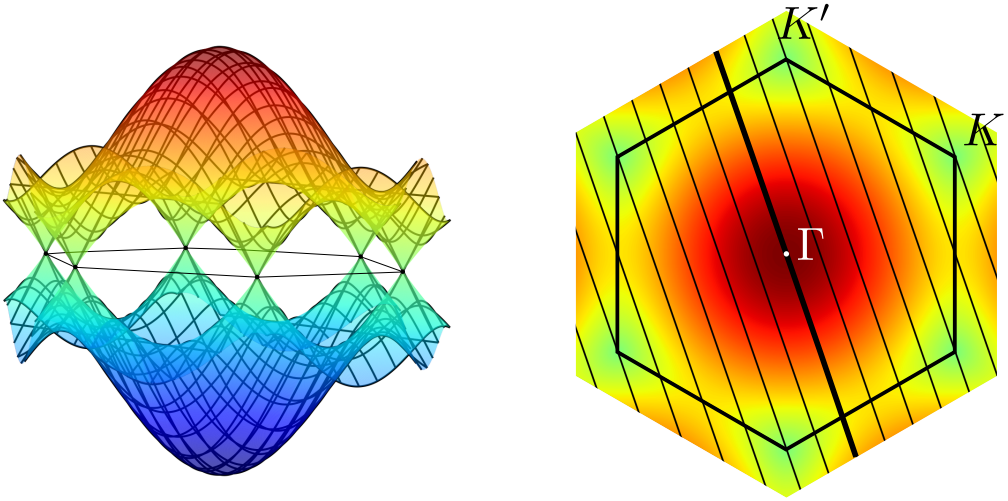

(a) Graphene band structure and Brillouin zone

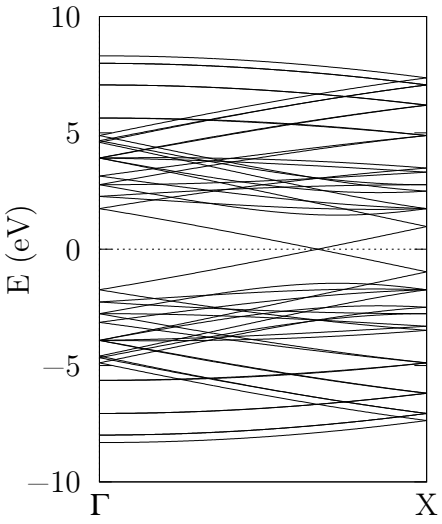

(b) $(8, 2)$ band structure

Figure 2.7: Top panel: the π/π^* band structure of graphene (Eqn. (2.15)). In the right panel, the Brillouin zone is indicated by the hexagon; the lines indicate the states of the $(8, 2)$ CNT that are allowed under the zone-folding approximation. The resulting $(8, 2)$ one-dimensional band structure is shown in the lower panel.

2.3.2 Zone-folding approximation

To relate the band structure of graphene to the band structure of CNTs the periodicity around the CNT circumference must be imposed on the wavefunction

$$\psi_{\mathbf{k}}(\mathbf{r} + \mathbf{C}_h) = e^{i\mathbf{k}\cdot\mathbf{C}_h}\psi_{\mathbf{k}}(\mathbf{r}) = \psi_{\mathbf{k}}(\mathbf{r}), \tag{2.17}$$

where the first equality is due to Bloch's theorem. Consequently, the imposed periodicity restricts the values that the electron momentum can take such that $\mathbf{k} \cdot \mathbf{C}_h = 2\pi\ell$ for integer ℓ, which corresponds to the allowed values of $\mathbf{k}$ being confined to discrete lines, termed subbands, within the graphene Brillouin zone. This is shown in Fig. 2.7a where we show these allowed lines for the $(8, 2)$ CNT. The momentum along these subbands is the axial momentum and can take a continuous range of values; for each subband there is a single azimuthal momentum. Depending on the symmetry of the CNT, two distinct cases are possible: metallic and semiconducting CNTs, which we now describe in turn.

Metallic CNTs

If a subband includes the K point, the CNT will maintain the linear dispersion relations of the graphene Brillouin zone and will therefore be metallic. The condition to achieve this is $\mathbf{K} \cdot \mathbf{C}_h = 2\pi\ell$ which can be straightforwardly shown to be equivalent to $n - m = 3\ell$. All armchair (n, n) CNTs and subset of zig-zag $(n, 0)$ and chiral CNTs are therefore metallic. The low energy excitations retain the linear dispersion relations of the graphene excitations but the axial momentum where the bands cross, the Fermi momentum k_F, depends on the chirality

$$E(k) = \pm\hbar v_F|k - k_F|, \tag{2.18}$$

where k is the axial momentum and $v_F = \sqrt{3}at_0/2\hbar$ defines the Fermi velocity. In Fig. 2.7b and Fig. 2.8 we show the dispersion relations of the metallic $(8, 2)$, $(9, 0)$ and $(5, 5)$ CNTs under the zone-folding approximation. In Fig. 2.8 we also plot the densities of states for the $(9, 0)$ and $(5, 5)$ CNTs. The divergences are called Van Hove singularities and are a result of the quasi one dimensional nature of CNTs and their functional dependence scales as the inverse of the energy difference to the band edge ($1/\sqrt{E - E_b}$).

Semiconducting CNTs

In the case that no subband includes the K point, i.e. when $n - m = 3\ell \pm 1$, the CNT will be semiconducting and there exists a band gap. Expanding the low energy excitations for

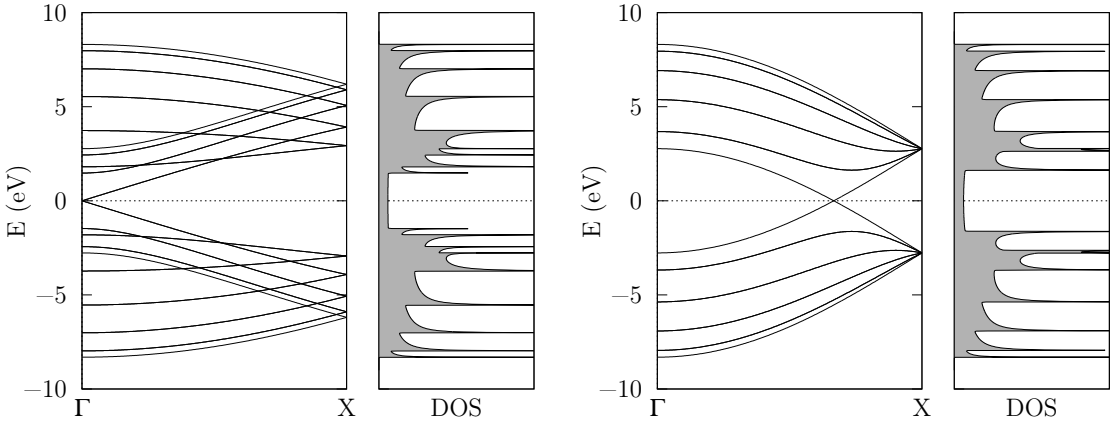

(a) $(9, 0)$ **(b)** $(5, 5)$

Figure 2.8: The band structures and densities of states (DOS) of the achiral $(9, 0)$ and $(5, 5)$ metallic CNTs as calculated using the π/π^* tight-binding model under the zone-folding approximation. After [22].

the subband closest to the K point results in a dispersion relation[22]

$$E(k) \approx \pm\frac{\sqrt{3}a}{2}t_0\sqrt{\left(\frac{2\pi}{3|\mathbf{C}_h|}\right)^2 + k^2}, \tag{2.19}$$

with a band gap opening at the Fermi energy

$$E_g = \frac{2\pi a t_0}{\sqrt{3}|\mathbf{C}_h|}. \tag{2.20}$$

This is shown in the left panel of Fig. 2.9 where we plot the band structure of the semiconducting $(10, 0)$ CNT; in the right panel we superimpose one of the lowest-energy CNT subband on the low-energy dispersion relation of graphene. The size of the band gap is inversely proportional to the CNT diameter ($d = |\mathbf{C}_h|/\pi$) and is approximately 0.6 eV for CNTs with diameter of 1 nm.[28, 27] The effective mass of the charge carriers, given by the curvature at the band edges, can be derived to be

$$m^* = \frac{1}{\hbar}\left[\frac{\partial^2 E}{\partial k^2}\right]^{-1} = \frac{2\pi\hbar}{3|\mathbf{C}_h|v_F} \tag{2.21}$$

and therefore also depends on the inverse of the diameter.

The complex dependence of bandstructure character on the (n, m) indices in turn introduces a sensitive dependence on the tube diameter (Eqn. (2.4)), and CNTs with similar diameter but different (n, m) may have strikingly different electronic structures. A particular synthesis route will typically create CNTs with a range of diameters and therefore also a

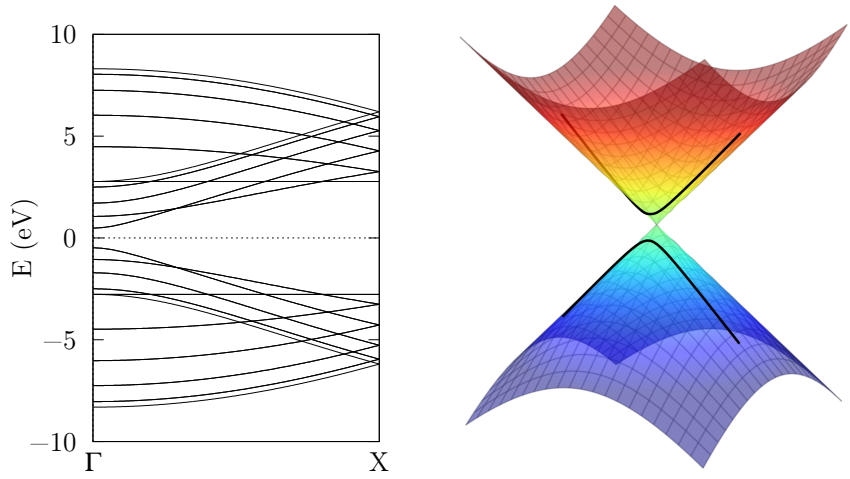

Figure 2.9: The band structure of the achiral $(10, 0)$ semiconducting CNT as calculated using the π/π^* tight-binding model under the zone-folding approximation. The left panel indicates the allowed subband closest to the K point of the graphene Brillouin zone.

range of electronic characters. The ratio of metallic to semiconductor CNTs, which strongly affects the conductivity of a CNT network, is therefore not easy to control at synthesis.

2.3.3 Beyond the π/π^* zone-folding model

The successes of the π/π^* tight-binding model and zone-folding approximation arise from the resulting analytic expression that effectively captures the electronic structure of a wide range of CNTs. Some deficiencies are notable, however.

Firstly, it is assumed that the p_z orbitals do not interact with the σ bonds. Whilst for a perfectly flat graphene sheet this is true by symmetry, the introduction of curvature can allow for coupling between the σ bonds and the π/π^* manifold. For narrow diameter CNTs (< 1 nm), the strong curvature allows mixing of the σ and π bands and the π/π^* model can fail to describe the electronic structure. Calculations derived from first principles (see chapter 4) have shown that hybridization between the π^* and σ^* can lower the energy of low-lying conduction bands considerably[29] reducing, or even closing, the band gaps of small-diameter CNTs that the zone-folding approximation predicts to be semiconducting[30, 31]. Further, high curvature reduces the Fermi wave-vector compared to the result derived from the zone-folding approximations[32].

Curvature effects are less prominent in larger diameter CNTs and do not significantly change the electronic character predicted by the zone-folding model for large diameter semiconductor or armchair metallic CNTs. In zig-zag and chiral metallic CNTs, the

curvature creates a small ($\sim 20\ \mathrm{meV}$) band gap, however this can be ignored at ambient temperatures due to thermal excitation of the electronic occupancies.[33]

A second implicit assumption within the graphene tight-binding model is symmetry between the two sheets of the Brillouin zone (Eqn. (2.15)), resulting in a symmetry between the valence and conduction bands describing the electrons and holes. First-principles calculations show that the symmetry of the valence and conduction bands is indeed broken, as shown in Fig. 2.5. Whilst this effect can be corrected by extending the π/π^* model to include non-orthogonal overlap elements between the p_z orbitals[34], in the vicinity of the K points first-principles calculations still predict the linear-dispersion relations showing that these corrections are largely unnecessary for studying conduction at low-bias.

2.3.4 Electronic structure of carbon nanotube bundles

Where CNTs bundle together, their electronic structure can be modified by the interactions between the tubes. Whilst this interaction is weak, arising from van der Waals interactions, the low-energy excitations can be strongly modified due to the lowering of symmetry which can open band gaps in the low energy dispersion relations. In bundles of $(10, 10)$ CNTs, it was shown theoretically that the tube-tube interaction induces a pseudogap of around $0.1\ \mathrm{eV}$ at the Fermi energy [35], a result that was confirmed experimentally using low-temperature scanning tunnelling spectroscopy[36]. Where the bundles retain the symmetry of the individual CNTs, for example in bundles of symmetrically aligned $(6, 6)$ CNTs, no pseudogap is opened [37]. Similarly, pseudogaps were also predicted for CNTs bundles containing a range of metallic chiralities, however the reduction in densities of states is much smaller in magnitude and occurs over a wider range of energies around the Fermi level[38]. Equivalent modifications to the band structures are calculated in multi-walled CNTs.[39, 40]

At ambient temperatures, however, these modifications to the electronic band structures have little impact on the bundle conductance. Whilst the opening of the pseudogap reduces the density of states precisely at the Fermi energy, the redistribution of the state energies ensures that the average density of states in the vicinity of the Fermi level remains constant. A finite electronic temperature comparable to the magnitude of the pseudogap ensures that the number of states that contribute to conductance is unchanged by the symmetry breaking. Furthermore, ambient thermal energies are also sufficient to overcome the weak inter-tube interaction, which is of order $8\ \mathrm{meV/atom}$[41], allowing the significant contribution of lower-symmetry, pseudogapless configurations to the ensemble-averaged electronic properties.

Therefore, the electronic structure of bundles of CNTs at ambient temperatures can be well approximated by the superposition of the electronic structures of individual CNTs,[38] which itself can be well described by the π/π^* tight-binding model. The advantage of this model lies with the simple analytic expression for the band structure and its ability to capture well the low energy excitations.

2.4 Summary

In this chapter we have introduced the basic electronic properties of carbon nanotubes. Using a simple tight-binding model, we have reviewed the electronic properties of CNTs and have shown that their electronic structure can be metallic or semiconducting in character depending on their structure and chirality. For metallic CNTs, the low energy dispersion relations were demonstrated to depend linearly on the electron momentum. We discussed how this result is modified by the use of more sophisticated calculations, however we concluded that these corrections do not strongly modify the result determined by the simple tight-binding model.

We have also discussed the conductive properties of CNT wires, made from fibres of many individual CNTs, and noted that the electrical performance of this material is considerably lower than expected based on the conductances of the individual constituent CNTs. One approach for improving the conductivity of CNT fibres is to develop an understanding of the theoretical mechanisms that inhibit conductance. In the next chapter, we introduce a theoretical formalism to study the conductances of CNTs.

CHAPTER

THREE

MESOSCOPIC CURRENT AND BALLISTIC CONDUCTANCE

In this chapter we introduce the methodology used throughout this dissertation for computing the conductance of carbon nanotubes. We first describe the role of scattering lengths in determining how electrons conduct in a material, and show how the very large scattering lengths measured in carbon nanotubes require their conduction to be described using a mesoscopic formalism. We describe such a methodology, the Landauer-Büttiker formalism, that forms the primary method used within this dissertation for computing conductances, and discuss its approximations and limitations.

3.1 Introduction

One of the simplest relations of circuit theory is Ohms' law. For materials that obey this law, a potential bias V applied across a wire made from this material creates a current I flowing through that wire, the magnitude of which is directly proportional to the magnitude of the bias $I = GV$.[1] The quantity G is the conductance of the wire, which for macroscopic wires can be written in terms of the wire diameter A, length L, and a quantity intrinsic to the material of the wire, σ, the conductivity

$$G = \frac{\sigma A}{L}. \tag{3.1}$$

For microscopic wires, however, Eqn. (3.1) is no longer appropriate. As the size of the wire reaches the atomic scale, the conductivity can no longer be defined macroscopically

[1] In this dissertation, we will focus only on current flow in the steady-state at zero frequency.

and instead the quantum-mechanical nature of the electrons must be accounted for. As a result, a vastly different picture of conductance is found on the atomic scale. Indeed, the failure of Ohm's law has been observed in experiments on quantum point-contacts[42], atomic wires[43] and carbon nanotubes[44].

The transition between the macroscopic and microscopic description of conductance is governed by three length-scales: the *de Broglie* or *Fermi* wavelength λ_F; the momentum-relaxation length or *mean free path* ℓ_e; and the *phase-relaxation* or *coherence* length L_φ. The Fermi wavelength λ_F is related to the kinetic energy of electrons at the Fermi energy. The mean free path ℓ_e defines the typical distance an electron travels before appreciably changing its momentum due to any scattering events, for example from defects or impurities or inelastic scattering. The coherence length L_φ is the typical distance an electron travels before losing phase coherence due only to inelastic scattering events such as electron-phonon or electron-electron scattering. Over distances shorter than L_φ, the phase of the electron is well defined along its path and so it can interfere with other electrons as well as with itself.

A wire usually exhibits Ohmic behaviour when its length L is much greater than any of these lengths[2] $L \gg \lambda_F, \ell_e, L_\varphi$. This condition is certainly not satisfied in microscopic wires, where sizes are comparable to the Fermi wavelength $L \sim \lambda_F$, but can also be violated in wires with size between the microscopic and macroscopic scales, termed *mesoscopic*, where $L \gg \lambda_F$ but still shorter than the mean free path or coherence length. In these mesoscopic wires, significant deviation from Ohm's law can be observed, and we note here three important limiting cases.

When the wire is much larger than either the mean free path or the coherence length, $L \gg L_\varphi, \ell_e$, conductance is said to be *diffusive* and the classical limit is retrieved. Phase coherency is destroyed by each scattering event and the resistance is proportional to the total length of the wire. When the coherence length is large but the mean free path is much shorter than the wire, $\ell_e \ll L \ll L_\varphi$, conductance is said to be *localised*. Inelastic scattering may be neglected, but localisation results from the accumulation of quantum interference due to many elastic scattering events, and resistance is found to grow exponentially with wire length. In contrast with this, *ballistic* conductance occurs when the wire length is much shorter than both the coherence length and the mean free path, $L \ll \ell_e, L_\varphi$. In this case, electrons can propagate without any significant scattering and the conductance becomes independent of length of the wire (see Fig. 3.1 and section 3.3.2).

[2]The conductance also behaves classically when the coherence length is very short compared to any other length scale. Due to a rapid loss of phase coherence, the effect of coherent interference at each scattering event can be neglected and Ohm's law can be recovered[45].

For a macroscopic CNT fibre, conductance is within the diffusive regime; the description of conductance within that wire, and in particular between the individual CNTs in that wire, may deviate significantly from the classical limit. This is a result of the scattering length-scales associated with CNTs, which we now discuss.

3.2 Scattering lengths in carbon nanotubes

Experimental investigations have found remarkably large scattering lengths in carbon nanotubes. In Table 3.1 we summarise experimental measurements from the literature, from which it can be seen that scattering lengths as large as $10\ \mu\mathrm{m}$ are found in metallic CNTs, or bundles of CNTs, even at room temperature; scattering lengths are found to be somewhat shorter for semiconducting CNTs, yet these can still approach $100\ \mathrm{nm}$. The differences in the observed scattering lengths are due to the precise experimental conditions and different CNT samples. Nonetheless, the largest scattering lengths presented in Table 3.1 can be considered as minimum bounds for the maximum possible scattering lengths. For comparison, the typical electron scattering length in copper is $40\ \mathrm{nm}$ at room temperature[46].

Fig. 3.1 demonstrates the measurement of ballistic conductance in metallic CNTs. The left panel shows the experimental setup consisting of a probe with protruding metallic CNTs that can be lowered into a liquid mercury contact. In the right panel, the resulting conductance of the CNT is shown as a function of the depth z of the CNT tip in the mercury. The conductance is found to be constant over large regions of z, indicating that conductance is ballistic. The step-like increases in conductance occur due to additional CNTs coming into contact with the mercury.[3]

The reason for such large scattering lengths comes down to the unique properties of CNTs. Elastic scattering by long-range perturbations, varying on scales much larger than the inter-atomic distance, has been shown to be forbidden due to symmetry considerations.[48, 49] The elastic mean free path associated with short-range (Anderson-type) random disorder has been calculated to be of order $1\ \mu\mathrm{m}$ [50]. Particularly pristine CNT structures can be produced, with distances between defects as large as microns[51] or greater. These considerations result in elastic mean free paths of order microns.

Inelastic scattering is dominated by acoustic-phonon scattering, however this scattering

[3] We note for completeness that a recent study[47] has questioned the observation of ballistic conductance as reported in Ref. [44] (Fig. 3.1) and similar studies. It has been suggested that nanoscale contacts directly between the probe and mercury may have been mistaken for ballistic-conductor CNTs. Nevertheless, extremely large electron scattering lengths have been inferred in CNTs using independent methods as shown in Table 3.1.

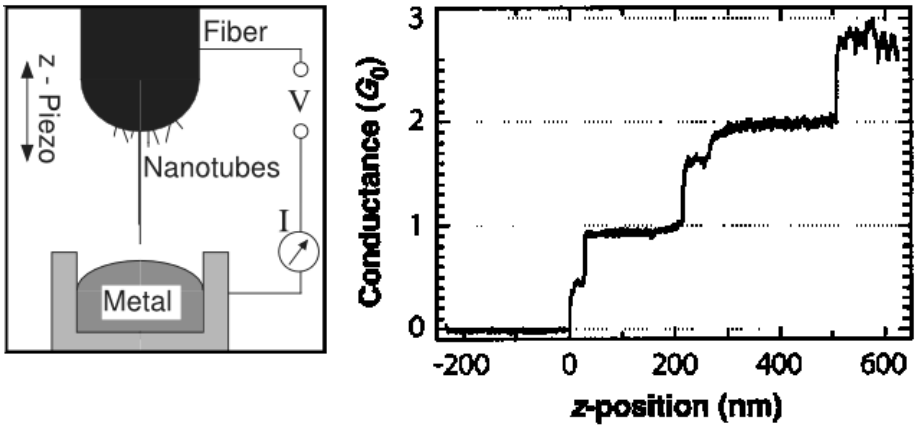

Figure 3.1: Ballistic conductance measured in metallic CNTs. The conductance is in terms of the quantum conductance (see section 3.3.2). Modified from Ref. [44]. Reprinted with permission from AAAS.

is found to be weak[52, 53]. Inelastic acoustic-phonon scattering lengths at room temperature have been measured to be larger than $L_\varphi \sim 1\ \mu\mathrm{m}$[54, 55]. Optical phonons are unpopulated at ambient temperatures as the strong interatomic bonding results in optical phonon excitation energies greater than thermal energies. Optical-phonon scattering is therefore typically found to be negligible. At high temperatures or large bias, however, optical-phonon scattering can be much greater and inelastic scattering lengths can be as short as $10\ \mathrm{nm}$.[54] The contribution to scattering from electron-electron scattering is smaller than the electron-phonon contribution.[33, 55] Inelastic scattering lengths can therefore be of order microns.

As the calculations within this dissertation focus on relatively small CNTs ($L \lesssim 50\ \mathrm{nm}$), the effects of inelastic scattering can be neglected and conductance can be assumed phase coherence and ballistic-like. The effects of elastic scattering are incorporated but only those arising from the precise geometry of the system; elastic scattering from electron-phonon and electron-electron scattering are neglected. To calculate the effects of geometric scattering on the conductance, the Landauer-Büttiker formalism is used which we now describe.

3.3 Conductance in mesoscopic materials: the Landauer-Büttiker formalism

In mesoscopic systems, coherent electron conduction ($L_\varphi = \infty$) can be rigorously investigated with either the Kubo-Greenwood [64, 65] or Landauer-Büttiker formalisms[66, 67,

Scattering length	CNT type	Method	Ref.
$\ell > 3\ \mu\mathrm{m}$	metallic	CB; LT	[56]
$\ell > 10\ \mu\mathrm{m}$		IV; RT	[57]
$\ell = 10\ \mu\mathrm{m}$		CB; LT	[58]
$L_\varphi = 1.6\ \mu\mathrm{m}$ (phonon-scattering)		IV; RT	[54]
$L_\varphi = 300\ \mathrm{nm}$ (phonon-scattering)		IV; RT	[59]
$L_\varphi \approx 100\ \mathrm{nm}$		MR; LT	[60]
$\ell = 100\ \mathrm{nm}$	semiconductor	CB; LT	[58]
$\ell = 2\ \mathrm{nm}$		IV; RT	[61, 58]
$\ell_e \approx 250\ \mathrm{nm}$, $L_\varphi \sim 500\ \mathrm{nm}$ (electron-electron scattering)	metallic, *p*-doped	IV; LT	[62]
$\ell > 200\ \mathrm{nm}$	bundles	CB; LT	[63]
$\ell > 600\ \mathrm{nm}$		IV; RT	[44]

Table 3.1: Experimentally-determined scattering lengths in CNTs. The symbol ℓ refers to the measured scattering length where no mechanism is identified. The methods used to determine the scattering length are defined using the following key: CB: inferred from coulomb blockade measurements;
IV: direct measurement of conductance inferred from IV characteristics;
MR: inferred from magnetoresistance measurements;
LT: at low temperature;
RT: at room temperature.

68]. Whilst these two formalisms have been shown to be formally equivalent[69], the former is better suited to the diffusive regime where elastic scattering is relatively strong. Where the mean free path ℓ_e becomes larger than the CNT being simulated, the Landauer-Büttiker formalism is more appropriate, and further, its formal extensions for incorporating inelastic electron-electron scattering (the Meir-Wingreen formalism[70]) or conduction out of equilibrium or at finite bias (the nonequilibrium Green's function (NEGFs) and Keldysh formalisms[71, 72]) allow a wide range of physical effects to be incorporated.

Prior to Landauer, the flow of current was conventionally interpreted as the response of the system to an electric field within the wire. This electric field results in the electrons accelerating within the material, and scattering is introduced as resistance to this acceleration.[4] Landauer's realisation, however, was that conductance could also be interpreted as the flux of current into a system with a net current flowing due to an imbalance in the number of electrons entering the system with different velocities. The causative agent for conductance here is instead a difference in carrier concentration, equivalent to the chemical potential, on either side of a wire. This is shown schematically in Fig. 3.2. A net flow of electrons then occurs from high chemical potential to low chemical potential. An electric field is still present, however unlike the conventional interpretation, it arises as a reaction to the bias in chemical potential and to scattering within the wire.

Landauer's idea was generalised by Fisher and Lee [75] for multi-channel, three-dimensional conductors, and then further generalised by Büttiker[68] for multi-channel devices connected to multiple probes. The theory is also often referred to as the Landauer-Büttiker formalism. A comprehensive introduction to this formalism can be found in [45, 76].

3.3.1 Current from transmission

In the Landauer-Büttiker formalism, resistance arises due to scattering which affects the *transmission probability* that electrons pass through the wire. The conceptual set-up for a wire is shown in Fig. 3.2. The conductance to be calculated is that of the central device region, which is connected to two reservoirs that supply the current. The reservoirs are assumed to be in local equilibrium with some local chemical potential $\mu_{\mathrm{L,R}}$, and are assumed to be very large such that they can accept or donate an arbitrary number of electrons without changing their internal state. Due to the asymmetry of the system, each reservoir is only able to inject electrons into the device region from one direction. If the reservoirs have a different local chemical potential, there is then an imbalance in carrier densities travelling

[4] This was in fact the picture first proposed by Drude in 1900, which pre-dates quantum theory[73, 74].

each direction and a net current flows. This is shown schematically in the lower panel of Fig. 3.2.

It is assumed that the current flowing through the device is in the steady state and is therefore time-independent. It is also assumed that the electrons can be treated independently in a mean-field approximation.[76]

The contribution to the current through the device from electrons that originate in the left reservoir in the energy interval $[E, E + \delta E]$ is

$$\begin{aligned}\delta i_{\mathrm{L}} &= -\frac{2e}{L}\sum_m v_{g,m}(E)T_m(E)\rho_m(E)\ \delta E \\ &= -\frac{2e}{h}T(E)\ \delta E \end{aligned} \tag{3.2}$$

where L is the size of the device, $v_{g,m}$ and $\rho_m(E)$ are the electron group velocity and density of states of the m^{th} conduction channel within the device, and $T_m(E)$ is the transmission probability of the electron passing through the device.[5] The sum is performed over all conduction channels within the device and the factor of 2 is assuming spin degeneracy. The second line in Eqn. (3.2) is reached by noting the cancellation between the group velocity $v_{g,m} = (1/\hbar)\partial E_m/\partial k$ and the density of states in quasi-one dimensions $\rho_m = L/(\pi\partial E_m/\partial k)$. Due to this cancellation, the transmission from each channel can be amalgamated into a total transmission $T(E) = \sum T_m(E)$, which may be greater than unity where multiple channels contribute.

The total conductance is the difference between the left- and right-travelling electrons

$$I_{\mathrm{L}\to\mathrm{R}} = -\frac{2e}{h}\int_{-\infty}^{\infty}\mathrm{d}E\ \Big[f_{\mathrm{L}}(E;\mu_{\mathrm{L}}) - f_{\mathrm{R}}(E;\mu_{\mathrm{R}})\Big]T(E) \tag{3.3}$$

$$= -\frac{2e}{h}\int_{\mu_{\mathrm{R}}}^{\mu_{\mathrm{L}}}\mathrm{d}E\ T(E), \quad \mathcal{T}\to 0, \tag{3.4}$$

where $f_{\mathrm{L,R}}(E;\mu_{\mathrm{L,R}}) = [1+\exp((E-\mu_{\mathrm{L,R}})/k_B\mathcal{T})]^{-1}$ is Fermi-Dirac function at temperature $\mathcal{T}$ defining the (local) thermal equilibrium populations within the reservoirs and in the final line we have taken the limit of zero temperature.

The same formalism holds for devices that connect to multiple reservoirs, with a current and transmission defined between each pair of reservoirs.

[5] The lead region that connects the reservoirs to the device is assumed to do so adiabatically, and therefore does not introduce any additional scattering. Scattering at this location is referred to as contact resistance[45]. In addition, we have assumed time-reversal symmetry so that the transmission is not dependent on the direction of travel of the electrons. Such an assumption is broken in the presence of a magnetic field[45].

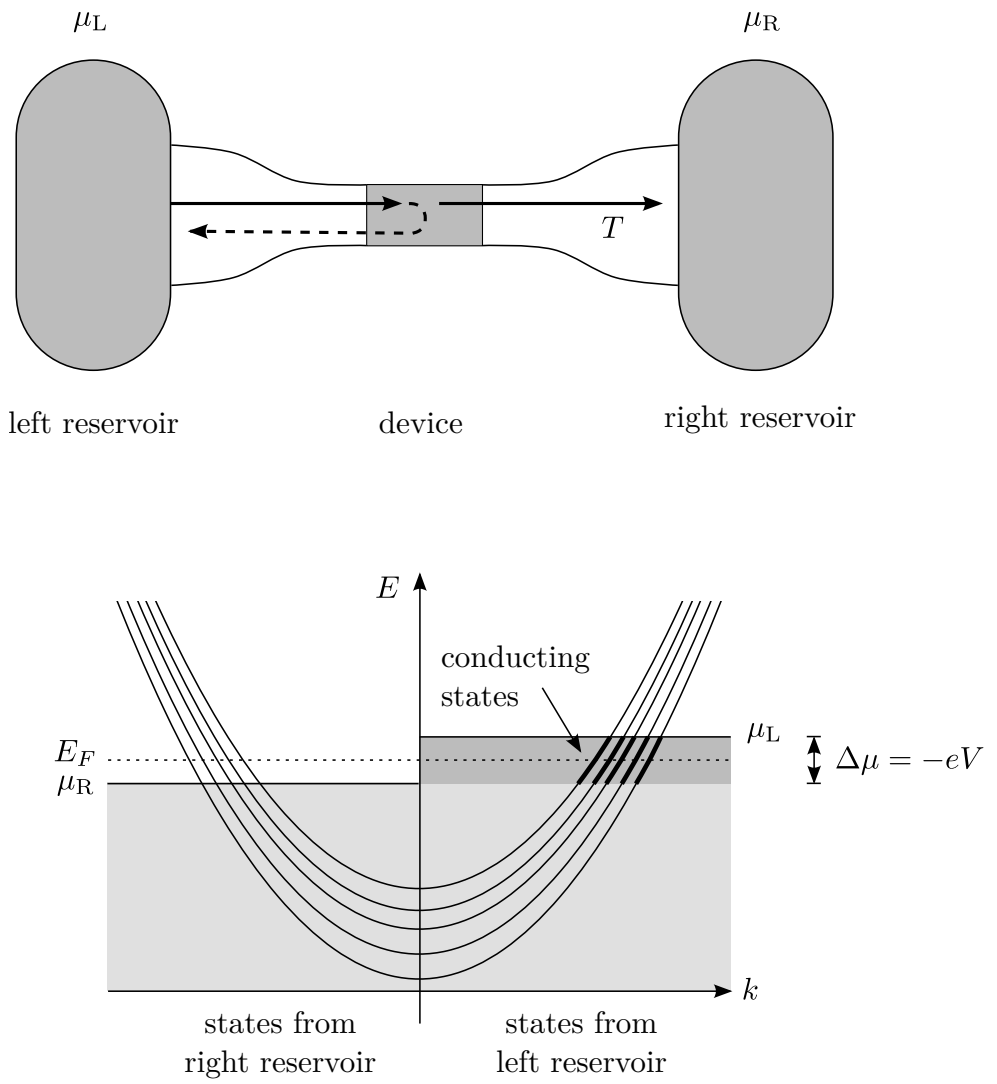

Figure 3.2: Upper panel: the schematic geometry used in the Landauer formalism for a device connected to two reservoirs at chemical potentials μ_{L} and μ_{R}. The arrows represent the propagation of electrons through the device region, with a probability T of being transmitted to the right reservoir. Lower panel: the schematic band structure of electrons propagating through the device. Multiple bands at a given energy correspond to multiple conduction channels at that energy. The states from the left (right) reservoir travel forward (backwards) with respect to the geometry shown in the upper panel. The grey shading indicates the occupied bands for states travelling in each direction: the light grey region indicates states that contribute no net current; the dark grey region has states travelling in the forward direction only contributing a net current.

3.3.2 Ballistic conductance

In the limit of no scattering, conduction is said to be *ballistic*. The transmission is unity for all conduction channels allowing Eqn. (3.4) to be evaluated exactly. An electric potential bias can be assigned as $V = (\mu_{\mathrm{L}} - \mu_{\mathrm{R}})/(-e)$ permitting a conductance to be defined

$$G = \frac{I_{\mathrm{L}\to\mathrm{R}}}{V} = \frac{2e^2}{h} M(V) = G_0 M(V) \tag{3.5}$$

where $M(V)$ is simply the number of conduction channels available in the bias window, and the constant $G_0 = 2e^2/h \approx 7.74 \times 10^{-5}$ S is known as the quantum conductance. This total conductance represents the maximum-possible conductance of the device; the observation that it is finite is a consequence of the Pauli exclusion principle. Note that ballistic conductance is independent of the length of the wire L, marking a significant deviation from Ohmic conductance. Where weak scattering occurs, conductance can still be said to be ballistic if the conductance is approximately independent of the wire length.

Fig. 3.3 is remarkable experimental confirmation of the existence of quantized conductance, where conduction through the constriction is observed to be ballistic and quantized in units of G_0. As the gate voltage is adjusted, the number of conduction channels available changes, resulting in abrupt step-like changes in the conductance. Ballistic conduction has also been observed in CNTs at room temperature, as shown in Fig. 3.1. In Fig. 3.4, the conductance of a micrometer-length metallic CNT is found to be comparable to the quantum conductance indicating that scattering is weak, even at room temperature, and conduction is ballistic-like.

3.3.3 Conduction at low bias and linear-response

In the limit of low bias, conduction is dominated by electrons with energy close to the Fermi energy E_F.[6] Expanding Eqn. (3.3) to first order in the bias $\Delta\mu = \mu_{\mathrm{L}} - \mu_{\mathrm{R}} = -eV$, the low bias current and conductance are

$$I_{\mathrm{L}\to\mathrm{R}} \approx -\frac{2e}{h} \int_{-\infty}^{\infty} \mathrm{d}E \left.\frac{\partial f}{\partial \mu}\right|_{E=E_F} T(E)\Delta\mu \tag{3.6}$$

$$G \approx \frac{2e^2}{h} T(E_F) \tag{3.7}$$

where the bias and temperature are assumed sufficiently small that the transmission can be approximated as constant in the vicinity of the Fermi energy $E = E_F \pm k_B\mathcal{T}$ where

[6] The Fermi energy may be modified through a gate voltage or through doping; the effect of charge doping in CNTs due to water is the focus of chapter 8.

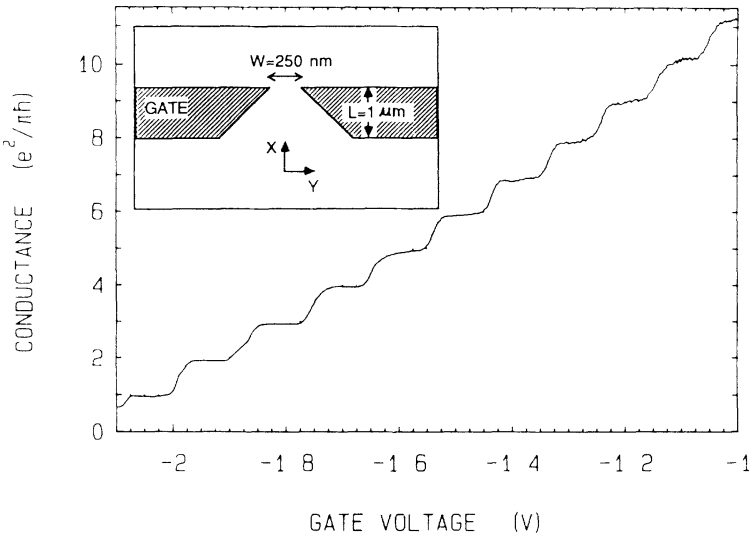

Figure 3.3: The point-contact conductance as a function of gate voltage for a current passing through the restriction shown in the inset. The conduction shows plateaus at multiples of $G_0 = 2e^2/h$. Adapted with permission from van Wees *et al.*, Phys. Rev. Lett., vol. 60, p. 848 1988. Copyright 1988 by the American Physical Society.

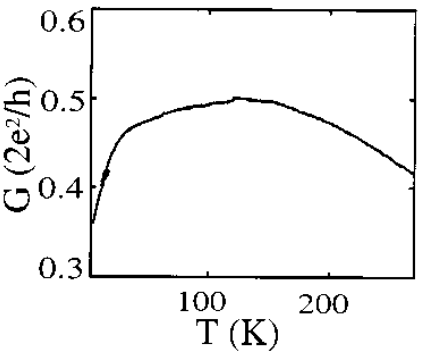

Figure 3.4: The temperature dependence of the conductance of a micrometer-length single-walled metallic CNT. Modified with permission from [57]. Copyright 1999, AIP Publishing LLC.

the derivative of the Fermi function is non-zero. Eqn. (3.7) shows that the transmission spectrum may be directly interpreted as the low-bias conductance as a function of the carrier energy: $G(E)$.

3.3.4 Transmission from Green's functions

The key task, therefore, is to compute the transmission spectrum $T(E)$, which can be done using either the Fisher-Lee relation[75], which relates transmission to the transmission amplitude matrix (see appendix A.5), or using a Green's function approach[71, 76]. Whilst both methods are equivalent, computational efficiencies to be discussed in chapter 5 favour the latter approach for the applications used in this dissertation.

The most significant advantage of the Green's function methodology is that the entire system including the semi-infinite reservoirs can be described in terms of the finite device region, making this approach more amenable to a numerical implementation. Further, the methodology can be naturally extended to compute conduction at finite-bias. Here we focus only on the main results; an outline of the somewhat algebraically-tedious proof of the formulae presented in this section can be found in appendix A.

For a device connecting an arbitrary number of leads to the same number of reservoirs, the Green's function for the device region is given by

$$G_{\mathrm{d}}(E) = \big[(E + i\eta) - H_{\mathrm{d}} - \Sigma_1(E) - \Sigma_2(E) - \dots\big]^{-1} \tag{3.8}$$

where H_{d} is the device Hamiltonian and $\Sigma_i(E)$ is the self energy for lead i. The self energies account for the perturbation to the device region due to the leads, which act as current sources and sinks. The reservoirs are included indirectly and determine the chemical potential and carrier population within the leads.

The transmission coefficient between leads i and j is given by[76]:

$$T_{ij}(E) = \mathrm{tr}\Big[\Gamma_i \; G_{\mathrm{d}} \; \Gamma_j \; G_{\mathrm{d}}^{\dagger}\Big]. \tag{3.9}$$

where $\Gamma_i(E)$ are the coupling matrices defined in terms of the corresponding lead self energy

$$\Gamma_j = i\big(\Sigma_j - \Sigma_j^{\dagger}\big). \tag{3.10}$$

In addition to the transmission coefficients, the device Green's function allows the device density of states to be computed using

$$\mathcal{N}_d(E) = -\frac{1}{\pi}\,\mathrm{Im}\,\mathrm{tr}\big[G_{\mathrm{d}}(E)\big]. \tag{3.11}$$

For a detailed discussion of these relations, see [45, 76].

3.3.5 Limitations of the Landauer-Büttiker formalism

As inelastic processes are neglected, the Landauer-Büttiker formalism applies only to non-interacting charge carriers. The validity of this approximation improves at higher temperatures where thermal fluctuations suppress interactions. Within this dissertation, we therefore restrict our attention to conductance at ambient temperatures, permitting a mean-field approach.

We note, for completeness, that at very low temperatures this approximation is insufficient and instead correlation of the charge carriers must be described by the Tomonaga-Luttinger-liquid theory[77, 78, 79, 80]. For reviews of Tomonaga-Luttinger-liquid theory and its applications to CNTs see [81, 82].

The Landauer-Büttiker formalism also does not explicitly provide a methodology for computing transmission at finite bias. This problem is addressed in the nonequilibrium Green's function (NEGF) and Keldysh formalism,[71, 72] which is discussed briefly in appendix A.

3.4 Summary

In this chapter, we have introduced the ideas behind the Landauer-Büttiker formalism for ballistic electronic conductance and justified the need for its use when calculating the conductance of carbon nanotubes. A Green's function approach was described that allows the conductance of a device to be computed from a description of the device Hamiltonian and self energies. These quantities are unique to any system, and a method must be found to obtain the matrix elements by which they are defined.

One approach is to use a tight-binding model for the matrix elements parameterised from known features about the system, such as the bulk band structure. This approach allows for rapid determination of the device electronic structure and is the approach adopted in chapter 6 where we use the graphene π/π^* model introduced in chapter 2 to study very large systems of bulk-like CNT networks.

For more complex devices, suitable tight-binding models are more difficult to identify and the applicability of such models to a range of device geometries is not assured. Instead approaches that derive these matrix elements directly from first-principle calculations, that is without prior assumptions about the device other than the electrons obey the Schrödinger equation, offer a great predictive advantage. A procedure to achieve this is the focus of chapter 5, which constitutes the main technique by which conductance is calculated in this dissertation. First, we discuss the theoretical ideas that underlie practical first-principle

schemes.

CHAPTER

FOUR

FIRST-PRINCIPLES METHODS

In the previous chapter, we demonstrated how the conductance through a device can be calculated from a quantum-mechanical description of the system. In this chapter, we consider the problem of determining this quantum-mechanical description, focusing on methods that do this without any prior assumption about our device, other than it obeys the Schrödinger equation. This approach is referred to as a *first-principles* method, and draws significant success from its ability to predict new and unexpected phenomena.

We first explore the computational difficulty associated with determining the exact electronic structure when working directly with the many-body wavefunction. We then introduce the formalism of density functional theory, wherein the key parameter is the electronic density rather than the wavefunction. Through a series of approximations, we show how this formalism can be made practical for computing electronic structures from first principles, and discuss the limitations it holds that are particularly relevant to the study of electronic transport. We conclude this chapter with a discussion of the particular implementations used in this work.

4.1 Quasi-particles

The Hamiltonian for any system is known exactly, and can be written down as a sum of the electron kinetic energies and the interactions present in the material[1,2]

$$\begin{aligned}\hat{H} &= \hat{T} + \hat{U}_{\mathrm{e-e}} + \hat{V}_{\mathrm{ext}} \\ &= -\frac{1}{2}\sum_i \nabla_i^2 + \frac{1}{2}\sum_{i\neq j}\frac{1}{|\mathbf{r}_i - \mathbf{r}_j|} - \sum_{i,\alpha}\frac{Z_\alpha}{|\mathbf{r}_i - \mathbf{R}_\alpha|}.\end{aligned} \tag{4.1}$$

The three terms within this Hamiltonian represent the electron kinetic energy $\hat{T}$, the Coulombic electron-electron interaction $\hat{U}_{\mathrm{e-e}}$, and the electron-nuclei interaction $\hat{V}_{\mathrm{ext}}$. Latin indices correspond to sums over electrons, which are located at the positions $\mathbf{r}_i$; the Greek index is a sum over nuclei, located at positions $\mathbf{R}_\alpha$ with charge Z_α.

Whilst Eqn. (4.1) is exact, the form of this Hamiltonian is not well suited to quantum conductance calculations. The Landauer formalism is valid only in the limit of non-interacting particles, but making this approximation directly in Eqn. (4.1) corresponds to neglecting the strong interaction between the electrons, equivalent to setting $\hat{U}_{\mathrm{e-e}} = 0$, and is a poor approximation.

The interactions contained within Eqn. (4.1) are written in terms of individual electrons. Within a material, however, the notion of individual electrons becomes somewhat meaningless as the interaction between the electrons is strong and the motion of an individual electron is correlated with those around it. The fundamental excitations of a material are collective modes of many electrons, with behaviour that can be described as an ensemble of interacting particles, but with an interaction strength that is often much weaker than that between the individual electrons. These collective modes are termed quasi-particles, and are the fundamental excitations responsible for current flow within a material. To compute the conductance of a material, therefore, the Hamiltonian given in Eqn. (4.1) must be solved to determine its weakly-interacting quasi-particles.

[1] Here and throughout this thesis we make the adiabatic approximation[74], also known as the Born-Oppenheimer approximation, that neglects the quantum-mechanical nature of the ionic nuclei and treats them instead as stationary, charged classical particles. This is justified by the large difference in mass between electrons and the nuclei, a factor of ≈ 2000 for Hydrogen and larger for heavier nuclei, which results in the electronic structure relaxing rapidly to changes in the nuclear positions. In terms of the system Hamiltonian, this approximation neglects the kinetic energy of the nuclei and interactions between electrons and the lattice vibrations (electron-phonon interactions). The Coulombic interactions between pairs of nuclei are included simply as a classical electrostatic energy.

[2] We adopt atomic units: $e = 1$, $\hbar = 1$, $m_e = 1$.

4.2 The exact solution to the Schrödinger equation

For all but the most trivial of systems, there exists no analytic solution for the eigenstates of a Hamiltonian and instead numerical approaches are required. One method to do this is using the variational approach, which is in principle exact, however a direct approach to determine the eigenstates for a system is unfortunately unfeasible, as we now show.

4.2.1 The variational principle

Finding the eigenstates of the system Hamiltonian is equivalent to finding the stationary points of the energy functional

$$E[\Psi] = \frac{\langle\Psi|\hat{H}|\Psi\rangle}{\langle\Psi|\Psi\rangle}, \tag{4.2}$$

i.e. solving the variational equation $\delta E[\Psi] = 0$.

The proof of this comes by considering a small change to the wavefunction $|\Psi\rangle \rightarrow |\Psi\rangle + |\delta\Psi\rangle$. The corresponding change to the functional Eqn. (4.2) is

$$\begin{aligned}
\delta E[\Psi] &= E[\Psi + \delta\Psi] - E[\Psi] \\
&= \frac{\langle\Psi + \delta\Psi|\hat{H}|\Psi + \delta\Psi\rangle}{\langle\Psi + \delta\Psi|\Psi + \delta\Psi\rangle} - \frac{\langle\Psi|\hat{H}|\Psi\rangle}{\langle\Psi|\Psi\rangle} \\
&= \frac{\delta(\langle\Psi|\hat{H}|\Psi\rangle)}{\langle\Psi|\Psi\rangle} - \frac{\langle\Psi|\hat{H}|\Psi\rangle}{(\langle\Psi|\Psi\rangle)^2}\delta(\langle\Psi|\Psi\rangle) + O(\delta\Psi)^2 \\
&= \frac{1}{\langle\Psi|\Psi\rangle}\Big[\langle\delta\Psi|(\hat{H} - E[\Psi])|\Psi\rangle + \text{c.c.}\Big] + O(\delta\Psi^2),
\end{aligned} \tag{4.3}$$

where c.c. denotes the complex conjugate of the previous term and the Hermiticity of the Hamiltonian has been used. The variation $\delta E[\Psi] = 0$ is true to first order in $\delta\Psi$ when $\hat{H}|\Psi\rangle = E[\Psi]|\Psi\rangle$ which is exactly the condition that $|\Psi\rangle$ is an eigenstate of the Hamiltonian. The value of the energy functional at this stationary point is the corresponding eigenenergy of this state.

Furthermore, the wavefunction that places the $E[\Psi]$ at its global minimum stationary point is the ground-state wavefunction, with $E[\Psi]$ equal to the ground-state energy at that point. The proof of this statement comes by considering a wavefunction that is close to the ground-state $|\Psi_0\rangle$ with contributions from higher-energy states $|\Psi_i\rangle$, $i > 0$,

$$|\Psi\rangle = |\Psi_0\rangle + \sum_{i=1}^{\infty} c_i|\Psi_i\rangle. \tag{4.4}$$

Inserting Eqn. (4.4) into Eqn. (4.2) and using the orthogonality of the eigenstates gives

$$\begin{aligned} E[\Psi] &= \frac{E_0 + \sum_{i=1}^{\infty} E_i |c_i|^2}{1 + \sum_{i=1}^{\infty} |c_i|^2} \\ &= E_0 + \frac{\sum_{i=1}^{\infty} (E_i - E_0)|c_i|^2}{1 + \sum_{i=1}^{\infty} |c_i|^2} \end{aligned} \tag{4.5}$$

where E_0 is the ground-state energy and $E_i > E_0$ are the energies of the excited states. Therefore $E[\Psi] \geq E_0$, with equality only at the ground-state where $|\Psi\rangle = |\Psi_0\rangle$.[3]

The ground-state can therefore be computed, in principle, by minimising $E[\Psi]$ with respect to all trial wavefunctions $|\Psi\rangle$ that are anti-symmetric with respect to electron exchange as required for Fermionic statistics. Higher excited states can be computed by repeating this procedure for each desired state with the additional constraint that each subsequent eigenstate is orthogonal to all those previously calculated.

4.2.2 Exponential scaling

Although this procedure is exact and guaranteed to produce the entire spectrum of eigenstates, from a computational view it is completely impractical for all systems containing more than a few electrons. The issue arises because the method deals directly, and in an exact fashion, with the many-body wavefunction. In a real-space approach, the wavefunction depends on the positions of all N electrons in the system

$$\langle \{\mathbf{r}_i\} | \Psi \rangle = \Psi(\mathbf{r}_1, \mathbf{r}_2, \ldots, \mathbf{r}_N) \tag{4.6}$$

and is therefore an object of dimension $3N$. The size of this object therefore scales exponentially with number of electrons in the system and the Schrödinger equation rapidly becomes impossible to solve exactly, even numerically.

As an example, consider the memory requirements to store numerically the wavefunction for the first six atoms, up to carbon, of the periodic table. Here we consider only describing the wavefunction for a single isolated atom within a cubic box, a problem that bears little physical interest. Assuming a (somewhat coarse) discretisation of real space into 10 grid points in each cardinal direction, the number of grid points to describe the many-body wavefunction increases by a factor of $10^3 = 1000$ for each additional electron added to the system. Assuming a single byte of data storage per grid point (for simple estimation purposes), the memory foot print for each atom is of order: 1 kB for hydrogen; 1 MB for

[3] For systems with degenerate ground-states, the upper bound on the ground-state energy still holds; the corresponding wavefunction is contained within the subspace of degenerate ground-state wavefunctions.

helium; 1 GB for lithium, . . ., 1 EB for carbon *etc.*.[4]

Dealing directly with the wavefunction without any simplifying approximation is therefore unsuitable for any useful theoretical strategy. Whilst several approximation schemes that work with the wavefunction have been developed over the past century[83, 84, 85, 86], the method used within this thesis works instead directly with the electronic *density*, as we now explain.

4.3 Density functional theory

In 1964, Hohenberg and Kohn showed that there exists a route to the ground-state using the electronic density directly as the fundamental parameter.[87] As the electronic density is a three dimensional quantity for a system containing any number of electrons, the exponential scaling shown in section 4.2.2 in principle vanishes, giving the method an exceptional advantage over wavefunction approaches. As a result, the method has arguably become the method of choice in studying materials from first principles.

The main result of Hohenberg and Kohn is that all ground-state properties, including the ground-state energy, are functionals of the ground-state electronic density, giving rise to the name *Density Functional Theory* (DFT).

Before entering a discussion of DFT, we note that it is useful to partition the Hamiltonian as

$$\begin{aligned} \hat{H} &= (\hat{T} + \hat{U}_{\mathrm{e-e}}) + \hat{V}_{\mathrm{ext}} \\ &= \hat{F} + \hat{V}_{\mathrm{ext}} \end{aligned} \tag{4.7}$$

where $\hat{F} = \hat{T} + \hat{U}_{\mathrm{e-e}}$ is defined to be the sum of the kinetic and electron-electron Coulomb interactions and $\hat{V}_{\mathrm{ext}}$ is the electron-nuclei Coulomb interactions. This partitioning divides the Schrödinger equation into a part, $\hat{F}$, identical for all N-electron systems, and a part, $\hat{V}_{\mathrm{ext}}$, unique to the system under study.

4.3.1 The Hohenberg-Kohn theorems

The proof of Hohenberg and Kohn comes within two theorems. The first Hohenberg-Kohn theorem states:

HK 1. *The ground-state charge density for an N-electron system uniquely defines the external potential that it is generated by, up to a global constant.*

[4] Somewhat coincidentally, the memory footprint for carbon in this estimation scheme corresponds, roughly, to the maximum memory address space that can be stored within a 64-bit computer architecture.

The proof of this theorem proceeds by contradiction in two steps. Firstly we show that there is a one-to-one mapping between the external potential and its corresponding ground-state wavefunction. We then show that there is a one-to-one mapping between the ground-state wavefunction and the electronic density. The proof we show below relies on the assumption that the Hamiltonian has a non-degenerate ground-state, however the theorem can be extended to systems with degenerate ground-states using the formalism of Levy[88].

Consider two potentials $\hat{V}_{\text{ext}}$ and $\hat{V}'_{\text{ext}}$ that differ by more than an additive constant:

$$V'_{\text{ext}}(\mathbf{r}) - V_{\text{ext}}(\mathbf{r}) \neq \text{constant}. \tag{4.8}$$

Suppose that the N-electron ground-states for these potentials are $|\Psi_0\rangle$ and $|\Psi'_0\rangle$, with energies E_0 and E'_0 respectively. The Schrödinger equations for these potentials then satisfy

$$\hat{H}|\Psi_0\rangle = (\hat{F} + \hat{V}_{\text{ext}})|\Psi_0\rangle = E_0|\Psi_0\rangle \tag{4.9}$$

$$\hat{H}'|\Psi'_0\rangle = (\hat{F} + \hat{V}'_{\text{ext}})|\Psi'_0\rangle = E_0|\Psi'_0\rangle. \tag{4.10}$$

Assume now that the two potentials give rise to identical ground-states: $|\Psi_0\rangle = |\Psi'_0\rangle$. Subtracting Eqn. (4.9) from Eqn. (4.10) gives

$$(\hat{V}'_{\text{ext}} - \hat{V}_{\text{ext}})|\Psi_0\rangle = (E'_0 - E_0)|\Psi_0\rangle. \tag{4.11}$$

Inspecting this in a real-space representation, $\hat{V}_{\text{ext}}$ and $\hat{V}'_{\text{ext}}$ are multiplicative operators, meaning that for Eqn. (4.11) to hold

$$V'_{\text{ext}}(\mathbf{r}) - V_{\text{ext}}(\mathbf{r}) = E'_0 - E_0. \tag{4.12}$$

This violates our earlier assumption that the two potentials differ by more than an additive constant, thus proving that a given ground-state arises from a unique potential up to an additive constant and that there is a one-to-one mapping between the external potential and the ground-state wavefunction

$$\hat{V}_{\text{ext}} \Rightarrow \Psi_0. \tag{4.13}$$

For the second part of the proof, consider the relationship between the ground-state wavefunction and the ground-state density

$$n_0(\mathbf{r}) = N \int \Big(\prod_{i=2}^{N} \mathrm{d}^3\mathbf{r}_i \Big) \big|\Psi_0(\mathbf{r}, \mathbf{r}_2, \ldots, \mathbf{r}_N)\big|^2. \tag{4.14}$$

Assume that there are two different N-electron ground-states, $|\Psi_0\rangle$ and $|\Psi'_0\rangle$, that give rise to the same electronic density. As shown just now, these ground-states must arise from

different external potentials $\hat{V}_{\text{ext}}$ and $\hat{V}'_{\text{ext}}$, and hence different Hamiltonians $\hat{H}$ and $\hat{H}'$. The corresponding ground-state energies are $E_0 = \langle\Psi_0|\hat{H}|\Psi_0\rangle$ and $E'_0 = \langle\Psi'_0|\hat{H}'|\Psi'_0\rangle$. The variational principle asserts the strict inequality[5]

$$\begin{aligned} E_0 < \langle\Psi'_0|\hat{H}|\Psi'_0\rangle &= \langle\Psi'_0|\hat{H}' + \hat{V}_{\text{ext}} - \hat{V}'_{\text{ext}}|\Psi'_0\rangle \\ &= E'_0 + \int \mathrm{d}^3\mathbf{r}\,\big(V_{\text{ext}}(\mathbf{r}) - V'_{\text{ext}}(\mathbf{r})\big)n_0(\mathbf{r}). \end{aligned} \tag{4.15}$$

A similar argument starting with E'_0 gives

$$\begin{aligned} E'_0 < \langle\Psi_0|\hat{H}'|\Psi_0\rangle &= \langle\Psi_0|\hat{H} + \hat{V}'_{\text{ext}} - \hat{V}_{\text{ext}}|\Psi_0\rangle \\ &= E_0 + \int \mathrm{d}^3\mathbf{r}\,\big(V'_{\text{ext}}(\mathbf{r}) - V_{\text{ext}}(\mathbf{r})\big)n_0(\mathbf{r}). \end{aligned} \tag{4.16}$$

Summing these inequalities leads to the contradiction

$$E'_0 + E_0 < E_0 + E'_0 \tag{4.17}$$

proving that there is a one-to-one mapping between the ground-state wavefunction and ground-state density

$$\Psi_0 \Rightarrow n_0. \tag{4.18}$$

Combining Eqns. 4.13 and 4.18 establishes a one-to-one mapping between the external potential and the ground-state electronic density

$$\hat{V}_{\text{ext}} \Rightarrow \Psi_0 \Rightarrow n_0, \tag{4.19}$$

proving the first Hohenberg-Kohn theorem.

The first Hohenberg-Kohn theorem therefore proves that a given *N*-electron ground-state charge density uniquely determines the external potential that creates that density, the ground-state wavefunction and hence also all ground-state properties of the system.

Due to the mapping between the ground-state wavefunction and density, a functional can now be defined for an arbitrary external potential $V(\mathbf{r})$ unrelated to $V_{\text{ext}}(\mathbf{r})$

$$E_V[n] = \langle\Psi[n]|\hat{F} + \hat{V}|\Psi[n]\rangle = F[n] + \int \mathrm{d}^3\mathbf{r}\,V(\mathbf{r})n(\mathbf{r}) \tag{4.20}$$

where square brackets indicate an implicit functional dependence of the quantity on the electronic density and $F[n] = \langle\Psi[n]|\hat{F}|\Psi[n]\rangle$ is a functional universal for all *N*-electron systems.

From this, the second Hohenberg-Kohn theorem can be established

[5]Note that equality is not allowed as $|\Psi'_0\rangle$ cannot be the ground-state of $\hat{H}$ by the first part of the first Hohenberg-Kohn theorem. The wavefunctions are assumed normalised $\langle\Psi_0|\Psi_0\rangle = 1$.

HK 2. *$E_V[n] \geq E_0$ where E_0 is the ground-state energy, with equality occurring only where $n(\mathbf{r})$ is the ground-state density $n_0(\mathbf{r})$.*

Proof of this comes from the variational theorem. The trial density $n(\mathbf{r})$ determines an external potential $\hat{V}_{\text{ext}}$ and ground-state $|\Psi\rangle$. Using this ground-state as a trial ground-state for the Hamiltonian with external potential $\hat{V}$ gives

$$\begin{aligned}\langle\Psi[n]|\hat{H}|\Psi[n]\rangle &= \langle\Psi[n]|\hat{F}+\hat{V}|\Psi[n]\rangle \\ &= F[n] + \int \mathrm{d}^3\mathbf{r}\, V(\mathbf{r})n(\mathbf{r}) \\ &= E_V[n] \geq E_0. \end{aligned} \tag{4.21}$$

Therefore, the ground-state energy and density to the Schrodinger equation can be determined by minimising the functional in Eqn. (4.20) directly with respect to the electronic density.[6]

The Hohenberg-Kohn theorems provide a powerful proof that the ground-state electronic density contains, through a functional dependence, the information of all ground-state properties of a system of electrons interacting within an array of static nuclei. The exponential cost associated with working directly with the exact many-body wavefunction is lifted and replaced, in principle, with the linearly-scaling cost of the electronic density.

4.3.2 The Kohn-Sham mapping

Whilst the Hohenberg-Kohn theorems provide the proof of principle that the electronic density may be used as the fundamental parameter in determining the ground-state properties, a practical difficulty arises due to the universal *N*-electron functional $F[n]$ which is unknown except through its implicit dependence on the many-body wavefunction, itself a functional of the density. Dealing directly with the many-body wavefunction is unacceptable and exactly the problem that is to be avoided, and therefore a method to approximate $F[n]$ is required.

There exist a number of approaches that directly approximate the functional $F[n]$[92, 93, 94, 95, 96, 97, 98], but their success has been limited to bulk metallic systems where

[6] A small caveat exists with this approach as the minimisation must proceed only over those densities that can be created by an external potential, the so-called *v*-representability problem; examples have been found of trial densities for which there exists no external potential[89, 90, 91]. This problem can be solved by an alternative approach to the one presented here, the constrained search formulation,[88] that removes this constraint, and instead imposes much weaker constraints on the trial densities which are more generally satisfied.

the electron density more closely resembles the free electron gas, and these approaches are not appropriate for the study of carbon nanotubes. Indeed, the difficulties faced with generating approximations for $F[n]$ are associated with the inherently many-body aspect of the wavefunctions with which it is implicitly defined. An approach which has found much wider success is due to Kohn and Sham[99] as we now describe.

Considering the many-body interacting system, we may solve variationally for the ground-state density

$$\delta\left[F[n] + \int \mathrm{d}^3\mathbf{r}\; n(\mathbf{r})V_{\mathrm{ext}}(\mathbf{r}) - \mu\left(\int \mathrm{d}^3\mathbf{r}\; n(\mathbf{r}) - N\right)\right] = 0 \tag{4.22}$$

where we have introduced the Lagrange multiplier μ to constrain the number of electrons to be N.

Kohn and Sham suggested that one might hope that the functional $F[n]$ could be approximated by that for a non-interacting system of N electrons. They proposed partitioning the functional, without approximation, as

$$F[n] = T_s[n] + E_H[n] + E_{\mathrm{xc}}[n], \tag{4.23}$$

where, $T_s[n]$ represents the kinetic energy of the system of N non-interacting electrons,

$$E_H[n] = \frac{1}{2}\int \mathrm{d}^3\mathbf{r}\; \mathrm{d}^3\mathbf{r}'\; \frac{n(\mathbf{r})n(\mathbf{r}')}{|\mathbf{r}-\mathbf{r}'|} \tag{4.24}$$

the Hartree energy due to the classical electrostatic interactions of the electrons, and E_{xc} the exchange-correlation correction energy, which is by definition the difference between the non-interacting system and the interacting system, and is hoped to be the smaller contribution.[7]

The solution to Eqn. (4.22) is given by the Euler-Lagrange equation:

$$\frac{\delta T_s}{\delta n} + \int \mathrm{d}^3\mathbf{r}'\; \frac{n(\mathbf{r}')}{|\mathbf{r}-\mathbf{r}'|} + \frac{\delta E_{\mathrm{xc}}}{\delta n} + V_{\mathrm{ext}}(\mathbf{r}) = \mu \tag{4.25}$$

where $\delta T_s/\delta n$, $\delta E_{\mathrm{xc}}/\delta n$ represent the (unknown) functional derivatives of the non-interacting kinetic energy and the exchange-correlation energy.

The key observation of Kohn and Sham is that one arrives at the exact same solution for a system of non-interacting electrons moving in the potential

$$V_{\mathrm{KS}}(\mathbf{r}) = \int \mathrm{d}^3\mathbf{r}'\; \frac{n(\mathbf{r}')}{|\mathbf{r}-\mathbf{r}'|} + V_{\mathrm{xc}}[n](\mathbf{r}) + V_{\mathrm{ext}}(\mathbf{r}) \tag{4.26}$$

[7] The name exchange-correlation is historic due to the Hartree-Fock method for electronic structure, which preceded DFT; see section 4.3.3.

where $V_{\rm xc}[n](\mathbf{r}) = \delta E_{\rm xc}/\delta n$ implicitly defines the exchange-correlation potential.

The ground-state density for the exact interacting and the fictitious non-interacting Kohn-Sham systems are therefore identical, and can be obtained from the occupied eigenstates of the Kohn-Sham equation:

$$\Big[-\frac{1}{2}\nabla^2 + V_{\rm KS}(\mathbf{r})\Big]\psi_i(\mathbf{r}) = \epsilon_i\psi_i(\mathbf{r}) \tag{4.27}$$

$$n_0(\mathbf{r}) = 2\sum_i^{N/2} |\psi_i(\mathbf{r})|^2 \tag{4.28}$$

where the factors of 2 and $N/2$ in the sum account for double state occupancy due to an assumed (but not necessary) electron spin degeneracy and our notation makes clear the distinction between the many-body and single particle wavefunctions Ψ and ψ respectively. The Lagrange multiplier μ is set by the constraint on electron number, and must lie between the $\epsilon_{N/2}$ and $\epsilon_{N/2+1}$ eigenenergies of the non-interacting system.

As $V_{\rm KS}$ depends on $n(\mathbf{r})$, which in turn depends on $V_{\rm KS}$, one must look for a self-consistent solution for $V_{\rm KS}$ and $n(\mathbf{r})$, which can be achieved through iterative techniques.[100]

4.3.3 The exchange-correlation functional

The Kohn-Sham scheme is, again in principle, exact however the problem of the unknown universal functional $F[n]$ has been shifted to another unknown functional $E_{\rm xc}[n]$, the exchange-correlation functional, which must be approximated. What is remarkable about the Kohn-Sham scheme is that surprisingly crude approximations for the exchange-correlation functional can reproduce experimentally measured parameters with a good degree of accuracy. Indeed, it is important to bear in mind that it is only due to this agreement with experiment that the validity of calculations using DFT has received any confidence.

In the simplest approximation, exchange and correlation are dependent only on the local density and is known therefore as the Local Density Approximation (LDA):

$$E_{\rm xc,LDA}[n] = \int \mathrm{d}^3\mathbf{r}\; n(\mathbf{r})\epsilon_{\rm LDA}(n(\mathbf{r})), \tag{4.29}$$

$$V_{\rm xc,LDA}[n](\mathbf{r}) = \epsilon_{\rm LDA}(n(\mathbf{r})) + n(\mathbf{r})\frac{\partial\epsilon_{\rm LDA}(n(\mathbf{r}))}{\partial n}. \tag{4.30}$$

The function $\epsilon_{\rm LDA}(n(\mathbf{r}))$ has been determined analytically at high densities by Gell-Mann and Brueckner [101] and numerically at low densities by Ceperley and Alder [102] based on calculations of the homogeneous electron gas for which it is exact. In this work we use the parametrisation for $\epsilon_{\rm LDA}$ by Perdew and Zunger[103].

The LDA is typically better suited to materials in which the density is slowly varying, and hence most closely resembles the homogeneous electron gas from which it is derived. Great success has been found in the LDA for periodic crystalline materials where electron homogeneity is better observed, but finite-sized systems have proved more challenging as the transition from molecule to vacuum manifestly requires significant density gradients for which the exchange and correlation cannot be captured by the local density only. Indeed, the LDA results in an incorrect exponential localisation of the exchange-correlation energy density whereas the correct limit is asymptotically Coulombic into the vacuum[104, 105]. Furthermore, non-local effects such as van der Waals interactions cannot be described by the local functional. Consequently, the LDA description of inter-molecular binding is poor.

A first step beyond the LDA is to use a semi-local functional dependent on local density gradients $\nabla n(\mathbf{r})$, the so-called Generalised Gradient Approximations (GGA). This extension can be done in a manner that satisfies known conditions of the true exchange-correlation functional producing a gradient-corrected approximation to the true functional that is derived from first principles. These functionals are generally considered to improve the description of molecular systems and are the functionals of choice within this work for studying carbon nanotubes. In this dissertation, we use the GGA functional due to Perdew, Burke and Ernzerhof (PBE)[106].

Further classes of functionals exist that invoke different approximations or try to overcome various shortcomings found with other functionals (see section 4.3.5). We mention briefly a few relevant to this thesis.

An important method, which actually precedes DFT historically and is strictly a wavefunction-based method not a density functional, is that of Hartree-Fock (exact) exchange.[84] Here, the required anti-symmetry of the Fermionic electron wavefunction under exchange of electronic co-ordinates is explicitly enforced, e.g.

$$\Psi(\mathbf{r}_1, \mathbf{r}_2, \ldots) = -\Psi(\mathbf{r}_2, \mathbf{r}_1, \ldots), \tag{4.31}$$

and results in an exchange energy and a non-local exchange potential

$$E_x = -\frac{1}{2}\sum_{nn'} \int \mathrm{d}^3\mathbf{r}\, \mathrm{d}^3\mathbf{r}'\, \psi_n^*(\mathbf{r})\psi_n^*(\mathbf{r}')\frac{1}{|\mathbf{r}-\mathbf{r}'|}\psi_{n'}^*(\mathbf{r})\psi_{n'}^*(\mathbf{r}'), \tag{4.32}$$

$$\begin{aligned}\hat{V}_x\phi(\mathbf{r}) &= \int \mathrm{d}^3\mathbf{r}'\, V_x(\mathbf{r},\mathbf{r}')\phi(\mathbf{r}') \\ &= -\frac{1}{2}\sum_n \psi_n(\mathbf{r}) \int \mathrm{d}^3\mathbf{r}'\, \frac{\psi_n^*(\mathbf{r}')\phi(\mathbf{r}')}{|\mathbf{r}-\mathbf{r}'|}\end{aligned} \tag{4.33}$$

where the sums are performed over the occupied states ψ_n and $\phi(\mathbf{r})$ is an arbitrary state that is being acted upon by the non-local exchange operator $\hat{V}_x$. This method, which

should be noted is considerably more expensive than the semi-local functionals presented above, removes the interaction of an electron with its own electric field (the so-called self-interaction error, see section 4.3.5) by cancelling exactly the contribution to the Hartree energy that arises from an electron interacting with itself. Electron correlation effects are neglected entirely however, which can lead to poor agreement with experimental results. Hybrid functionals attempt to correct for this by incorporating fractions of exact exchange with contributions from semi-local functionals whilst retaining a non-local exchange-correlation potential and removing part of the self-interaction error.[107] The relative fractions of the local and non-local contributions are determined empirically however and therefore the use of hybrid functionals is not strictly a first-principles technique.

A somewhat recent development has been classes of non-local van der Waals density functionals (vdW-DF) which attempt to capture the weak dispersion interactions that are poorly described by semi-local functionals.[108] In section 7.5, we use the functional of Dion *et al.* in the efficient implementation of Román-Pérez and Soler[108, 109], to study from first principles the weak forces that arise from dispersion interactions between CNTs.

It is worth noting that the great number of proposed exchange-correlation functionals represents a philosophical challenge for marrying density functional theory with the goal of first-principles calculations. It is the opinion of this author that the theorist using density functional theory can learn most about an unknown system from using a small set of exchange-correlation functionals, with well understood limitations, and accepting that a calculated result will not exactly reproduce experiment. The predictive power of density functional theory comes not from getting a known answer right, but rather from being able to predict an unknown answer with a reasonable degree of confidence.

4.3.4 Quasi-particles from density functional theory

Despite the success of density functional theory, there is an elephant in the room for the purposes of this thesis. The foundations of the Hohenberg-Kohn theorems refer only to the ground-state properties of the system, yet the flow of current is not a ground-state property. Indeed, this chapter was started by discussing the need to calculate the quasi-particles of a system and density functional theory was suggested as a suitable method.

The resolution to this problem again comes from a theoretically dubious approximation that only becomes justified *post-hoc* by comparison of results generated by DFT to experiment and higher levels of theory. Throughout this work, we make the following assumption:

The quasi-particles to the real many-body system are the same as the corresponding

single-particle eigenstates of the Kohn-Sham Hamiltonian.

Heuristically, it appears reasonable that this approach may offer some success as the Kohn-Sham eigenstates are determined self-consistently with the mean-field potential and density. There is, however, no theoretical justification to this assumption as the Kohn-Sham system is an auxiliary system that was introduced solely because it produces the correct ground-state density and allows computation of the ground-state energy.

Theoretical investigations have shown that properties derived from the Kohn-Sham Hamiltonian are good approximations to those derived from the true interacting Hamiltonian [110, 111], at least for materials where the quasi-particles are not strongly interacting. Further, the agreement with experiment for DFT-calculated properties, such as band structures[112], electron energy loss spectra[113], NMR spectra[114], and most importantly electronic transport[115, 116], provide good confidence in the method. Note, however, that there are cases where the Kohn-Sham eigenvalues fail to reproduce experimentally-measured quantities, see section 4.3.5.

In this work, transport Hamiltonians that are determined from first principles make use of the Kohn-Sham Hamiltonian. The exact procedure for achieving this is the focus of chapter 5.

4.3.5 Limitations of density functional theory

Before discussing practical implementations, we finally note some additional known limitations with density functional theory, the problem of determining quasi-particles having already been discussed in section 4.3.4.

The Kohn-Sham band gap

In addition to problems with describing quasi-particles, the Kohn-Sham band gap, defined as the energy difference between the highest occupied and lowest unoccupied Kohn-Sham eigenvalues, is typically found to seriously underestimate the experimentally determined band gap. This problem is particularly severe for the semi-local functionals (LDA, or GGA levels of theory) where the calculated band gap can be a less than 50% of the measured value. For a detailed discussion of the origin of this problem, see [117].

The dispersion relations of conduction bands are typically found to be in good agreement with experiment, however, and a common fix to the band gap issue, where needed, is to shift the entire conduction spectrum of states upwards in energy to correct only for the band gap,

referred to as applying a scissor operator.[112, 118] Such an approach can be complicated, however, by defect states that are located within the gap.

In terms of electron transport calculations, aside from conductance within the conductance band occurring at lower energies, an underestimated band gap may have an impact on the calculated ballistic conductance in the valence or conduction bands. The effect is likely to be small, however, which can be understood from perturbation theory. Consider conductance in the valence band. The lowest-order scattering contribution involving the conduction band arises at second order as conductance is assumed ballistic: scattering must occur from an initial state in the valence band, to an intermediate conduction band state, and then finish in a valence band state. This second-order contribution is suppressed by a factor of $1/\Delta E$ where ΔE is the energy difference between the conduction and valence bands, and is of order the band gap. The suppression is automatically present in Kohn-Sham DFT, and such contributions are expected to be negligible for semiconductor materials where the band gap is $\gtrsim$ eV; increasing the band gap with a scissor operator correction will only suppress this small contribution further and does not appreciably change the calculated conductance.

Self-interaction error

As briefly mentioned in section 4.3.3, semi-local approximations to exchange and correlation introduce self-interaction error which introduces an incorrect interaction between an electron and its own electric field. This can be understood by comparing the Kohn-Sham equation for a single electron in an external potential

$$\Big[-\frac{1}{2}\nabla^2 + \int \mathrm{d}^3\mathbf{r}' \, \frac{n(\mathbf{r}')}{|\mathbf{r}-\mathbf{r}'|} + V_{\mathrm{xc}}[n](\mathbf{r}) + V_{\mathrm{ext}}(\mathbf{r}) \Big] \psi_i(\mathbf{r}) = \epsilon_i \psi_i(\mathbf{r}), \tag{4.34}$$

to the true Schrödinger equation, which is exactly

$$\Big[-\frac{1}{2}\nabla^2 + V_{\mathrm{ext}}(\mathbf{r}) \Big] \psi_i(\mathbf{r}) = \epsilon_i \psi_i(\mathbf{r}). \tag{4.35}$$

A self-interaction error arises in this case, but also more generally, if the exchange-correlation potential does not exactly cancel the interaction of the electron with its own electron density. For the one electron Hamiltonian in Eqn. (4.34) this corresponds to the violation

$$\int \mathrm{d}^3\mathbf{r}' \, \frac{n(\mathbf{r}')}{|\mathbf{r}-\mathbf{r}'|} + V_{\mathrm{xc}}[n](\mathbf{r}) \neq 0. \tag{4.36}$$

Note that Eqn. (4.36) can never be satisfied for a semi-local approximation to exchange and correlation.

The presence of this error causes an increased delocalisation of the occupied eigenstates due to repulsion from its own electronic density. This has the effect of decreasing the rate of decay of Hamiltonian matrix elements into the vacuum, resulting in an overestimation of tunnelling rates. This is of particular relevance to the conductance geometry discussed in chapter 7.

Dispersion interactions

As also briefly mentioned in section 4.3.3, semi-local functionals describe weak dispersion interactions poorly. These interactions are important in non-bonded systems, which include CNT bundles.

One solution is the non-local van der Waals functionals described in section 4.3.3, but an alternative is to introduce empirical corrections described as additional energy contributions dependent on the distances between pairs of nuclei.[119, 120] Whilst not a first-principles technique, this method offers a computationally inexpensive solution to the problem and is the method used in this thesis where a more accurate treatment of dispersion is not required.

4.4 Practical implementations

We now focus on the practical implementations of the Kohn-Sham DFT scheme that have been used in this work. The need for different implementations and approximations can largely be condensed into a compromise between the accuracy and computational cost of studying a system, and the principle factor that affects this compromise is the method used to describe the wavefunctions.

4.4.1 Basis sets

Within this work, two classes of codes are used which differ mainly in the choice of basis set to describe the wavefunctions that solve the Kohn-Sham equations (Eqn. (4.28)). Each wavefunction is considered a weighted sum of the basis functions

$$\psi_n(\mathbf{r}) = \sum_i c_{in}\phi_i(\mathbf{r}). \tag{4.37}$$

Whilst any basis set could in principle be used, practical considerations favour different choices which we now discuss, focusing on the implementations used in this work. Common amongst all implementations is truncation of the basis set, rendering the expansion in Eqn. (4.37) finite in size.

In all cases, the details of how the ground-state self-consistent electronic structure is reached is beyond the scope of this thesis, and we refer the reader to the specific references for that implementation.

Plane-wave basis: CASTEP**,** PWSCF

In a plane-wave implementation, the Kohn-Sham wavefunctions are described using a large number of plane-wave basis functions[8]

$$\phi_i(\mathbf{r}) = \exp\left[i\mathbf{G}_i \cdot \mathbf{r}\right]. \tag{4.38}$$

The c_{in} coefficients are exactly the Fourier transform, or the reciprocal-space representation, of the wavefunction.

To render the basis finite, two requirements are met. Firstly, the calculation is performed within a finite simulation cell, lattice vectors $\mathbf{a}_1$, $\mathbf{a}_2$, $\mathbf{a}_3$, with periodic boundary conditions forcing the plane-wave wavevectors $\mathbf{G}_i$ to be integer sums of the corresponding reciprocal lattice vectors $\mathbf{b}_1$ etc.:

$$\mathbf{G}_i = n_{1i}\mathbf{b}_1 + n_{2i}\mathbf{b}_2 + n_{3i}\mathbf{b}_3 \tag{4.39}$$

$$\mathbf{b}_1 = 2\pi\frac{\mathbf{a}_2 \times \mathbf{a}_3}{\mathbf{a}_1 \cdot \mathbf{a}_2 \times \mathbf{a}_3} \text{ etc..} \tag{4.40}$$

Secondly, the basis set is truncated by choosing a cut-off energy E_{cut} which defines the maximum kinetic energy of the plane waves included in the calculation

$$\frac{1}{2}|\mathbf{G}_i|^2 < E_{\text{cut}}. \tag{4.41}$$

The advantage of this approach is that a single parameter E_{cut} determines the quality of the basis set; increasing this parameter is guaranteed to improve the accuracy of the calculation by virtue of the variational principle (Eqn. (4.2)). For systems requiring large simulation cells, however, the number of basis functions becomes very large which limits the maximum system size that can be studied in a reasonable amount of time. For the study of CNTs, the plane-wave basis is particularly inefficient due to the large regions of vacuum which are described using the same level of detail as bonding regions. Furthermore, the basis functions are delocalised across the entire simulation cell meaning that a transformation to an equivalent localised basis, for example using maximally localised Wannier functions[121, 122], must be performed before this method can be used to compute quantum conductances (see chapter 5).

[8]Here we assume that the Brillouin zone is sampled at the Γ point only; see section 4.4.3.

Within this work, two plane-wave codes are used: CASTEP [123] and PWSCF, of the QUANTUM ESPRESSO package[124]. The use of these implementations is largely restricted to determining the optimum geometry for smaller systems containing up to several hundred atoms.

Localised numerical orbital basis: SIESTA

For the study of systems containing hundreds or thousands of atoms, an alternative approach is required. The SIESTA method[125] relies on a far smaller basis of non-orthogonal numerical orbitals, localised on each atom. As these orbitals are strictly localised in real-space, no basis function is required to describe regions where the wavefunction is negligibly small and hence the vacuum regions are essential free. Matrix elements can also be computed efficiently by noting that matrix elements between orbitals that do not directly overlap must be zero and therefore do not need to be calculated explicitly. Further, the quantum conductance can be computed directly within this basis.

These orbitals are generated by solving the Kohn-Sham equations for an isolated atom[9] and including orbitals with a desired symmetry or angular momentum. For example, a carbon atom may contribute one *s*-type and three *p*-type orbitals to the basis. The method is analogous to the linear combination of atomic orbitals method, or the tight-binding model introduced in section 2.3.1 except with the tight-binding parameters calculated from first principles. The electronic density itself is described on a real-space grid with grid-spacing determined by a cut-off energy, however adjusting this parameter should not be confused with changing the quality of the basis.

To improve the ability of the basis to describe more accurately a wider range of wavefunctions, the above minimal set of basis functions is augmented using a variety of schemes as described in Ref. [126]. One technique is to radially divide an orbital into two or more orbitals, referred to as ζ-splitting, to allow additional freedom in describing wavefunctions close to the nuclei and in the inter-atomic bonding regions. A second approach is to introduce higher angular momentum channels by exposing an orbital to an electric field and incorporating the first-order perturbation to the orbital into the basis. This is referred to as orbital polarisation. The difficulty with these approaches is in ensuring that the basis has sufficient freedom to describe the electronic structure, and improving the basis is more complicated than simply increasing the kinetic energy cut-off as done in a plane-wave approach.

[9] Strictly speaking, only the valence orbitals are solved for in the pseudo-atom; the orbitals from core electrons are removed by the pseudopotential approximation. See section 4.4.2.

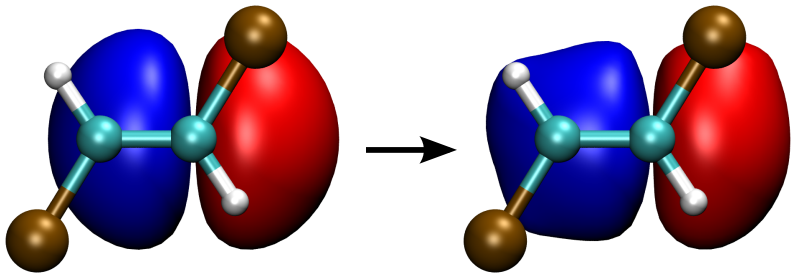

Figure 4.1: A single NGWF centred on one carbon atom of an trans-dichloroethene molecule before (left) and after (right) optimisation in ONETEP.

Optimised localised numerical orbital basis: ONETEP

The final and main implementation used within this thesis is the ONETEP method.[127] Similarly to the SIESTA implementation, a set of localised atom-centred numerical atomic orbitals are used as the basis. These orbitals are termed non-orthogonal generalised Wannier functions (NGWFs)[128].

Rather than working with a large set of fixed basis functions, a smaller set of NGWFs are used which are iteratively optimised *in situ* during the calculation to accurately describe the local chemical environment. Each NGWF is localised within a localisation radius and described in terms of a basis of periodic cardinal sine functions (*psincs*) which are equivalent to plane-waves.[128] The quality of the basis is guaranteed to improve by increasing the NGWF localisation radius and the equivalent kinetic energy cut-off of the *psinc* functions.

The resulting basis set of NGWFs is a compact yet accurate basis, allowing for the study of semiconducting/insulating[129] or metallic[130] systems containing thousands of atoms yet retaining the accuracy of plane-wave methods.[131, 132] In Fig. 4.1, we compare the initial guess for an NGWF to the fully optimised NGWF centred on one carbon atom of a dichloroethene molecule.

4.4.2 The pseudopotential approximation

An additional approximation used in all the implementations described in section 4.4.1 is the pseudopotential approximation which we now describe.

Each atom present in a neutral material contributes a number of electrons equal to its atomic number. The contribution from these electrons to bonding differs, however, based on the energies of those electrons in the neutral atom. The core electrons, lying lowest in energy, are tightly bound to the nucleus and therefore do not strongly interact with electrons

from other nuclei or contribute significantly to bonding. The valence electrons, lying highest in energy, are less strongly bound and dominate bonding.

The idea of the pseudopotential approximation is to remove the explicit inclusion of the core electrons, and instead reintroduce them as an effective screening of the bare-ionic Coulomb potential resulting in a much weaker effective potential close to the nucleus.

This procedure achieves two computational efficiencies. Firstly, the number of electrons in the system is reduced, thereby reducing the number of occupied Kohn-Sham eigenstates that must be computed. Secondly, the screening causes the valence wavefunctions to be much smoother, allowing the use of a much coarser real-space grid, or fewer plane waves with lower kinetic energy cut-off. This second point can be understood from the requirement that the true valence wavefunctions are orthogonal to the localised core wavefunctions, necessitating their rapid oscillation in the core-region. Removing the core wavefunctions allows the pseudised wavefunctions to be smoother within the core region. The relationships between the pseudised and all-electron wavefunctions and potential are illustrated in Fig. 4.2; note that the pseudised wavefunction is nodeless and considerably smoother than the all-electron wavefunction and so is expected to be described by a coarser real-space grid/fewer plane-waves with greater accuracy.

A detailed discussion of the procedure for generating and using pseudopotentials can be found in Ref. [133, 134]; we mention here the more pertinent points. A pseudopotential is defined with respect to an inner cut-off radius r_{c}, typically less than 1 Å for the lighter elements. Outside of this radius, the pseudopotential and pseudised wavefunction are identical to their all-electron counterparts

$$\begin{aligned} \psi_{\mathrm{ps}}(r) &= \psi(r) \\ V_{\mathrm{ps}}(r) &= V(r) \end{aligned} \quad \text{for } r > r_{\mathrm{c}}; \tag{4.42}$$

within the cut-off radius, a smoother pseudised wavefunction is chosen and the corresponding potential that creates this wavefunction, the pseudopotential, is calculated by inverting the Schödinger equation. The success of any pseudopotential comes from its ability to use the potential in different chemical situations, its *transferability*. One method to increase transferability is to ensure the same normalisation of the real and pseudised wavefunctions, a property referred to as *norm-conservation*[135]. In this work, we use norm-conserving pseudopotentials in the Kleinman-Bylander form[136] generated using the RRKJ method[137].

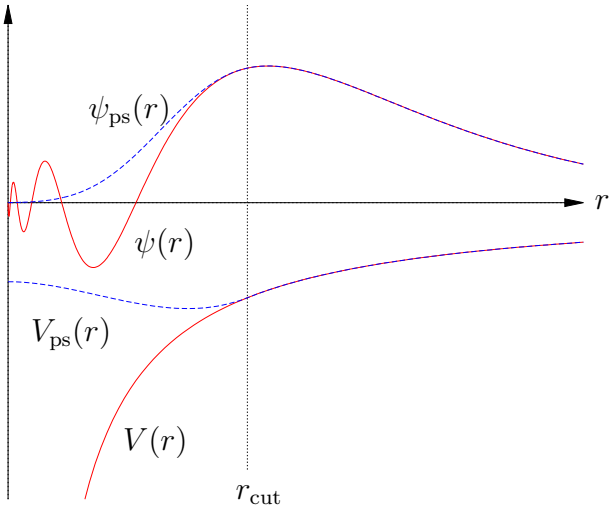

Figure 4.2: An illustration of the pseudopotential approximation. The all-electron wavefunction $\psi(r)$ and unscreened potential $V(r)$ are compared to their pseudised counterparts $\psi_{\rm ps}(r)$ and $V_{\rm ps}(r)$ for an isolated atom.

4.4.3 Periodic and aperiodic systems

In the final part of this chapter we discuss the boundary conditions used in the calculations in this thesis. In a plane-wave implementation, periodic boundary conditions are forced by the choice of basis; in local numerical orbital methods, any boundary condition could be used but computational efficiencies favour periodic boundary conditions,[10] and are the boundary conditions used within SIESTA and ONETEP. For a comprehensive discussion of periodic boundary conditions in electronic structure calculations, see [74].

Bloch's theorem[26] provides the methodology for computing electronic structure under periodic boundary conditions. The wavefunction becomes the product of a wave-like part and a function that satisfies the simulation cell periodicity

$$\psi_{n,\mathbf{k}} = \exp(i\mathbf{k}\cdot\mathbf{r})u_{n,\mathbf{k}}(\mathbf{r}). \tag{4.44}$$

[10]For instance, computing the Hartree potential can be performed most efficiently in reciprocal space:

$$V_{\rm H}(\mathbf{r}) = \int \mathrm{d}^3\mathbf{r}'\,\frac{n(\mathbf{r}')}{|\mathbf{r}-\mathbf{r}'|} \quad \rightarrow \quad \widetilde{V}_{\rm H}(\mathbf{G}) = \frac{4\pi}{\Omega_{\rm cell}}\frac{\widetilde{n}(\mathbf{G})}{|\mathbf{G}|^2}, \tag{4.43}$$

where $\widetilde{V}$, $\widetilde{n}$ are the Fourier transforms of the Hartree potential and electronic density, and $\Omega_{\rm cell}$ is the unit cell volume. The Hartree potential in real-space is then obtained by inverse Fourier transform. This procedure replaces integrals over the whole simulation cell for each $\mathbf{r}$ with the considerably computationally faster Fourier transform, multiplication and inverse transform.

Due to the periodicity of the wave-like part, the wavefunctions are unique only for vectors $\mathbf{k}$ lying within the principle Brillouin zone, defined as the primitive unit cell in reciprocal space.

In order to calculate quantities such as the electronic density, the wavefunctions must be sampled at every point within the Brillouin zone and the contributions integrated. In practice, wavefunctions with similar $\mathbf{k}$ are themselves sufficiently similar to allow the wavefunctions at one *k*-point to represent a region of the Brillouin zone. The integral over the Brillouin zone then becomes an average over a finite number of *k*-points.

The volumes of the simulation cell Ω_{cell} and Brillouin zone Ω_{BZ} are related by

$$\Omega_{\mathrm{BZ}} = \frac{(2\pi)^3}{\Omega_{\mathrm{BZ}}} \tag{4.45}$$

so that for very large unit cells the Brillouin zone can be accurately sampled by a single *k*-point only which is chosen in this work to be $\mathbf{k} = \mathbf{0}$, known as the Γ point.

Within this work, the study of aperiodic systems, or systems with periodicity in fewer than all three directions, is still performed with periodic boundary conditions. The aperiodic directions are made large to minimise fictitious interactions between periodic images. This is known as the supercell approximation, and is illustrated for a carbon nanotube in Fig. 4.3.

4.5 Summary

In this chapter, we have described an efficient methodology for calculating the electronic structure of an ensemble of atoms using density functional theory. We are now in a position to describe how these electronic structures can be used to compute the ballistic conductance of a material, which is the focus of the next chapter.

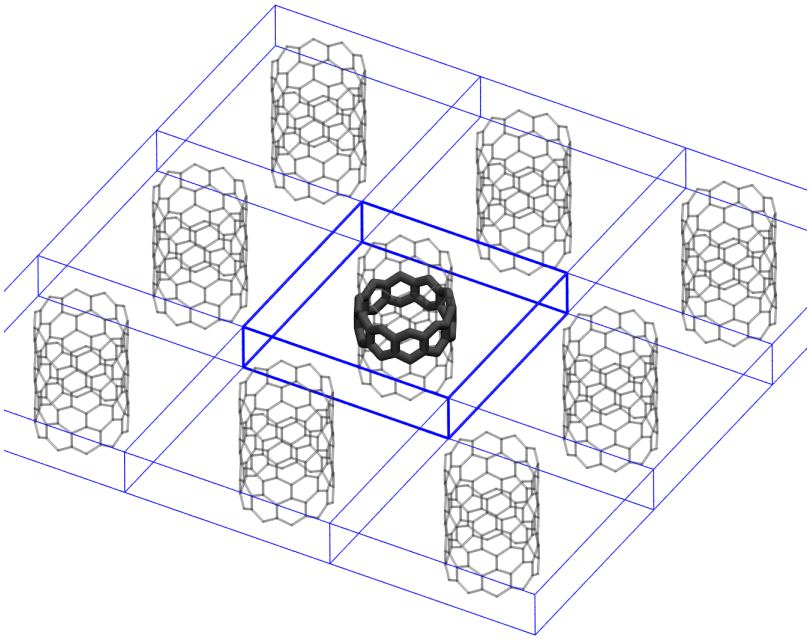

Figure 4.3: The simulation cell for a CNT. The atoms included in the calculation are shown by the heavy grey structure in the centre; its periodic images are shown in lighter grey. The blue boxes give the simulation cell and its periodic images. Directions perpendicular to the CNT axis are treated with the supercell approximation; directions along the CNT axis are properly periodic.

CHAPTER

FIVE

FIRST-PRINCIPLES ELECTRONIC TRANSPORT

In the previous chapter, we showed how the Hamiltonian that describes the electronic structure of a system can be computed using the density functional theory formalism to map the many-body problem onto an effective single-body problem of non-interacting electrons. Whilst the Hamiltonian for these non-interacting electrons is not identical to the true many-body Hamiltonian, we justified its use, with caution, by comparing results to those from experimental studies and higher levels of theory. In this chapter, we identify how the ground-state Kohn-Sham Hamiltonian can be used to build the Hamiltonian for a device. Whilst there exist formal procedures to couple density functional theory with the non-equilibrium Green's function (NEGF) technique, which self-consistently build the charge density from the scattering states within the device (e.g. see [138], see also appendix A), in this chapter we describe a simplification of this method that uses a non self-consistent approach whereby a conventional Kohn-Sham ground-state DFT calculation is used to describe conduction at zero-bias. This implementation is based within the ONETEP linear-scaling DFT project[127] and has been submitted for publication.[139]

5.1 Introduction

As a result of the drive towards miniaturisation of electronic devices and the fabrication of nanostructured materials, there is great interest in theoretical methods to calculate their charge transport characteristics. Approaches that provide a full atomistic description are particularly appealing, and are invaluable in improving our understanding of such devices, and optimising their performance.

A popular method to determine the conductance properties of nanoelectronic devices

combines the framework of Landauer transport [66, 67, 68] with a description of electronic structure determined from first-principles[87, 99]. As discussed in the previous chapter, the advantage of this approach is in its predictive power that comes from a fully-quantum mechanical treatment of conductance with an unbiased and accurate description of electronic structure. Whilst there are limitations regarding its validity in certain situation[140], approaches combining Landauer transport with density functional theory (DFT)[87, 99] have been remarkably successful in describing a wide variety of materials [141, 142, 143].

Several computational implementations of this approach exist [138, 144, 145, 146, 147, 148, 149, 150, 151, 152, 153] and, for a given amount of available computing resource, there is a trade-off to be made between accuracy and the size of the system that can be simulated. Existing implementations can be broadly categorized into two classes. The first relies on very large sets of simple basis functions, such as plane-waves, in order to compute the electronic structure accurately and with systematically improvable accuracy, within the limitations of the underlying theory (e.g., the choice of exchange-correlation functional, pseudopotentials, etc.). A subsequent transformation to a much smaller, if not minimal, set of localized Wannier functions then enables efficient transport calculations[121, 154, 146, 152, 153]. In this approach it is the computational cost of the underlying electronic structure calculation, which scales asymptotically cubically with respect to system size for traditional methods, that severely limits the ability of this method to study realistic devices.

In a second class of methods, the electronic structure is calculated using a fixed basis set of localised functions, such as Gaussians [145, 155] or numerical atomic orbitals [148, 138, 144], and the same basis set is then used to calculate the transport properties of the device. There are competing requirements here because an accurate description of the electronic structure often requires a large basis set, typically several times larger than the minimal Wannier function basis, yet using this same basis for calculating transport properties results in much higher computational cost than if a minimal basis is used. In the case of an atomic-like orbital basis, therefore, it is the cost of computing transport properties that often restricts the accessible system size.

The trade-off between accuracy and system-size poses a problem for simulations of realistic devices as, typically, several thousands of atoms or more may need to be included to capture the characteristics of the device faithfully.

In this chapter we present an approach that combines the advantages of both classes of method described above to calculate Landauer transport from first-principles using a small basis, whilst retaining plane-wave accuracy. Our implementation is within the ONETEP linear-scaling DFT project[127], which uses a small basis of localised orbitals, called non-

orthogonal generalised Wannier functions (NGWFs)[156], that are represented in terms of an underlying systematic basis of Fourier-Lagrange, or *psinc*, functions equivalent to a set of plane-waves[128]. The NGWFs are optimised *in situ* to their unique chemical environment[156] such that plane-wave accuracy is achieved. Transport properties are calculated efficiently within the same basis. See section 4.4.1 for more details of the ONETEP implementation.

Our implementation can be used to calculate transport through devices connected to an arbitrary number of leads and containing thousands of atoms on a routine basis using even relatively modest parallel computational resources. Chapter 7 demonstrates its scope and applicability through a study of inter-tube electron transport in carbon nanotube networks; the focus of this chapter is to describe our methodology.

The rest of this chapter is organised as follows: we first recapitulate the results of section 3.3.4, focusing specifically on their application to the ONETEP implementation; section 5.2 gives details of our specific implementation within the ONETEP code; we discuss the optimisations in our implementation that enable the study of transport in very large systems in section 5.3, and the calculation of the bulk-lead band structures and eigenchannels in multi-lead devices in section 5.4. In section 5.5, we give example applications of our method to conduction in a poly-acetylene molecular chain and conduction between end-terminated CNTs, focusing in both cases on the practical aspects[1]. Finally, in section 5.7 we summarise our findings.

5.1.1 Preliminaries and definitions

Recall from section 3.3.4 that the standard geometry considered in the Landauer-Büttiker formalism consists of a number of semi-infinite leads connected to a central scattering region. The leads act as current sources and sinks, and are assumed to couple only through the device region. Current must flow through the device region to travel between two leads. Scattering occurs in the central region only, and is assumed to occur elastically.

The most general transport setup involves transmission between leads of different material or structure, through a central device region with arbitrary geometry. We refer to this transmission as *device* transmission. A special case is when the full device, i.e. central region and leads, is formed from the same bulk material. Such a system has no scattering and transmission takes an integer value determined by the number of transmission modes available at that energy. We refer to this special case as *bulk* transmission.

[1] Chapter 7 presents a more detailed study of conduction between end-terminated CNTs.

5.1.2 Non-orthogonal basis

As the NGWF basis functions employed in the ONETEP method are non-orthogonal, the results presented in section 3.3.4 must be modified. It is straightforward to show[2] that the device Green's function is given by

$$\mathsf{G}_{\mathrm{d}}(E) = \left[(E + i\eta)\mathsf{S}_{\mathrm{d}} - \mathsf{H}_{\mathrm{d}} - \mathsf{\Sigma}_1(E) - \mathsf{\Sigma}_2(E) - \dots\right]^{-1}, \tag{5.1}$$

and the device density of states is

$$\mathcal{N}_{\mathrm{d}}(E) = -\frac{1}{\pi}\,\mathrm{Im}\,\mathrm{tr}\left[\mathsf{G}_{\mathrm{d}}\mathsf{S}_{\mathrm{d}}\right]. \tag{5.2}$$

where H_{d} is the device Hamiltonian, S_{d} is the overlap matrix and $\mathsf{\Sigma}_i(E)$ is the self energy for lead i, where all matrices are in the NGWF basis. The remaining quantities in section 3.3.4 remain unchanged.

5.2 Constructing the device matrices

In this section we describe our procedure for computing the transmission coefficients for a device and semi-infinite leads from a single ground-state DFT calculation. A transport calculation follows as a post-processing step after a ground state electronic structure calculation.

The method involves two structures, shown schematically for a two-lead system in Fig. 5.1. (Each lead is indexed by L/R to indicate the left/right lead. The geometries extend straightforwardly to multi-lead devices.) The geometry in Fig. 5.1a, which we refer to as the *transmission geometry*, is the system for which the transmission properties are to be calculated. The electronic structure of this representation, however, is not explicitly calculated. Instead, a ground-state electronic structure calculation is performed on what we refer to as the *auxiliary simulation geometry*, shown in Fig. 5.1b, which is then used to build the device Hamiltonian and overlap matrices of the transmission geometry of Fig. 5.1a. The transmission geometry is an open system with semi-infinite leads, whilst the auxiliary simulation geometry is, in our implementation, periodically repeated, due to the periodicity of the underlying psinc basis set used in the electronic structure calculation.

From Eqn. (5.1) it can be seen that the matrices required are the device Hamiltonian H_{d}, overlap S_{d}, and each lead self energy $\mathsf{\Sigma}_i$. These matrices are constructed from matrix blocks obtained from an electronic structure calculation on the auxiliary simulation geometry. As

[2] See the derivation presented in appendix A.

the NGWF basis functions are atom-centred, these matrix blocks can be unambiguously associated with regions of real space and the atoms contained within these regions.

Throughout this chapter, we will denote device matrices that have been *constructed* in uppercase sans-serif, e.g. H_d. These are large matrices that are the size of the entire device. The smaller matrix blocks used to build these matrices are *extracted* from the ground-state calculation on the auxiliary simulation geometry and are denoted in lowercase bold, e.g. $\boldsymbol{h}_{LC}$.

5.2.1 Lead self energies

We first focus on the matrix elements required to determine the lead self energies Σ_i. The electronic structure of the quasi-one dimensional leads can be efficiently described in terms of *principle layers*, defined as the minimal stacking unit that is sufficiently large that matrix elements between localised functions in non-adjacent principle layers are zero. With NGWFs, this is achieved exactly when the principle layer is larger than the maximum NGWF diameter, or can be approximated by neglecting matrix elements between non-adjacent principle layers.

The electronic structure of the lead is then defined exactly by two blocks of Hamiltonian and overlap matrix elements: the block between NGWFs within the same principle layer $\boldsymbol{h}_{00}$, $\boldsymbol{s}_{00}$, and the block between NGWFs in adjacent principle layers $\boldsymbol{h}_{01}$, $\boldsymbol{s}_{01}$. This structure can be seen in the two leads in Fig. 5.1a.

Once these matrix element blocks are determined, the calculation of the lead self energies can be efficiently performed using the iterative method of Lopez-Sancho *et al.*[157].

5.2.2 The auxiliary simulation geometry

We now discuss how the device Hamiltonian and overlap matrices are constructed from the auxiliary simulation DFT geometry. The auxiliary simulation DFT structure must contain enough of the device structure such that the device matrices H_d, S_d can be extracted directly. The definition of the device region is not unique, however, as an arbitrary amount of each lead can be included. The inclusion of large amounts of lead region is unnecessary and increases computational expense; by including just two principle layers of each lead, the device Hamiltonian and overlap matrices and the principle layer matrices necessary to construct the lead self energies, i.e., all matrices required to compute the transmission through the device, can be extracted from a single ground-state DFT calculation on the auxiliary simulation geometry.

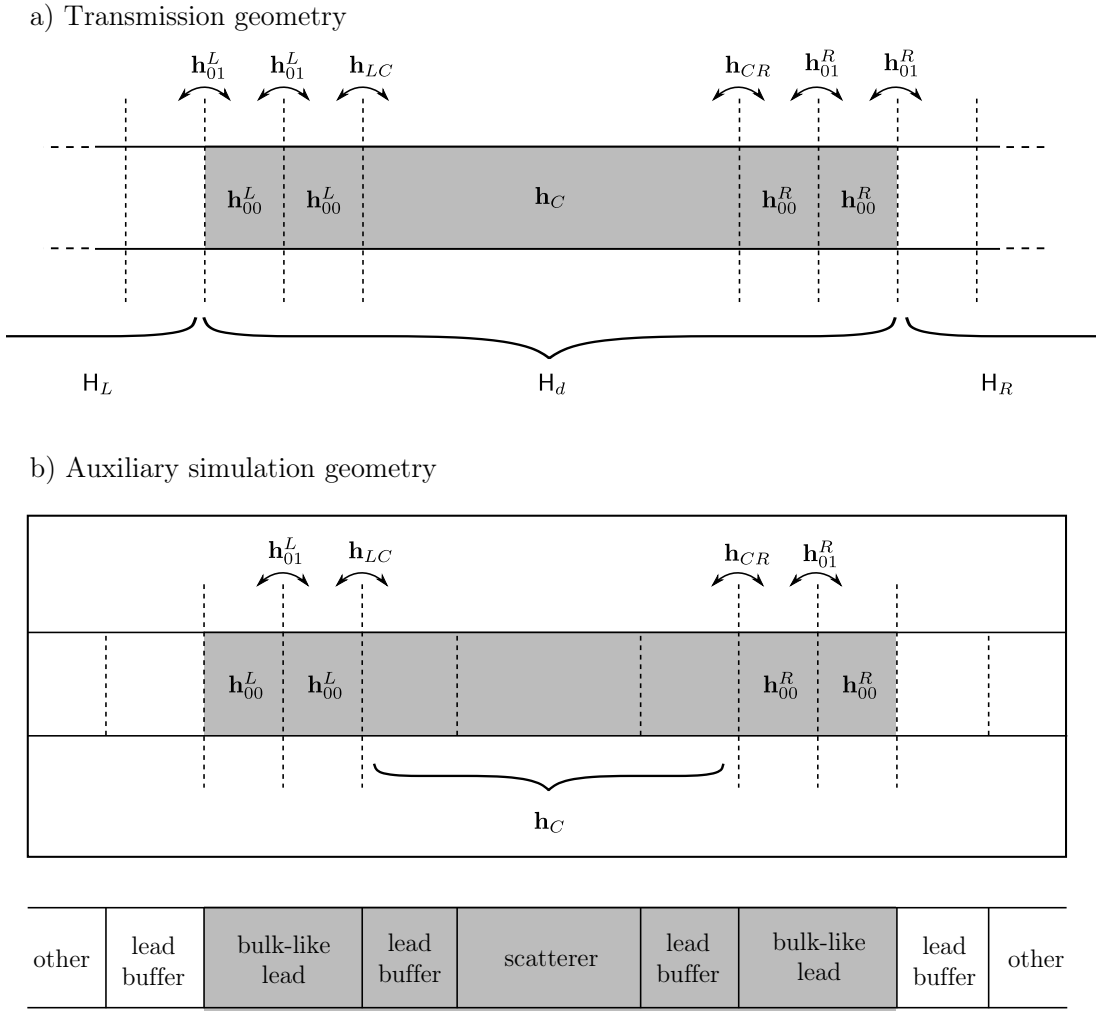

Figure 5.1: The schematic geometry of a two-lead device. a) The transmission geometry that is to be simulated. Dashed lines indicate the lead principle layers. Open boundary conditions are used and the left and right leads are semi-infinite. b) The auxiliary simulation geometry for which the DFT ground-state is computed. The surrounding black box gives the periodic DFT simulation cell. Matrix elements are extracted from this calculation and used to build the device matrices in the transmission geometry. Annotating each diagram are the location of the matrix elements within each structure (see main text, $\mathsf{H}_{L/R}$ are the Hamiltonians describing the leads). The bottom panel gives a description of each region within the auxiliary simulation geometry. The shading defines the regions that are included in building the device matrix elements; in the transmission geometry, the non-shaded region is included using the lead self energies; in the auxiliary simulation geometry, the non-shaded regions are used to achieve bulk-like electronic structure within the lead regions but are not included in the device matrices. The auxiliary simulation geometry may be a truncated/finite system, or use the simulation cell periodic boundaries.

In Fig. 5.1, the spatial extent of the device is indicated with a grey shaded box. The locations of the matrix blocks within this device are also indicated for each geometry.

To ensure that the lead self energies accurately represent their bulk form, the lead matrix blocks $\boldsymbol{h}_{00}$, $\boldsymbol{h}_{01}$ etc., must be extracted from a region where the local electronic structure has converged to the bulk for that lead. This can always be achieved by including a sufficient amount of 'buffer' lead material adjacent to the central scattering region such that the system contains lead regions that are bulk-like from which to extract $\boldsymbol{h}_{00}$ and $\boldsymbol{h}_{01}$. These buffer regions are then included as part of the Hamiltonian of the scattering region $\boldsymbol{h}_C$. If within the auxiliary simulation geometry the leads are terminated (e.g. Fig. 5.5), then there is also the need for buffer regions of lead material to screen the influence of the termination, as indicated in Fig. 5.1b.

Typically, a lead principle layer will contain multiple primitive lead unit cells. The periodic symmetry of these unit cell matrix elements is not guaranteed, however, as the unit cells are different distances from the central scattering region. To restore this periodicity, we explicitly symmetrise the lead Hamiltonian and overlap matrix elements by averaging equivalent matrix blocks.

Outside the device region, the auxiliary simulation geometry can take any form that is convenient for the ground-state DFT calculation. Our approach is very flexible and allows calculation of transmission through any device geometry connected to an arbitrary number of leads.

A major advantage of this procedure is the ease with which the device matrices can be constructed from a suitable auxiliary simulation geometry. All submatrices are automatically identified by a list of atoms that define the device, and the subsets of these atoms that form the two principle layers for each lead. As this can all be done using matrix elements from a single ground-state DFT calculation, the Hamiltonian blocks of the leads and device already share the same background potential. This contrasts with approaches that build the device matrices from multiple ground-state DFT calculations, where the local chemical potential must be aligned at the interface between matrix elements derived from different calculations.[146]

5.3 Optimisation strategies

We now discuss the particular optimisation strategies that we have used to increase the system sizes that can be studied using our method.

An important part of our implementation is its ability to exploit the sparsity of the

device Hamiltonian and overlap matrices as this greatly increases the capability of the implementation to study large systems.[145]

Due to the strict localisation of the NGWF basis functions, the device matrices are very sparse. For example, the device Hamiltonian for the two-lead system shown schematically in Fig. 5.1a takes a tri-diagonal form

$$\mathsf{H}_{\mathrm{d}} = \begin{pmatrix} \boldsymbol{h}_{00,L} & \boldsymbol{h}_{01,L} & \cdot & \cdot & \cdot \\ \boldsymbol{h}_{01,L}^{\dagger} & \boldsymbol{h}_{00,L} & \boldsymbol{h}_{LC} & \cdot & \cdot \\ \cdot & \boldsymbol{h}_{LC}^{\dagger} & \boldsymbol{h}_{C} & \boldsymbol{h}_{CR} & \cdot \\ \cdot & \cdot & \boldsymbol{h}_{CR}^{\dagger} & \boldsymbol{h}_{00,R} & \boldsymbol{h}_{01,R} \\ \cdot & \cdot & \cdot & \boldsymbol{h}_{01,R}^{\dagger} & \boldsymbol{h}_{00,R} \end{pmatrix}, \tag{5.3}$$

where the matrix blocks are defined in Fig. 5.1a and blocks of elements that are zero are denoted by a dot. The device overlap matrix takes the same form.

The lead self energies have greater sparsity, and are only non-zero on the block diagonal of the lead principle layer furthest from the central scattering region, e.g. for the left lead in Fig. 5.1a

$$\Sigma_L = \begin{pmatrix} \boldsymbol{\sigma}_L & \cdot & \cdot & \cdot & \cdot \\ \cdot & \cdot & \cdot & \cdot & \cdot \\ \cdot & \cdot & \cdot & \cdot & \cdot \\ \cdot & \cdot & \cdot & \cdot & \cdot \\ \cdot & \cdot & \cdot & \cdot & \cdot \end{pmatrix}. \tag{5.4}$$

This is a direct consequence of including at least one lead principle layer in the device region: the only spatial bulk-like region of the device that has non-zero matrix elements with the rest of the lead is the final principle layer of lead furthest from the central scattering region. The lead coupling matrices, Γ_L etc., take the same sparsity pattern, with the non-zero block denoted $\boldsymbol{\gamma}_L = i(\boldsymbol{\sigma}_L - \boldsymbol{\sigma}_L^{\dagger})$.

This sparsity can be used to improve the performance of the evaluation of the transmission coefficients. By evaluating the matrix products in Eqn. (3.9) and using the sparsity of the coupling matrices Γ_i, the transmission coefficients for a two-lead device can be evaluated as

$$T(E) = \mathrm{tr}\Big[\boldsymbol{\gamma}_L\, \boldsymbol{g}_{LR}\, \boldsymbol{\gamma}_R\, \boldsymbol{g}_{LR}^{\dagger}\Big], \tag{5.5}$$

where $\boldsymbol{g}_{LR}$ is the off-diagonal block of the retarded Green's function between all NGWFs belonging to the left and right leads. An identical relation is found for multi-lead devices.

For the two-lead device geometry in Fig. 5.1a, the required Green's function block is

located within the top right of the device Green's function

$$\mathsf{G}_{\mathrm{d}} = \begin{pmatrix} \cdot & \cdot & \cdot & \cdot & \boldsymbol{g}_{LR} \\ \cdot & \cdot & \cdot & \cdot & \cdot \\ \cdot & \cdot & \cdot & \cdot & \cdot \\ \cdot & \cdot & \cdot & \cdot & \cdot \\ \cdot & \cdot & \cdot & \cdot & \cdot \end{pmatrix}, \tag{5.6}$$

where the dots refer not to zero blocks, but instead to blocks that do not need to be calculated. Note that the sizes of the matrix blocks in Eqn. (5.5) depend only on the size of the lead principle layers and not on the size of the entire device.

The block $\boldsymbol{g}_{LR}$ is computed using a block tri-diagonal Gaussian elimination algorithm[158, 159]. This method is exact and directly computes this block only, removing the need to compute or store the dense device Green's function. At no point is it necessary to store the device Hamiltonian and overlap in dense form, allowing very efficient memory use. The device density of states Eqn. (5.2) can similarly be computed efficiently using the same block tri-diagonal algorithm.

The efficacy of the block tri-diagonal inverse algorithm depends on the particular transport geometry. However, for quasi one-dimensional systems, including devices connected by multiple quantum wires, it asymptotically scales linearly with number of basis functions in both operation count and memory requirements. This should be compared to standard dense matrix inversion routines, such as LAPACK[160], for which memory requirements and operation count scale respectively as the square and cube of the number of basis functions.

Our method has been implemented to make use of parallel architectures using the Message Passing Interface (MPI). The majority of the calculation is spent determining the transmission spectrum which is evaluated over a set of linearly-spaced energies within a user-defined energy window. As each evaluation of the transmission is independent, each MPI process takes a subset of the energies and performs the calculation in serial. Once matrix element data has been distributed among the processes, no communication between them is required and the calculation exhibits ideal scaling with the number of processes. As a result of these optimisations, our implementation is able to tackle very large systems.

5.4 Properties beyond the transmission coefficients

5.4.1 Properties of the leads

As the lead matrix elements and self energies are not derived from a separate bulk-lead calculation, it is important to be able to assess how accurately the bulk-like region of the auxiliary simulation geometry describes the true bulk lead. A simple assessment can be made by comparing the band structure generated by the lead matrix elements $\boldsymbol{h}_{00}$, $\boldsymbol{h}_{01}$ etc., which we will refer to as the *lead band structure*, to the true bulk band structure obtained from a separate calculation.

The lead band structure ϵ_{nk} is calculated using a non self-consistent Fourier interpolation approach, solving the generalised eigenvalue problem

$$\boldsymbol{h}_k \boldsymbol{u}_n = \epsilon_{nk} \boldsymbol{s}_k \boldsymbol{u}_n \tag{5.7a}$$

$$\boldsymbol{h}_k = \boldsymbol{h}_{00} + e^{ik}\boldsymbol{h}_{01} + e^{-ik}\boldsymbol{h}_{01}^\dagger \tag{5.7b}$$

$$\boldsymbol{s}_k = \boldsymbol{s}_{00} + e^{ik}\boldsymbol{s}_{01} + e^{-ik}\boldsymbol{s}_{01}^\dagger, \tag{5.7c}$$

where $\boldsymbol{h}_k$, $\boldsymbol{s}_k$ are the lead Hamiltonian and overlap matrices at a general k-point where k is in fractional units of the reciprocal lattice vector.[3] This procedure is computationally inexpensive allowing for a dense k-point sampling.

5.4.2 Eigenchannels for multi-lead devices

We have also implemented a method to decompose the total transmission into contributions from eigenchannels. Our implementation is, as far as we are aware, the first example within a modern first-principles code to allow eigenchannels to be computed for multi-lead devices. The procedure to generate the eigenchannels follows Paulsson and Brandbyge[161] (see also Appendix A); in the following discussion, we first outline this method for the special case of two-lead systems before providing our extension for multi-lead devices.

An eigenchannel decomposition achieves two things: firstly for leads with multiple conduction channels, the contributions from each channel can be isolated; and secondly the spatial form of the scattering state within the device can be computed, thus indicating the locations of scattering within the device.

[3] For principle layers containing multiple primitive lead unit cells, the band structure for a single primitive lead unit cell can be obtained by replacing the principle layer matrix blocks by equivalent primitive unit cell matrix blocks, and modifying Eqn. (5.7) to include contributions from non-adjacent primitive unit cells, e.g. introducing $\boldsymbol{h}_{02}$, $\boldsymbol{s}_{02}$ etc..

The channels are defined as superpositions of scattering states injected in a lead, and are non-mixing in the sense that the transmission of a scattering state $|\psi\rangle$ that is a superposition of multiple eigenchannels $|\chi_n\rangle$ is given by the corresponding weighted sum of the eigenchannel transmissions: i.e.

$$|\psi\rangle = \sum_n \alpha_n |\chi_n\rangle \tag{5.8a}$$

$$T \quad = \sum_n |\alpha_n|^2 T_n \tag{5.8b}$$

where $|\chi_n\rangle$ and T_n are eigenchannels and the corresponding eigenchannel transmissions. There is no interference term in the transmission as the channels are non-mixing.

We now summarise the results of Ref. [161]. For a two-lead device with leads labelled L, R, the (propagating and non-propagating) scattering states $|\widetilde{\chi}_l^L\rangle$ which are injected into the device by lead L can be computed by diagonalising the lead spectral function

$$\mathsf{A}_L = \mathsf{G}\mathsf{\Gamma}_L\mathsf{G}^\dagger = 2\pi \sum_l |\widetilde{\chi}_l^L\rangle\langle\widetilde{\chi}_l^L|. \tag{5.9}$$

These scattering states are used to compute the transmission matrix for this lead, defined using the Fisher-Lee relation[75] as

$$\mathsf{T}^L = (\mathsf{t}^L)^\dagger \mathsf{t}^L, \tag{5.10}$$

where t^L is the transmission amplitude matrix for scattering states originating in lead L. It is worth noting that the trace of Eqn. (5.10) gives the total transmission but the transmission matrix is not the same as the matrix products defined in Eqn. (3.9). The elements $(\mathsf{t}^L)_{lm}$ define the transmission amplitude for the scattering state $|\widetilde{\chi}_l^L\rangle$ injected in lead L, to the scattering state $|\widetilde{\chi}_m^R\rangle$ received in lead R. The indices l and m run over all scattering states in the left and right lead, respectively.

The matrix t^L is not explicitly computed, but instead the elements of the transmission matrix (Eqn. (5.10)) are calculated using

$$\left(\mathsf{T}^L\right)_{l'l} = 2\pi \langle\widetilde{\chi}_{l'}^L|\mathsf{\Gamma}_R|\widetilde{\chi}_l^L\rangle. \tag{5.11}$$

The unitary combination of scattering states that makes Eqn. (5.11) diagonal define the eigenchannels, which are computed as the eigenvectors of the matrix defined in Eqn. (5.11); the corresponding eigenvalues give the eigenchannel transmission. The superposition of scattering states can then be constructed in the NGWF basis to plot the spatial form of the eigenchannels.

The eigenchannels produced using this method are normalised, allowing direct comparison of multiple states by relative amplitude.

We now provide our extension for multi-lead devices. For devices containing more than two leads, we define the eigenchannels as the superposition of scattering states injected by lead i that are non-mixing. Note that eigenchannels are computed for each source lead with respect to all other leads together, rather than eigenchannels between each pair of leads. The eigenchannels calculated this way determine how a state injected into lead i propagates throughout the entire device, and contributions from this state may be received in *any* other lead $j \neq i$.

To achieve this, we return to the definition of the transmission matrix using the Fisher-Lee relation (Eqn. (5.10)). For multi-lead devices, the incident scattering state $|\widetilde{\chi}^i_l\rangle$ can be received in any conduction channel of a drain lead $|\widetilde{\chi}^j_{m_j}\rangle$. The transmission amplitude matrix must include separate contributions from each drain lead and has elements $(\mathsf{t}^i)_{lm}$, where l still runs over all scattering states in the source lead i, but now $m = \{m_j\}$ runs over all scattering states in all other leads $j \neq i$, with m_j indexing the scattering states in lead j. The elements of the transmission matrix become

$$(\mathsf{T}^i)_{l'l} = \sum_m (\mathsf{t}^i)^*_{l'm}(\mathsf{t}^i)_{lm} \tag{5.12a}$$

$$= \sum_{j\neq i} \Big[\sum_{m_j} (\mathsf{t}^i)^*_{l'm_j}(\mathsf{t}^i)_{lm_j} \Big]. \tag{5.12b}$$

The term in square brackets is recognised as the transmission matrix evaluated between the source lead and a single drain lead, and using Eqn. (5.11), the transmission matrix becomes

$$\big(\mathsf{T}^i\big)_{l'l} = 2\pi \sum_{j\neq i} \langle \widetilde{\chi}^i_{l'} | \mathsf{\Gamma}_j | \widetilde{\chi}^i_l \rangle. \tag{5.13}$$

The eigenchannels and their corresponding transmissions are computed by diagonalising Eqn. (5.13), with the scattering states determined as in Eqn. (5.9).

From Eqn. (5.13), it can be seen that the only modification is that the self energy of the drain leads $j \neq i$ is summed. This can be understood straightforwardly by considering all conducting channels of all drain leads together as part of a single effective lead. The self energy of this effective lead is simply the sum of the self energies of the constituent leads.

As the matrices involved in Eqns. (5.9) and (5.13) are the same size as the device Hamiltonian and, in contrast to the computation of the transmission coefficients, as the matrix sparsity cannot easily be exploited, calculating the eigenchannels is considerably more computationally demanding than computing the transmission coefficients alone. Plotting the eigenchannels, however, is typically only required at a few energies rather than across

the entire transmission spectrum. We therefore adopt a different parallelisation strategy for computing the eigenchannels, whereby each eigenchannel calculation is distributed over all processes and linear algebra operations occur in parallel using the ScaLAPACK library[162]. This implementation makes use of distributed memory and computation, greatly increasing the system size that can be studied.

If only the eigenchannel transmissions without spatial description are required, distributing the calculations over energy points is still possible by again exploiting again the sparsity of the coupling matrices Γ_i. The eigenchannel transmissions originating from lead i are computed as the eigenvalues of the matrix[161]

$$\bar{\boldsymbol{T}}^i = \sum_{j \neq i} \boldsymbol{\gamma}_i \boldsymbol{g}_{ij} \boldsymbol{\gamma}_j \boldsymbol{g}_{ij}^\dagger, \tag{5.14}$$

i.e. the sum of the matrices defined by the products in Eqn. (5.5). Note that this matrix is not the transmission matrix given in Eqn. (5.13), but shares the same eigenvalues and eigenvectors[161]. The sizes of these matrices depend only on the size of the principle layers in the leads and therefore the calculation scales independently of system size and can be computed in serial, as with the total transmission.

5.5 Applications

We apply our implementation to two systems to demonstrate the methods that we have developed. The first is a relatively small (67 atoms for the underlying DFT calculation) polyacetylene wire with a single nitrogen substitution, for which it is possible to make direct comparison with results obtained using other implementations for calculating conductance. The second system is much larger containing 610 atoms and computes the tunnelling current between two terminated carbon nanotubes.

Unless otherwise stated, electronic structures were determined using an $850\ \mathrm{eV}$ kinetic energy cutoff for the psinc basis, exchange and correlation was treated using the PBE generalised gradient approximation[106], and the Brillouin zone was sampled at the Γ point only. Core electrons were described using norm-conserving pseudopotentials in Kleinman-Bylander form[136], and non-periodic directions were treated using the supercell approximation, with at least $10\ \text{Å}$ separation between periodic images. A small basis of NGWFs were used, with four per carbon and nitrogen ion, and one per hydrogen ion. We define the Fermi energy as the average mean gap level of the leads of the device; throughout this section we set the Fermi energy to zero.

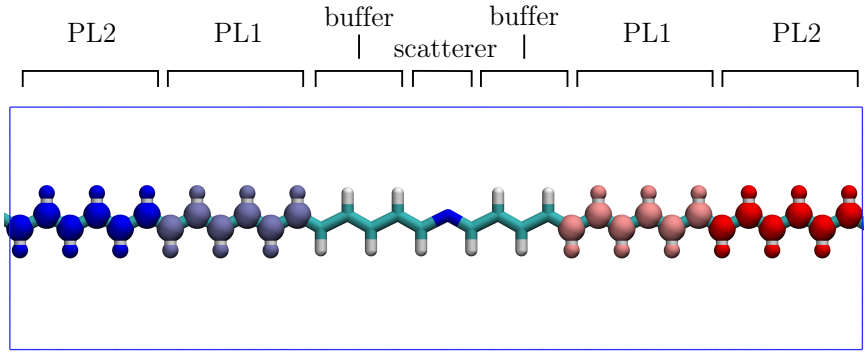

Figure 5.2: The geometry of the poly-acetylene wire with a single nitrogen substitution in the centre. The lead principle layers (PL) are indicated by dark/light coloured spheres and labelled above the geometry. The periodic simulation cell is donated by the surrounding blue box.

5.5.1 Poly-acetylene wire

We first describe our results for a 67 atom poly-acetylene wire with a single nitrogen substitution as shown in Fig. 5.2. The entire auxiliary simulation geometry is included in the device; in the auxiliary simulation geometry, periodic boundary conditions make the two leads adjacent meaning that each acts as a bulk-lead buffer region for the other lead ensuring that the local lead electronic structure is bulk-like. The short-circuit between the leads across the periodic boundary is automatically removed when building the device Hamiltonian/overlap using the method described in section 5.2. The NGWF localisation radius was set to 3.7 Å, which results in lead principle layers defined exactly by three primitive unit cells, as indicated in Fig. 5.2.

In Fig. 5.3, we compare the lead band structure that is derived from the auxiliary simulation geometry (solid lines) to the bulk lead band structure calculated for a single periodic poly-acetylene unit cell (open circles) calculated separately using the plane-wave DFT code CASTEP [123][4]. The agreement is very good for the valence bands and first conduction band, confirming that the leads are sufficiently far from the nitrogen substitution that the electronic structure has converged to that of the bulk lead. We note that a series of bands appearing above 3 eV are not captured by our method. These correspond to states that are delocalised in the vacuum and not on the poly-acetylene molecule and are therefore properties of the vacuum and depend on the size of the simulation cell. Contributions from these states to conduction in the poly-acetylene molecule appear only at high energies where

[4]The calculation uses the same pseudopotentials and, as far as possible, parameter set. During the self-consistent field calculation of the ground state, the Brillouin zone was sampled at 8 equally spaced points along the periodic direction.

electrons are ionised. Neglecting these contributions is an excellent approximation when studying low-bias conduction.

The device and bulk transmission are compared in Fig. 5.4, where it is found that the nitrogen substitution causes little back scattering in the vicinity of the Fermi level. This may be understood as a result of the nitrogen retaining the sp^2 hybridisation of the substituted carbon, and therefore maintaining the π/π^* channels that are responsible for low-bias conduction. Scattering due to this substitution is weak as the π/π^* are not strongly perturbed.

In Fig. 5.4, we also show a comparison between our method and a similar calculation using a basis of maximally-localised Wannier functions (MLWFs)[122, 163, 121] extracted from eigenstates determined from a plane-wave DFT calculation.[5]

We note that whilst the physical motivation behind MLWFs and NGWFs are similar[128], the MLWFs form an orthogonal basis whereas the NGWFs are non-orthogonal. Further, unlike the NGWFs, the MLWFs are not fully localised within a given radius. Some truncation of the lead principle layers must therefore be made. Three primitive lead unit cells in each principle layer are found to be sufficient to accurately describe the lead band structures. Increasing the primitive layers to four primitive unit cells changes the lead band structures by no more than $3\ \mathrm{meV}$.

Fig. 5.4 shows that transmission calculated using the NGWF basis is in excellent agreement with the MLWF method. This confirms that the quality of transmission calculated using the NGWF basis is equivalent to that of the plane-wave basis that underlies the MLWF results.

As a further example, we consider the transmission between the nitrogen-substituted poly-acetylene chain and a polyyne carbon chain which acts as a probe. The probe has alternating bond lengths of 1.27 Å and 1.30 Å and is placed 2.4 Å from the poly-acetylene carbon backbone. The auxiliary simulation geometry is shown in the bottom panel of Fig. 5.5 and consists of 91 atoms, of which 82 are included in the three-lead transmission geometry. In the upper two panels of Fig. 5.5 we compare the form of the two eigenchannels that originate in the polyyne probe with energy $2\ \mathrm{eV}$ below the Fermi energy. Within the probe, the two channels have similar π/π^* forms, as expected from the form of the bulk polyyne eigenstates. Only electrons in the first channel are able to tunnel into the poly-acetylene chain as the axes of the polyyne and poly-acetylene π/π^* states are aligned;

[5] Plane-wave eigenstates were calculated using the QUANTUM ESPRESSO package[124] using the same pseudopotentials and, as far as possible, calculation parameters. A set of 102 MLWFs were extracted from lowest 170 bands resulting in 68 MLWFs localised in the bonding region between species, 32 p_z type orbitals centred on carbon atoms, and two additional MLWFs on the nitrogen lone pairs.

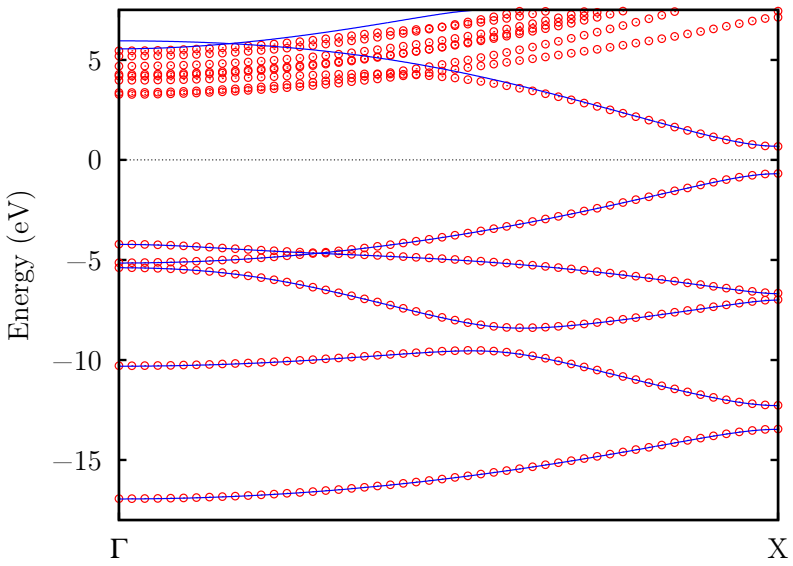

Figure 5.3: The band structure of the left lead of the poly-acetylene wire shown in Fig. 5.2. The solid (blue) lines give the interpolated band structure calculated in the NGWF basis; the red circles give the band structure calculated separately for bulk poly-acetylene using the plane wave DFT code CASTEP. The Fermi level has been been set to zero.

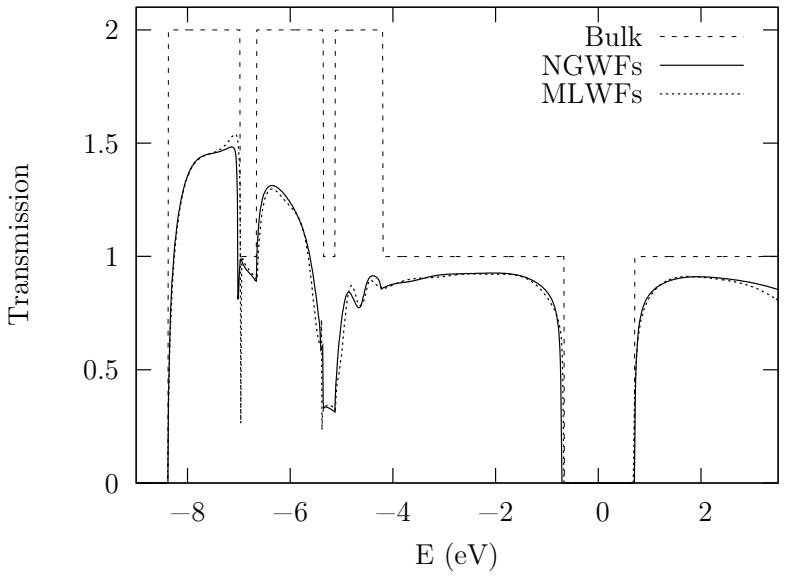

Figure 5.4: The transmission calculated for the poly-acetylene wire shown in Fig. 5.2. The solid and dashed lines give, respectively, the device and left lead bulk transmission in the NGWF basis using the method described in this work; the dotted line gives the device transmission calculated using maximally localised Wannier functions (MLWFs).

electrons in the second channel cannot couple with the poly-acetylene π/π^* states due to poorly-aligned symmetry and transmission of this channel therefore is negligible. Within the probe, both channels are approximately standing waves, which reflects the low transmission between the probe and the poly-acetylene molecule. Within the poly-acetylene molecule, the first eigenchannel shows an increasing complex phase indicating that the eigenchannel is propagating.

5.5.2 Conduction between terminated carbon nanotubes

We now apply our implementation to a more complex problem, namely the conductance between two terminated carbon nanotubes (CNTs). In this section, we focus on the particular details relevant to the large-scale transport calculations; a more detailed discussion of the conductance characteristics will be provided in chapter 7.

We next consider the inter-tube tunnelling between two hydrogen-terminated $(5, 5)$ CNTs in the geometry shown in Fig. 5.6.[6] The electronic ground state is determined for a 73 Å long CNT fragment containing 29.5 unit cells of a $(5, 5)$ CNT. Each terminating carbon atom is passivated with a single hydrogen atom, giving the simulation cell a total of 610 atoms. Periodic boundary conditions are used and there is 10 Å overlap between the terminated ends. The inter-tube separation was chosen to be 3.4 Å, the inter-layer separation in graphite. The relative orientation of the hexagonal lattice in the contact region gives a graphite Bernal-like stacking. The dark/light spheres indicate the atoms that define the lead principle layers, each of which consist of four primitive unit cells of the CNT. Unless otherwise stated, the NGWF localisation radii for all atoms are set at 4.2 Å.

The full calculation for the DFT ground state and subsequent transport calculation was performed using 64 Intel Sandy Bridge cores (2.60 GHz, E5-2670 processors), requiring 94 minutes, of which under 2 minutes were required to compute the transmission spectrum evaluated at 1000 energies, i.e., only 2% of the total calculation time. The transmission calculation used 2380 NGWF basis functions, with a memory requirement of 150 MB per core.

The main results of this calculation are given in Fig. 5.7. The left panel gives the band structure of the left lead (the band structure for the right lead is indistinguishable) which is as expected for a metallic $(5, 5)$ CNT: two bands cross the Fermi energy with linear

[6] We note that as a consequence of the connection between the leads across the periodic boundary, the auxiliary simulation geometry in Fig. 5.6 can only study conductance between CNTs of the same chirality. The results presented in chapter 7 use an alternative geometry consisting of finite CNT fragments that allows for the study of conduction between CNTs of different chirality.

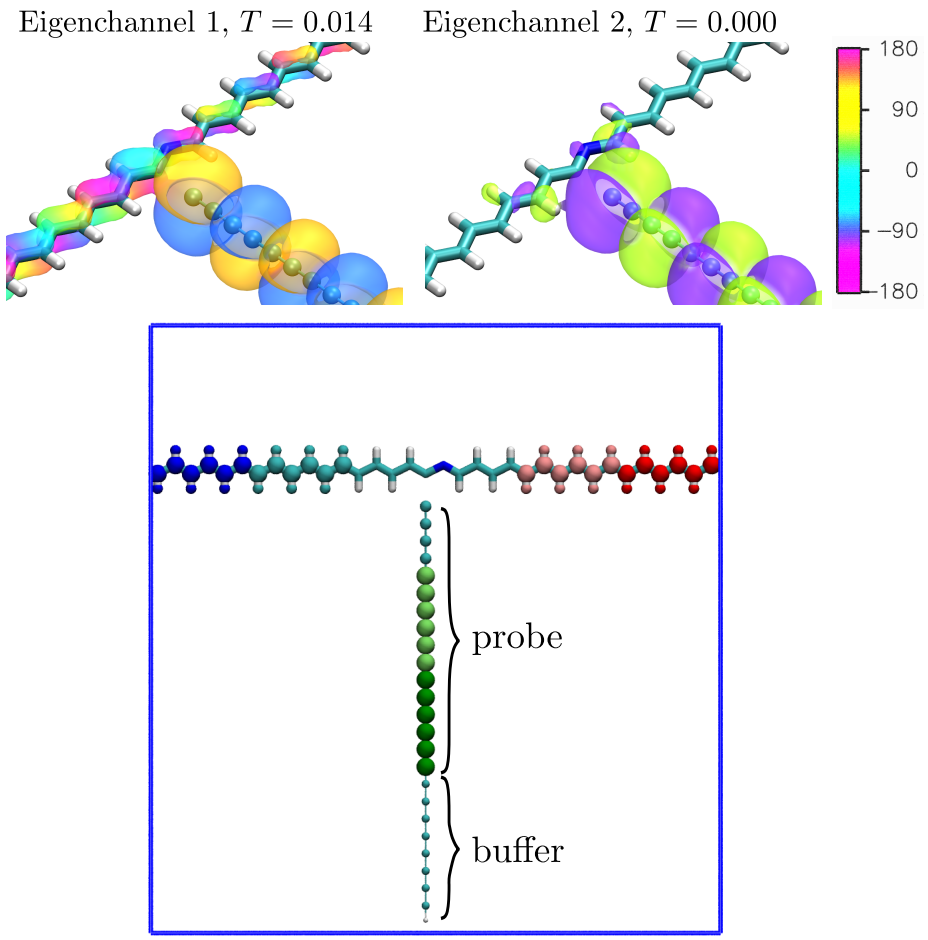

Figure 5.5: Bottom panel: the auxiliary simulation geometry for the nitrogen-substituted poly-acetylene chain with a polyyne chain acting as a probe. The lead principle layers are given by dark/light spheres; a region of buffer polyyne chain is included in the auxiliary simulation geometry, but excluded from the transmission geometry, to ensure that the polyyne lead principle layers are bulk-like. The blue box gives the periodic supercell. Top panels: the two eigenchannels originating from the polyyne probe at energy 2.0 eV below the Fermi energy. The isosurface represents the absolute value of the eigenchannel, with the complex phase indicated by the shading and the color bar. The transmission for each channel, T, gives the total transmission from the probe into either of the leads on the poly-acetylene chain.

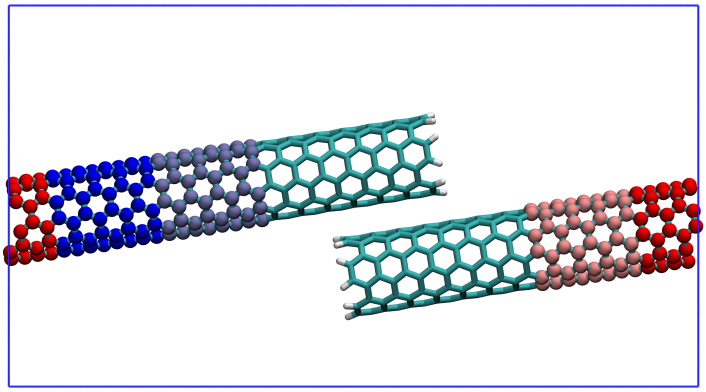

Figure 5.6: The auxiliary simulation cell geometry for inter-tube conductance between two terminated $(5, 5)$ CNTs. The system contains 610 atoms. The lead principle layers, indicated with light and dark coloured spheres respectively, correspond to four CNT primitive unit cells. The blue box gives the periodic boundary of the simulation cell.

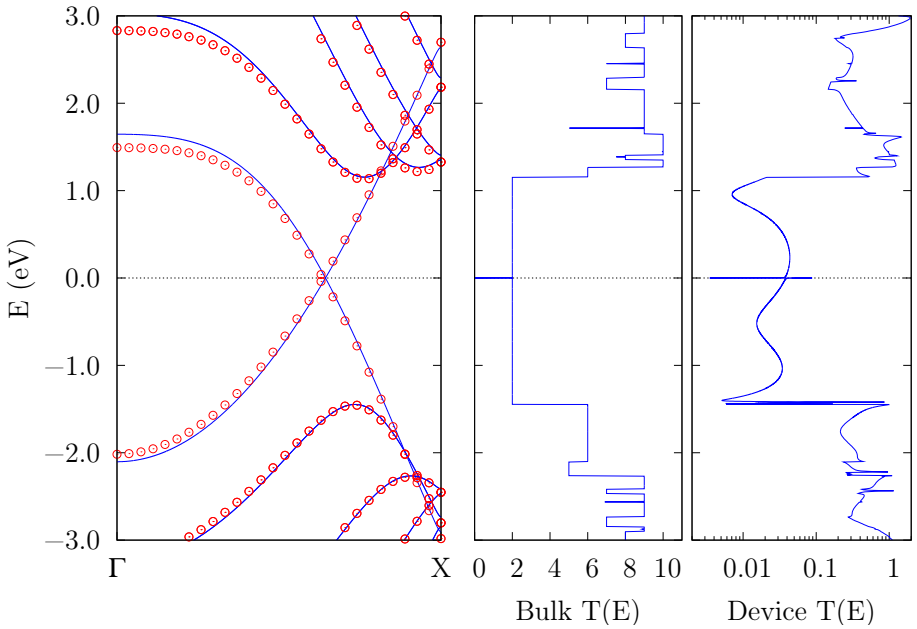

Figure 5.7: The computed transmission and related quantities for the end-end geometry shown in Fig. 5.6a. Left: the band structure of the left lead (solid blue) and the bulk (red circles). Centre: the bulk transmission of the left lead. Right: the device transmission between the two leads in the device (note the logarithmic scale).

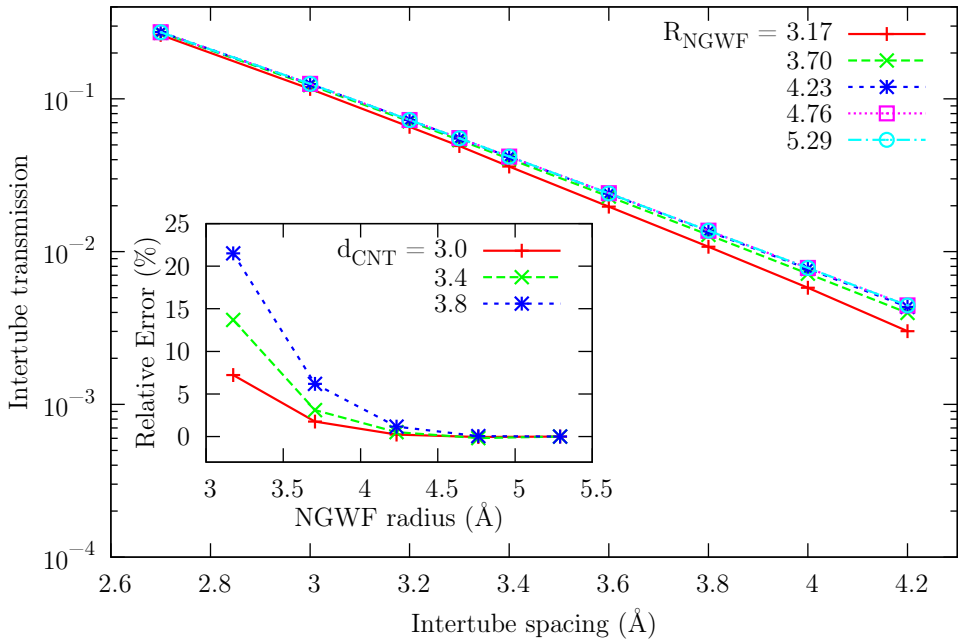

Figure 5.8: The device transmission at the Fermi energy between CNTs in the geometry shown in Fig. 5.6a as a function of inter-tube spacing and NGWF radius. The inset gives the relative error in the transmission $|(T - T_0)/T_0|$ for several inter-tube separations d_{CNT} as a function of NGWF radius; the reference value T_0 is taken to be the transmission for NGWF radius $R_{\mathrm{NGWF}} = 5.29$ Å.

dispersion. The lead band structure derived from the auxiliary simulation geometry is found to be very similar to the bulk $(5, 5)$ CNT band structure (red circles) calculated separately using the plane-wave DFT code CASTEP. This demonstrates that the lead principle layers are sufficiently far from the scattering region and the local electronic structure has converged to the bulk. The two band structures do not agree exactly, which may be due to too small NGWF localisation radius, but for states in the vicinity of the Fermi energy, which have the dominant contribution to low-bias conduction, the agreement is excellent.

The bulk transmission, shown in the central panel, agrees with the lead band structure with one unit of transmission for each band present at a given energy. Around the Fermi level the bulk transmission is 2, as expected for a metallic CNT and from the two bands that cross the Fermi level. The right panel gives the device transmission between the semi-infinite CNTs (note the logarithmic scale). Transmission is low as there is no bonded connection between the CNTs, and transmission occurs via tunnelling.

In Fig. 5.8 we consider the effect of the NGWF radius on the inter-tube transmission evaluated as a function of the CNT separation. As the set of NGWFs that directly overlap changes with the NGWF radius, the inter-tube tunnelling transmission might be expected

to be sensitively dependent on the NGWF localisation radius making this weakly-coupled system an excellent test of our method. As shown in Fig. 5.8, we observe rapid convergence of inter-tube transmission as the NGWF radius increases confirming the applicability of our method to this system. Note also that whilst the use of larger NGWF localisation radii increases the computation time to reach the DFT ground state, the total number of NGWF basis functions remains constant. Although the number of primitive unit cells that define a lead principle layer may increase with larger radii NGWFs, these matrices are still small when compared to the device matrices and the increased computational cost is not severe. This means that the time required to compute the transmission spectrum is therefore almost independent of the accuracy of the NGWF basis set.

Finally, we note that in chapter 7 we use the implementation presented in this chapter to study conduction in systems containing up to 4028 atoms (in the geometry shown in Fig. 7.3b, the transmission geometry corresponds to the entirety of the auxiliary simulation geometry). The largest calculation, when parallised over 416 cores (Intel Sandy Bridge, 2.60 GHz, E5-2670), required 12 minutes to evaluate the transmission spectrum evaluated at 1500 energies with a memory footprint for the transport calculation of 1.44 GB per processor. This calculation illustrates the ability of this implementation to study conductance through extremely large devices.

5.6 Outstanding issues

To conclude this chapter, we discuss a technical issue with our implementation that remains to be fully resolved. It is known that whilst the optimised NGWFs describe valence states with excellent accuracy, the description of the conduction states can be poor.[164] Part of the issue is the greater delocalisation of the conduction states, which require NGWFs with a larger localisation radius, but more fundamentally the NGWF optimisation procedure only optimises for the occupied states. A solution to this problem has recently been implemented whereby a second set of *conduction* NGWFs are generated and optimised to describe only the lowest-lying conduction states.[164] By combining the standard valence NGWFs and the conduction NGWFs, this *joint* NGWF basis is able to describe simultaneously a range of occupied and unoccupied states around the Fermi energy.

The transport implementation described in this chapter is in principle automatically compatible with the joint NGWF basis as this basis does not differ conceptually from the valence NGWF basis. Test calculations using the joint basis were often found to provide an inaccurate description of the transport characteristics, however, even at energies deep

within the valence bands where the ordinary valence NGWFs alone are sufficient to describe transport.

The origin of this issue was identified as ill-conditioning in the joint basis, arising from near-degeneracies in the valence and conduction NGWFs. These degeneracies arise as the valence and conduction states in the vicinity of the Fermi level often have similar character, yet each are described using a separate set of NGWFs. This results in numerical instabilities when computing the lead self energies and leads to a poor description of the transport properties. The effect of this degeneracy on the lead self energies can be more easily understood in terms of the equivalent instability when computing the lead band structures.

To ensure that the lead bandstructure computed using Eqn. (5.7) is physically acceptable and has real eigenenergies, the overlap matrix at a general k-point $\boldsymbol{s}_k$ must be positive definite. This is equivalent to the condition that $\boldsymbol{s}_k$ has all positive eigenvalues. An overlap matrix is said to be ill-conditioned when the ratio of the largest to smallest eigenvalues, termed the *condition number*, is much greater than unity. In general, an overlap matrix is always positive definite. However, extracting matrix elements from the auxiliary simulation produces only an approximation to the proper overlap matrix. Recall that $\boldsymbol{s}_k$ is constructed from the $\boldsymbol{s}_{00}$ and $\boldsymbol{s}_{01}$ matrices that are extracted from the two lead principle layers. As these principle layers are different distances from the device region, the NGWFs in these layers are in general different. The extraction of the $\boldsymbol{s}_{01}$ matrix is therefore only an approximation: in an exact calculation of $\boldsymbol{s}_{01}$, the NGWFs in both principle layers would be identical. There is therefore an error associated with $\boldsymbol{s}_{01}$.

The error in $\boldsymbol{s}_{01}$ introduces a perturbation to the eigenvalues of $\boldsymbol{s}_k$, and the magnitude of this error depends on the condition number of $\boldsymbol{s}_k$. If the condition number is small, as in the valence NGWF basis, the perturbation does not strongly perturb these eigenvalues and $\boldsymbol{s}_k$ remains positive definite: in this case the error in the lead self energy introduced by the error in $\boldsymbol{s}_{01}$ is negligible. If the condition number is larger, however, the perturbation can be sufficient to make one or more eigenvalues of $\boldsymbol{s}_k$ negative. Consequently, certain lead band energies become complex and unphysical, and the corresponding eigenstates decay rather than propagate through the device resulting in an incorrect transmission spectrum.

To illustrate this problem, we consider transmission between two polyyne probes. Transmission is calculated using a valence basis with NGWF radius 4.2 Å, and a joint basis using the same valence NGWFs and optimising conduction NGWFs of radius 6.4 Å to describe the 11 lowest lying conduction states. Using the valence basis only, the condition number and minimum eigenvalue of $\boldsymbol{s}_k$ at the Γ point are 19.5 and 0.102 respectively. The

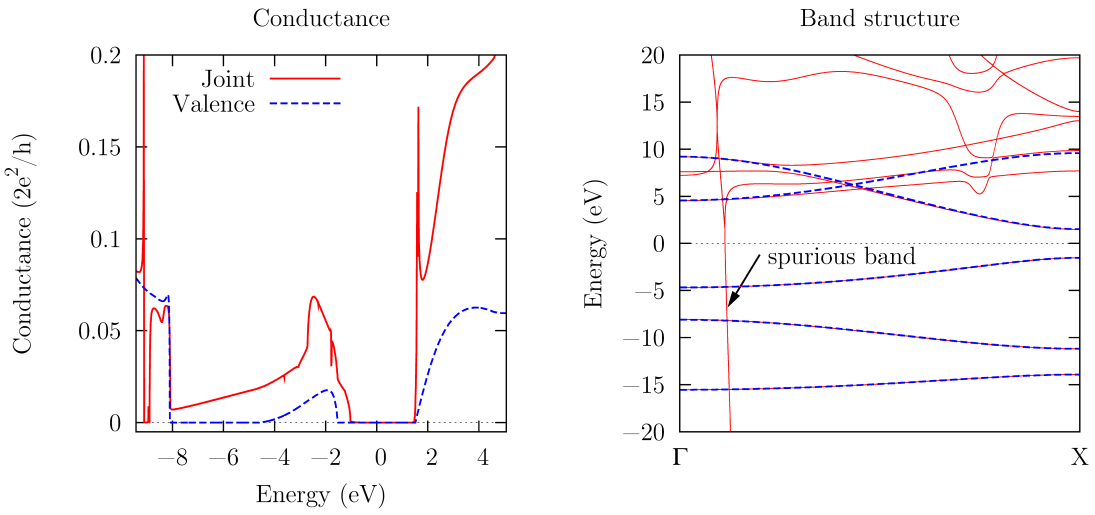

Figure 5.9: The transmission and lead band structure for conductance between two polyyne probes using the joint and valence NGWF bases. For the joint basis calculation, only the real part of the band energies are shown. The Fermi energy is set to zero.

maximum change of this minimum eigenvalue over the Brillouin zone is 0.003 indicating that transmission calculations performed using this basis will be stable. When using the joint NGWF basis, the condition number of $\boldsymbol{s}_k$ at the Γ point increases to 10386. The minimum eigenvalue of $\boldsymbol{s}_k$ is found to vary over the Brillouin zone between -2×10^{-3} and -1×10^{-4}. As this quantity is negative, the calculation of the lead band structure and lead self energies both become numerically unstable. Indeed, in the joint basis, the lead band structure is found to contain complex eigenvalues with an imaginary component as large as 270 eV. Fig. 5.9 compares the lead band structure and transmission between two polyyne probes calculated using the valence and joint basis. The spurious band that is introduced in the joint basis band structure contains a large imaginary component where the real part of the band energy is approximately 6 eV. This figure demonstrates that the ill-conditioning of the joint NGWF basis can calculate a transmission spectrum that is not even in qualitative agreement with the valence calculation.

One solution to this problem is to ensure that both principle layers use the same subset of NGWFs. This may not completely solve the problem, however, as the calculation of each $\boldsymbol{s}_{01}$ element is performed on a real-space grid, and if that grid is not commensurate with the periodic length of the lead principle layer then the NGWF is not invariant upon translation by a fraction of the grid.[7] For an arbitrary device containing at least two leads, it is not

[7]The variation in the real-space integral as atoms are shifted a fraction of a grid-spacing is known as the egg-box effect.[165]

possible to guarantee a commensurate grid spacing and a non-positive definite overlap may still be encountered.

A potentially more promising solution is to directly address the problem of ill-conditioning. One approach is to perform a transformation of the existing joint basis within the lead principle layers to eliminate the ill-conditioning[166]. A simpler physically-motivated solution, however, may be to modify the conduction NGWF optimisation procedure to ensure that the conduction and valence NGWFs on a given atom are always orthogonal. This could be achieved by expanding the low-energy conduction states in the valence and conduction NGWFs, and optimising only the conduction NGWFs whilst keeping the valence NGWFs fixed. In addition to improving the calculation of the lead band structures and self energies, this approach would also remove any ill-conditioning of the device overlap matrix and may offer better numerical stability overall.

The calculations presented in this chapter and in chapter 7 use only the valence NGWF basis. Comparison of the lead and corresponding bulk band structures shown in Fig. 5.3 and Fig. 5.7, and the transmission calculated using the MLWF basis shown in Fig. 5.4, suggest that the valence NGWFs do provide a good description of the low-lying conduction bands thus justifying this approximation.

5.7 Summary

In this chapter, we have presented an implementation of a method to model the zero-bias ballistic electronic transport through a multi-lead device using the Landauer-Büttiker formalism. The method is implemented into the ONETEP code and uses matrix elements derived from first-principles calculations using density functional theory. Our implementation has been specifically designed to study transport through very large systems, and enables the calculation of electronic transport properties of systems consisting of thousands of atoms on a routine basis. This brings the possibility of studying more realistic nano-electronic devices than has been previously possible with first-principles techniques. Key features of our implementation include: a highly compact basis set of localised non-orthogonal Wannier functions that are optimised *in situ* to achieve near basis set complete accuracy; transmission calculations for devices containing an arbitrary number of leads; calculation on highly parallel computer architectures; efficient exploitation of matrix sparsity; computing and plotting the eigenchannel decomposition in multi-lead devices.

Several example calculations have been presented in this chapter to demonstrate the accuracy and capability of the computational methodology. This implementation is used

extensively in chapter 7 where we perform calculations on very large systems to explore a mechanism that enhances the inter-tube conductance in arrays of carbon nanotubes. The theoretical evidence for the existence of this mechanism is the focus of the following chapter.

CHAPTER

SIX

MOMENTUM-RESONANT TUNNELLING BETWEEN CARBON NANOTUBES

The focus of this chapter is an investigation into the mechanisms that affect the conductance between carbon nanotubes. Possible mechanisms for the transfer of electrons between the tubes are myriad, and a search using the first-principles methods presented earlier is not only computationally impractical but also unsuitable for this problem. Instead, we adopt an analytical approach and use computationally inexpensive empirical tight-binding models which allows us to constrain the types of interactions that facilitate conduction between CNTs.

Using analytical results based on scattering theory, and validated by numerical tight-binding simulations, we show that significant enhancements of conductance between CNTs can arise from relatively weak interactions with the surrounding environment. The origin of the enhancement is that these interactions enable momentum-conserving tunnelling to occur by accepting any momentum difference between the initial and final states. The improvement in the conductance is very general and applies to metallic as well as doped semiconductor CNT networks. A key point to this mechanism is that the interaction with the environment need only be weak and can therefore be effected without chemical bonding, relying instead on weaker inter-molecular interactions. It is likely that this mechanism contributes significantly to the conduction in CNT networks, arising from weak-disorder and impurities in the nanotube system that remain from synthesis. Our conclusions lead to the counter-intuitive realisation that removing this disorder may in fact reduce the conductance of CNT networks.

Parts of this chapter have been published [167].

6.1 Introduction

In a wire made from a macroscopic network of CNTs, no single CNT spans the two ends of the wire and so to traverse the length of the wire, electrons must travel through pathways involving many CNTs. The overall conductivity of the wire, therefore, is determined not only by the intrinsic (intra-tube) conductivity of the individual CNTs, but also by the morphology of the network [168] and by the inter-tube conductivity.

Appreciating the importance of the role of inter-tube conductivity is vital to understand how to retain the properties of individual CNTs when scaling up to macroscopic wires and devices. For example, the conductivity of CNT wires is orders of magnitude lower than expected from the theoretical conductivity of individual CNTs and poor inter-tube conductance is believed to be a dominant cause [169, 8, 9, 10]. One route to improving network conductivity is, therefore, to improve inter-tube tunnelling.

There have been several studies on inter-tube transport between the ends of capped or terminated CNTs [170, 171, 172]. The tendency for CNTs to align axially in bundles however[173], together with their high aspect ratio, gives a relatively larger side-wall contact region over which inter-tube tunnelling could take place [174]. Side-wall inter-tube conduction between perfect CNTs has been shown to be strongly suppressed for CNTs of different chirality when compared to those of the same chirality [38, 175]. This is a consequence of the sensitivity of the electronic structure of the CNT to chirality and the requirement for both momentum and energy conservation in the tunnelling process.[1]

As typical synthesis methods generate CNT networks with a range of chiralities, the overall conductance of the CNT network may be strongly suppressed even if the constituent CNTs are defect free, perfectly aligned and only metallic in character.

It has proved difficult to improve the total conductance of CNT networks by enhancing side wall conductance as modifications that strongly interact with the CNTs, say through covalently bonded groups [176], defects[175], or adsorbed transition metal ions[174], dramatically reduce the intrinsic conductance of individual CNTs. Weak interactions with adsorbed molecules have been shown to improve side-wall conductance through energy-

[1]Here we neglect the possibility of energy non-conserving scattering arising from, e.g., inelastic phonon scattering. As discussed in section 3.2, whilst optical phonons could in principle allow energy dissipation in scattering events, the high optical phonon energy makes these modes thermally unpopulated at ambient temperatures and therefore unable to contribute to inelastic scattering. As acoustic phonons have far smaller energies, of order $10\ \mathrm{meV}$, inelastic acoustic phonon scattering can be approximated as elastic and momentum conserving if the momentum is understood as the sum of the phonon and electron momenta. Phonon-assisted inter-tube scattering is discussed briefly in section 6.8 but how it may contribute to inter-tube conductance remains an open question.

resonant tunnelling[177], but this mechanism requires molecular states close in energy to the CNT Fermi energy and, therefore, the effectiveness of this approach is dependent on extrinsic factors that may be difficult to control.

In this chapter we consider the general problem of electron transport between CNTs of arbitrary chirality. We focus on transport between metallic CNTs, but our conclusions equally apply to semiconducting ones and to bulk inter-sheet conduction in twisted bilayer graphene[178]. The main result is that transport between tubes of different chirality can be greatly enhanced by the presence of a *weak* external potential that achieves momentum-conserving tunnelling by enabling momentum exchange by scattering off the potential. The fact that the potential need only be weak removes the need to modify the bonding structure of the CNTs and, hence, the intrinsic CNT conductance is unaffected. Furthermore, for a potential that varies on length-scales larger than inter-atomic bond lengths, back-scattering is forbidden and the total conductivity of the network is only improved by its presence. We conclude that interactions between the CNTs and environmental impurities are likely to accomplish this enhancement and that, counter-intuitively, the presence of weak disorder in CNT networks is vital to ensuring a high network conductivity.

In section 6.2 we use perturbation theory to identify a mechanism to improve the side-wall inter-tube conductance; in section 6.3 a tight-binding model is introduced which is then used in sections 6.4–6.7 to explore and numerically verify the predictions made from perturbation theory.

6.2 Linear-response from perturbation theory

We first investigate the factors that affect tunnelling between CNTs using scattering theory within a perturbative framework. We consider a system containing two metallic CNTs of arbitrary chirality axially aligned as shown schematically in Fig. 6.1. We denote the intrinsic tunnelling interaction between the CNTs by the operator $\hat{H}_T$; this interaction is assumed to be weak, arising from non-bonding interactions, thus allowing for it to be treated within a perturbative expansion.

Taking $|\psi_1\rangle$ and $|\psi_2\rangle$ to be electronic states at the Fermi energy E_F localised in each CNT, respectively, the contribution from these states to the small bias conductance $G_{1\to2}$ can be calculated using linear response theory. To first order,

$$G_{1\to2} = 2e^2\Gamma^{(1)}_{1\to2}\rho_1(E_\mathrm{F}), \tag{6.1}$$

$$\Gamma^{(1)}_{1\to2} = \frac{2\pi}{\hbar}\rho_2(E_\mathrm{F})\left|\langle\psi_1|\hat{H}_T|\psi_2\rangle\right|^2, \tag{6.2}$$

where $\Gamma^{(1)}_{1\to2}$ is the first-order tunnelling rate between $|\psi_1\rangle$ and $|\psi_2\rangle$, and $\rho_1(E_\mathrm{F})$ and $\rho_2(E_\mathrm{F})$ are the densities of states at the Fermi level for the two CNTs.

The most relevant term in Eqn. (6.2) is the matrix element and its dependence on the momenta of the initial and final electronic states and, in turn, on the chiralities of the two CNTs. In typical networks, the CNT diameters are sufficiently large that the electronic states of the CNTs and their momenta are well described by the band-structure of graphene under a zone-folding approximation (see section 2.3.2). For two weakly-interacting axially-aligned CNTs we may consider two graphene Brillouin zones, each rotated by the chiral angle of the respective CNTs such that their axial momenta are aligned[38], as shown schematically in Fig. 6.3. Scattering between CNT states at the Fermi energy is equivalent to scattering between the Dirac points of these rotated Brillouin zones[38], which in general have different momenta. This difference in momentum, containing both axial and azimuthal components, increases as the difference in chiral angle increases.

For two CNTs that are commensurate (i.e., the ratio of the unit cell lengths is a rational fraction), the tunnelling interaction is translationally invariant and momentum must be strictly conserved[38], resulting in the remarkable conclusion that conductance between pristine CNTs of different chirality is zero. The more common scenario, however, is that the CNTs are incommensurate, in which case translational invariance is broken [38, 179], and the requirement for momentum conservation is no longer strictly applicable. Nonetheless, it has been shown that inter-tube conductance at first order is still strongly suppressed for CNTs of different chirality due to the momentum mismatch of initial and final states [38, 179]. Irrespective of whether commensurate or not, therefore, there is a strong suppression of inter-tube transport between CNTs of mismatched chirality.

How may the inter-tube conductance between CNTs of different chirality be improved? There are two general statements that can be made about any additional tunnelling interaction: (1) it must couple two states that are spatially separated and localised on different CNTs; (2) it must accept any momentum difference between the conducting states.

We now consider the effect of an extrinsic *weak* local potential $V_\mathrm{ext}(\mathbf{r})$ (which may be thought of as arising from the interaction of the environment with the CNTs) and consider the conditions it must satisfy to improve the inter-tube conductance. To improve conductance at first order, because the initial and final states are localised to different CNTs, V_ext would need to perturb the contact region between the CNTs where there is greatest spatial overlap. Whilst defects[175], functionalization[174] and structural deformations[175, 180] may achieve this, they may also significantly reduce the intrinsic intra-tube conductance [176, 181] and, particularly in the case of side-wall functionalization, may increase the

inter-tube separation and hence the width of the tunnelling barrier.

In order to circumvent these problems, we consider alternative mechanisms to this first-order process and examine the second order scattering rate:

$$\Gamma^{(2)}_{1\to 2} = \frac{2\pi}{\hbar}\rho_2(E_\mathrm{F})\Big|\sum_m \frac{\langle\psi_1|\hat{H}'_T|m\rangle\langle m|\hat{H}'_T|\psi_2\rangle}{E_\mathrm{F}-E_m}\Big|^2, \tag{6.3}$$

where $\hat{H}'_T$ is the sum of the tunnelling interaction and the extrinsic potential, $\hat{H}'_T = \hat{H}_T + \hat{V}_\mathrm{ext}$, and the sum runs over all possible states $|m\rangle$. Expanding the matrix element gives four terms

$$\begin{aligned}\langle\psi_1|\hat{H}'_T|m\rangle\langle m|\hat{H}'_T|\psi_2\rangle = \\ \langle\psi_1|\hat{H}_T|m\rangle\langle m|\hat{H}_T|\psi_2\rangle + \langle\psi_1|\hat{H}_T|m\rangle\langle m|\hat{V}_\mathrm{ext}|\psi_2\rangle + \\ \langle\psi_1|\hat{V}_\mathrm{ext}|m\rangle\langle m|\hat{H}_T|\psi_2\rangle + \langle\psi_1|\hat{V}_\mathrm{ext}|m\rangle\langle m|\hat{V}_\mathrm{ext}|\psi_2\rangle.\end{aligned} \tag{6.4}$$

These four terms are represented schematically in Fig. 6.2. The first and final terms correspond to an even number of inter-tube scatterings and hence do not contribute to the inter-tube conductance. The remaining two terms, however, do contribute to inter-tube conductance and can be large if V_ext strongly couples states in the same CNT but with different momenta.

The third term, for example, represents scattering the initial state $|\psi_2\rangle$ to an intermediate state $|m\rangle$ localised within the same CNT possibly with different momentum, which then scatters into state $|\psi_1\rangle$ of the other CNT. If $\hat{V}_\mathrm{ext}$ is chosen such that the intermediate state has the same momentum as the final state, then inter-tube tunnelling by $\hat{H}_T$ is no longer suppressed, and can be much larger than first order tunnelling. From this analysis it can be concluded that the undesirable consequences associated with improving the inter-tube conductance at first order may be avoided by focusing instead on improving the second order tunnelling rate.

6.3 Tight-binding model

We validate the above mechanism with numerical results using a tight-binding model. The system Hamiltonian is given by

$$\hat{H} = \sum_{\alpha=1}^{2}\hat{H}_\alpha + \hat{H}_T + \hat{V}_\mathrm{ext}, \tag{6.5}$$

where $\alpha = 1, 2$ indexes the two CNTs.

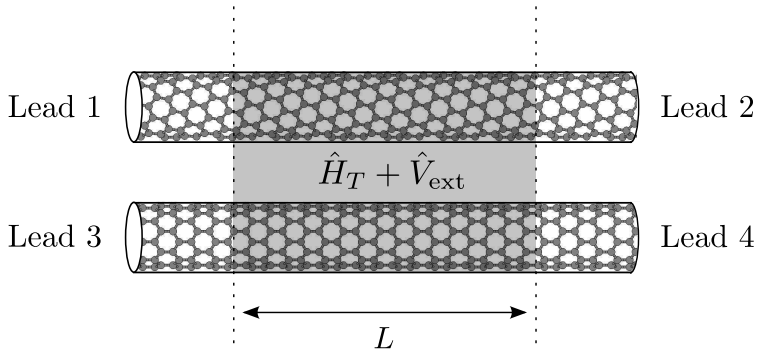

Figure 6.1: The four-lead side-wall tunnelling geometry considered in this chapter. The tunnelling and external interaction occur in the shaded region, over a length-scale L, outside of which the leads are isolated.

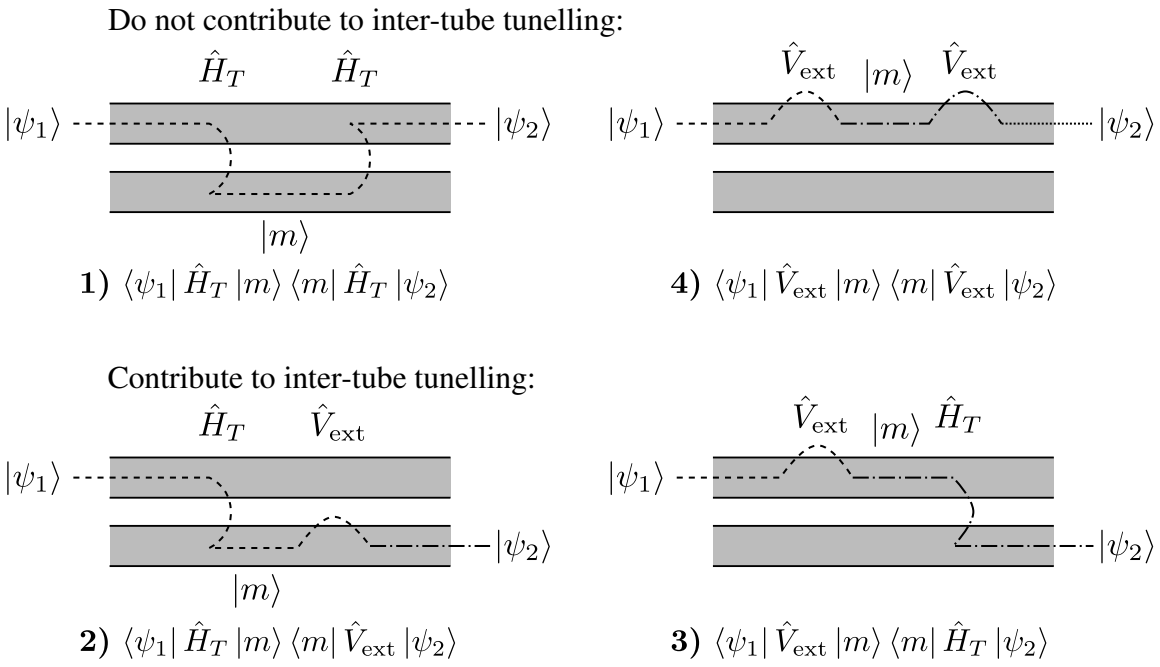

Figure 6.2: A diagrammatic representation of the four second-order scattering processes in Eqn. (6.4). Each curved line represents a scattering event; the different dashes on the lines represent different state momenta.

The band structures of the CNTs are described using a π-orbital model including only nearest neighbour hopping

$$\hat{H}_\alpha = -t_0 \sum_{\langle i,j \rangle} \left(c^\dagger_{i\alpha} c_{j\alpha} + c^\dagger_{j\alpha} c_{i\alpha} \right), \tag{6.6}$$

where $c^\dagger_{i\alpha}$ and $c_{i\alpha}$ are the creation and annihilation operators, respectively, for an electron on atomic site i, at position $\mathbf{r}_i$, belonging to CNT α.

The summation is performed over nearest neighbour sites $\langle i, j \rangle$ on a rolled hexagonal lattice, with interatomic bond lengths $a_{\mathrm{C-C}} = 1.415$ Å. The Fermi energy is set to zero and the hopping parameter $t_0 = 2.77$ eV, as in [175].

The intrinsic tunnelling interaction between the CNTs is taken to be

$$\hat{H}_T = -\sum_{ij} t_{ij} \left(c^\dagger_{i1} c_{j2} + c^\dagger_{j2} c_{i1} \right), \tag{6.7}$$

where atom sites i, j are on different CNTs. Following Refs. [38] and [175], the tunnelling matrix element is

$$t_{ij} = t_\perp e^{-|\mathbf{r}_i - \mathbf{r}_j|/\delta}, \tag{6.8}$$

with $t_\perp = 492$ eV and $\delta = 0.5$ Å. The separation between the surfaces of the CNTs is 3.4 Å which is the inter-layer separation in graphite.

For the external potential, we make the ansatz $V_{\mathrm{ext}}(\mathbf{r}) = V_0 \sin(\Delta k z)$, (the z-axis is chosen as the CNT axial direction). When written in a plane-wave representation, it is seen that this potential couples strongly two states in the same CNT with axial momenta differing by Δk.

In the tight-binding basis, this potential is approximated as diagonal

$$\hat{V}_{\mathrm{ext}} = \sum_{i\alpha} V_0 \sin(\Delta k z_{i\alpha}) c^\dagger_{i\alpha} c_{i\alpha}, \tag{6.9}$$

and, therefore, does not directly couple the two CNTs. The amplitude $V_0 = 0.1$ eV (i.e. $V_0 \ll t_0$), which is sufficiently small to be characteristic of a weak perturbation rather than a bonding interaction. A physical external potential can be considered as a sum of these Fourier components.

The form of this external potential allows only axial momentum exchange, however the azimuthal momentum difference between the Dirac points involved in scattering is not conserved as rotational symmetry is broken by the side-by-side geometry of the CNTs.

We use the damping function of Ref. [175] to mutually isolate the leads with negligible contact-induced scattering:

$$t_{ij} \to t(\mathbf{r}_i, \mathbf{r}_j) \times f_d(z_i; L, L_c) f_d(z_j; L, L_c) \tag{6.10}$$

$$V_{\mathrm{ext}}(\mathbf{r}) \to V_{\mathrm{ext}}(\mathbf{r}) \times f_d(z; L, L_c) \tag{6.11}$$

with

$$f_d(z; L, L_c) = \left[(e^{(z-L)/L_c} + 1)(e^{-z/L_c} + 1)\right]^{-1}. \tag{6.12}$$

This introduces a contact length-scale L_c over which the intrinsic and external interactions activate. We choose $L_c = 5$ Å which is larger than the inter-tube separation (3.4 Å) and therefore is not the dominant source of momentum relaxation, and has negligible effect on the inter-tube conductance[175]. The length L defines the contact length over which the CNTs interact (Fig. 6.1), which we set to $L = 190$ Å.

The ballistic conductance between the four semi-infinite leads is calculated using the Landauer-Büttiker formalism via a Green's function approach [45]. We define the inter-tube conductance as the sum of the conductances between a lead and the two leads of the other CNT.

By ensuring that $V_{\rm ext}$ varies only on length-scales greater than the inter-atomic bond length a_{C-C}, back-scatting is vanishingly small[48], corresponding to a maximum momentum exchange presented in this work

$$\Delta k_{\rm max} \;=\; \pi/a_{\rm C-C}. \tag{6.13}$$

In the remainder of this chapter, resonant momentum exchanges and corresponding potentials are denoted as as $\Delta k^\star$ and $V_{\rm ext}(\Delta k^\star)$ respectively.

6.4 Resonant tunnelling between CNTs

In Fig. 6.3 we plot the inter-tube conductance between two CNT pairs at the Fermi energy as a function of the momentum exchange Δk. The results are typical for CNT pairs with low intrinsic inter-tube conductance. We observe resonant peaks where the inter-tube conductance increases greatly.[2] The momentum exchanges Δk correspond precisely to the axial momentum difference between Dirac points. We indicate these predicted positions with arrows and show for selected peaks (Fig. 6.3, top) the corresponding Dirac point scatterings.[3] Off momentum-resonance, the inter-tube conductance is unaffected by the weak potential, but for small momentum exchanges there is no decrease in the intra-tube conductance (see section 6.7).

[2]The amplitudes of the peaks are dependent on the specific form of the tight-binding model and are therefore not of direct interest to the discussion of the mechanism.

[3]We also note that additional peaks exist for momentum exchanges larger than the maximum exchange $\Delta k_{\rm max}$ presented here. These processes involve scattering between Dirac points outside the first graphene Brillouin zone. For incommensurate CNTs, these Dirac points are not equivalent to those in the principle Brillouin zone as the combined CNTs have no overall periodicity.

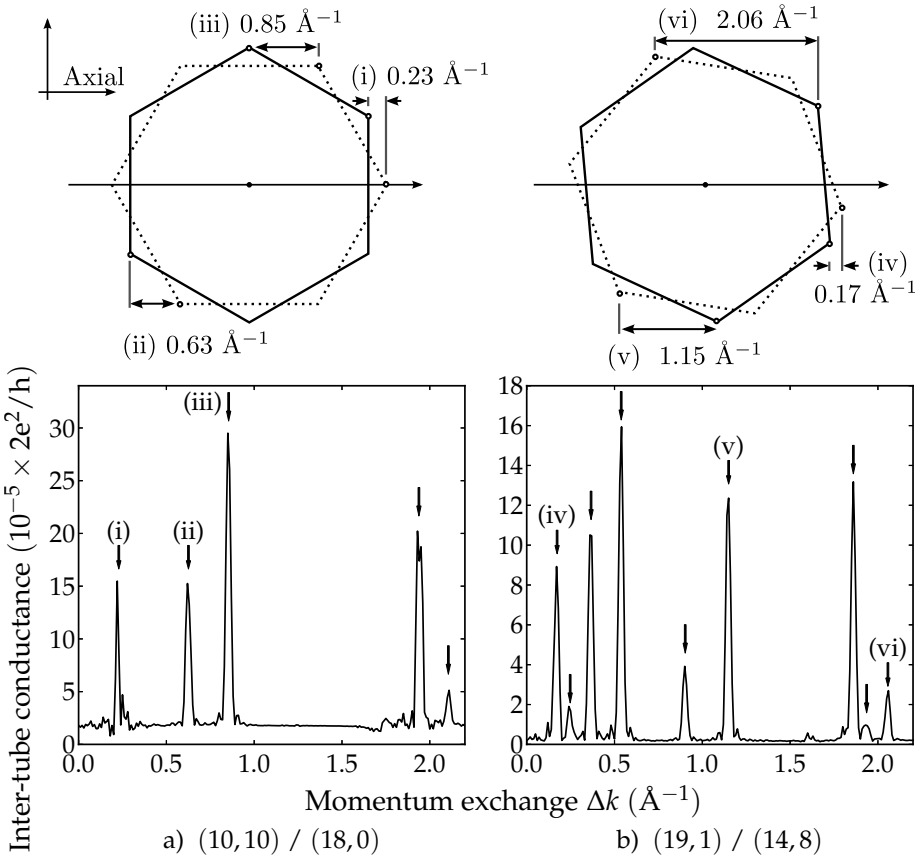

Figure 6.3: Top: schematic representation of tunnelling between CNTs. The hexagons represent the first graphene Brillouin zone (BZ) for CNT pairs: a) $(10, 10)/(18, 0)$ (dotted line/solid line) and b) $(19, 1)/(14, 8)$ (dotted/ solid). Each BZ has been rotated so that the axial momentum lies along the horizontal. The metallic states are at the BZ corners. Bottom: corresponding momentum exchange dependence of inter-tube conductance at the Fermi level. Vertical arrows indicate the predicted momentum exchanges corresponding to scattering between Dirac points. For selected peaks, we show in the top panel the Dirac points involved in the scattering.

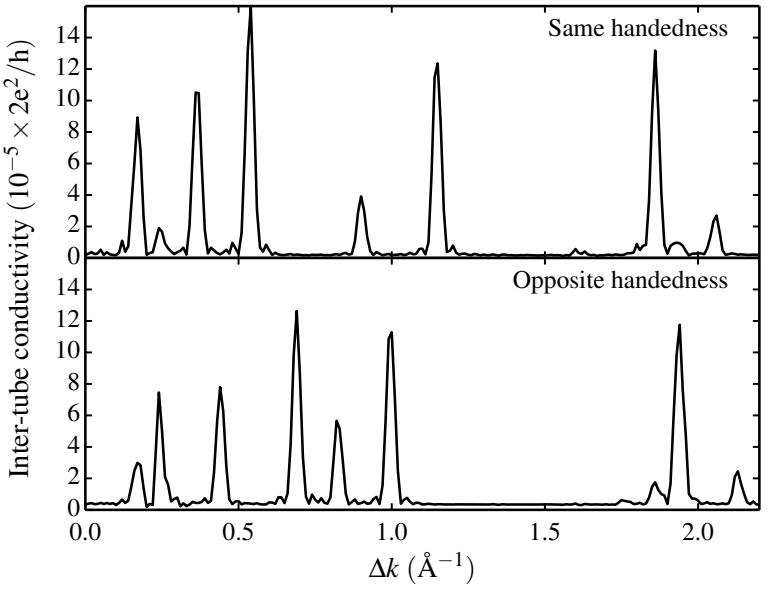

Figure 6.4: The inter-tube conductance between the $(19, 1)/(14, 8)$ CNT pair as a function of momentum exchange. Top panel: same handedness; bottom panel: opposite handedness.

Where both CNTs are chiral, the relative handedness of the CNTs may be the same or opposite. Chemically, the situations are almost identical, however different momentum resonances are predicted as a change in handedness results in the two graphene Brillouin zones being rotated in the opposite direction. This gives rise to different momentum differences between Dirac points, and hence a separate set of resonant momentum exchanges. This is confirmed in Fig. 6.4 where we show the inter-tube conductance at the Fermi energy as a function of momentum exchange for the $(19, 1)/(14, 8)$ CNT pair with the same and opposite relative handedness.

The momentum resonance occurs not only between metallic CNTs, but also semiconductor CNTs. In Fig. 6.5 we show the inter-tube conductance between the semiconducting $(20, 0)/(14, 7)$ CNT pair at $E = 0.4$ eV, with the peaks in conductance corresponding to momentum-resonant tunnelling.

6.4.1 Scaling relations of the momentum-resonant scattering mechanism

We compare the external potential amplitude V_0 and contact length L dependence of the numerical results presented in section 6.4 to the analytic results of Eqn. (6.4) to confirm that these resonances are due to the second-order mechanism described in section 6.2.

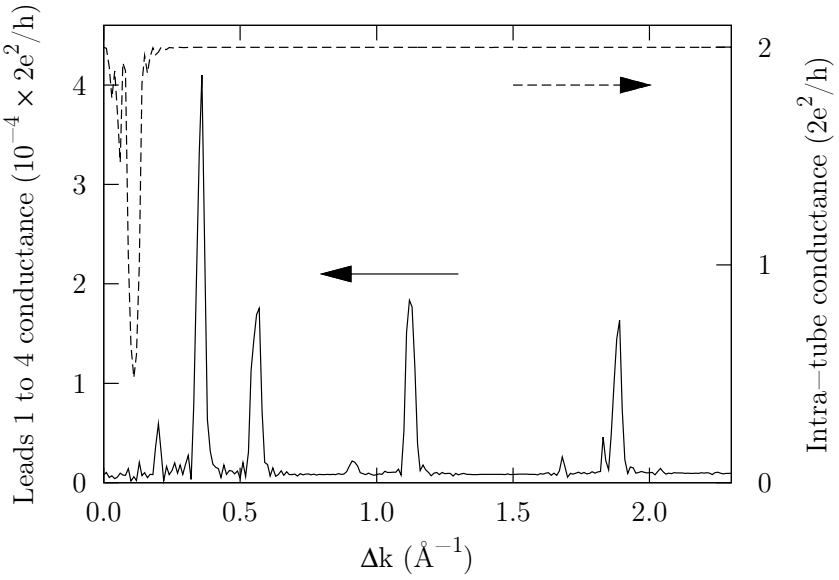

Figure 6.5: Solid line: the conductance between leads 1 and 4 at $E = 0.4$ eV for the $(20, 0)/(14, 7)$ CNT pair. Dashed line: intra-tube conductance for the $(20, 0)$ CNT.

The second-order scattering rate is predicted to scale quadratically with V_0 which is indeed found to be the case as can be seen in Fig. 6.6a. For sufficiently large interaction strength, scattering becomes non-perturbative and the inter-tube conductance decreases greatly. The density of states at the Fermi level is strongly modified, resulting in increased back-scattering which, in turn, strongly reduces the overall conductivity of the network.

In Ref. [175], it was shown that the intrinsic tunnelling matrix element $\langle m|\hat{H}_T|\psi_2\rangle$ oscillates as a function of L in cases where momentum-conservation is not satisfied, a consequence of interference, and that at momentum resonance it grows linearly with L. Consequently, the second-order scattering rate is oscillatory off resonance and grows quadratically with L at momentum-resonance. In Fig. 6.6b we show the dependence of inter-tube conductance at the Fermi energy on the overlap length L for the $(9, 0)/(5, 5)$ CNT pair. Off resonance ($\Delta k = 0.45$ Å^{-1}), the second-order contribution is negligible and the inter-tube conductance is oscillatory due to the dominant non-resonant first-order contribution. At momentum-resonance ($\Delta k = 0.63,\ 0.85$ Å^{-1}), the total conductance is the sum of the quadratically-growing second-order term and an oscillatory interference term due to the non-resonant contribution arising at first order. These scalings therefore confirm that the resonance does, indeed, arise from the mechanism presented in section 6.2.

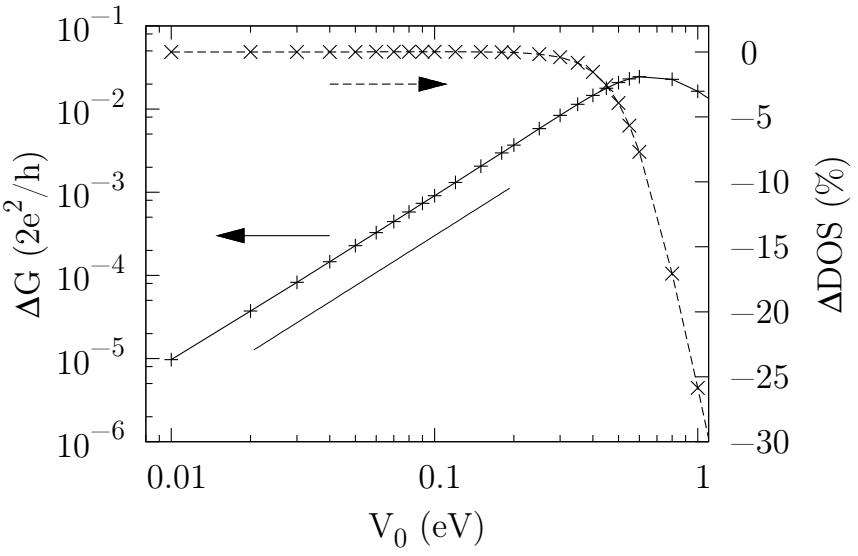

(a) Interaction strength dependence

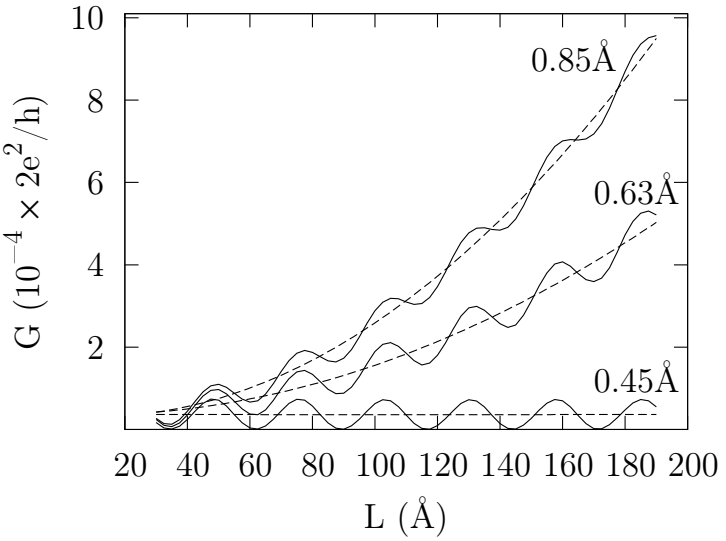

(b) Overlap length dependence

Figure 6.6: Top: the dependence of resonant inter-tube conductance and density of states (DOS) on the external potential amplitude V_0. The intrinsic contribution (i.e. with $V_0 = 0$) is subtracted to show only the momentum-resonant contribution ΔG, $\Delta\mathrm{DOS}$; resonance is $\Delta k^\star = 0.85$ Å^{-1}. The line segment shows a quadratic dependence $\Delta G \sim V_0^2$. Bottom: the dependence of inter-tube conductance on the overlap length L for resonant ($\Delta k^\star = 0.63,\ 0.85$ Å^{-1}) and non-resonant ($\Delta k = 0.45$ Å^{-1}) momentum exchanges. The dotted lines show quadratic fits to guide the eye. In all cases, conductance is between the $(9,0)/(5,5)$ CNT pair; quantities are evaluated at the Fermi energy.

6.5 Momentum resonances in compositionally disordered networks

Real CNT networks are compositionally disordered in the sense that they contain CNTs with a range of chiralities.[182] As the tunnelling between the CNTs is weak, inter-tube conductance in the whole network can be approximated accurately as tunnelling between pairs of CNTs, ignoring scattering events involving three or more CNTs[38]. Under this approximation, the effect of momentum resonant conductance on the entire network can be studied by considering the pair-wise interactions of the candidate CNTs within that network.

The left panels of Fig. 6.7 shows the intrinsic inter-tube conductance ($V_{\mathrm{ext}} = 0$) at the Fermi energy between all pairs of metallic CNTs in the diameter range $1.2 - 1.6\ \mathrm{nm}$ with the CNTs ordered by increasing chiral angle. We consider pairs of CNTs with opposite and same handedness separately. From the peak along the diagonal, it is evident that inter-tube conductance is large between CNTs of the same or similar chirality. As the difference in chirality between the two CNTs increases, however, momentum-conserving tunnelling is not possible and the inter-tube conductance is strongly suppressed.

The right panel of Fig. 6.7 shows the inter-tube conductance upon the introduction of the momentum-resonant potential $V_{\mathrm{ext}}(\Delta k^{\star})$, at which the inter-tube conductance is a maximum. The conductance between CNTs of the same chirality is unaffected and remains high, whilst there is a strong enhancement of the inter-tube conductance for CNTs of different chirality. The same conclusions can be drawn for conduction between pairs of metallic CNTs of either handedness[4] and for semiconductor CNTs, as shown in Fig. 6.8.

For different CNT pairs, the inter-tube conductance is maximised at different values of momentum exchanges $\Delta k^{\star}$ (see, e.g., Fig. 6.3). These are found to be distributed across a broad range of momentum as shown in Fig. 6.9a. The external potential, therefore, should contain a wide range of resonant momenta to improve the conductance of a network consisting of a set of CNTs with a wide range of chiralities. Thus, there is no need to fine-tune the external potential.

In Fig. 6.9b we show the relative improvement in the inter-tube conductance for all pairs of metallic CNTs considered as a function of the difference in chiral angle. We define the relative improvement as the ratio of the maximum improvement at momentum-resonance

[4]The reduced intrinsic conductance between CNTs of the same handedness, when compared to the opposite handedness calculations, can be understood due to a greater registry mismatch between the two graphene lattices in the former. For sufficient contact interaction length for incommensurate CNTs this relative handedness effect will diminish as the irrational unit cell length ratio removes any pseudo-alignment of the graphene lattices.

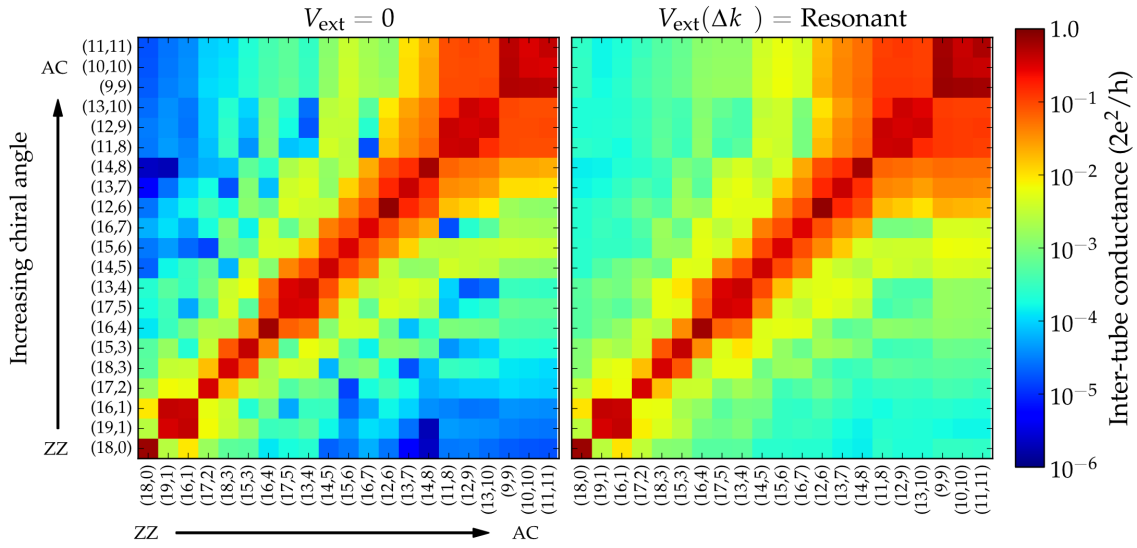

(a) Opposite handedness

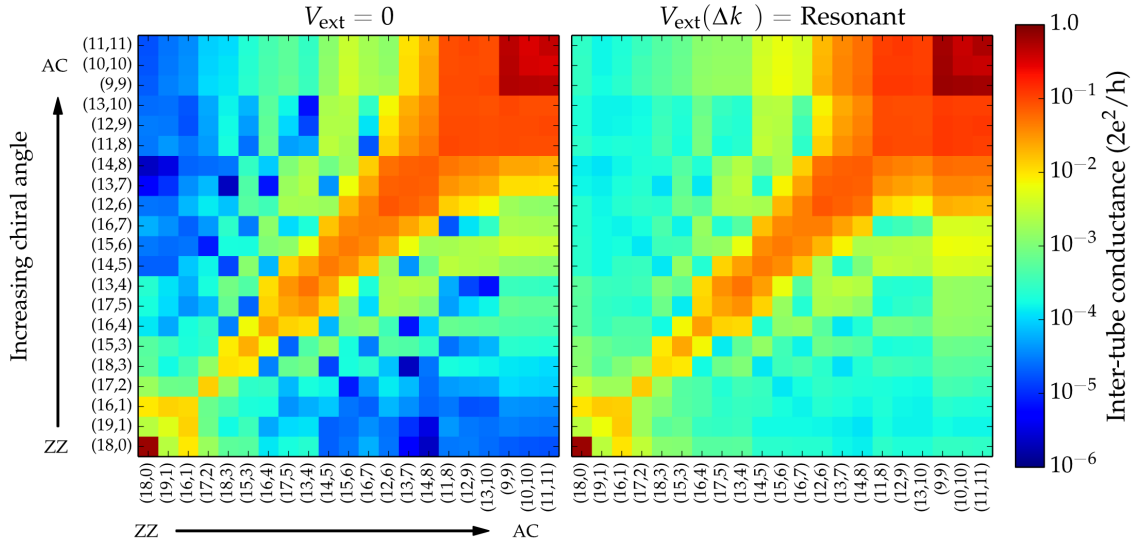

(b) Same handedness

Figure 6.7: The inter-tube conductance between all pairs of metallic CNTs in the diameter range $1.2 - 1.6$ nm. For each subfigure: left: intrinsic conductance $V_{\text{ext}} = 0$; right: maximum enhanced conductance (V_{ext} resonant). The CNTs are ordered according to increasing chiral angle and labelled by the (n, m) chiral indices.

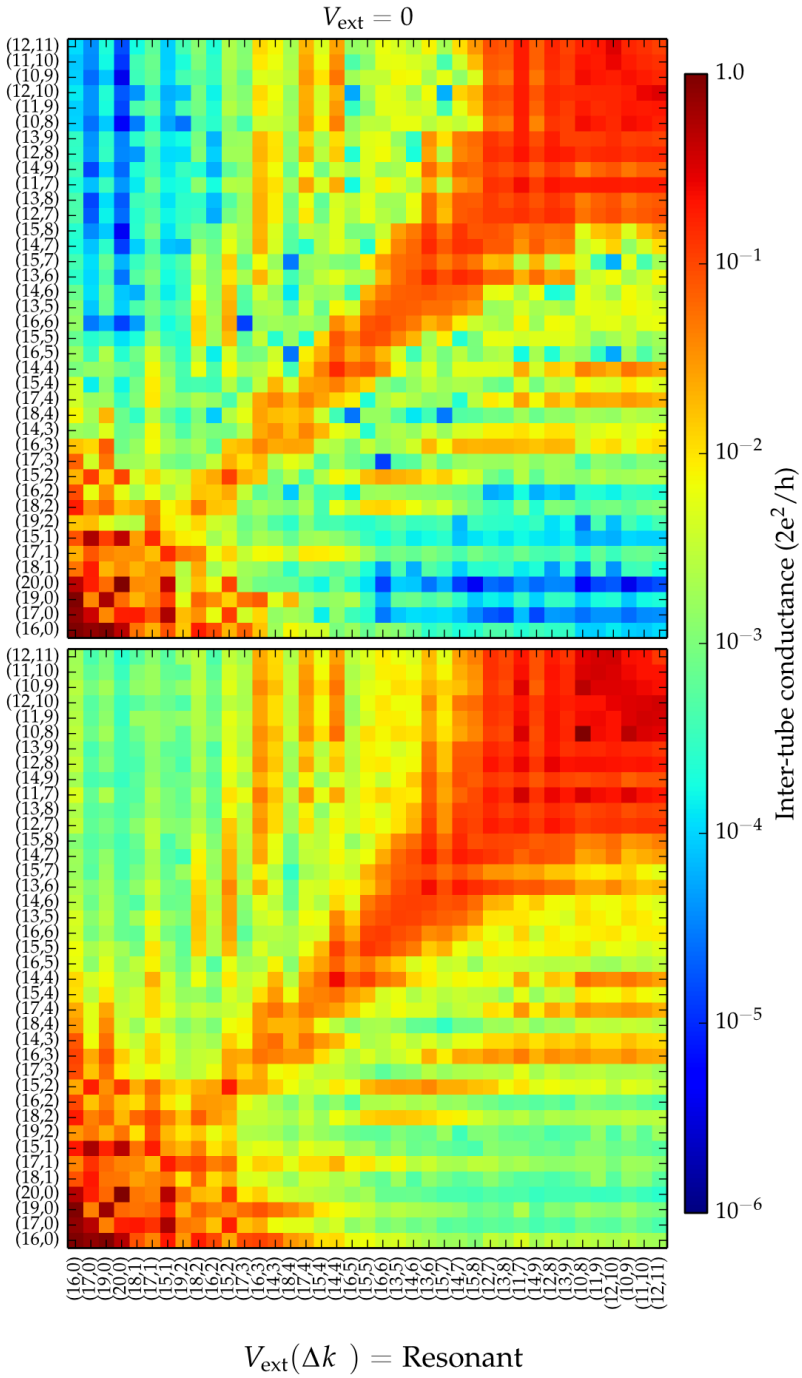

Figure 6.8: The inter-tube conductance between all pairs of semiconductor CNTs in the diameter range $1.2 - 1.6$ nm. We show CNTs of opposite handedness only. Left: intrinsic conductance $V_{\text{ext}} = 0$; right: maximum enhanced conductance (V_{ext} resonant). The CNTs are ordered according to increasing chiral angle and labelled by the (n, m) chiral indices.

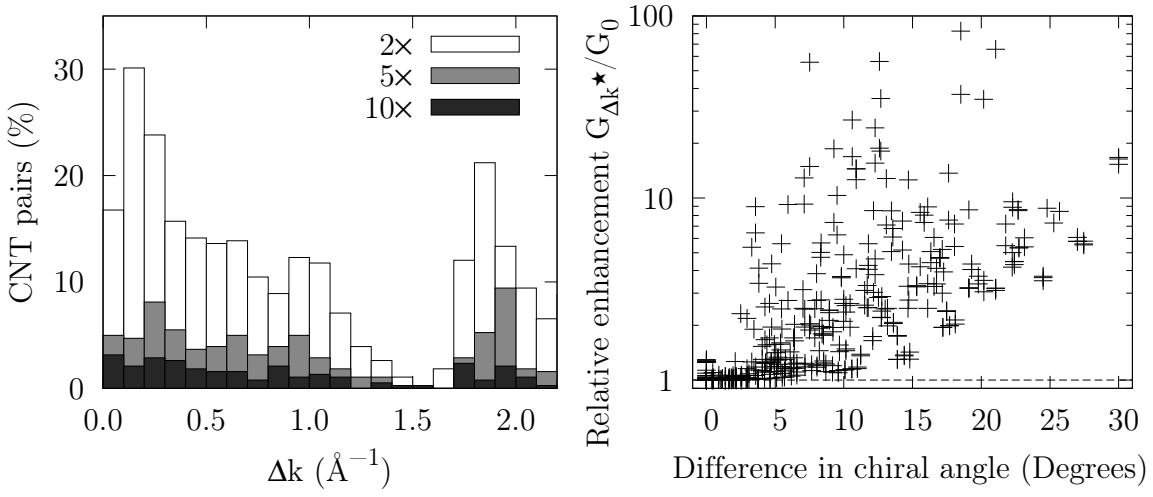

(a) **(b)**

Figure 6.9: Left: the fraction of the 382 CNT pairs studied that have a given momentum resonance that increases inter-tube conductivity by factors of at least 2, 5 and 10. Right: the enhancement in the inter-tube conductance as a function of the difference between the chiral angles of the CNTs. The enhancement is defined as the ratio of the maximum inter-tube conductance when the external potential is at momentum-resonance $G_{\Delta k^\star}$ to the intrinsic conductance G_0.

to the intrinsic inter-tube conductance. For CNTs with similar chiral angles, there is no improvement in the inter-tube conductance as energy-momentum-conserving tunnelling can occur at first-order, and hence this conductance is already large even in the absence of an external potential. For CNTs with chiral angles differing by more than 3°, there is an improvement in the conductance by up to two orders of magnitude due to the momentum-resonant external potential. We reiterate again that for non-resonant momentum exchanges, the weak external potential does not decrease the inter-tube conductance.

6.6 Momentum resonances in doped nanotubes

In addition to momentum-resonant conduction at the Fermi energy, we can also consider the effect of this mechanism over a wider range of energies and thereby understand how momentum resonance improves the inter-tube conductance in doped CNTs and CNTs at finite bias. As a result of the linear dispersion relations around the Dirac points, for electronic states propagating in the same direction in both CNTs, the momentum exchange is resonant over a wide band of energies around the Fermi level. This effect can be seen in Fig. 6.10a where we plot the transmission spectrum between leads 1 and 4, corresponding

to tunnelling between initial and final states that propagate in the same direction, for a range of momentum exchanges near resonance. As the inter-tube conductance is improved over a wide range of energies in the vicinity of the undoped Fermi energy, a change to the Fermi energy due to doping will not reduce the improvement in the inter-tube conductance due to momentum resonance. [33] and applies to doped CNT networks.

For pairs of semiconductor CNTs with similar diameter the valence and conduction bands become aligned and an equivalent broad-energy inter-tube conductance is observed as shown in Fig. 6.10b. At the valence and conduction band edges, the improved inter-tube conductance is further enhanced by the large density of states at the van Hove singularities.

Transmission between leads 1 and 3 requires the coupling of states travelling forward in one CNT, and backward in the other CNT, corresponding to coupling bands with opposite Fermi velocities. In Fig. 6.11 we compare the transmission spectra with and without the external potential as a function of momentum exchange for the metallic $(9,0)/(5,5)$ CNT pair. In the absence of the external potential, two peaks[5] exist at $\sim \pm 0.70\,\mathrm{eV}$, corresponding to energies where the two CNT dispersion relations cross. At these energies, momentum conserving tunnelling can occur at first order, and the conductance is not suppressed, as discussed in Ref. [175]. Due to the linear dispersion relations around the Fermi energy, for CNTs with different chiralities these peaks are guaranteed to lie away from the (un-doped) Fermi energy and will therefore generally not contribute to the inter-tube conductance.

In the presence of an external potential that is slightly off-resonance, additional peaks appear in the transmission between leads 1 and 3 due to the second-order mechanism. These peaks correspond to tunnelling between states that are separated by this momentum exchange, but they do not lie at the Fermi energy, as indicated in the inset to Fig. 6.11. As the momentum exchange approaches a resonant value, these additional peaks move towards the Fermi energy, and transmission at the Fermi energy is momentum-resonant for states propagating in either direction after tunnelling.

6.7 Resonant back-scattering

Finally, we discuss the effect of the external potential on back-scattering within the individual CNTs. Back-scattering by potentials which vary on length-scales larger than the carbon-carbon bond-length has been shown to be vanishingly small for metallic CNTs [48]. To put this into the context of this work, we consider the intra-tube conductance corresponding to transmission from lead 1 to lead 2 (Fig. 6.1). In Fig. 6.12a we show the

[5] The side lobes associated with these peaks are a result of interference due to finite overlap length L[175].

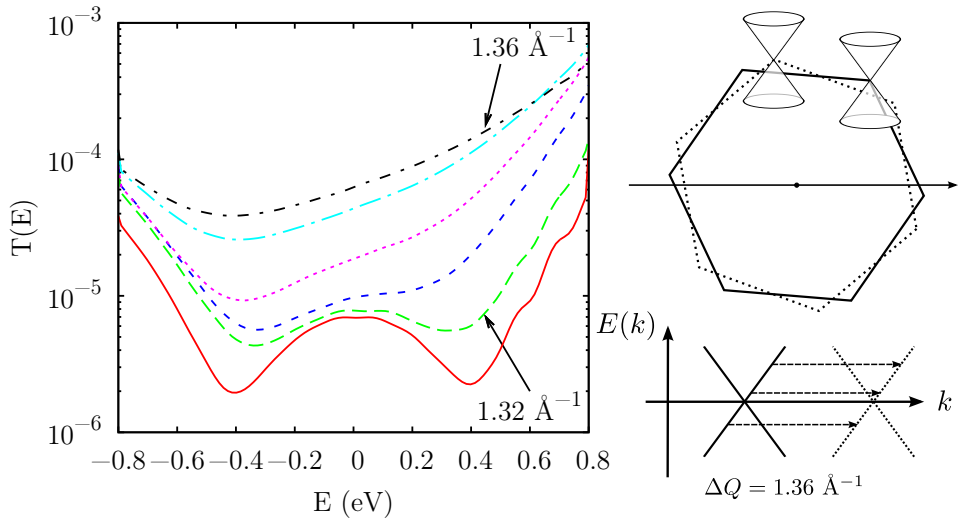

(a) Metallic

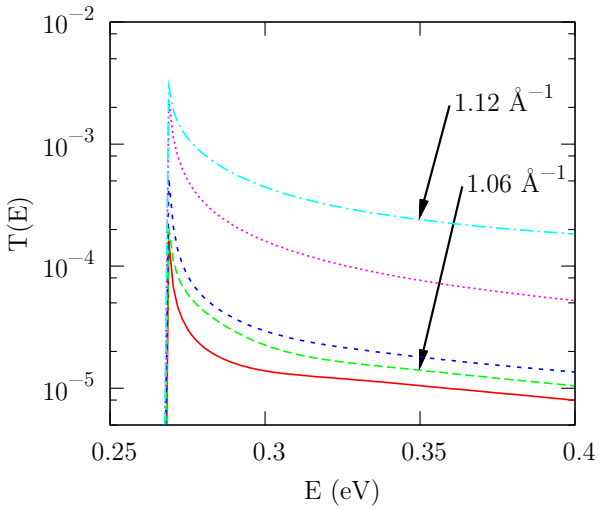

(b) Semiconductor

Figure 6.10: Top left: the transmission between leads 1 and 4 for the metallic $(12, 9)/(13, 4)$ CNT pair as a function of electron energy for $\hat{V}_{\text{ext}} = 0$ (solid red), and for momentum transfer increasing in steps of 0.01 Å^{-1} from $\Delta k = 1.32$ Å^{-1} (dashed green) to $\Delta k = 1.36$ Å^{-1} (dot-dashed black) where momentum- resonance occurs. The transmission increases as resonance is approached. The Fermi energy is zero. Top right: the Dirac points involved in this resonance, and the projection of the dispersion relation onto the axial momentum axis. The momentum exchange, indicated by the arrows, is resonant over a wide range of energies around the Fermi level. Bottom: the same for the semiconductor $(20, 0)/(14, 7)$ CNT pair. Resonance is at 1.12 Å^{-1} (dot-dashed, cyan).

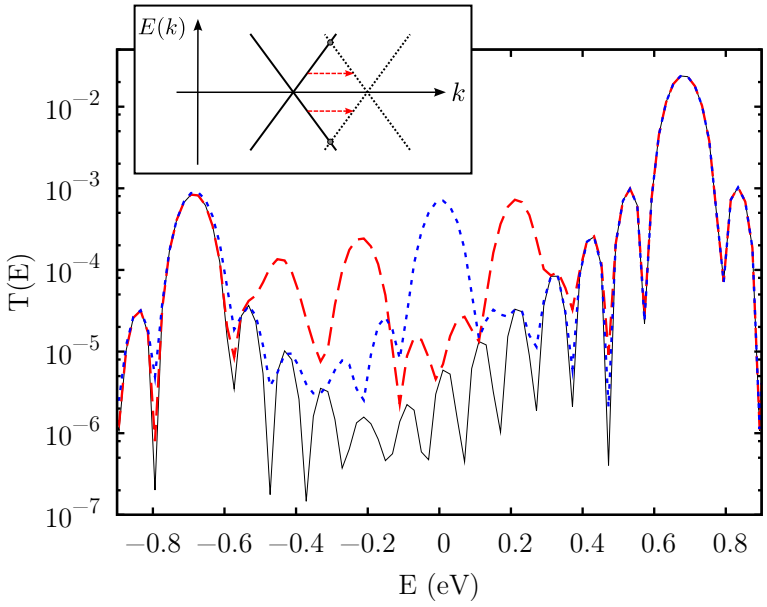

Figure 6.11: Main: transmission between leads 1 and 3 for the $(9,0)/(5,5)$ CNT pair as a function of electron energy for $\hat{V}_{\text{ext}} = 0$ (solid black), off-resonance $\Delta k = 0.78$ Å^{-1} (long-dashed red) and at resonance $\Delta k = 0.85$ Å^{-1} (short-dashed blue). The Fermi energy is zero. Inset: the projection of the dispersion relations onto the axial momentum axis. The states involved in scattering for $\Delta k = 0.78$ Å^{-1} are shown by the arrows.

intra-tube conductance at the Fermi energy as a function of momentum exchange for the $(18, 0)/(10, 10)$ CNT pair. For most momentum exchanges, there is no noticeable decrease in intra-tube transmission, in agreement with Ref. [48]. However, for three momentum exchanges, sharp reductions in the conductance appear. The momentum exchange associated with these features correspond precisely to the momentum difference between different Dirac points belonging to the same CNT. This is illustrated in the inset to Fig. 6.12a. At these momentum exchanges, the electronic states at two different Dirac points can mix causing strong back-scattering, greatly reducing the intra-tube conductance. As a result of this mixing and the local change in the conducting states/density of states, the inter-tube conductance may also be increased, as shown in Fig. 6.12b. This enhancement in inter-tube conductance is not a consequence of the second order mechanism presented in section 6.2, but rather is due to the resonant back-scattering in the intra-tube conductance. Note, however, that the decrease in the intra-tube conductance is far greater than the increase in the inter-tube conductance indicating that the overall resistance of the CNT pair greatly decreases. Mixing between states away from the Fermi energy but at the same Dirac point is forbidden by the orthogonality of the subbands, thus preventing back-scattering for small momentum exchanges. Resonant back-scattering is also found in semiconducting CNTs as shown in Fig. 6.5, but differs from pairs of metallic CNTs as back-scattering is strong for small momentum exchanges. This arises due to scattering within the low-energy states of the conduction or valence band. In contrast with metallic CNTs, this low-momentum scattering is not forbidden as scattering takes place between two states belonging to the same subband. Note that there is no inter-tube enhancement associated with the resonant back-scattering observed in Fig. 6.5, suggesting that the inter-tube enhancements associated with back-scattering, as shown in Fig. 6.12b, are not general.

Finally, we note that these conclusions about the effects of resonant back-scattering are not uniquely associated with the second-order mechanism described in this chapter, and are general for any perturbation to individual, or bundles of, metallic or semiconducting CNTs. What is important about our proposed mechanism is that it can be effected using metallic only CNTs and long-ranged weak perturbations without introducing significant back-scattering.

6.8 Summary

To summarise the results of this chapter, we have presented a mechanism that increases the side-wall inter-tube conductance between CNTs of different chirality. The results from

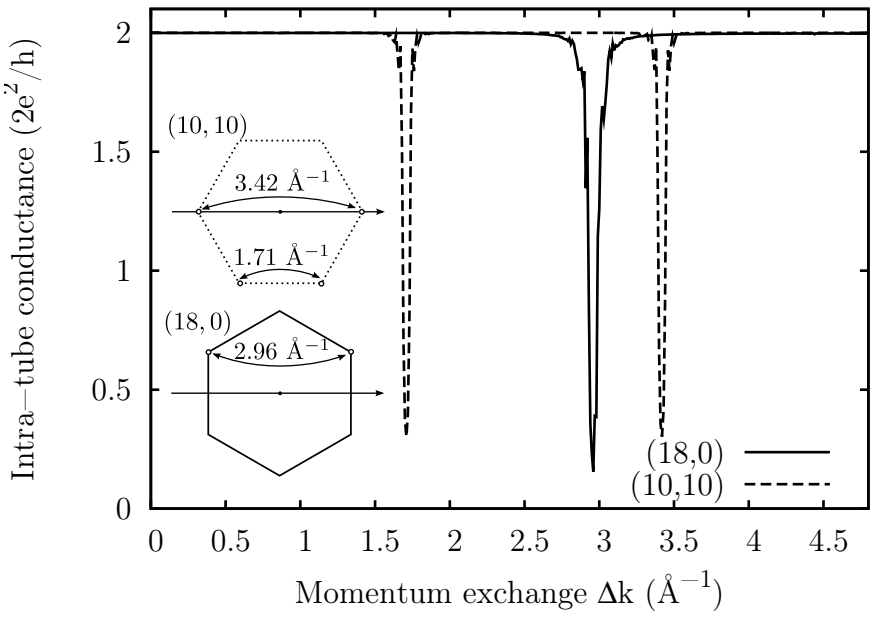

(a)

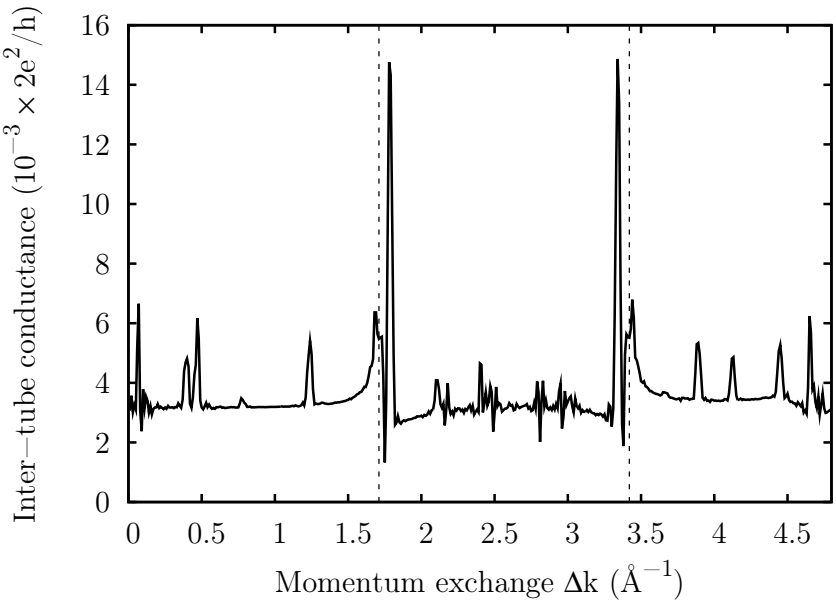

(b)

Figure 6.12: Top: the intra-tube conductance for the $(10, 10)/(18, 0)$ CNT pair. The inset shows the Dirac points involved in the resonant back-scattering processes. Bottom: the inter-tube conductance between the $(10, 10)/(13, 4)$ CNT pair. In addition to the peaks arising due to the second-order mechanism discussed in the main text, two additional peaks at $\Delta k \approx 1.7$ Å^{-1} and 3.4 Å^{-1} are present due to resonant back-scattering in the $(10, 10)$ CNT shown in the left panel. The dashed lines give the positions of these back-scatterings.

this chapter suggest that the greatest improvement in inter-tube conductance can be made by reducing the range of chiralities present in a network. However, in the continuing absence of an experimental method to reliably achieve this at the bulk scale, then significant increases in the inter-tube conductance can also be made with a weak external potential allowing momentum exchange with the environment promoting momentum conserving scattering. By ensuring that the potential varies slowly compared to the inter-atomic distance, back-scattering will be vanishingly small[48], and as the mechanism is second order in the inter-tube interaction, the perturbation can be localised away from the contact region. Chemical bonding is not required, and instead weaker, long-range physical interactions can be utilised. Possible candidates include electrostatic influences of adsorbed molecules; substrate surface reconstructions; Moiré patterns induced in multi-walled CNTs [183]; phonon-assisted tunnelling[6]; and polymer-wrapped CNTs[184]. Indeed, we expect that enhancements due to this mechanism are already present in CNT wires and networks due to naturally-occurring disorder. Improving the quality of the material by removing this disorder may, counter-intuitively, reduce the conductance of these CNT networks.

In the next chapter, two candidate sources of momentum scattering are described and investigated: that of scattering at CNT terminations, and scattering at CNT bends. The transport properties of these configurations are investigated using the first-principles methodologies described in chapter 5 thus providing an unprejudiced description of their relative contributions to conduction in carbon nanotube networks.

[6]Due to the low energies of the acoustic phonon modes, phonon-assisted tunnelling can be considered as quasi-elastic. The higher energy optical phonons are unpopulated at room temperature.

CHAPTER

SEVEN

FIRST-PRINCIPLES CONDUCTANCE BETWEEN CARBON NANOTUBES

7.1 Introduction

In the previous chapter, we showed that the inter-tube conductance between CNTs of different chirality can be strongly affected by weak perturbations to the electronic structure of the CNTs. The origin of this mechanism lies in the momentum difference between the conducting states in each CNT: where the chirality mismatch between the CNTs is large, the conducting states in each CNT have very different momentum which suppresses the intrinsic inter-tube conductance; the addition of the weak perturbation creates momentum scattering which can compensate for the momentum difference between these states and greatly enhance the inter-tube conductance. Several candidate sources of perturbations were suggested at the end of the previous chapter, but it is neither known which perturbations may be more effective at improving the inter-tube conductance, nor whether any significant improvement over the intrinsic inter-tube conductance can be achieved.

A number of studies have used tight-binding models to investigate inter-tube tunnelling in the presence of defects, structural distortions and terminations to the CNT structure.[185, 186, 175, 187, 188] However, as a variety of tight-binding models have been used in these studies, it is difficult to compare the relative enhancements to the inter-tube conductance. Moreover, the reliability of these models when describing different geometries and conformations is *a priori* unknown, and indeed may be particularly deficient when describing defects and/or terminated CNTs where the electronic structure is significantly different from the bulk.

Several studies have calculated conductances between terminated CNTs using electronic

structures derived from first-principles calculations[170, 171, 172, 174], however these studies have focused on conduction between CNTs of the same chirality with a single termination geometry, such as hydrogen passivation or fullerene capping, and are therefore not representative of the range of geometries and chiralities observed experimentally. There is, therefore, a need for a comprehensive study, using calculations performed on a single theoretical footing, that addresses different sources of momentum-scattering and compares how they can affect inter-tube conductances.

In this chapter, we focus on two candidate perturbations to the structure of CNTs that cause momentum scattering between the electronic states in axially aligned CNTs, namely: bends and terminated ends. We concentrate on the two axially-aligned geometries shown schematically in Fig. 7.1: the first (Fig. 7.1a) is used to study tunnelling between the side-walls of two CNTs with arbitrary termination and chirality and overlap length L; the second (Fig. 7.1b) is used to study tunnelling between the side-walls of two CNTs of which one has two bends with mean slope ϕ as defined in Fig. 7.1. In both cases the first-principles methodology developed in chapter 5 is used to calculate inter-tube conductances.

Our main conclusion from these calculations is that terminations and bends increase the inter-tube conductance, with the magnitude of the increase consistent with the magnitude of the momentum-scattering introduced by the perturbation. Neither perturbation, however, fully compensates for the suppression of inter-tube conductance due to chirality mismatch suggesting that, whilst introducing sources of momentum scattering will increase the conductance of CNT networks, reducing the range of CNT chiralities present in a network is the best way of improving the overall network conductivity. Nonetheless, we observe up to ten-fold increases in inter-tube conductances between chirality-mismatched CNTs with realistic bends and terminations.

The remainder of this chapter is organised as follows. We first describe in section 7.2 our methods used to generate the geometries and electronic structures. In section 7.3 we discuss how momentum scattering at bends in the CNT structure may improve the inter-tube conductance; in section 7.4 we then address the role of different end termination geometries affects the inter-tube conductance. Finally, in section 7.5, we explore how the inter-tube conductances may be affected by non-equilibrium forces arising due to a finite bias applied across the junction. Parts of this chapter are being prepared for publication[189].

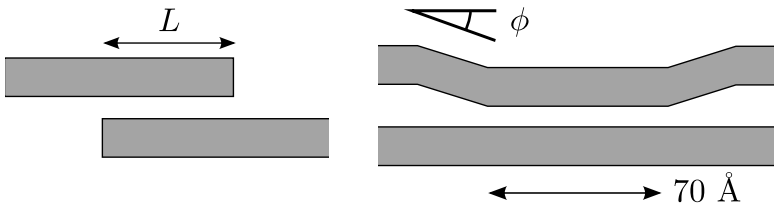

Figure 7.1: The schematic geometries of the CNTs in the end-scattering and bend-scattering configurations. L is the overlap length in the end-scattering geometry; a number of end termination geometries are considered. In the bend-scattering geometry, ϕ describes the bend angle and the contact length between the onset of the two bends is taken to be 70 Å. The actual bend geometries studied are smoother than the representation in this figure.

7.2 Methods

Conductances are calculated using the methodology discussed in chapter 5. The auxiliary simulation geometries for the end-scattering and bend-scattering configurations are shown in Fig. 7.3. In the end-scattering configuration (Fig. 7.3a), which consists of two finite CNT fragments, the structure represented by the thick lines forms the device geometry. Lead self energies are constructed using matrix elements derived from the extreme left/right of the device geometry; buffer atoms, indicated in grey, are included to ensure that the local electronic structure in this region is bulk-lead like, which is confirmed by inspecting the lead bandstructure as discussed in section 5.5.2. The bend-scattering configuration (Fig. 7.3b) is a four-lead geometry, with the lead regions taken to be at the far left/right of each CNT in the structure shown; no buffer atoms are necessary for this geometry.

The electronic structures of these auxiliary simulation geometries are computed using a minimal basis of four NGWFs per carbon atom and one per hydrogen atom, each with a localisation radius of 4.2 Å. An equivalent kinetic energy cutoff of 850 eV is used for the underlying psinc basis, and the Brillouin zone is sampled at the Γ point only. Periodic boundary conditions are used throughout, with non-periodic directions treated using the supercell approximation and with a distance of at least 12 Å separating atoms in the periodic images. Exchange and correlation are treated using the PBE expression of the generalised gradient approximation[106]; dispersion interactions are included with empirical corrections[190].[1] In all calculations, we define the Fermi energy as the average chemical potential of the leads, which is set to zero.

[1] Note that these empirical dispersion corrections do not directly affect the electronic structure, but do affect the optimised geometry.

7.2.1 Generating the structure

The atomic structures shown in Fig. 7.3 are generated for four CNT chiralities: $(5,5)$, $(7,4)$, $(8,2)$, $(9,0)$. In all cases, relaxed bulk CNT structures were used as the starting point for obtaining the atomic geometries shown in Fig. 7.3 and other similar structures used in this study, which are described in more detail below. Full first-principles geometry relaxations of the entire perturbed structure are not performed due to the high computational cost and because the precise structure has bearing on the main conclusions of this work. The bulk CNT structures are generated by relaxing the geometry using the plane wave DFT code CASTEP. A maximum force and stress tolerance of $5\ \mathrm{meV/\AA}$ and $0.02\ \mathrm{GPa}$, respectively, is used in this optimisation. For each CNT, the Brillouin zone was sampled with a single *k*-point in non-periodic directions, and a uniform mesh of *k*-points along the periodic direction with spacing no larger than $0.05\ \mathrm{\AA}^{-1}$. All other parameters were equivalent, in so far as possible, to those used in the ONETEP calculations for determining the ground state electronic structure of the final perturbed structures (i.e. the auxiliary simulation geometries).

For the terminated geometry, we focus on achiral $(5,5)$ and $(9,0)$ metallic CNTs, and consider the five different termination geometries shown in Fig. 7.2: the none/sp^2/sp^3 terminations (shown in Fig. 7.2a–c) saturate the terminating carbons with no hydrogen atoms/a single hydrogen atom/two hydrogen atoms, retaining the zig-zag/armchair termination geometry of the original CNT; the slant geometry (Fig. 7.2d) replaces the zig-zag edge with an armchair edge and *vice versa*; and, the capped geometry (Fig. 7.2e) terminates the CNTs with half a C_{60} fullerene molecule. Experimentally, it is difficult to determine the precise termination geometry of any CNT termination although it is known that both fullerene capped and open CNTs exist.[191] Our justification for considering these five terminations is that they cover a range of possible geometries that are relatively clean and may exist after purification of CNT samples.

The termination geometries are generated using CASTEP by relaxing a CNT fragment at least $10\ \mathrm{\AA}$ in length containing the required termination. Relaxations are performed on non-magnetic electronic structures though relaxation under spin-unrestricted conditions was not found to appreciably change the geometries. The fragment was then attached to bulk CNT structure (calculated as described above) without further optimisation to form the full fragment. Two such fragments were then axially-aligned with a $3.3\ \mathrm{\AA}$ separation between the CNT surfaces which is close to the graphite interlayer distance, with an overlap length L, defined as the axial difference between the extremal carbon atoms of the two CNTs.

In the bend geometry, we consider inter-tube conductance between a $(5,5)$ and (n,m)

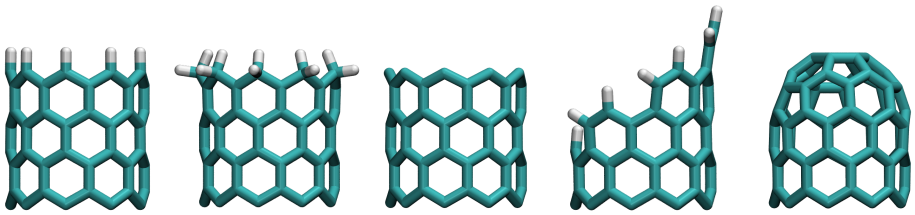

Figure 7.2: The different passivation schemes considered to terminate the $(9, 0)$ zig-zag CNT. Equivalent terminations were used for the $(5, 5)$ arm chair CNT. Chiral CNTs were terminated using a slant-like hydrogen passivation.

CNT, where (n, m) is one of the four chiralities considered in this work. Bends were created in each end of the $(5, 5)$ CNT, as shown in Fig. 7.3b, by displacing at least 8 primitive CNT unit cells off-axis by 5.2 Å. Both of these regions were divided into two four-primitive unit cell principle layers in order to define the leads of this CNT; principle layers were defined at equivalent locations within the unbent CNT containing four, three, two, and one primitive unit cells for the $(5, 5)$, $(9, 0)$, $(8, 2)$ and $(7, 4)$ CNTs, respectively. The resulting separation between the principle layers of each lead is 8.5 Å, which is larger than twice the NGWF radius thus resulting in no direct coupling between the leads. For the bends, a region of bulk-like CNT is introduced to connect the principle layers to the central contact region. The angle of the bend is controlled by modifying the number of primitive unit cells within the bend region. The geometry within each bend region is fully relaxed using the Brenner empirical bond-order potential[192, 193, 194], whilst holding fixed the geometry of the contact region, the lead principle layers and the entirety of the unbent CNT.[2] This procedure allows for the bend slope to be defined as shown in Fig. 7.1. The length of the contact region is taken to be 70 Å in all cases.

Three bend angles are considered, $\phi = 4.9°, 7.4°, 9.9°$. As each CNT chirality has a different unit cell length, it is not possible to ensure that each unbent CNT has the same length. To fit the bent CNT into the same periodic simulation cell as the unbent CNT, the geometries of the bends introduced cannot be identical across all CNT pairs for a given bend angle. The perturbation induced by the bend will not be identical for different CNT pairs with the same bend angle. We have chosen our simulation cells to minimise this difference and have confirmed that similar bond strains are produced for a given bend angle. We believe that this procedure controls the difference in strains sufficiently well to allow for

[2]The pristine structure generated by the Brenner potential and PBE functional with empirical dispersion interactions are found to be very similar, with structural parameters (bond lengths, diameter, unit cell length) differing by less than 1%.

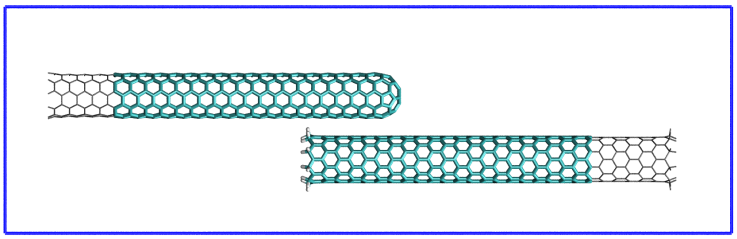

(a) end-scattering

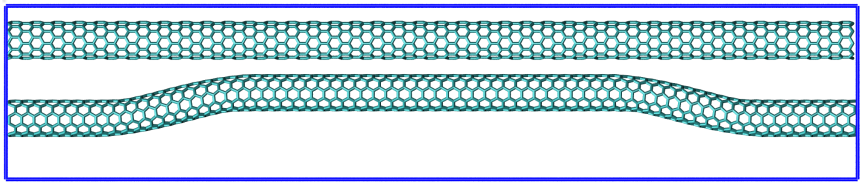

(b) bend-scattering

Figure 7.3: The auxiliary simulation geometries from which transport matrix elements are extracted. (a) The end-scattering geometry. Grey atoms are buffer atoms, included in the DFT calculation, but excluded from the transport calculation. (b) The bend-scattering geometry. The blue boxes indicate the size of the periodic simulation cell.

meaningful comparison of inter-tube conductances for each CNT pair.

7.3 The role of bend angle

The inter-tube conductance between pairs of CNTs with a large difference in chiral angle is found to have a strong dependence on bend angle. Fig. 7.4a compares the inter-tube conductance of the $(9,0)/(5,5)$ CNT pair as a function of energy for three bend angles, showing that as the bend angle is reduced the conductance around the Fermi energy can decrease by an order of magnitude. Fig. 7.4b compares the inter-tube conductance 0.2 eV below the Fermi energy for the same CNT pair and for the $(5,5)/(5,5)$ pair, where there is no chiral difference between the CNTs. The inter-tube conductance for the $(5,5)/(5,5)$ pair is found to be approximately constant with bend angle. These results can again be understood as a consequence of the momentum scattering provided by the bends: for a large chiral angle difference, the steeper the bend the greater the momentum scattering, permitting greater coupling between the states in each CNT; for the case where there is no chiral angle difference, momentum-scattering is not required to facilitate conductance and the bend has minimal effect on the inter-tube conductance.

Whilst we compare these bends largely by the difference in slope angle, the strain

Bend angle:	$9.9°$	$7.4°$	$4.9°$
	rms (max)	*rms* (max)	*rms* (max)
$(5,5)/(5,5)$	1.9 (5.1)	1.0 (2.9)	0.8 (2.3)
$(7,4)/(5,5)$	2.2 (5.3)	1.1 (3.0)	1.3 (2.8)
$(8,2)/(5,5)$	1.8 (5.0)	1.7 (3.7)	1.5 (3.1)
$(9,0)/(5,5)$	2.0 (5.3)	1.7 (3.7)	0.9 (2.3)

Table 7.1: The *rms* and maximum bond strains (in $\%$) within the bend region for the different CNT pairs and bend angles. The bends are introduced to the $(5,5)$ CNT.

induced by the bends is an equally important physical parameter. In Table 7.1, we show the *rms* and maximum bond strains induced in the structure for the three bends and for the different CNT chirality combinations, indicating that the strain and bend angle are correlated, as expected. The correlation is a complex one due to the computational constraint of periodic boundary conditions which requires the length of the bent $(5,5)$ CNT to coincide with an integer number of primitive unit cells of the unbent CNT; using our technique, it is not possible to systematically change the strain rate values. Nonetheless, the maximum strains are much lower than the elastic yield strain predicted for CNTs ($\approx 30\%$ [195]), and are smaller than the maximum average strain observed experimentally ($\approx 6\%$ [196]) which are believed to be entirely plausible structures, if not much less extreme deformations than those likely present in a CNT network. As a consequence of the low strains, all of the structures maintain their tubular shape and there are no kinks. The resulting weak perturbation has been shown to introduce little backscattering in individual CNTs [197]. In Fig. 7.4c we compare the sum of the intra- and inter-tube conductances to the backscattered conductance and the results show that very little current is backscattered into the original source lead. Similar results are found for the all bend angles considered. Hence the magnitude of the backscattering is not strongly dependent on the bend angle for the relatively shallow bends studied, indicating that the bend itself is not a significant source of backscattering, as expected. The effect of the bends, therefore, is only to improve the inter-tube conductance without significantly increasing the resistance of the individual CNTs, confirming the mechanism proposed in [167].

As further evidence of the impact of the bends on the inter-tube conductance, we compare the spatial extent of the transmission eigenchannels for the $(5,5)/(5,5)$ and $(9,0)/(5,5)$ CNT pairs. In the top two panels of Fig. 7.5 we plot the modulus-square density of these eigenchannels, integrated over the direction perpendicular to the plane containing the two CNT axis; the lower panel of Fig. 7.5 shows the inter-tube eigenchannel

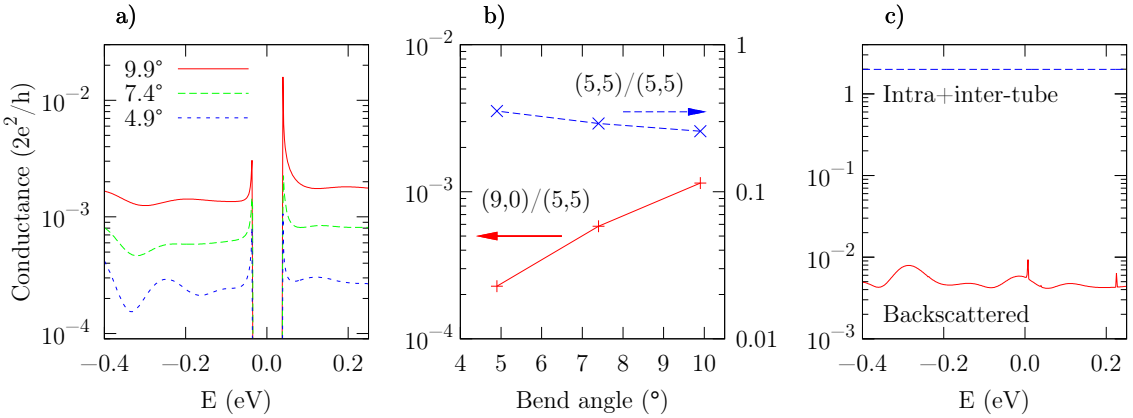

Figure 7.4: Left panel: the inter-tube conductance spectrum between $(9,0)/(5,5)$ CNTs for three bend angles. Centre panel: the bend angle dependence of the inter-tube conductance 0.2 eV below the Fermi energy for the $(9,0)/(5,5)$ and $(5,5)/(5,5)$ CNT pairs. Right panel: the backscattering conductance and sum of intra- and inter-tube conductances for the $(9,0)/(5,5)$ pair with $9.9°$ bend.

density as a function of length along the CNT axis, which is obtained by integration over the second (non-source) CNT only. For the $(5,5)/(5,5)$ pair, where there is no chiral mismatch, the weight of the eigenchannel on the second CNT increases over the overlap region indicating that tunnelling between the CNTs is occurring due to the proximity of the CNTs. The amplitude of the eigenchannel density integrated on the second CNT is found to increase approximately quadratically as the state propagates in the contact region, in agreement with previous analytic calculations.[175] In contrast, however, the eigenchannel for the $(9,0)/(5,5)$ pair is approximately constant within the contact region but increases dramatically at the location of the bend. This confirms that it is the presence of the bend that is responsible for the inter-tube conductance when there is a mismatch in chirality between the CNTs.

These simulations therefore highlight the importance of weak sources of momentum scattering on the conductance of the network as a whole. The source of weak momentum scattering in these simulations is the perturbation introduced by a relatively shallow bend in the CNT structure.

7.3.1 The effect of chirality mismatch

In Fig. 7.6 we compare the inter-tube conductance in the bend scattering geometry for a range of differences in chiral angles between the CNTs. We plot the conductance evaluated

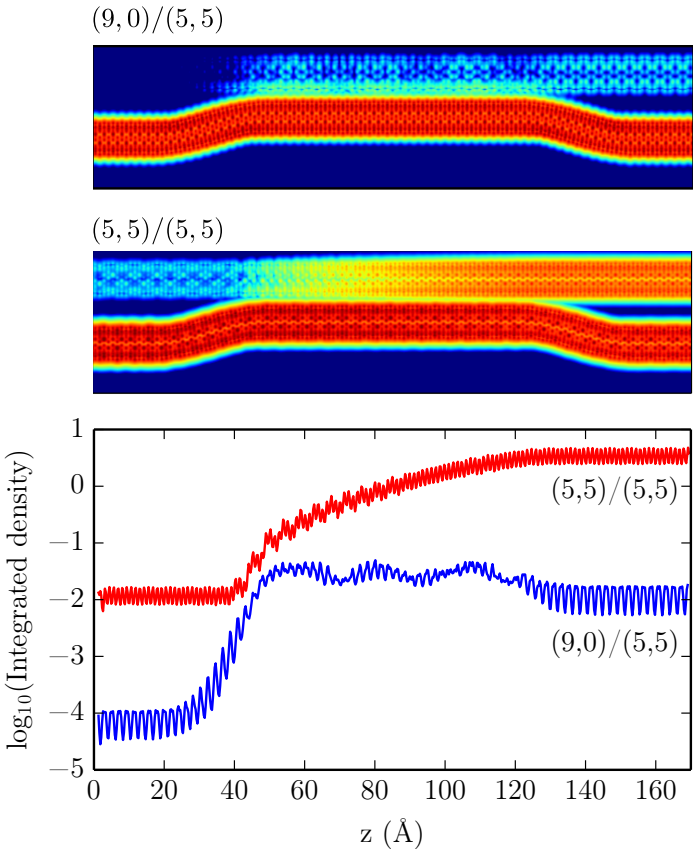

Figure 7.5: The probability density of the first eigenchannel evaluated 0.35 eV below the Fermi energy for the $(5,5)/(5,5)$ and $(9,0)/(5,5)$ CNT pairs with $9.9°$ bends. In the top two panels, the eigenchannel is integrated over the direction perpendicular to the plane containing both CNT axes. The lower panel gives the same quantity integrated over the two axes perpendicular to the CNT axis within the spatial region of the second (non-source) CNT only. The state is injected into the bottom left lead.

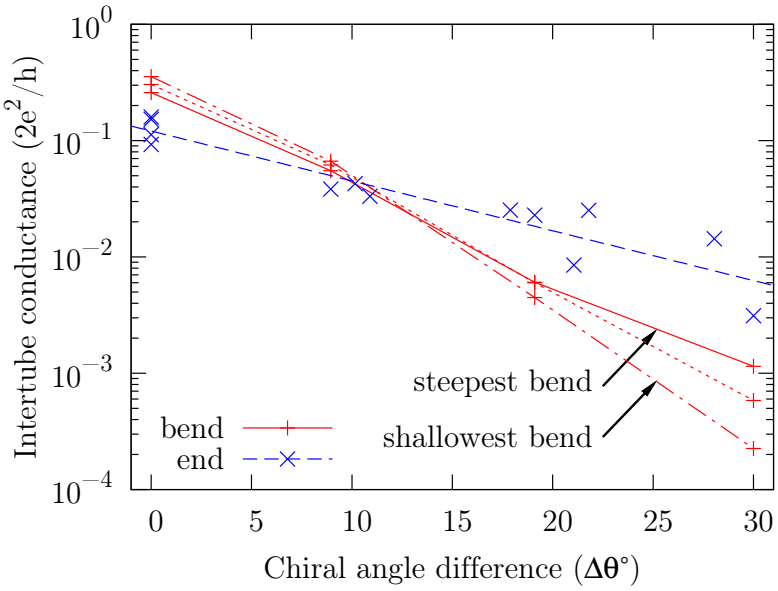

Figure 7.6: A comparison of the inter-tube conductance as a function of difference in chiral angle for pairs of CNTs in end-scattering and bend-scattering geometries. For the bend-scattering geometries, conductance is given for states 0.2 eV below the Fermi energy. Three bend angles are considered $\phi = 4.9^\circ$ (shallowest), 7.4°, 9.9° (steepest). For the end-scattering geometry, the quantity is the characteristic conductance $\langle G \rangle$ defined in Eqn. (7.6); the dashed line gives an exponential fit to guide the eye.

0.2 eV below the Fermi energy, away from the van Hove singularities associated with the band gap and in a region where the inter-tube conductance is approximately constant over a range of energies. For each chirality pair, we show the inter-tube conductance for the three bend angles considered. We find that there is an exponential suppression of the inter-tube conductance with increased chirality mismatch. The introduction of steeper bend angles improves the inter-tube conductance most between the CNTs with largest chirality mismatch, whereas for much smaller chirality differences there is less or no improvement. This result can be understood in terms of the momentum scattering that is required to couple the states in each CNT. For small chirality mismatch, little momentum scattering is required and the scattering introduced by any of the bends is sufficient to enhance the inter-tube conductance. For larger chirality mismatch, the stronger scattering introduced by the steeper bend angle better satisfies the momentum scattering required to effect the inter-tube conductance.

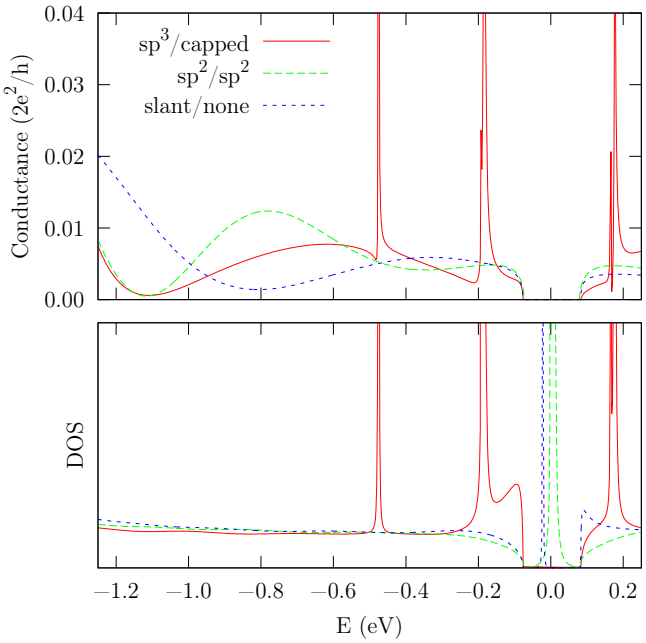

Figure 7.7: Top panel: the conductance spectra between $(9,0)$ and $(5,5)$ CNTs in the end-scattering geometry, for three pairs of terminations. The first termination in the label refers to the termination of the $(9,0)$ CNT. Bottom panel: the corresponding device density of states. The Fermi energy is set to zero.

7.4 The role of end termination

We now describe our investigations into momentum scattering at CNT end terminations. We first focus on the role of the end termination geometry before considering the effect of chirality mismatch.

In Figs. 7.7 and 7.8 we show the conductance spectra for several termination geometries for the $(9,0)/(5,5)$ and $(9,0)/(9,0)$ CNT pairs respectively. We find that the form of the inter-tube conductance in the end-scattering geometry can be understood in terms of two main features, which are consistent across the different chirality pairs and termination combinations.

The first feature we note is the sharp peaks in conductance that occur over a narrow energy range, e.g. at -0.2 eV and -0.5 eV in both figures. As these peaks occur for only some of the termination combinations (in particular ones involving the *none* and sp^3 termination of the $(9,0)$ CNT), they can be understood to arise from the termination itself, and not from the bulk CNT.

There are sharp rises in the density of states associated with each of these peaks in conductance, as shown in the lower panels to Figs. 7.7, 7.8. This indicates that at these

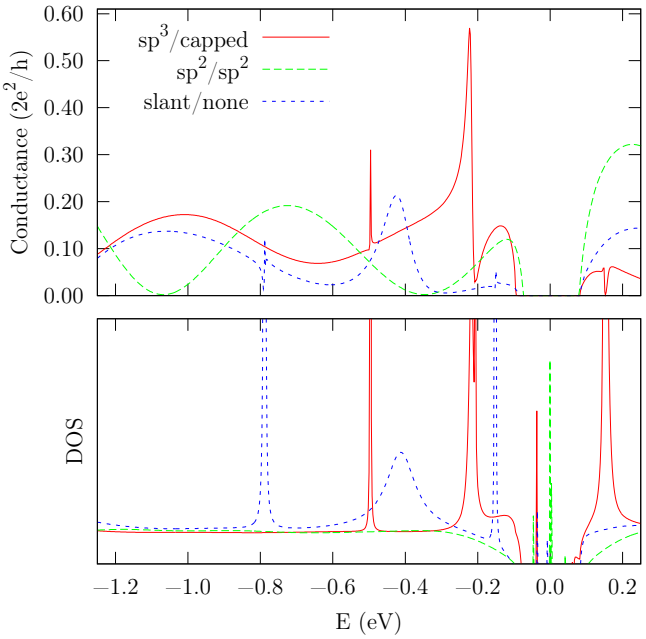

Figure 7.8: Top panel: the conductance spectra between $(9, 0)$ and $(9, 0)$ CNTs in the end-scattering geometry, for three pairs of terminations. Bottom panel: the corresponding device density of states. The Fermi energy is set to zero.

energies there exist localised or quasi-localised states, which are known to be present in terminated CNTs[198, 199, 200], and the rise in conductance is due to resonant scattering from these localised states. The asymmetry of these resonances is typical for Fano-resonant scattering[201], which arises from scattering of continuum states by a localised state.

The importance of the localised state to this resonance is confirmed in Fig. 7.9 where we show the eigenchannel decomposition and the eigenchannels themselves[161]. The top panel of Fig. 7.9 shows the two propagating eigenchannels which are both observed to exhibit resonances at the same energies. This indicates that these resonant features are independent of the eigenchannels themselves which is consistent with scattering from a localised end state. In the bottom panel, we compare the eigenchannels at the two energies indicated in the top panel. One of these energies is resonant whilst the other is non-resonant. The non-resonant eigenchannel is well localised within the source CNT and propagates little onto the second CNT. It is almost entirely real and characteristic of a standing wave, reflecting the fact that the inter-tube conductance is low in this case. At resonance, significant eigenchannel weight is found to exist on the second CNT and, deep into this CNT, the eigenchannel phase is increasing indicating a propagating electronic state. Close to the second CNT termination, however, the eigenchannel remains standing

wave-like indicating no propagation. The form and energy of the eigenchannel within this region is very similar to those of the localised end state of the finite CNT fragment, shown in the bottom panel of Fig. 7.9, confirming that the resonant tunnelling is due to scattering from a localised end state. An equivalent observation is made when inspecting the eigenchannels at the resonance at $-0.2\ \mathrm{eV}$ and the corresponding localised end state. Fano resonant conduction has also previously been observed in crossed CNTs[202, 203].

The enhancement in the inter-tube conductance caused by these localised states should also be compared to resonant back-scattering in individual CNTs that is caused by quasi-localised states associated with defects.[181] In the present case, as the localised states are located at the end of the CNT their additional contribution to back-scattering is minimal when compared to the reflection caused by the termination itself. The presence of the localised states, therefore, primarily acts to increase the inter-tube conductance, albeit within narrow ranges of energy.

The second prominent feature in Figs. 7.7 and 7.8 is the oscillation in conductance that occurs over a broad energy range. This feature can be understood in terms of interference arising from the finite spatial overlap of the CNTs and can be accounted for using a simple analytic model. At first order in perturbation theory, the conductance between the two states $|\psi_1\rangle$, $|\psi_2\rangle$ that originate in different CNTs is approximately proportional to the square of the overlap of those states

$$T(E) \propto |\langle\psi_1|\psi_2\rangle|^2. \tag{7.1}$$

When the CNTs are isolated, the two states will be standing waves with a node at the CNT end and with a periodicity determined by the state wave vector k_i where $i = 1, 2$ indexes the CNTs. Treating the wavefunctions as simple one-dimensional waves, the wavefunction overlap is

$$\begin{aligned} |\langle\psi_1|\psi_2\rangle| &\propto \int_0^L \mathrm{d}z\ \sin[k_1(z-L)]\sin(k_2 L) \\ &\propto \begin{cases} \dfrac{k_2\sin(k_1 L) - k_1\sin(k_2 L)}{k_1^2 - k_2^2} & \text{for } k_1 \neq k_2, \\ \dfrac{\sin(k_1 L) - k_1 L\cos(k_1 L)}{2k_1} & \text{for } k_1 = k_2. \end{cases} \end{aligned} \tag{7.2}$$

For a given pair of CNTs, the contribution to the overlap matrix element from the azimuthal momenta of the two states is approximately the same for all end termination geometries and overlap lengths and can therefore be neglected in Eqn. (7.2). The wave vector for both states is dependent on the state energy and CNT chirality, and is given by the lead band

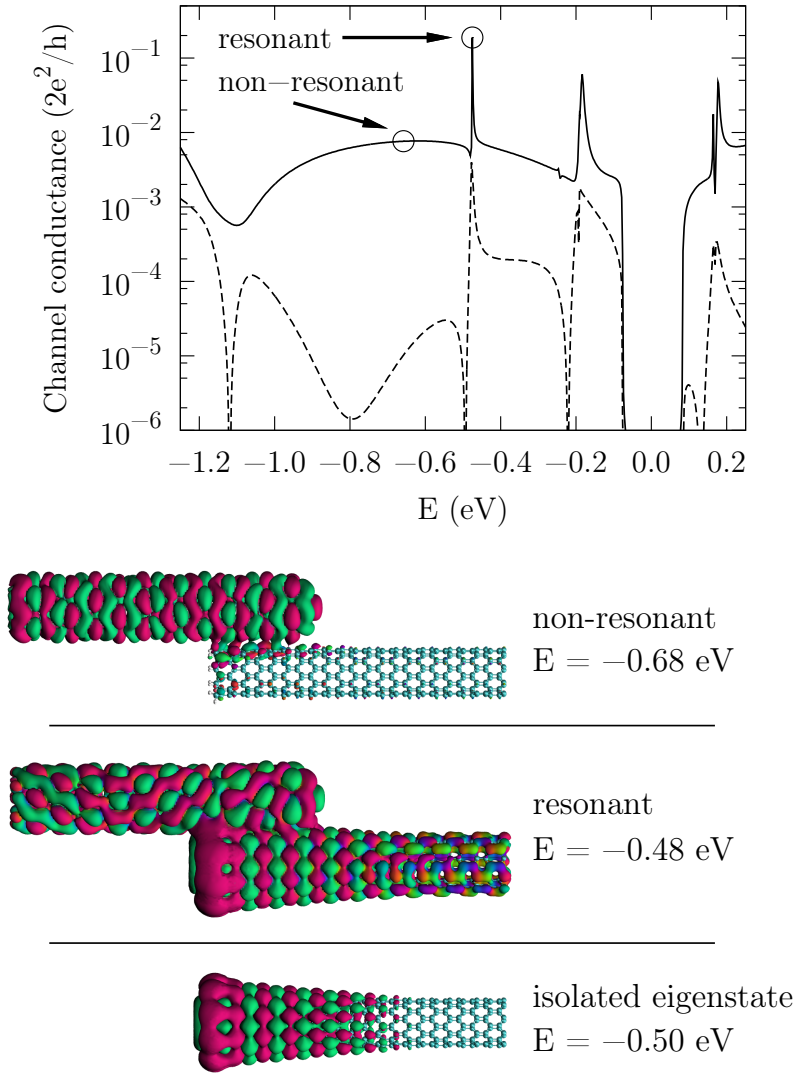

Figure 7.9: Top panel: the eigenchannel decomposition for conductance between a fullerene-terminated $(5, 5)$ CNT and sp^3 terminated $(9, 0)$ CNT. Lower panel, top: the conductance eigenchannel for a non resonant channel. Lower panel, centre: the conductance eigenchannel for a resonant channel. Lower panel, bottom: the localised end state of the isolated $(9, 0)$ fragment. The energies of these three states are given on the right. Each eigenchannel/eigenstate is plotted at an arbitrary isosurface and coloured by the complex phase, and the eigenchannels are injected into the left CNT.

structure, which is linear in the vicinity of the Fermi energy

$$k_i(E) = k_{F,i} \pm \frac{E}{\hbar v_{F,i}}. \tag{7.3}$$

The Fermi momentum $k_{F,i}$ and Fermi velocity $v_{F,i}$ for each lead CNT can be determined directly from the bulk CNT band structure, leaving only the overlap length L, and the overall amplitude as free parameters. As the terminated CNT does not obey periodic symmetry, the Brillouin zone for the system is vanishingly small. It was shown in Ref. [38] however that states of the (extended) CNT Brillouin zone still prove a useful basis for the states involved in conductance, with the caveat that states outside the first Brillouin zone are inequivalent to those within and must be considered separately. This corresponds to considering wave vectors that are a sum of a wave vector $k_{i,(0)}$ from the first Brillouin zone and an integer number α of reciprocal lattice vectors G_i:[3]

$$k_i = k_{i,(0)} + \alpha G_i. \tag{7.4}$$

The dominant contribution to the conductance may not be one from a state within the first Brillouin zone[38, 175]; in the following we find that the dominant contribution is from $\alpha = 1$ and $\alpha = 0$ for the $(9,0)$ and $(5,5)$ CNTs, respectively, in agreement with the results presented in Ref. [175].

In Fig. 7.10 we show the calculated inter-tube conductance for two sp^2 terminated $(9,0)$ CNTs and for fullerene capped $(5,5)$ and $(9,0)$ CNTs. We compare these numerical results to the model presented in Eqn. (7.2); the Fermi momenta and velocities are determined for each CNT separately using the corresponding bulk lead band structure, while the overlap length L and overall amplitude are determined by fitting the model to the conductance calculated from first principles within the valence band over the linear region of the bulk CNT band structures where Eqn. (7.2) is valid.[4] The fitted overlap lengths are 22.6 Å for $(9,0)/(9,0)$ and 14.6 Å for $(9,0)/(5,5)$, which compare excellently with the axial distance between the terminal atoms on each CNT which are 23.2 Å and 15.4 Å, respectively.

Further verification that the interference model captures the main behaviour of the inter-tube conductance is provided in Fig. 7.11 where we plot the conductance between CNTs in the end-scattering geometry evaluated 0.2 eV below the Fermi energy as a function of the overlap length. The model (dashed line) accurately reproduces the periodicity of the

[3] For achiral CNTs, the two reciprocal lattice vectors of the CNTs differ only in their azimuthal momentum and have the same axial momentum. Therefore, only a single integer α is required to describe the addition of the reciprocal lattice vectors.

[4] The fit is restricted to the valence band due to the difficulty in describing the higher-energy conduction band states using the valence NGWF basis (see section 5.6).

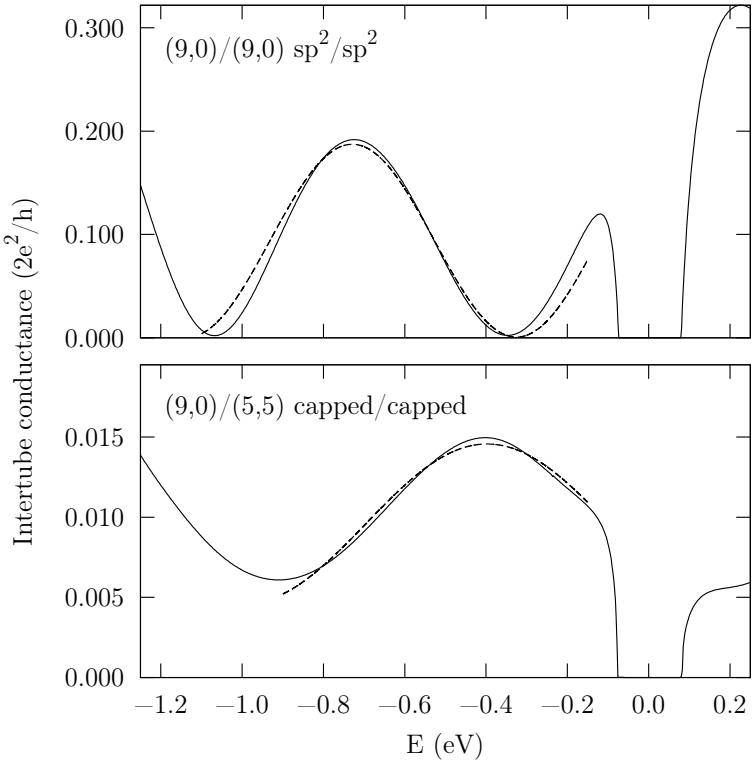

Figure 7.10: A comparison of the calculated (solid line) verses model (dashed line, Eqns. 7.1 and 7.2) inter-tube conductance spectra in the end-scattering geometry. The model is fitted over the linear region of the bulk CNT band structures, indicated by the range of the dashed line.

calculated conductance (solid line), confirming that interference is the predominant factor influencing the inter-tube conductance. This finding is in agreement with several other works that have highlighted the importance of interference effects in inter-tube scattering between terminated CNTs.[185, 186, 204]

As the dominant factors that affect inter-tube conductance between terminated CNTs can be understood in terms of resonant tunnelling due to localised end states and interference effects, some more general conclusions can be drawn. Firstly, we expect these factors to remain dominant in metallic CNTs of other chiralities as the local chemical structure is unchanged by the chirality. Where the CNTs are of different chirality, Eqn. (7.2) predicts that inter-tube conductance is oscillatory with overlap length and therefore increasing overlap length does not always improve the conductance. Where two CNTs have the same chirality, Eqn. (7.2) predicts that the inter-tube conductance grows quadratically with overlap length L, with an additional oscillatory envelope due to interference caused by the standing wave states in each CNT. This is a consequence of tunnelling between the initial and final states

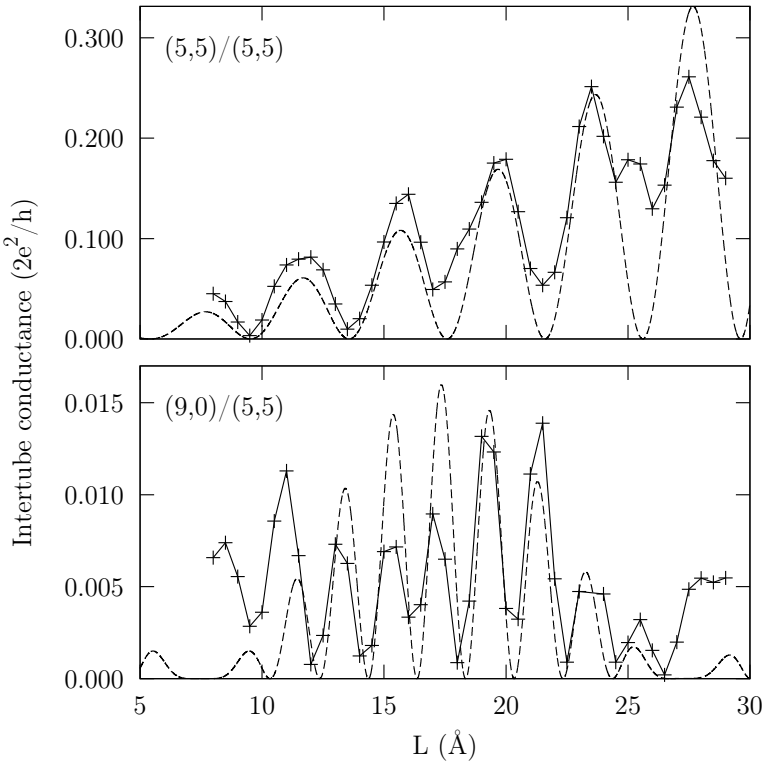

Figure 7.11: A comparison of the calculated (solid line) verses model (dashed line, Eqns. 7.1 and 7.2) inter-tube conductance spectra in the end-scattering geometry. Top panel: conductance between two $(5, 5)$ CNTs; bottom panel conductance between $(9, 0)$ and $(5, 5)$ CNTs; all CNTs are terminated with the sp^2 passivation scheme (see Fig. 7.2). Conductance is evaluated 0.2 eV below the Fermi energy, as a function of overlap length, defined as the axial distance between terminal atoms of each CNT.

being permitted over the entire contact region. The same interference/quadratic growth behaviour has been found for conductance between side-walls of CNTs[175], obtained from tight-binding models; our results confirm this behaviour for terminated CNTs using a first-principles approach. For CNTs of the same chirality, the quadratic growth in conductance means that the effects of the end termination become negligible; for CNTs of different chirality, however, the effect of the end termination does not become negligible with large overlap length. Indeed, the momentum scattering provided by the end termination means that, in this geometry, the termination is the dominant contributor to conductance between CNTs of different chirality.

The different inter-tube conductances calculated for the different terminations can largely be accounted for by the number and energies of the end states present. Whilst it would be desirable to construct CNT terminations with end states located at the Fermi energy, thereby increasing the inter-tube conductance, such an approach is likely to be impractical given the level of structural fine-tuning that would be required. Furthermore, dynamical effects arising from finite temperature will modify the termination geometry and therefore also the energy of these localised states, reducing the effectiveness of this approach. We therefore do not consider these resonances to be a practical route to enhance the inter-tube conductance.[5]

Whilst we argue that the energy resonances associated with different termination geometries are not of practical interest, the amplitude of the interference component of the inter-tube conductance (i.e. the amplitude of Eqn. (7.2)) may depend significantly on the termination geometry. Inspection of the range of non-resonant conductances observed in Figs. 7.7 and 7.8, however, suggests that this is not the case. To make a more concrete comparison, we consider the average inter-tube conductance over the valence band and compare this for different terminations. Specifically, we set the overlap length L such that the distance between terminal carbon atoms for each CNT is 20 Å and define a characteristic conductance $\langle G \rangle$ as the mean conductance of electrons in the valence band in the range $-0.8\ \mathrm{eV} < E < -0.2\ \mathrm{eV}$. The contributions from resonant scattering are excluded by removing from this average contributions where the device density of states $\mathcal{N}(E)$ increases

[5]This conclusion also justifies *a posteriori* our neglecting magnetism at the end terminations which results mainly in different energies of these localised states whilst leaving the bulk states unaffected.

by more than 10% of the bulk value $\mathcal{N}_{\text{bulk}}$. More formally,

$$\langle G \rangle = \frac{1}{w_0} \int_{-0.8\text{ eV}}^{-0.2\text{ eV}} \mathrm{d}E\, G(E) w(E), \tag{7.5}$$

$$w_0 = \int_{-0.8\text{ eV}}^{-0.2\text{ eV}} \mathrm{d}E\, w(E), \tag{7.6}$$

$$w(E) = \begin{cases} 1 & \text{if } \mathcal{N}(E) \leq 1.1\, \mathcal{N}_{\text{bulk}} \\ 0 & \text{otherwise} \end{cases}. \tag{7.7}$$

This approach helps to remove the effect of resonances and the dependence of conduction on the overlap length, both of which depend on the end termination in a manner that is difficult to otherwise isolate, and allows for a better isolation of any residual dependence of inter-tube conductances on the end termination geometry. By comparing this quantity calculated for an sp^2-terminated $(9,0)/(5,5)$ CNT pair for a range of overlap lengths around 20 Å, we estimate that $\langle G \rangle$ is independent of resonances and overlap length to within a factor of 2. The dependence of the inter-tube conductance on the chirality mismatch is found to be much larger than this. In Fig. 7.12, we show the average value of $\langle G \rangle$ for the different combinations of the five end termination geometries. The error bars give the maximum and minimum value of $\langle G \rangle$ for that pair of CNTs. These quantities are compared for the three pairwise combinations of the $(5,5)$ and $(9,0)$ CNTs which shows that conductance between CNTs of different chirality is approximately an order of magnitude lower than conductance between CNTs of the same chirality.

We conclude therefore that the dominant effect determining the inter-tube conductance is the difference in chirality rather than the geometry of the termination. It is this conclusion that then allows us to meaningfully compare in Fig. 7.6 the inter-tube conductance between the different pairs of CNT chiralities which necessarily have different end terminations.

7.4.1 The effect of chirality mismatch

Superimposed on the bend scattering chirality dependence shown in Fig. 7.6, we show the dependence of the end-scattering inter-tube conductance on the chirality mismatch. As we concluded in the previous section that the dominant effect determining the inter-tube conductance is the chirality mismatch, we use the same termination scheme for all CNTs and passivate dangling bonds with a single hydrogen in the slant geometry. For this termination scheme, all end states are located within the gap and therefore no tunnelling resonances were found. To help isolate interference effects, for each chirality pair we calculate $\langle G \rangle$ as defined in Eqn. (7.6), with the same overlap length $L = 20$ Å for each geometry.

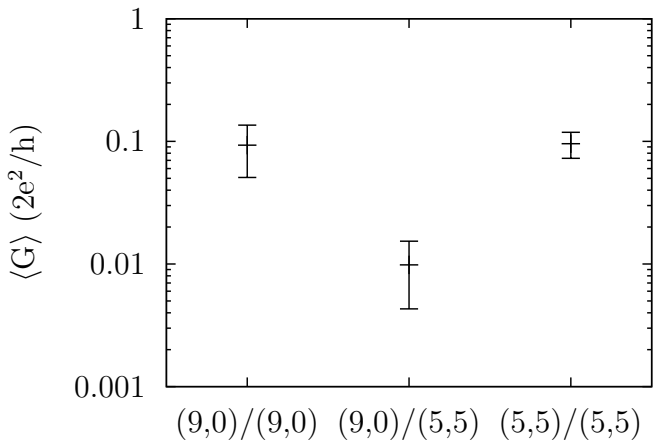

Figure 7.12: The mean and range of the characteristic conductance $\langle G \rangle$, as defined in the main text, for all combinations of end terminations in the $(9,0)/(9,0)$, $(9,0)/(5,5)$ and $(5,5)/(5,5)$ CNT pairs in the end-scattering geometry. The error bars give the maximum and minimum value of $\langle G \rangle$ for each pair of CNTs. The dependence of the inter-tube conductance on the chirality mismatch is found to be larger than the dependence on the end termination.

For the end-scattering geometry, we find a similar exponential suppression of inter-tube conductance as the chirality mismatch increases. When compared to the bend-scattering conductances, however, the suppression is less severe and for larger differences in chiral angle the inter-tube conductance in the end-scattering geometry is several times greater. This reflects the greater momentum scattering introduced by the termination: a termination is a spatially localised defect which therefore introduces a stronger momentum scattering when compared to the bend defect which is more spatially delocalised. For large differences in chiral angles, therefore, inter-tube conductance is dominated by momentum scattering arising from the end termination as shown in Fig. 7.6. For small differences in chiral angles, no momentum scattering is required to facilitate conductance and so inter-tube conductance is larger in the bend-configuration where the overlap length between the CNTs is greater. These conclusions indicate that the primary means by which to increase the inter-tube conductance, and therefore also the conductivity of CNT networks, is to reduce the range of chiralities present in the network.

7.5 Conductance between terminated nanotubes at finite bias

Finally in this chapter, we consider how a finite bias might affect the inter-tube conductance, focusing in particular on conductance between terminated CNTs. Recall that a bias is applied across a device by connecting the two sides of the device to leads which are themselves connected to reservoirs with different chemical potentials and which inject electrons into the device with energy up to the chemical potential for that reservoir. As a result of this non-equilibrium set up, the chemical potential throughout the device is not spatially constant but instead varies between the chemical potentials defined by the leads. The locations where the local chemical potential varies most rapidly are the locations where the leads are most weakly coupled, and hence where the resistance is greatest, which is an effect entirely equivalent to the conventional understanding of classical circuit theory, where large resistances accompany large drops in electric potential.

The weak coupling between the CNTs is expected to create a large bias drop between the CNTs when a bias is applied. It is straightforward to conjecture, therefore, that the bias drop will result in a large electric field between the CNTs and generate forces in this non-equilibrium current carrying system that are not present in the system in the absence of current. This mechanism is entirely analogous to the classical force between capacitor plates. These forces may then modify the inter-tube separation distance which, in turn, due to the exponential dependence of tunnelling on barrier width, may strongly modify the inter-tube conductance as a function of bias. The current-bias characteristics for such a device would be highly non-linear and might somewhat resemble the exponential characteristics of a diode.

7.5.1 Methods

To test this hypothesis, the electronic structure of two sp^2 hydrogen-terminated axially aligned $(5, 5)$ CNTs in the geometry shown in Fig. 7.13 were calculated using the NEGF formalism coupled with DFT. Calculations were performed using the tranSIESTA extension to the SIESTA DFT package.[125, 138] A double-ζ with polarisation (DZP) pseudo-atomic basis set was used, and the charge density was described with a well-converged grid cutoff of $350\ \mathrm{Ry}$. The contour integrals to determine the NEGF electron density were performed using six Fermi poles and 30 and 8 energy points for the circular and line part, respectively, of the equilibrium contour; a fine spacing of $0.01\ \mathrm{eV}$ was used for the non-equilibrium contour. Under the PBE exchange-correlation density functional, it is known that the attractive

van der Waals force between CNTs is severely underestimated.[109] This under-binding does not affect the previous sections of this chapter as the main focus was the electronic structure. To study the inter-tube forces and their dependence on non-zero bias, however, a more accurate first-principles description of the van der Waals interactions is required. In this section, we use the non-local van der Waals functional of Dion et al.[108, 109] which has been shown to accurately describe binding in carbon-based systems.[109] The separation between the CNTs was adjusted to 3.25 Å corresponding to the equilibrium binding separation between two axially aligned periodic $(5, 5)$ CNTs. The overlap length between the CNTs, defined as the distance between the terminal hydrogen atoms, was set at 20 Å, and the terminating hydrogen atoms and CNT fragments were relaxed for this exchange-correlation functional using the method described section 7.2. No further relaxation of the geometry was performed. The CNT axes are aligned with the z-axis with both axes contained within the yz-plane.

7.5.2 Bias drop

In Fig. 7.13, we plot the difference in the local electrostatic potential (Hartree and ionic) calculated for zero bias and $\Delta\mu = 0.5\,\mathrm{eV}$ bias. The potential drop between the CNTs occurs in the non-bonded vacuum region between the CNTs, whilst throughout the individual CNTs the potential remains largely at the value of the lead connected to that CNT ($\pm\Delta\mu/2$). The local potential is a good indicator of the local chemical potential, confirming that the bias drop in this system occurs in the vacuum region between CNTs. Similar results are observed for different potential differences, down to $\Delta\mu = 0.1$ eV, the smallest value considered.

7.5.3 Non-equilibrium forces

As the structure of the CNT system was generated without full relaxation of the geometry, the residual forces at zero bias were not within standard convergence tolerances, but were all no more than $0.2\,\mathrm{eV/Å}$. The additional *non-equilibrium* contribution to the forces arising at finite bias can be calculated by subtracting this equilibrium contribution.

In the top three panels of Fig. 7.14, we compare the non-equilibrium forces on the atoms as a function of bias. The light lines give the forces for each individual atom, with the red/blue lines distinguishing to which CNT that atom belongs. An increase in the non-equilibrium force with the bias is found, however this increase is quite modest, requiring a bias of over 0.2 V before the non-equilibrium forces increase by more than a typical

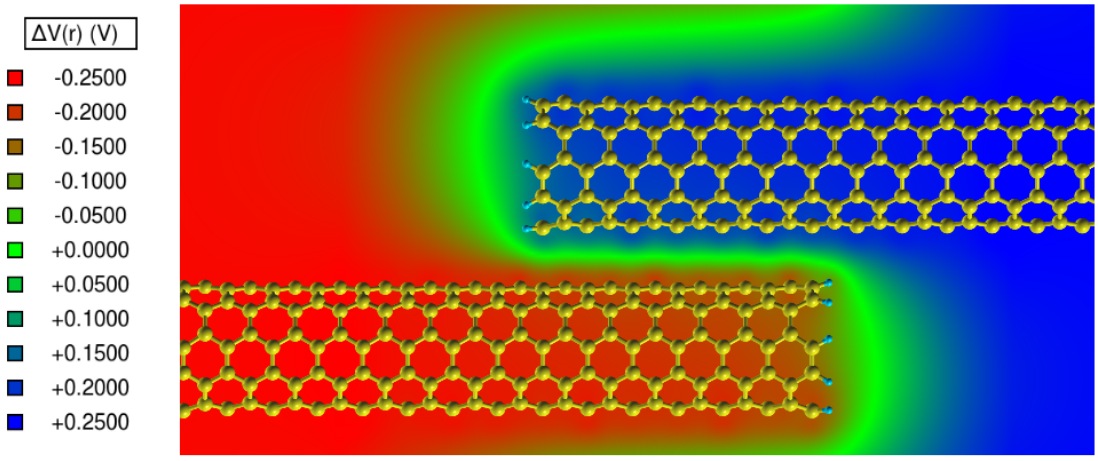

Figure 7.13: The difference between the electrostatic local potentials (Hartree and ionic) for the $(5,5)/(5,5)$ CNT pair at 0.5 V and 0 V bias, plotted in the plane containing both CNT axes.

convergence tolerance of 5 meV/Å. The forces are found to act with almost equal spread in positive and negative directions for both CNTs. In particular, the forces between the CNTs, shown in Fig. 7.14b, act almost equally in a repulsive and attractive manner for both CNTs, suggesting that there is no net force between the CNTs.

To quantify this further, we consider the average force acting on the carbon atoms within the contact region. This average is carried out for atoms belonging to each CNT separately, resulting in an effective measure of the average non-equilibrium force acting on each CNT. We show these averages and the corresponding standard deviations by the dark solid and dashed lines, respectively. If there existed an attractive inter-tube force arising at finite bias, the force between the CNTs (Fig. 7.14b) would show the average forces on each CNT acting in opposing directions. As the average force is seen to be approximately independent of the applied bias, the inter-tube force arising due to non-equilibrium appears to be negligible. Fig. 7.14d shows spatial directions of the non-equilibrium forces at 0.5 V bias, confirming that there is negligible attractive inter-tube force at finite bias.

The absence of an attractive inter-tube force might be explained by screening effects, and there is some evidence to suggest this given by the redistribution of the electron density shown in Fig. 7.15. At finite bias, some electron density is redistributed to the CNT connected to the lower bias reservoir, which acts to screen the bias drop between the CNTs. This screening might be expected to be visible in Fig. 7.13 with some bias drop occurring within the CNTs in addition to a drop in the vacuum, however this is not observed in Fig. 7.13. Further, the large non-equilibrium forces within the bulk-like region of the

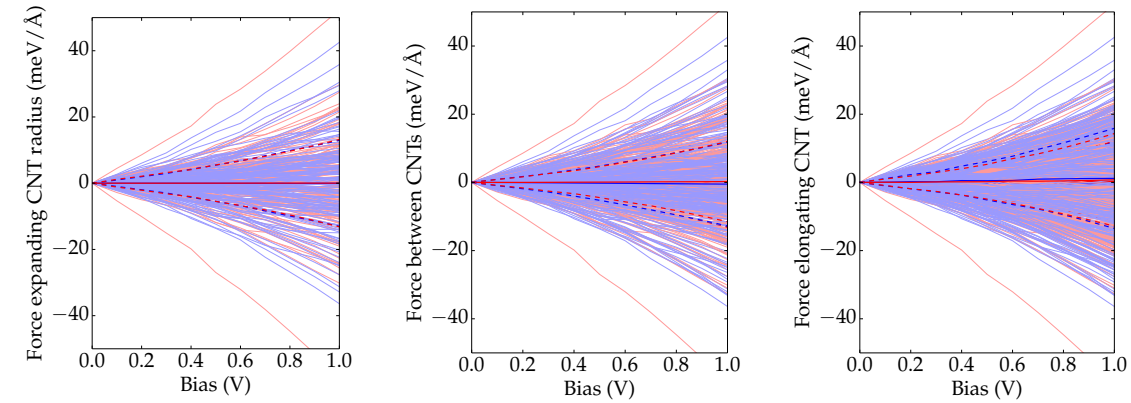

(a) F_x **(b)** F_y **(c)** F_z

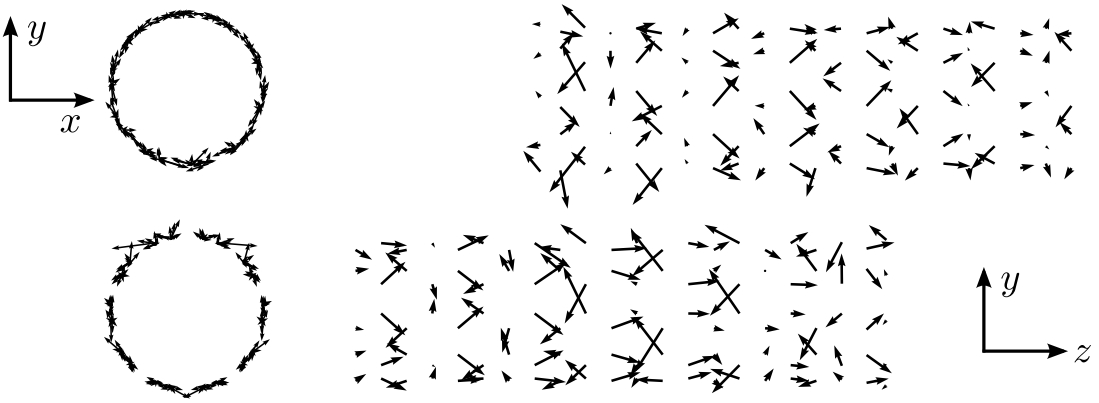

(d)

Figure 7.14: The non-equilibrium forces arising at finite bias. Top panels: the bias dependence of the non-equilibrium forces for the atoms within the contact region. The light coloured lines indicate the forces on individual atoms; the red/blue lines distinguish to which CNT that atom belongs. The solid and dashed dark coloured lines are the average and standard deviation of the forces acting on the atoms in each CNT. Bottom panel: the directions and magnitudes of the non-equilibrium forces at 0.5 V bias.

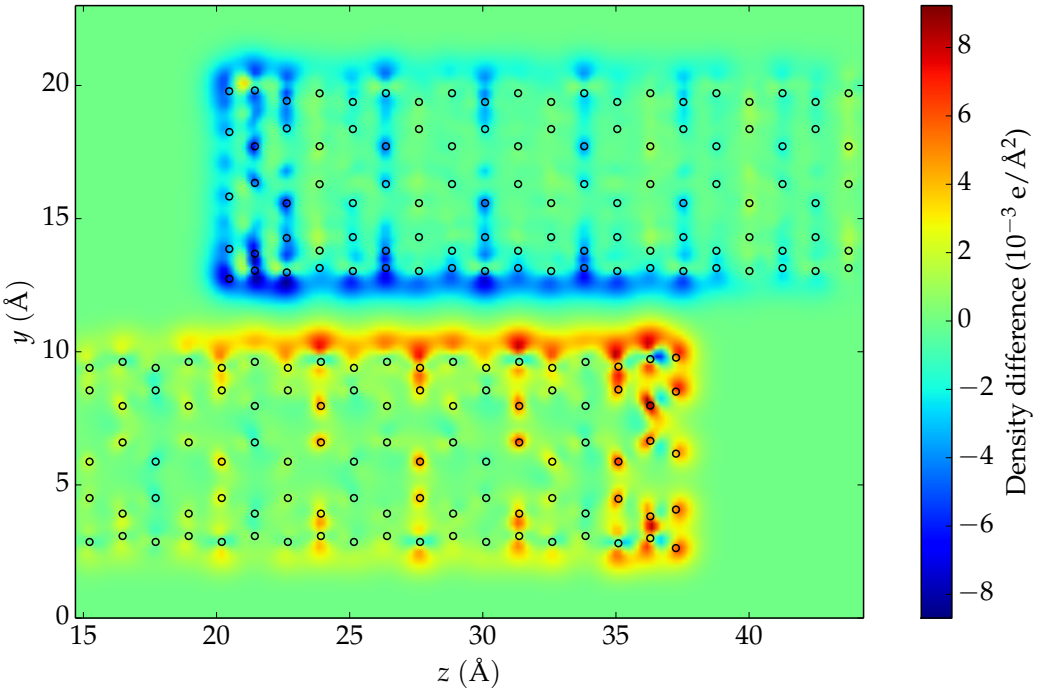

Figure 7.15: The electron density difference between the 0.5 V bias, and zero-bias calculations. The density has been integrated over the x-axis.

CNT and away from the contact region, as shown in Fig. 7.14d, are unexpected as the local electrostatic potential is almost constant here. This should make the local electronic structure bulk-like, resulting in only small residual non-equilibrium forces.

Whilst care was taken to ensure that convergence was achieved in these calculations, we speculate that the computed forces may be unreliable possibly due to incorrect convergence or due to an error in their calculation within the tranSIESTA implementation. Similar calculations for the $(9,0)/(5,5)$ CNT pair were found to be difficult to converge, requiring an order of magnitude more self-consistent iterations than for the $(5,5)/(5,5)$ CNT pair. Furthermore, the drop in bias was found to occur within the bulk CNT and not in the vacuum suggesting that a different minimum was reached at convergence. It may, therefore, indeed be that the non-equilibrium forces presented in this section are unreliable and the presence of an inter-tube force arising at finite bias remains an open question.

7.6 Conclusions

Using electronic structures derived from first principles, we have studied the role of end terminations and bends on the conduction between axially aligned CNTs. We find that the predominant factor influencing inter-tube conductance in both geometries is a difference in CNT chirality: the larger the chirality difference, the more the inter-tube conductance is suppressed. This conclusion confirms earlier empirical tight-binding calculations[38, 175], but also demonstrates that the momentum-scattering provided by end termination and bend defects does not fully remove the suppression of inter-tube conductance due to momentum mismatch. For large chirality mismatch, the strong momentum-scattering provided by an end termination makes the termination a significant source of inter-tube conduction. Therefore, the presence of the end terminations cannot be neglected in the study of conduction in CNT networks. This contrasts with the negligible effect that an end termination has on the intrinsic conduction within the bulk-like region (i.e. far from the end termination) of individual CNTs.

Tunnelling between the ends of two terminated CNTs is found to be well described by an interference mechanism arising from finite spatial overlap of the conducting states in the two CNTs, and is predominantly dependent on the relative chirality mismatch and not on the geometry of the end termination. The main difference arising from the different end terminations is the presence of resonant tunnelling phenomena where conductance rises by over an order of magnitude. These occur due to scattering from defect-states localised at the ends of the CNTs. The energies of these states, and hence the resulting resonances, are dependent on the particular termination geometry and the magnetic structure at the termination[198, 199, 200]. We do not consider these resonances to be a practical route to enhancing inter-tube conductances, however, due to the difficulty in generating precise termination geometries to ensure that they are located at the Fermi energy and, further, because thermal effects are likely to broaden the resonant energy, reducing the resonant tunnelling amplitude. These conclusions therefore extend the range of validity of earlier studies that have considered only one termination geometry or overlap length by demonstrating that these effects can be accounted for using simple interference and resonant tunnelling models.

The inter-tube conductance between bent CNTs with a large chiral mismatch is found to be strongly dependent on the bend angle, which can be understood in terms of the greater momentum-scattering introduced by a sharper bend. The scattering from the bend is much weaker than that from an end termination and consequently the bend introduces little backscattering. The presence of these shallow bends in a network of CNTs, therefore

only acts to improve the conductance of the network without increasing the resistance of the individual CNTs.

We note that whilst DFT using semi-local functionals (including PBE) is known to introduce a spurious self-interaction error (see section 4.3.5), which results in an erroneously-increased delocalisation of the electronic eigenstates, this does not affect our overall conclusions as we compare conductances between calculations that will have similar such errors. The absolute conductances may, however, be overestimates of their true value by as much as an order of magnitude[142, 205].

We have also investigated the possibility of non-equilibrium forces that may arise at finite bias. Our calculations do not support the presence of such forces, however physical intuition suggests that the large electric field that is calculated to exist between the CNTs at finite bias should introduce significant non-equilibrium forces. We suspect that these calculations are erroneous and further investigation is suggested.

The overall conclusion from this chapter is that weak perturbations to the CNT electronic structure, in this case as a result of bends of end terminations introduced to the geometric structure, can enhance the inter-tube conductance. This finding therefore provides theoretical first-principles verification of the inter-tube conductance mechanism proposed in chapter 6.

CHAPTER

EIGHT

CHARGE DOPING IN WATER-ADSORBED CARBON NANOTUBES

In the previous chapters, we have largely focused on the role of transmission between CNTs and its effect on the conductance of the network as a whole. In this chapter we investigate a separate mechanism, that of charge doping due to adsorbed water molecules, and consider its effect on the conductivity of individual CNTs.

The effect of water on the electrical properties of carbon nanotubes (CNTs) has been controversial for some time. Theoretical calculations have suggested that water dopes CNTs, predicting a strong dependence of CNT conductivity on humidity. The theoretical evidence for doping in this system has been questioned, however, and experimental studies have not been able to clearly confirm or refute this model. In this chapter, we propose that the theoretical methods used in previous calculations are indeed insufficient. We investigate in detail the conditions that must be satisfied for charge doping to occur, and provide a theoretical method, based on large-scale density functional theory calculations, to identify the presence of charge doping. Key to our analysis is the isolation of electrostatic effects, which we do using a novel application of maximally-localised Wannier functions. Our findings lead us to conclude that water does not dope CNTs.

Parts of this chapter have been published [206].

8.1 Introduction

The optimal performance of CNT devices often requires the CNTs to have a particular electronic character, whether semiconducting or metallic. The control of chirality, and hence the electronic character, during CNT synthesis is challenging, which has led to the

development of alternative in-solution techniques for separating bulk-grown CNT samples with respect to electronic type. Examples include density gradient ultracentrifugation[207, 208], polymer wrapping[209, 210] and chromatography[211, 212].

As a consequence of this post-processing, residual water may remain adsorbed to the CNTs. Therefore it is important to understand the influence that water has on the electronic structure of CNTs.

Experimental investigations of the effect of water vapour on the conductivity of mats and fibres of CNTs have reached contradictory conclusions with both increases[213, 214, 215, 216, 217] and decreases[218, 219, 220] in conductivity observed. The lack of agreement may be attributable to an abundance of factors, including the CNT sample composition and purity, the presence of impurities and their composition, contact resistances with external electrodes and between the CNTs themselves, and the alignment and connectivity of CNTs in the mat/fibre network. The relative contribution of these factors, and their dependence on local water concentration, may be significantly different between the different samples used in the reported experiments, and are difficult to isolate.

Theoretical calculations based on density functional theory (DFT) have shown that water interacts weakly with CNTs, binding by physisorption.[221, 222, 219, 223, 224] This weak interaction has been shown to cause little scattering, and the conductance of individual CNTs when hydrated is little changed from when dry[225, 222].

Charge transfer analyses, also performed within DFT, have suggested that water may *n*-dope CNTs[221, 222, 219, 223, 224]. The conductance of semiconductor CNTs is sensitive to the amount of doping, and in Ref. [217] a mechanism based on charge transfer between water and CNTs has been proposed to explain experimental observations.

There are, however, several issues with the charge transfer analyses used to determine this mechanism. Most fundamentally, there is no unique formalism to partition the DFT-derived ground-state charge density among different species in a system. The magnitude of charge transfer is sensitive to the details of the calculations, including the choice of functional for exchange and correlation[226], the basis set[227, 228, 229], and the partitioning method used[227, 229]. Changing the partitioning method will often alter the computed partial charges by $0.1\,\mathrm{e}$ or more[228, 229], which is comparable to the proposed water/CNT charge transfer.[221, 222, 219, 223, 224] These theoretical calculations may still, therefore, be consistent with no charge transfer or even *p*-doping. Indeed, it has been suggested by some authors that there is no overall charge transfer.[223, 218, 230]

Regardless of the method used to determine the charge partitioning, it is also not clear that charge doping can be determined by considering only the total partial charge of the CNT,

as used in previous studies[221, 222, 219, 223, 224]. In principle, doping is manifested by additional or reduced electron charge density, as compared to the bulk, far from the defect that may be causing the doping, such that all electrostatic perturbations have been screened. Only this *delocalised* charge transfer can result in doping and contribute to conductance; localised charge transfer will in fact act to scatter current and decrease the conductance. Accordingly, the long-range spatial distribution of the electron charge density must be considered to determine whether doping occurs.

Neither experiment nor theory, therefore, have reached agreement over the interaction between CNTs and water and further analysis of the calculated charge transfers is required to support a doping hypothesis. In this chapter, we revisit the problem of charge transfer between water and CNTs. Working directly with the charge density, derived from first-principles calculations, we calculate the long-range perturbation to the CNT charge density due to the water molecule. Our main result is that the interaction is a long-ranged electrostatic polarisation that arises due to the dipole moment of the water molecule which cannot be fully captured within a small simulation cell. Using large simulation cells, we isolate the contribution to the density perturbation due to the water dipole moment by using a simple classical model for the electrostatic effects of the adsorbed water molecules. This allows us to estimate the residual charge transfer between a CNT and water molecule which we find to be negligible. We therefore conclude that water does not *n*-dope CNTs.

The remainder of this chapter is organised as follows: we first give details of our methods; we then analyse the electrostatic interaction between the CNT and water molecule, and introduce an electrostatic model to disentangle charge transfer from charge polarisation; we then discuss why this picture does not change when including thermal effects; the effectiveness of the classical model allows us to then make an estimate for the residual charge transfer between water and CNT; and finally, we discuss the wider context of these conclusions.

8.2 Methods

We consider supercells containing a single water molecule adsorbed on one of two CNT structures: 16 unit-cells of a semiconducting $(10, 0)$ CNT; and 28 unit-cells of a metallic $(5, 5)$ CNT. The overall length of each supercell is 68.5 Å and 69.1 Å, respectively.

Electronic structures are calculated using ONETEP. Four NGWFs per carbon and oxygen atom and one per hydrogen atom are used, with a generous localisation radius of 5.3 Å in order to capture charge polarisation accurately.

Equivalent plane-wave kinetic energy cutoffs of $1000\ \mathrm{eV}$ and $4000\ \mathrm{eV}$ are used for the psinc basis sets representing the NGWFs and charge density, respectively, and the Brillouin zone is sampled at the Γ point only.

All calculations in this chapter employ the PBE generalised gradient approximation for exchange and correlation[106]; our conclusions are unchanged when equivalent calculations are performed using the local density approximation (LDA)[103]. The PBE functional results in no binding between water and CNT and so dispersion interactions are corrected for empirically[190]. Note that this correction affects only the total energy and not electronic densities.

Periodic boundary conditions are used along the CNT axis, which is denoted as the z-direction; directions perpendicular to the axis are treated with the supercell approximation with at least 12 Å separating periodic images.

The atomic structures of the atoms in the CNT unit cells are determined using CASTEP. A fully-converged Brillouin zone sampling scheme of 16 and 28 equally-spaced k-points, including the Γ point, is used for the $(10, 0)$ and $(5, 5)$ CNTs, respectively. The states sampled are equivalent to those sampled in the larger supercell. The same pseudopotentials and parameter set, as far as possible, are used as for the ONETEP calculations.

After relaxation, the maximum residual forces and stress are $5\ \mathrm{meV/Å}$ and $0.02\ \mathrm{GPa}$ respectively. Calculated C–C bond lengths are 1.424 Å and 1.432 Å for the $(10, 0)$ CNT, and 1.429 Å and 1.431 Å for the $(5, 5)$ CNT; and the relaxed periodic unit cell lengths are 4.279 Å and 2.469 Å, respectively.

The water molecule is similarly relaxed in isolation in a 22 Å cubic simulation cell within the supercell approximation. Previous calculations have shown that the change to the structure of CNT and water is negligible when water is adsorbed[224], therefore the geometry of the composite structure is not relaxed further. We have verified for a selection of structures that our conclusions are unaffected by this lack of further relaxation.

The maximally-localised Wannier functions[122, 154] used for the point charge model of section 8.3 are calculated using the QUANTUM ESPRESSO interface to WANNIER90.[121]

8.3 Computing the charge polarisation

Our key result is given in Fig. 8.1 where we show the long-range electron density redistribution for a $(10, 0)$ semiconducting CNT with a single water molecule adsorbed (solid lines). The supercell is 68 Å in length along the CNT axis and the oxygen ion of the water molecule is directly above a carbon site, at a distance of 3.20 Å which is approximately the

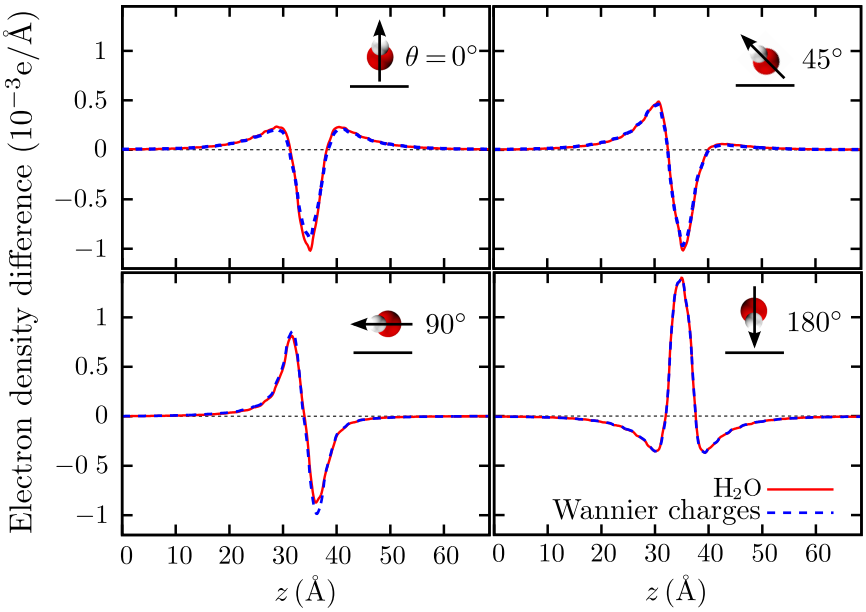

Figure 8.1: The laterally-integrated density difference profile for a 68 Å $(10, 0)$ CNT supercell with a single water molecule adsorbed (full DFT calculation, solid lines). Also shown (dashed lines), the corresponding induced polarisation when the water molecule treated as classical Wannier charges (see main text). The angle θ corresponds to the angle between the water dipole vector and the normal to the CNT surface as shown in Fig. 8.2.

average equilibrium binding distance of these orientations, and is positioned at the centre of the CNT supercell ($z \approx 34$ Å). The water molecule is oriented such that the normal to the atomic plane makes an angle θ to the radial vector of the CNT as shown in Fig. 8.2. The four panels show different orientations of the water molecules that are thermally accessible at room temperature. As we will show shortly, the precise CNT/water geometry does not strongly affect the interactions present, precluding the need for a detailed thermodynamic analysis.

The induced density polarisation is calculated through the charge density difference, defined as the difference between the density for the CNT and water combined $n_{1,2}(\mathbf{r})$, and the isolated CNT and water molecule alone $n_1(\mathbf{r})$, $n_2(\mathbf{r})$:

$$\Delta n(\mathbf{r}) = n_{1,2}(\mathbf{r}) - n_1(\mathbf{r}) - n_2(\mathbf{r}). \tag{8.1}$$

Three separate calculations per configuration are performed to determine the density difference. The periodicity due to the underlying atomic lattice is smoothed out by convolving this quantity with a window function $w(z)$ with width equal to the CNT unit cell length L_{uc}. In order to smooth out the large variations due to the underlying ionic lattice, we integrate this quantity over planes perpendicular to the CNT axis defining an electron density difference

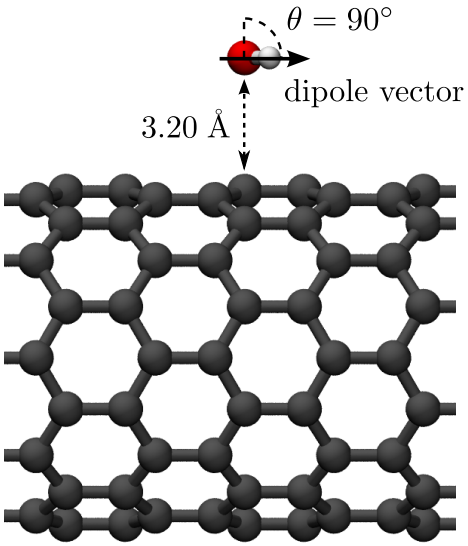

Figure 8.2: The structure of the water molecule adsorbed on a (10,0) CNT. The water oxygen ion is situated 3.20 Å above a carbon, with the water dipole making an angle θ to the CNT axis. Shown here is $\theta = 90°$. Only the part of the CNT closest to the water molecule is shown, the CNT extends for an additional ≈ 30 Å in both directions to form the full supercell.

per unit length,

$$\lambda(z) = \int \Delta n(x', y', z') w(z - z') \mathrm{d}x' \, \mathrm{d}y' \, \mathrm{d}z' \,, \tag{8.2}$$

$$w(z) = \begin{cases} 1/L_{\mathrm{uc}} & |z| < L_{\mathrm{uc}}/2 \\ 0 & \text{otherwise} \end{cases} \,. \tag{8.3}$$

The charge redistribution shown in Fig. 8.1 is remarkably long-ranged, occurring over a length-scale greater than 30 Å. As this is much larger than the CNT unit cell length, this long-range polarisation cannot be observed in the smaller supercells used in previous calculations.[221, 222, 219, 223, 224]

The form of the charge polarisation is strongly dependent of the orientation of the water molecule, but correlates well with the direction of the water dipole. For example, at $\theta = 0°$, the dipole points away from the CNT and electron density is repelled; at $\theta = 180°$, the dipole is towards the CNT and electron density is attracted.

The dominant effect of the water molecule on the CNT appears to be purely electrostatic in origin. In order to demonstrate this more rigorously, we calculate the charge polarisation of the system using a purely electrostatic model for the water molecule, i.e., without explicit inclusion of the real electron density of the water molecule in the system. The water

molecule is treated as a set of point charges, whose influence appears as a correction to the local Kohn-Sham potential[231]

$$\delta V_{\mathrm{loc}}(\mathbf{r}) = \sum_i \frac{q_i}{\left|\mathbf{r} - \mathbf{r}_i\right|}, \tag{8.4}$$

where $\mathbf{r}_i$ and q_i are the position and magnitude, respectively, of each point charge. Positive (ionic) charges are located at the ionic positions with magnitudes given by those of the corresponding pseudo-ions. For the negative (electronic) charges, the positions are the centres of the maximally-localised Wannier functions (MLWFs)[122, 121] obtained by subspace rotation of the manifold of occupied eigenstates of an isolated water molecule.[1] The magnitude of each electronic charge is then the integrated charge density of each MLWF. Due to the unitarity of the Wannier transformation, this gives $-2\,\mathrm{e}$, with the factor of two being a result of spin degeneracy. In practice, to prevent unphysical "charge-spilling" into the deep Coulombic potential, these point charges are smeared with a Gaussian function of half-width 0.16 Å.[231] The geometry of the MLWF centres in relation to the ionic positions is shown in Fig. 8.3 (bottom left). Our method is similar in spirit to that of Ref. [232], but differs in that the procedure is parameter free and requires no fitting.

The difference in electronic density induced by this classical electrostatic model for the water molecule can be calculated using the equivalent of Eqn. (8.1) and is shown in Fig. 8.1 (dashed lines). The agreement with the full DFT calculation (solid lines) is excellent for all configurations. This can be understood by comparing the long-range electrostatic potential corresponding to the MLWF model and that of the water molecule from DFT. This comparison is shown in the top two panels of Fig. 8.3. The classical model reproduces the potential to high accuracy, with only small differences very close to the water molecule where the detailed charge density distribution is important. Equivalent calculations performed on a metallic $(5, 5)$ CNT produce similar results as shown in Fig. 8.4, left panel, providing evidence for the general applicability of our model.

It is interesting to note that simpler models for the water electrostatics also reproduce the density polarisation well. In Fig. 8.4 we compare the density polarisation induced in a metallic $(5, 5)$ CNT for three different models. The left panel gives the Wannier charge model which most accurately reproduces the DFT induced polarisation. The central panel uses a classical dipole model for the water potential, with classical charges of magnitude $\pm 8\,\mathrm{e}$ at the centres of positive and negative charge of the isolated water molecule; the CNT is still treated using DFT. The agreement between this model and the DFT induced polarisation

[1] Taking the MLWF centres from an isolated molecule is an excellent approximation: when adsorbed on the CNT, the MLWF centres of the water molecule are found to change by less than 3×10^{-3} Å.

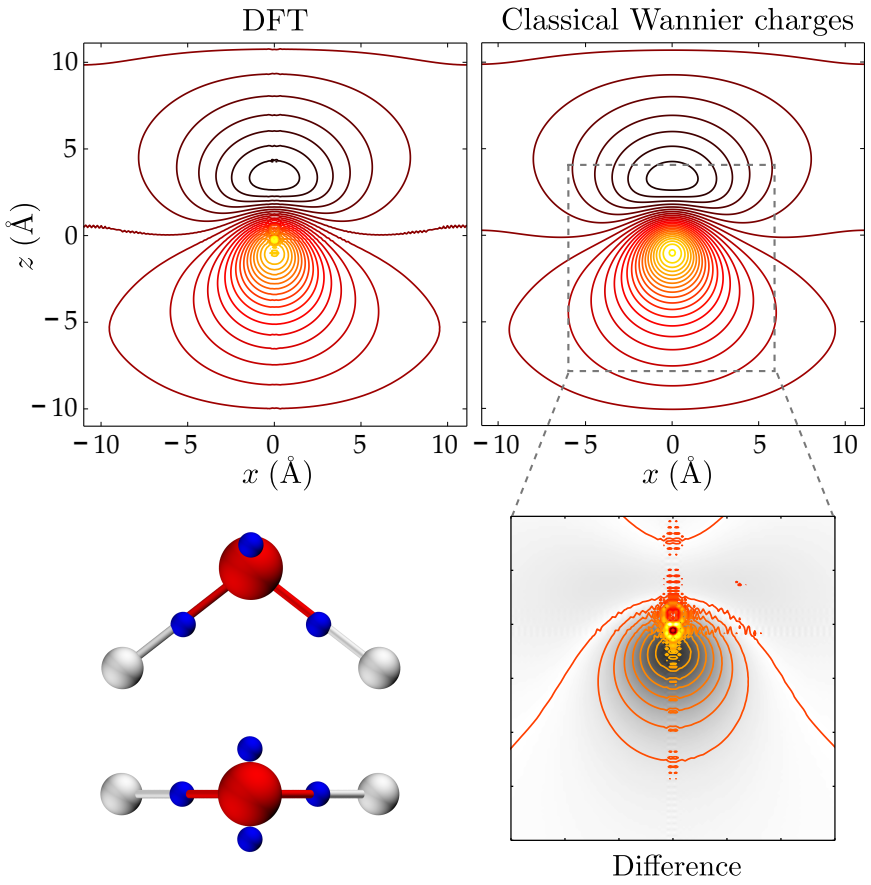

Figure 8.3: Top panels: a comparison between the electrostatic potential (local ionic and Hartree) for the isolated full DFT water molecule (left), and the classical Wannier charge representation (right). Contours are in steps of $20\ \mathrm{meV}$, in the plane $3.20\ \text{Å}$ below the water molecule, where the surface of the CNT would be when the water is in the $90°$ orientation. The water oxygen ion is located at the origin. The inset in the bottom right panel gives the difference between the two potentials in the region indicated by the dashed box. Contours are in steps of $5\ \mathrm{meV}$, and the shading gives the absolute difference between $0\ \mathrm{meV}$ (white) and $50\ \mathrm{meV}$ (black). Outside the region shown, the difference between the potentials is less than $5\ \mathrm{meV}$. Bottom panel, left: the positions of the Wannier charge centres (blue spheres) and oxygen/hydrogen ions.

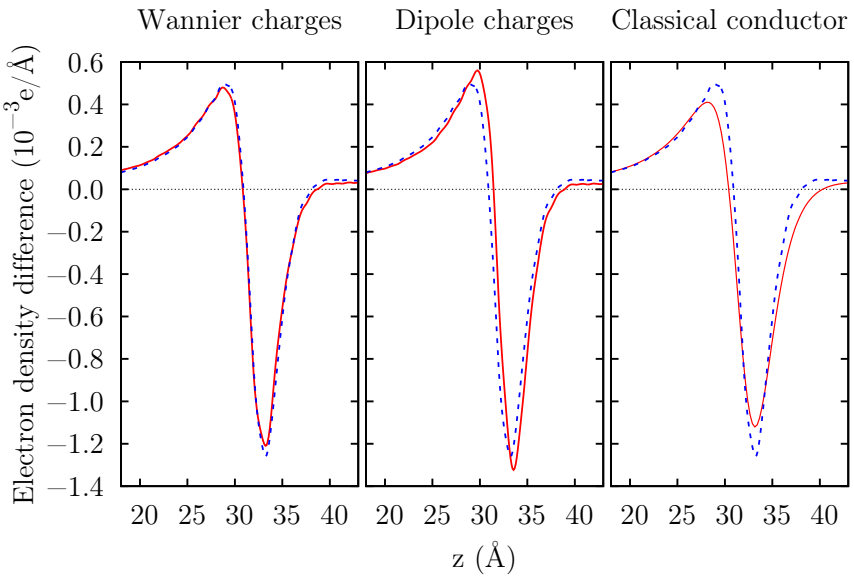

Figure 8.4: Comparison of the different electrostatic models for the water molecule adsorbed on a $(5, 5)$ CNT in the $\theta = 45°$ orientation. Left panel: point charge (MLWF) model for the water molecule; centre panel: dipole model for the water molecule; right panel: classical conducting cylinder model (see main text for details). In all cases the dashed blue line gives the full DFT result.

is still excellent, however differences between the classical and DFT electrostatic potential in the near-field produce a small lateral shift in the polarisation along the z-direction. The right panel shows the induced charge density for the simplest model where the CNT is treated as a classical conducting cylinder. The water molecule is described as a series of classical point charges, as in the Wannier charge model, with the induced density calculated by solving the classical Poisson equation, as detailed in Appendix C. We note that the classical induced polarisation calculated by this crude final model captures well the main form of the full DFT induced polarisation supporting the conclusion that the dominant interaction is electrostatic.

Similar results are obtained for the $(10, 0)$ CNT, as shown in Fig. 8.5, including the classical conducting cylinder model despite the CNT being semiconducting.

8.4 Thermal effects

At ambient temperatures, the structure of the water on the CNT cannot be considered static and instead the system explores a range of thermally-accessible configurations. It is therefore important to consider how thermal effects might change the electrostatic picture

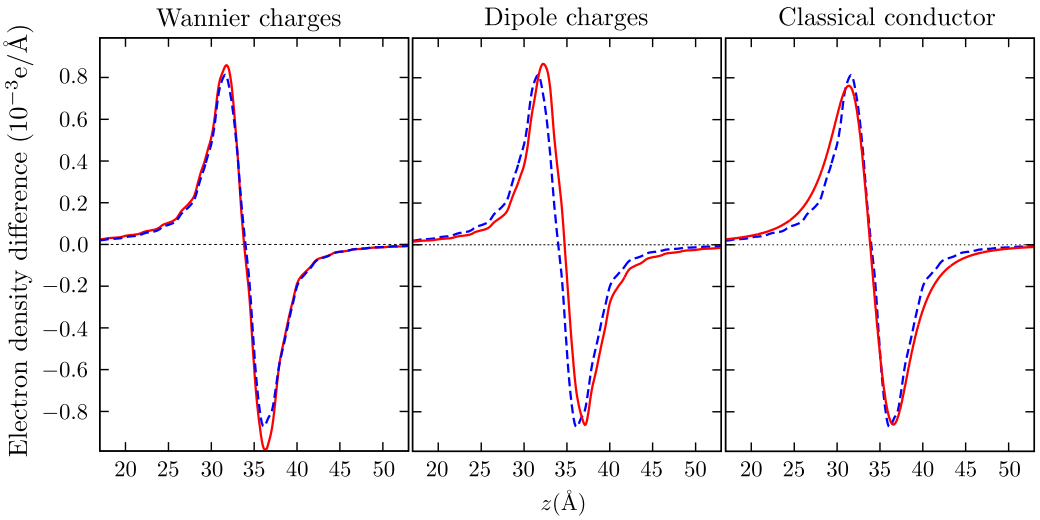

Figure 8.5: Comparison of the different electrostatic models for the water molecule adsorbed on a $(10, 0)$ CNT in the $\theta = 90°$ orientation, as in Fig. 8.4. Left panel: point charge (MLWF) model for the water molecule; centre panel: dipole model for the water molecule; right panel: classical conducting cylinder model (see main text for details). In all cases the dashed blue line gives the full DFT result.

present above.

The problem of temperature and pressure can be understood simultaneously as factors that affect the range of binding distances and orientation angles between CNT and water. Fig. 8.6 gives the binding energy curves for a single water molecule on a (10,0) CNT, calculated for the water molecule orientations shown in Fig. 8.1. The binding energies and distances are in good agreement with previous studies[221, 222, 219, 223, 224]. At room temperature (25 meV), the water molecule is unlikely to explore binding distances less than 3.0 Å due to the large energy penalty associated with these configurations.

In Fig. 8.7, the electronic charge density difference is compared for three binding distances, 2.48 Å, 2.96 Å, 3.67 Å, in the $\theta = 0$ orientation. For binding distances of 2.96 Å and 3.67 Å, the density perturbation induced by the Wannier charge model agrees well with the full DFT treatment of the water molecule. Small differences can be seen at close range, as in Fig. 8.1, but this can be related either to localised charge transfer, which, as discussed in section 8.3, cannot contribute to doping, or to details of the electrostatic potential of the water molecule in the near field that are not captured by the Wannier charge model.

Most importantly, however, the long-range behaviour of the electronic charge density is described very accurately by the Wannier charge model indicating that the dominant long range interaction between CNTs and water is electrostatic and not due to charge transfer.

It is only for binding distances less than 2.5 Å that the long-range charge redistribution

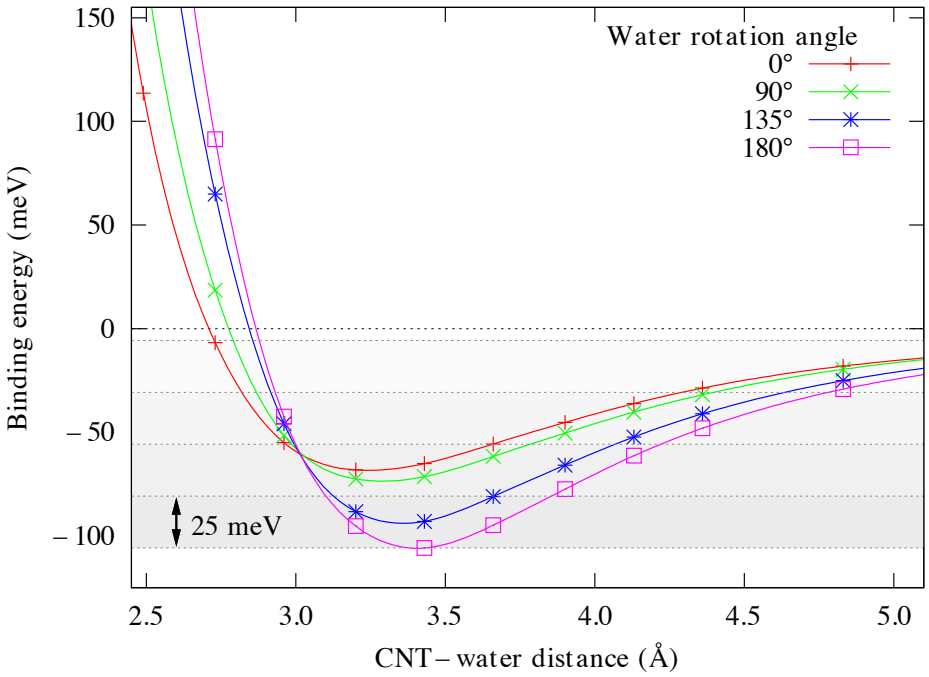

Figure 8.6: The binding energy curves for a single water molecule adsorbed on a $(10, 0)$ CNT. The shading illustrates the thermal energy at room temperature (shown up to 4×25 meV). The CNT–water distance is defined as the distance between the CNT and the oxygen nucleus.

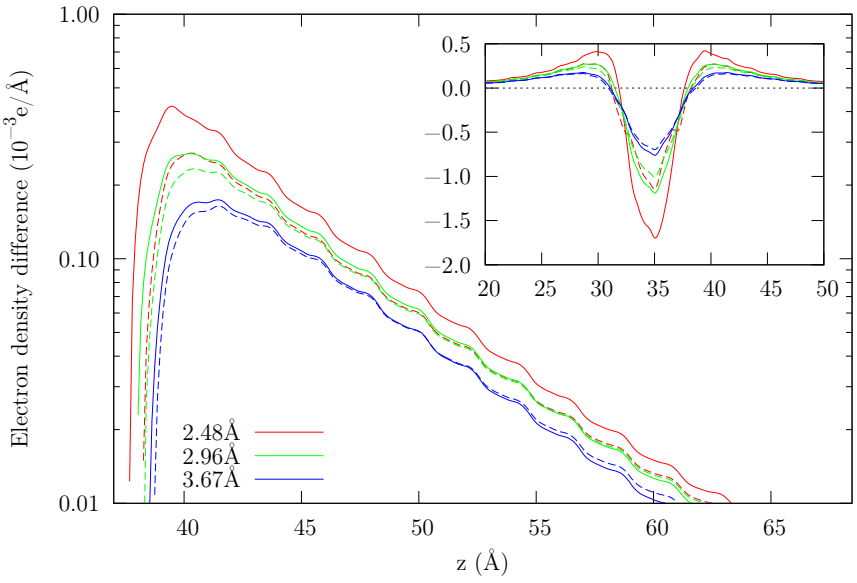

Figure 8.7: The density difference profile for water in the $\theta = 0°$ orientation for three different binding distances. The solid line treats the water explicitly using DFT; the dashed lines use the Wannier charge model.

is not well-described by the Wannier charge model. At these separations it is possible, therefore, that charge transfer is taking place. Such small separations, however, incur a serious energy penalty of at least $200\ \mathrm{meV}$ (or $8k_BT$ at ambient temperature) above the lowest energy configuration shown in Fig. 8.7. The Boltzmann weights for such configurations are vanishingly small and, therefore, these configurations can be safely neglected at the ambient conditions at which experiments take place.

For a single water molecule we conclude that it is unnecessary to take further account of thermal effects as for all thermally-accessible configurations the interaction between the CNT and water is primarily electrostatic.

For CNTs with clusters of adsorbed water molecules, the electrostatic interaction is still expected to dominate. The weak binding between CNT and water should not change and the short (< 2.5 Å) binding distances required to potentially achieve charge transfer will remain thermally inaccessible at ambient conditions.

8.5 Estimating the residual charge transfer

In any calculation of the electronic density, the difference in charge density given by Eqn. (8.1) consists of both charge polarisation $\Delta n_{\mathrm{p}}(\mathbf{r})$ and charge transfer $\Delta n_{\mathrm{t}}(\mathbf{r})$ components,

$$\Delta n(\mathbf{r}) = \Delta n_{\mathrm{p}}(\mathbf{r}) + \Delta n_{\mathrm{t}}(\mathbf{r}). \tag{8.5}$$

A convincing indicator of charge transfer would be additional charge delocalised in the CNT, far from the water molecule. As shown by the results above, however, the charge polarisation induced by the water dipole moment is very long-ranged. In principle, the charge transfer contribution could be determined by increasing the system size to screen the electrostatic perturbation, and considering regions where $\Delta n_{\mathrm{p}}(\mathbf{r}) \to 0$.[2] Such an approach is impractical, especially for low-dimensional systems such as CNTs in which the relatively weak screening necessitates the use of very large systems. The larger the system size, the more accurately the charge densities must be determined as any charge transfer ΔQ becomes delocalised over a larger volume V, and the associated density difference becomes smaller: $\Delta n_{\mathrm{t}}(\mathbf{r}) \sim \Delta Q/V$. Discerning small amounts of charge transfer accurately in this way is challenging from a computation point of view.

Instead, we approximate the polarisation contribution to the charge density difference in the full DFT calculation $\Delta n_{\mathrm{p}}(\mathbf{r})$ (Fig. 8.4, dashed lines) as exactly the density difference

[2] This method cannot determine charge transfer that remains localised, however localised charge transfer does not contribute additional conductance.

calculated by the Wannier charge model $\Delta n^{\mathrm{WF}}(\mathbf{r})$ (Fig. 8.4, left panel, solid line) in which the charge density difference is entirely due to electrostatic polarisation: i.e. $\Delta n_{\mathrm{p}}(\mathbf{r}) \approx \Delta n^{\mathrm{WF}}(\mathbf{r})$. The residual charge transfer is then approximated as

$$\Delta n_{\mathrm{t}}(\mathbf{r}) \approx \Delta n(\mathbf{r}) - \Delta n^{\mathrm{WF}}(\mathbf{r}). \tag{8.6}$$

Summing $\Delta n_{\mathrm{t}}(\mathbf{r})$ over the unit cell furthest from the water molecule provides an estimate of the charge transfer between the CNT and the water molecule, which we find to be no more than $|\Delta Q| \lesssim 10^{-4}$ e, independent of orientation. This is three orders of magnitude lower than the value calculated by Mulliken population analysis, and shows that there is negligible charge transfer in this system.

8.6 Considerations of the electronic energy level alignment

Finally, we consider the evidence for charge transfer in terms of the energy levels of the CNT and water systems. Previous calculations have shown that water interacts weakly with a CNT [221, 222, 219, 223, 224]. As there is little chemical bonding, the eigenstates of the isolated water and CNT are expected to be little perturbed.

This is confirmed in Fig. 8.8, which compares the density of states of a 16 unit cell $(10, 0)$ semiconductor CNT and a water molecule when mutually isolated, and the corresponding CNT/water local density of states[3] (LDOS)[233] with the water adsorbed. Indeed, the LDOS/DOS of the CNT are indistinguishable. The same result is found for multiple adsorbed water molecules, as shown in Fig. 8.9.[4]

For significant charge transfer between CNT and water to occur, charge must transfer from the highest occupied molecular orbital (HOMO) of the water molecule to the CNT conduction band. As the water HOMO lies almost 4 eV below the CNT conduction band, this transfer would involve a large energy penalty, the magnitude of which is dependent on the CNT band gap.

The energy penalty for metallic CNTs is smaller than for semiconducting CNTs, and so calculations for these systems should show a large difference in either the binding energy or the charge transferred to the CNT. As neither of these effects are observed in

[3] See Appendix D for a definition of the local density of states.

[4] The water geometry was generated using classical molecular dynamics as implemented in the Gromacs 4.5.5 package[234, 235, 236, 237] with the GROMOS96 force field and 43a1 parameter set[238] and SPC water model[239] using NVT dynamics[240] at 300 K for 20 ps. The water cluster was chosen as the first hydration shell surrounding a fully hydrated $(10, 0)$ CNT. The electronic structure was calculated using ONETEP.

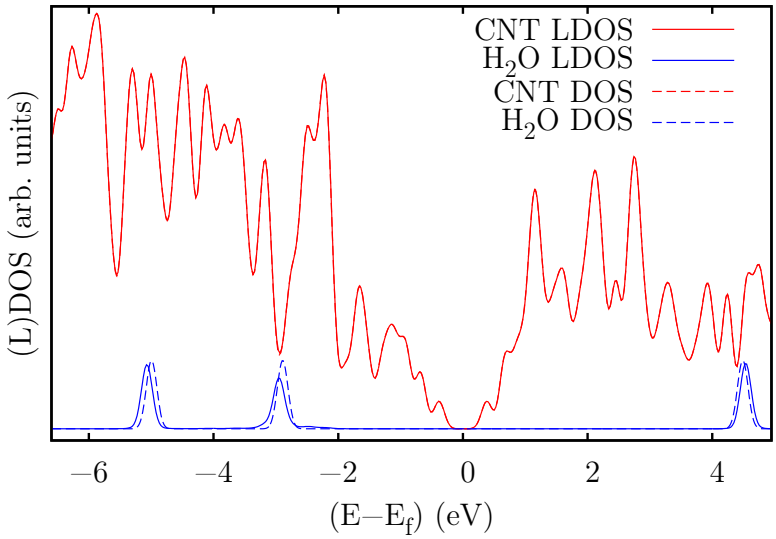

Figure 8.8: A comparison of the density of states (DOS) for a $(10, 0)$ CNT and water molecule when isolated (dashed red/blue respectively), and the local density of states (LDOS) of the CNT and water molecule (solid red/blue) when the water is adsorbed 3.20 Å above the CNT in the $90°$ configuration. A Gaussian smearing of 0.1 eV has been used. The CNT LDOS and DOS are indistinguishable. For each calculation, energies have been aligned by the potential far into the vacuum.

calculation[224, 221], we conclude that if charge transfer occurs then it must be very small, consistent with our estimation from the previous section. We also conclude that the Mulliken population analysis reported in previous calculations[221, 222, 219, 223, 224] is not suitable for determining charge transfer in this system.

Whilst the energy levels calculated by Kohn-Sham DFT do not correspond to the true quasi-particle energy levels, the many-body correction to the energy levels is likely to be smaller than the large difference between water and CNT states. Moreover, the correction to the under-estimated DFT band gap will increase the energy difference between the occupied water states and the CNT conduction band. Therefore we do not believe that this conclusion will change under a higher level of theory. For other adsorbed molecules, significant charge transfer would be possible if the molecular levels better align with the CNT states. For example, molecular oxygen in the triplet spin state has been calculated to have an unoccupied molecular level that sits within the CNT band gap.[241] We therefore do not dispute the conclusion that oxygen may *p*-dope semiconductor CNTs.[242, 230]

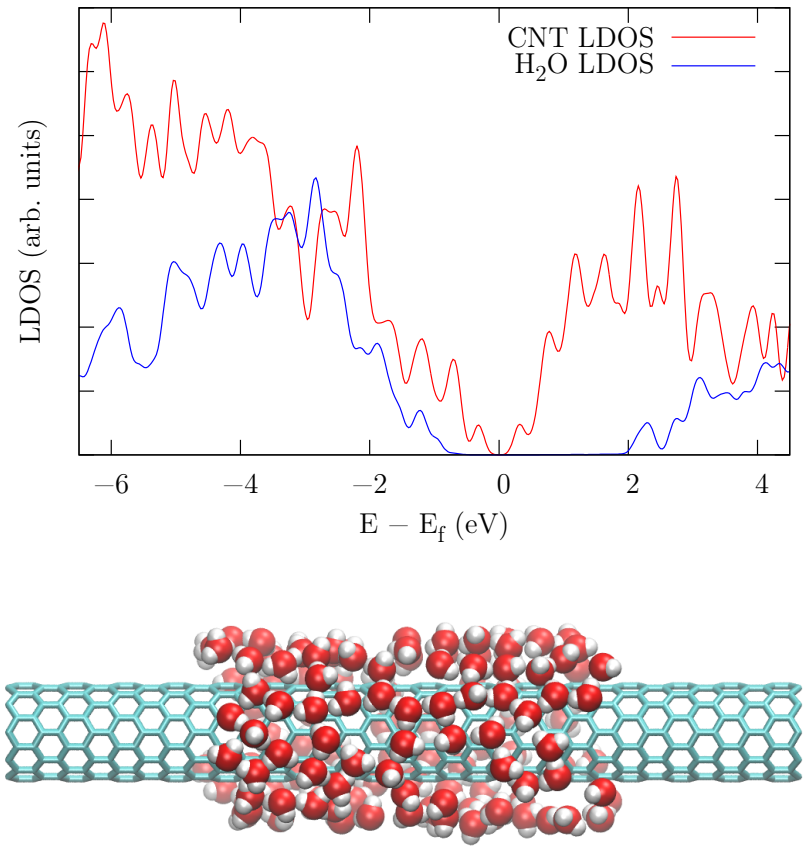

Figure 8.9: The CNT and water local density of states (LDOS) for the (10,0) CNT with an adsorbed water cluster in the geometry shown in the bottom panel.

8.7 Summary

In this chapter, we have used large-scale density-functional theory simulations to calculate the long-range electronic effects of a water molecule adsorbed onto a CNT. We have shown that the interaction is described very well with classical electrostatics: the permanent dipole moment of the water molecule induces a polarisation of the electronic charge density of the CNT that is remarkably long-ranged, occurring over a length-scale greater than 30 Å.

By comparing our full DFT calculations with ones in which the water molecule is treated as a classical charge distribution defined by its Wannier charge centres, we estimate that the charge transfer between CNT and a water molecule is no more than 10^{-4} e. We therefore conclude that water does not significantly dope CNTs. This conclusion is supported by the poor alignment of the relevant energy levels of the water molecule and the CNT, and contrasts with previous results, based on Mulliken charge partitioning in small supercells, that suggest much greater charge transfer.

As a consequence of the lack of charge transfer and the weak interaction between CNT and water, we conclude that water has a very weak effect on the conductivity of *individual* CNTs.[225, 222] In order to understand the origin of the humidity-dependent conductivities observed in experiments on CNT fibres and mats, therefore, it is vital to go beyond the effect of water on individual CNTs, and consider also the effect of water on the conductivity of *networks* of CNTs, i.e., on the conductivity between CNTs.

CHAPTER

NINE

CONCLUSIONS

9.1 Summary

In this dissertation I have presented an investigation into that mechanisms that affect the conduction of networks of carbon nanotubes. In chapter 6 a novel mechanism was proposed that improves the conductance between CNTs of different chirality using resonant momentum scattering to promote momentum-conserving inter-tube tunnelling. A key feature of this mechanism is that it arises from weak interactions between the CNTs and the surrounding environment and can result in an improvement in inter-tube conductance without penalising the intrinsic conductance of the constituent CNTs. This mechanism leads to the wholly unintuitive conclusion that cleaning CNT networks by removing impurities may not improve the network conductance, and may in fact lead to decreases in the conductance of the network as a whole. Further, it highlights the importance of considering the interactions between CNTs and the environment which have often been neglected in previous theoretical studies. This conclusion applies only to networks containing a range of CNT chiralities.

Aspects of this mechanism were investigated further using the computational methodology developed in chapter 5. In particular, the role of momentum scattering at terminations and bends in CNTs on the inter-tube conductance were investigated. These results were found to support the mechanism and demonstrated that relatively weak perturbations, in the form of bends in the CNT structure, can strongly enhance the inter-tube conductance due to the promotion of momentum-conserving inter-tube tunnelling. In addition, chirality mismatch was found to be the predominant factor that affects conductance between CNTs with the end termination and bend severity taking lesser roles. The strong dependence

on relative CNT chirality underlines the importance of considering the effect of chirality mismatch when investigating mechanisms that affect inter-tube conductance.

Finally, the evidence for charge doping of CNTs by adsorbed water molecules was investigated. By combining large-scale first-principles simulations with semi- and fully-classical models it was shown that the predominant effect of water adsorbed in CNTs is a charge polarisation due to the permanent dipole moment of the water molecule. An estimation of the residual charge transfer, once charge polarisation effects were removed, was made indicating that negligible charge transfer occurs between water and CNTs.

In addition to the study of CNTs, the computational methodology described in chapter 5 can be used to study electronic transport from first principles in a wide range systems. This implementation has been specifically designed to simulate systems containing thousands of atoms with systematically controllable accuracy, and brings into scope the possibility of studying more realistic nano-electronic devices than has been previously possible with first-principles techniques.

9.2 Further work

The factors that affect conduction in carbon nanotube networks are still far from well understood, and it remains unclear to what extent the remarkable electronic properties of individual CNTs can be achieved in these macroscopic networks. Unless this goal is achieved, the answer to this problem cannot come from experiment. Instead, it is necessary to study theoretically the factors that limit the conduction and to understand how these mechanisms may be passivated.

Whilst the developments presented in chapter 5 greatly increase the system sizes that can be studied using high-accuracy first-principles calculations, the calculations in isolation are not the right tool for identifying these mechanisms. The extremely large system sizes required to study inter-tube conductance, compounded by the number of unknown potential external influences such as impurities, make the search phase space too large and computationally expensive to be studied with density functional theory alone. Further under such an approach, as demonstrated in chapter 7 by the coupling of resonant and interference effects, decoupling the different mechanisms becomes difficult.

Instead, a more fruitful approach is to identify potential mechanisms using analytic approaches or computationally inexpensive tight-binding models. The use of density functional theory then comes in verifying and quantifying these mechanisms, and allowing for the identification of their relative contributions, which is the approach that has been

adopted in this dissertation.

Confirmation of the momentum exchange mechanism introduced in chapter 6 represents a primary goal of future work. Whilst the results of chapter 7 do support this mechanism, the smoking gun evidence would be strong enhancements of inter-tube conductances by weakly adsorbed molecules, such as water. Some preliminary investigations into resonant momentum scattering by adsorbed water molecules were indeed performed. The magnitude of the long-range Fourier components of the perturbation induced by the water molecule was found to be comparable to the 0.1 eV used in chapter 6, yet the enhancement to the inter-tube conductance was found to be very small if present at all. These preliminary calculations do not rule out the contribution of the mechanism, however, as computational constraints required the introduction of bends to the CNTs which, as shown in chapter 7, introduce momentum scattering and strongly influence the inter-tube conductance. Furthermore, as semi-local exchange-correlation functions were used, self-interaction error (see section 4.3.5) likely overestimates the wavefunction delocalisation. The inter-tube tunnelling interaction is therefore likely overestimated, masking the enhancement due to the momentum-resonant tunnelling. These caveats highlight the difficulty of isolating the different mechanisms that affect inter-tube conductance when performing first-principles calculations.

One method to tackle this problem is to build a tight-binding model that describes the inter-tube interactions using calculations derived from first-principles. This could be done using localised Wannier functions, either NGWFs or maximally localised Wannier functions, that are derived from first-principles calculations using any desired level of theory, for example to minimise self-interaction error. The computational expense associated with building such a model is offset by its use in inexpensive tight-binding calculations in which sources of momentum scattering can be isolated.

Additional potential avenues of research could include the effects of phonon-assisted tunnelling on the inter-tube conductance, which has already received some attention[243, 244], or the mechanisms behind the observed increases in CNT network conductivity due to polymer-wrapping[184]. Due to the size of the systems involved and the difficulty in creating reliable empirical models to describe the nanotube/polymer interactions, this last suggestion is a prime candidate for first-principles investigation using the methodology developed in chapter 5.

Further theoretical investigation into the mechanisms by which water affects the CNT network conductivity are also of significant interest. There is considerable experimental evidence that water affects the conductivity of CNT networks[213, 214, 215, 216, 217, 218,

219, 220], but the origins of these variations are not well understood. Whilst water does not dope pristine CNTs, as shown in chapter 8, the interaction between water and defects in the CNT lattice may present new mechanisms, and indeed there is experimental evidence that water interacts more strongly with defects[245]. Such interactions are highly suited for study using first-principles techniques.

To understand the nature of conductance in CNT networks will require a combination of theoretical and experimental studies. Only by identifying the mechanisms that affect conductance in CNT networks will it be possible to determine the true capability of this material.

APPENDIX

A

TRANSMISSION FROM GREEN'S FUNCTIONS

In this appendix we prove Eqn. (3.9) for computing transmission through a device and the non-equilibrium Green's function equations for computing the scattering-state density matrix, following the derivation given in Ref. [161]. We focus on a two-lead device; the extension to multi-lead devices follows straightforwardly. The route that we will take is to propagate the states that exist deep within a lead into the central device region using a Green's function technique. These states are referred to as scattering states. From these scattering states, the total current that propagates between leads can then be calculated.

A.1 Preliminaries

For a two-lead device, the one-particle Hamiltonian can be written in operator matrix form as

$$\begin{aligned} H &= H_0 + V \\ &= \begin{pmatrix} H_L & 0 & 0 \\ 0 & H_d & 0 \\ 0 & 0 & H_R \end{pmatrix} + \begin{pmatrix} 0 & V_{Ld} & 0 \\ V_{dL} & 0 & V_{dR} \\ 0 & V_{Rd} & 0 \end{pmatrix} \end{aligned} \tag{A.1}$$

where the $H_{L,R}$, H_d are the Hamiltonians describing the isolated leads and central device region, and V is the coupling between the leads and the device region. The partitioning in this matrix operator represents the operators describing the interactions between the left lead, device, and right lead regions respectively. We define a set of operators which project

onto the device region P_d and the left/right leads $P_{L,R}$ (note $P_L + P_d + P_R = I$)

$$P_L = \begin{pmatrix} 1 & 0 & 0 \\ 0 & 0 & 0 \\ 0 & 0 & 0 \end{pmatrix}, \quad P_d = \begin{pmatrix} 0 & 0 & 0 \\ 0 & 1 & 0 \\ 0 & 0 & 0 \end{pmatrix}, \quad P_R = \begin{pmatrix} 0 & 0 & 0 \\ 0 & 0 & 0 \\ 0 & 0 & 1 \end{pmatrix}, \tag{A.2}$$

where 1 is the identity operator for that subspace. For example, $H_L = P_L H P_L$, or $V_{Rd} = P_R H P_d$. Note that the two leads do not directly couple, $P_L H P_R = 0$, which forces a current flowing between leads to do so through the device region, but otherwise the form of Eqn. (A.1) is completely general.

The retarded Green's function can be defined for the system using the eigenstates of the Hamiltonian $H|\Psi_m(E)\rangle = E|\Psi_m(E)\rangle$

$$\begin{aligned} G(E) &= [E + i\delta - H]^{-1} \\ &= \int \mathrm{d}E' \sum_m \frac{|\Psi_m(E')\rangle\langle\Psi_m(E')|}{E + i\delta - E'} \end{aligned} \tag{A.3}$$

where m indexes any degenerate states at a given energy and the infinitesimal energy $\delta = 0^+$ is used to select the retarded response in the system; in the following we will neglect explicitly writing δ for clarity. The Green's function can be written similarly in operator matrix form as

$$G = \begin{pmatrix} G_L & G_{Ld} & G_{LR} \\ G_{dL} & G_d & G_{dR} \\ G_{RL} & G_{Rd} & G_R \end{pmatrix}. \tag{A.4}$$

The device part of the Green's function can be computed from the relation between the Green's function and the Hamiltonian $(E - H)G(E) = 1$, i.e.

$$\begin{pmatrix} E - H_L & -V_{Ld} & 0 \\ -V_{dL} & E - H_d & -V_{dR} \\ 0 & -V_{Rd} & E - H_R \end{pmatrix} \begin{pmatrix} G_L & G_{Ld} & G_{LR} \\ G_{dL} & G_d & G_{dR} \\ G_{RL} & G_{Rd} & G_R \end{pmatrix} = \begin{pmatrix} 1 & 0 & 0 \\ 0 & 1 & 0 \\ 0 & 0 & 1 \end{pmatrix}. \tag{A.5}$$

Considering the products involving the second column of the Green's function operator matrix, three equations are identified

$$(E - H_L)G_{Ld} - V_{Ld}G_d = 0, \tag{A.6}$$

$$-V_{dL}G_{Ld} - H_d G_d + V_{dR}G_{Rd} = 1, \tag{A.7}$$

$$- V_{Rd}G_d + (E - H_R)G_{Rd} = 0. \tag{A.8}$$

Using the first and last of these results,

$$G_{Ld} = g_L V_{Ld} G_d, \tag{A.9}$$

$$G_{Rd} = g_R V_{Rd} G_d, \tag{A.10}$$

where $g_{L,R} = [E - H_{L,R}]^{-1}$ are the Green's functions of the isolated leads. Combining these results with Eqn. (A.7) results in

$$G_d = [E - H_d - \Sigma_L - \Sigma_R]^{-1}, \tag{A.11}$$

where

$$\Sigma_L = V_{dL} g_L V_{Ld},$$
$$\Sigma_R = V_{dR} g_R V_{Rd},$$

are the lead self energies.

From the Green's function, the spectral function can be defined

$$\begin{aligned} A(E) &= i\Big(G(E) - G^\dagger(E)\Big) \\ &= 2\pi \sum_n |\Psi_n(E)\rangle\langle\Psi_n(E)|. \end{aligned} \tag{A.12}$$

We also define the coupling matrices

$$\Gamma_L = i\big(\Sigma_L - \Sigma_L^\dagger\big),$$
$$\Gamma_R = i\big(\Sigma_R - \Sigma_R^\dagger\big).$$

A.1.1 State normalisation

The normalisation of the states is chosen such that each state injects the same current flux into the device, a property referred to as *flux normalisation*. States with this property can be combined together using a unitary transformation whilst retaining the flux normalisation.

Deep within the leads where there is no scattering, the scattering states are Bloch waves $|u_l(k)\rangle$ where l denotes the band index. If these Bloch states are normalised in the conventional manner over the entire semi-infinite leads

$$\langle u_l(k)|u_{l'}(k')\rangle = \delta_{ll'}\delta(k - k'), \tag{A.13}$$

then flux normalised Bloch states are generated by dividing the Bloch state by $\sqrt{v_l}$ where $v_l = (1/\hbar)d\epsilon(k)/dk$ is the Bloch state group velocity. Using Eqn. (A.13), the condition for flux-normalised states is then

$$\begin{aligned} \frac{1}{\sqrt{v_l}}\langle u_l(k)|u_{l'}(k')\rangle\frac{1}{\sqrt{v_{l'}}} &= \frac{1}{v_l}\delta_{ll'}\delta(k - k') \\ &= \hbar\delta_{ll'}\delta(E - E'). \end{aligned} \tag{A.14}$$

Therefore, scattering states generated from incoming energy-normalised states will also be flux-normalised, up to a factor of $\hbar$.

A.2 Scattering states from the leads

For the two-lead system there exist two sets of scattering states, each set originating from each of the reservoirs connected to the leads. The scattering states originating from one lead can be computed by considering the isolated eigenstates of the semi-infinite lead and treating the interaction between the leads as a perturbation. If $|U^{(L)}\rangle$ is an orthogonal and energy-normalised eigenstate of the isolated left lead, then this state can be propagated into the device region

$$|\Psi^{(L)}\rangle = GV|U^{(L)}\rangle + |U^{(L)}\rangle, \tag{A.15}$$

where the bracketed superscript indicates that this state originates from the left reservoir. In the spatial partitioning, the states $|\Psi^{(L)}\rangle$ and $|U^{(L)}\rangle$ are given as

$$|U^{(L)}\rangle = \begin{pmatrix} |u^{(L)}\rangle \\ 0 \\ 0 \end{pmatrix}, \quad |\Psi\rangle = \begin{pmatrix} |\psi_L^{(L)}\rangle \\ |\psi_d^{(L)}\rangle \\ |\psi_R^{(L)}\rangle \end{pmatrix}.$$

Using the operator block structure of G and V, the block components of $|\Psi\rangle$ can be computed as

$$|\psi_d^{(L)}\rangle = G_d V_{dL}|u^{(L)}\rangle, \tag{A.16}$$

$$\begin{aligned} |\psi_L^{(L)}\rangle &= (1 + g_L V_{Ld} G_d V_{dL})|u^{(L)}\rangle \\ &= |u^{(L)}\rangle + g_L V_{Ld}|\psi_d^{(L)}\rangle, \end{aligned} \tag{A.17}$$

$$\begin{aligned} |\psi_R^{(L)}\rangle &= g_R V_{Rd} G_d V_{dL}|u^{(L)}\rangle \\ &= g_R V_{Rd}|\psi_d^{(L)}\rangle. \end{aligned} \tag{A.18}$$

The set of states $|\Psi(E)\rangle$ are orthogonal and energy normalised, which can be shown using Eqn. (A.15) and the Lippmann-Schwinger equation

$$|\Psi_n(E)\rangle = G_0(E)V|U_n(E)\rangle + |U_n(E)\rangle, \tag{A.19}$$

where $G_0 = \big(E + i\delta - H_0\big)^{-1}$ is the unperturbed Green's function:

$$\langle\Psi_n(E)|\Psi_{n'}(E')\rangle = \langle U_n(E)|\Psi_{n'}(E')\rangle + \langle U_n(E)|V^\dagger G^\dagger(E)|\Psi_{n'}(E')\rangle \tag{A.20}$$

$$\begin{aligned} &= \langle U_n(E)|U_{n'}(E')\rangle + \langle U_n(E)|G_0(E')V|\Psi_{n'}(E')\rangle + \\ &\quad \langle U_n(E)|VG^\dagger(E)|\Psi_{n'}(E')\rangle \end{aligned} \tag{A.21}$$

$$\begin{aligned} &= \delta_{nn'}\delta(E - E') + \\ &\quad \langle U_n(E)|V|\Psi_{n'}(E')\rangle \left(\frac{1}{E' - E + i\delta} + \frac{1}{E - E' - i\delta}\right) \end{aligned} \tag{A.22}$$

$$= \delta_{nn'}\delta(E - E') \tag{A.23}$$

where $n,\ n'$ indexes degenerate states, and we have used the fact the V is Hermitian and that $|U_n(E)\rangle$ and $|\Psi_n(E)\rangle$ are eigenstates of G_0 and G respectively.

A.3 Device spectral function

Within the device region, the spectral function is defined by the sum of contributions arising from each reservoir. The contribution to the device spectral function from states originating from the left reservoir is

$$\begin{aligned} A_d^{(L)} &= 2\pi \sum_l |\psi_{d,l}^{(L)}\rangle\langle\psi_{d,l}^{(L)}| \\ &= 2\pi \sum_l G_d V_{dL} |u_l^{(L)}\rangle\langle u_l^{(L)}| V_{Ld} G_d^\dagger \\ &= G_d V_{dL} a_L V_{Ld} G_d^\dagger \\ &= G_d \Gamma_L G_d^\dagger \end{aligned} \tag{A.24}$$

where the sum is performed over all the eigenstates states of the isolated left lead $\{|u_l^{(L)}\rangle\}$, and $a_L = i(g_L - g_L^\dagger) = 2\pi \sum_l |u_l^{(L)}\rangle\langle u_l^{(L)}|$ is the spectral function of the isolated left lead. An equivalent expression is found for scattering states originating from the right lead and the total density matrix is the sum of the contributions from each lead.

The density matrix within the device in non-equilibrium is then given as

$$\rho = \frac{1}{2\pi} \int_{-\infty}^{\infty} \mathrm{d}E \left[f_L(E) A_d^{(L)}(E) + f_R(E) A_d^{(R)}(E) \right], \tag{A.25}$$

where $f_{L,R}$ is the Fermi function of the leads that populates the scattering injected scattering states. To compute the integral over energy within Eqn. (A.25), analytic continuation of the device Green's function is used and the integral is performed as a contour integral in the complex plane, as shown in Fig. A.1. Away from the real axis, the Green's function is smoother and a relatively coarse Gaussian quadrature, typically consisting of a circular arc segment and a linear segment, can be used to perform the integration more efficiently than a direct integration along the real axis. Note that Eqn. (A.25) can only account for states within the device region that can be accessed by states originating in the leads; states that are localised within the device region and do not interact with the scattering states must be included separately. Eqn. (A.25) is the relation central to the non-equilibrium Green's function formalism, from which the electron density can be computed using the diagonal elements $n(\mathbf{r}) = \langle \mathbf{r}|\rho|\mathbf{r}\rangle$. Coupling this with density functional theory, a self-consistent procedure for computing the electronic structure of a device at finite bias can be constructed[138].

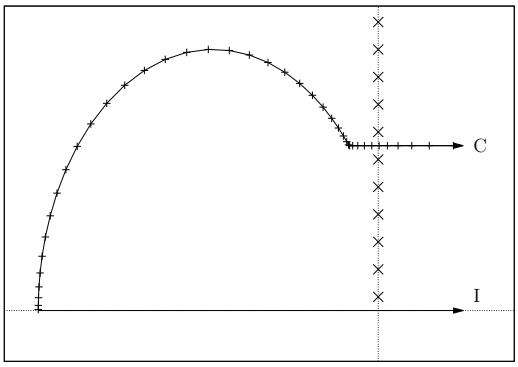

Figure A.1: The complex contour C used to calculate the integral I defined in Eqn. (A.25). By the residue theorem, I is equal to C with an additional term arising from the residues of the poles of the Fermi function (represented by crosses) that are included within the contour. The pluses represent the points at which the Green's functions are evaluated to compute the integral. The contour is computed using two separate Gaussian quadrature integrations, evaluated along the curved and linear part of the contour C.

A.4 Current operator

The number of electrons in lead R is described by the projection operator P_R. The operator for current into the right lead can therefore be determined as the time derivative of this operator which results in

$$J_R = 2e\dot{P}_R = \frac{i2e}{\hbar}[H, P_R] \tag{A.26}$$

where the factor of two is for spin degeneracy.

The contribution to the current between the left and the right leads from the state $|\Psi^{(L)}\rangle$ can then be computed

$$\begin{aligned} j^{(L)} &= \langle\Psi^{(L)}|J_R|\Psi^{(L)}\rangle \\ &= \frac{i2e}{\hbar}\Big(\langle\psi_d^{(L)}|V_{dR}|\psi_R^{(L)}\rangle - \langle\psi_R^{(L)}|V_{Rd}|\psi_d^{(L)}\rangle\Big) \\ &= \frac{i2e}{\hbar}\Big(\langle\psi_d^{(L)}|V_{dR}g_RV_{Rd}|\psi_d^{(L)}\rangle - \langle\psi_d^{(L)}|V_{dR}g_R^\dagger V_{Rd}|\psi_d^{(L)}\rangle\Big) \\ &= \frac{2e}{\hbar}\langle\psi_d^{(L)}|\Gamma_R|\psi_d^{(L)}\rangle \end{aligned} \tag{A.27}$$

where we have expanded the commutation relation in Eqn. (A.26) and used the block partitioning of the wavefunction and have used Eqn. (A.18).

The total current arising from all states originating the in the left lead is the sum over all

scattering states $|\psi_{d,l}^{(L)}\rangle$, indexed by l,

$$\begin{aligned} j_{\mathrm{tot}}^{(L)} &= \frac{2e}{\hbar}\sum_{l}\langle\psi_{d,l}^{(L)}|\Gamma_R|\psi_{d,l}^{(L)}\rangle \\ &= \frac{2e}{2\pi\hbar}\sum_{m}\langle m|\Gamma_R\Big(2\pi\sum_{l}|\psi_{d,l}^{(L)}\rangle\langle\psi_{d,l}^{(L)}|\Big)|m\rangle \\ &= \frac{2e}{h}\mathrm{tr}\Big[\Gamma_R G_d \Gamma_L G_d^{\dagger}\Big], \end{aligned} \tag{A.28}$$

where in the second line, we have used the resolution of identity within the device region and introduced a complete set of states $|m\rangle$, and used the device spectral function defined in Eqn. (A.24). On comparison to Eqn. (3.2), the transmission function can be identified with the operator trace within Eqn. (A.28) thus proving Eqn. (3.9).

A.5 The transmission amplitude matrix and the Fisher-Lee relation

The transmission may also be equivalently calculated using the Fisher-Lee relation[75]. If a state $|u_l^{(L)}\rangle$ is a Bloch state originating in the lead of a two-lead device, then after propagation through the device, this state becomes a superposition of the Bloch states in the right lead

$$|u_l^{(L)}\rangle \rightarrow \sum_r t_{lr}|u_r^{(R)}\rangle. \tag{A.29}$$

The t_{lr} elements collectively define the transmission amplitude matrix $\boldsymbol{t}$. The transmission probability for this state is then $T_l = \sum_r |t_{lr}|^2$ and the total transmission between the left and right leads is the sum over all such probabilities for Bloch states originating in the left lead

$$\begin{aligned} T &= \sum_l T_l = \sum_{lr} t_{lr}t_{lr}^* \\ &= \mathrm{tr}\big[\boldsymbol{t}^{\dagger}\boldsymbol{t}\big]. \end{aligned} \tag{A.30}$$

Eqn. (A.30) is known the Fisher-Lee relation and relates the transmission amplitude matrix to the total transmission.

A.6 Computing the transmission matrix and eigenchannels

Comparison of Eqn. (A.27) to Eqn. (3.2) shows that $2\pi\langle\psi_{d,l}|\Gamma_R|\psi_{d,l}\rangle$ may be associated as the transmission probability for that scattering state (we omit the superscripts that define the source lead of that state for clarity). At a given energy, a number of degenerate scattering states may exist, and therefore new states can be formed using a linear combination of the original states

$$|\phi_{d,n}\rangle = \sum_{l'} M_{nl}|\psi_{d,l}\rangle \tag{A.31}$$

where $M_{ll'}$ is a unitary matrix that preserves the flux normalisation of the original states. The total transmission (c.f. Eqn. (A.28)) is then

$$\begin{aligned} T_{\text{tot}} &= 2\pi \sum_{nml} M^\dagger_{ln} M_{ml} \langle\phi_{d,n}|\Gamma_R|\phi_{d,m}\rangle \\ &= \sum_{nml} M^\dagger_{ln} M_{ml} T_{nm} \\ &= \text{tr}\big[M^\dagger T M\big] \end{aligned} \tag{A.32}$$

where we have defined the transmission matrix

$$T_{nm} = 2\pi\langle\phi_{d,n}|\Gamma_R|\phi_{d,m}\rangle \tag{A.33}$$

which is in general non-diagonal. As Γ_R is Hermitian, there must exist a unitary rotation M_{ml} that makes the transmission matrix diagonal, i.e. $T_{nm} = \text{diag}\{T_i\}$, where the eigenvalues are $T_i = 2\pi\langle\phi_{d,i}|\Gamma_R|\phi_{d,i}\rangle$, and $2\pi\langle\phi_{d,i}|\Gamma_R|\phi_{d,j}\rangle = 0$ for $i \neq j$.

The scattering states $|\phi_{d,i}\rangle$ are known as the eigenchannels of the device, with T_i the corresponding eigentransmission, and have the useful property that they propagate through the device without mixing with other scattering states. Any scattering state can be decomposed as a weighted sum of the set of eigenchannels at that energy, and the total transmission of that scattering state is given by the corresponding weighted sum of the eigentransmissions

$$|\chi_d\rangle = \sum_i \alpha_i |\phi_{d,i}\rangle, \tag{A.34}$$

$$T_{\text{tot}} = \sum_i |\alpha_i|^2 T_i. \tag{A.35}$$

The eigenchannels can be constructed by first generating the scattering states by diagonalising the spectral function (Eqn. (A.24))

$$A^{(L)} = \sum_l |\widetilde{\psi}^{(L)}_{d,l}\rangle\lambda_l\langle\widetilde{\psi}^{(L)}_{d,l}| = 2\pi \sum_l |\psi^{(L)}_{d,l}\rangle\langle\psi^{(L)}_{d,l}| \tag{A.36}$$

where $|\psi_{d,l}^{(L)}\rangle = \sqrt{\lambda_l/2\pi}|\widetilde{\psi}_{d,l}^{(L)}\rangle$. These scattering states are then used to compute the transmission matrix (Eqn. (A.33)) which is then diagonalised to generate the eigenchannels and corresponding eigentransmissions. The eigenchannels can then be plotted for visualisation, and the process repeated for each lead acting as the source.

APPENDIX

B

BLOCK TRI-DIAGONAL MATRIX INVERSION

Here we list the results of Ref. [159] for computing the matrix inverse via block tri-diagonal Gaussian elimination for a matrix in block tri-diagonal form

$$\mathsf{A} = \begin{pmatrix} \boldsymbol{a}_{11} & \boldsymbol{a}_{12} & & & & \\ \boldsymbol{a}_{21} & \boldsymbol{a}_{22} & \boldsymbol{a}_{23} & & & \\ & \boldsymbol{a}_{32} & \boldsymbol{a}_{33} & \boldsymbol{a}_{34} & & \\ & & \boldsymbol{a}_{43} & \boldsymbol{a}_{44} & \boldsymbol{a}_{45} & \\ & & & \ddots & \ddots & \ddots \end{pmatrix} \tag{B.1}$$

where $\boldsymbol{a}_{ij}$ are themselves submatrices, zero submatrices are left blank and A is partitioned into $n \times n$ submatrix blocks.

Selected matrix blocks, according to the same block tri-diagonal form, can be computed using the following recursion relations using a forward (left) and backward (right) pass through the matrix blocks of A. We use the same notation as in Ref. [159]. The left pass:

$$\boldsymbol{d}_{ii}^{L} = \boldsymbol{a}_{ii} + \boldsymbol{c}_{i-1}^{L}\boldsymbol{a}_{i-1,i} \quad \text{for } i = 2, 3, \ldots, n \tag{B.2}$$

$$\boldsymbol{c}_{i}^{L} = -\boldsymbol{a}_{i+1,i}(\boldsymbol{d}_{ii}^{L})^{-1} \quad \text{for } i = 1, 2, \ldots, n-1 \tag{B.3}$$

$$\boldsymbol{d}_{11}^{L} = \boldsymbol{a}_{11}. \tag{B.4}$$

The right pass:

$$\boldsymbol{d}_{ii}^{R} = \boldsymbol{a}_{ii} + \boldsymbol{c}_{i+1}^{R}\boldsymbol{a}_{i+1,i} \quad \text{for } i = n-1, n-2, \ldots, 1 \tag{B.5}$$

$$\boldsymbol{c}_{i}^{R} = -\boldsymbol{a}_{i-1,i}(\boldsymbol{d}_{ii}^{R})^{-1} \quad \text{for } i = n, n-1, \ldots, 2 \tag{B.6}$$

$$\boldsymbol{d}_{nn}^{R} = \boldsymbol{a}_{nn}. \tag{B.7}$$

Defining

$$\left.\begin{aligned} \boldsymbol{c}^R_{1,2,\ldots,i} &= \boldsymbol{c}^R_1 \boldsymbol{c}^R_2 \cdots \boldsymbol{c}^R_i \\ \boldsymbol{c}^L_{i,i-1,\ldots,1} &= \boldsymbol{c}^L_i \boldsymbol{c}^L_{i-1} \cdots \boldsymbol{c}^L_1 \end{aligned}\right\} \quad \text{where } i = 1, 2, \ldots n, \tag{B.8}$$

a selected submatrix block of the inverse of A, $\mathsf{G} = \mathsf{A}^{-1}$ can then be computing using

$$\boldsymbol{g}_{ii} = \big(-\boldsymbol{a}_{ii} + \boldsymbol{d}^L_{ii} + \boldsymbol{d}^R_{ii} \big)^{-1} \quad \text{where } i = 1, 2, \ldots n \tag{B.9}$$

$$\boldsymbol{g}_{ij} = \boldsymbol{g}_{ii} \boldsymbol{c}^R_{i+1,i+2,\ldots,j-1,j} \quad \text{for } i < j \tag{B.10}$$

$$\boldsymbol{g}_{ij} = \boldsymbol{g}_{ii} \boldsymbol{c}^L_{i-1,i-2,\ldots,j+1,j} \quad \text{for } i > j. \tag{B.11}$$

Operations on submatrix blocks are performed using dense matrix algebra implemented in standard LAPACK routines.[160]

APPENDIX

C

CLASSICAL ELECTROSTATIC CHARGE POLARISATION MODEL

In Chapter 8.3, we model the interaction between a CNT and an adsorbed water molecule as a classical conducting cylinder interacting with point charges. The cylinder radius is set as the radius of the CNT. The water molecule is modelled as point charges placed at the centres of the Wannier/ionic charges, as described in Section 8.3. We calculate the charge density profile induced in the conducting cylinder due to the classical charges.

The electric potential is calculated by solving for the Green's function to the Poisson equation subject to the constant potential Dirichlet boundary condition on the cylinder

$$\nabla^2\phi(\mathbf{r}) = 4\pi \sum_i q_i \delta(\mathbf{r} - \mathbf{r}_i) \tag{C.1}$$

where we have adopted atomic units.

In the limit of an infinite radius cylinder, the conductor becomes an infinite conducting plane and the solution is obtained using the method of images in a simple analytic form. For a single charge a position $\mathbf{r}_i = (x_i, 0, 0)$ above a conductor in the yz plane, the potential is

$$\phi(\mathbf{r}) = \frac{q}{|\mathbf{r} - \mathbf{r}_i|} - \frac{q}{|\mathbf{r} - \mathbf{r}_i^m|} \tag{C.2}$$

where $\mathbf{r}_i^m = (-x_i, 0, 0)$ is the position of the mirror charge.

The surface charge of the conductor is calculated using Gauss' law giving $\sigma(y, z) = 1/(2\pi)E_x|_{x=0}$, where $E_x|_{x=0}$ is the electric field perpendicular to the plane, evaluated at the plane. The charge density per unit length of CNT is given by the sum of the surface charge along a direction perpendicular to the CNT axis, i.e.

$$\lambda(z) = \int dy\ \sigma(y, z) = \frac{q}{\pi} \frac{x_i}{z^2 + x_i^2}. \tag{C.3}$$

The charge density due to multiple charges is generated through superposition. To compare to the charge polarisation derived from the DFT calculations, this quantity is convolved with the same window function given in Eqn. (8.3).

Whilst the shape of the induced density calculated using this model is in excellent qualitative agreement with our DFT calculations, the amplitude is an order of magnitude too large. Heuristically, this can be understood to arise from the difference in screening in the metallic cylinder as compared to a real CNT. We account for this by including a single parameter to the model that scales all the classical charges by the same factor, and choose its value such that the best fit to the DFT data is obtained. For the calculations shown in the right panels of Fig. 8.4 and Fig. 8.5, the fitted scaling factors are 0.13 and 0.28 respectively.

The same calculation can be performed treating the finite radius of the CNT explicitly by calculating the Green's function using cylindrical polar symmetry[246]. The corresponding induced charge density per unit length of CNT for a single point charge at cylindrical co-ordinate (z_1, r_1) is (Ref. [246], Eqn. (45))

$$\lambda_{\mathrm{cyl}}(z) = \frac{q}{\pi} \int_0^\infty \mathrm{d}k \, \cos\left[k(z - z_1)\right] \frac{K_0(kr_1)}{K_0(ka)} \tag{C.4}$$

where the CNT axis is aligned with $r = 0$, a is the CNT radius and K_0 is the zeroth-order modified Bessel function of the second kind.

The difference between the induced charge density in the planar and cylindrical geometries is found to be negligible, however, as seen in Fig. C.1. This observation is reasonable as the CNT diameter (≈ 8 Å) is much larger than the distance between point charges and CNT surface (3.20 Å). Regardless, we find that the classical model captures well the main features of the charge polarisation due to the water molecule.

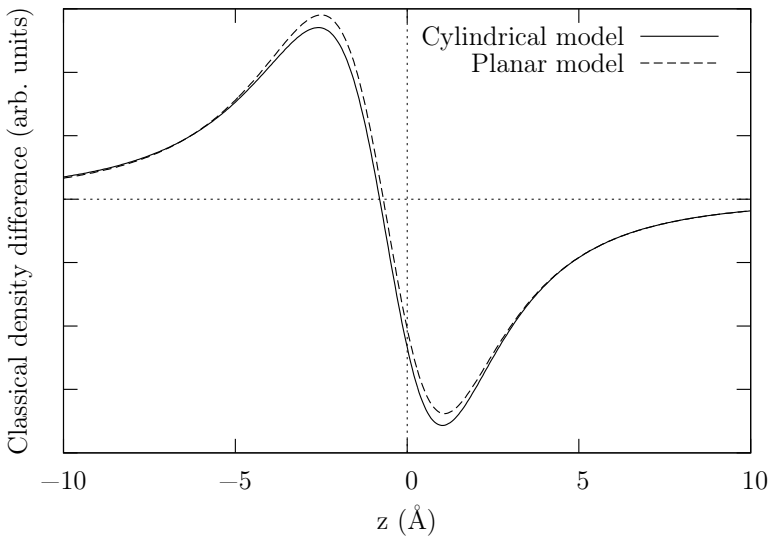

Figure C.1: The difference between the classical induced charge density difference in the cylindrical geometry (Eqn. (C.4)) and the planar geometry (Eqn. (C.3)). The point charges are for the Wannier charge model with the water in the $\theta = 90^\circ$ orientation with the charge due to the oxygen nucleus at $z = 0$; the CNT radius is 4.0 Å.

APPENDIX

D

LOCAL DENSITY OF STATES

The local density of states (LDOS) provides simultaneously a description of the energetic and spatial distribution of the electronic structure of a material, and is thus an invaluable tool used in section 8.6 for probing the possibility of bonding between two molecular fragments.

An LDOS decomposition is achieved by diagonalising the Hamiltonian and then projecting the resulting eigenstates onto a set of spatially-localised orbitals; within ONETEP, the NGWFs themselves are used as the localised basis.[233]

The generalised eigenproblem that must be solved is

$$\sum_{\beta} H_{\alpha\beta} M_n^{\beta} = \epsilon_n \sum_{\beta} S_{\alpha\beta} M_n^{\beta} \tag{D.1}$$

where $H_{\alpha\beta}$, $S_{\alpha\beta}$ are the Hamiltonian and overlap matrices in the NGWF basis and ϵ_n is the eigenenergy of the n^{th} state. The matrix M_n^{β} describes the eigenvectors in terms of the NGWF basis $|\psi_n\rangle = \sum_{\beta} M_n^{\beta} |\phi_{\beta}\rangle$ where $|\phi_{\beta}\rangle$ are the NGWFs. The total density of states can be calculated as

$$\mathcal{N}(E) = \sum_{n} \delta(E - \epsilon_n), \tag{D.2}$$

where the Dirac δ-function is, in practice, replaced with a Gaussian broadening typically of order 0.1 eV.

The partitioning of the density of states is performed according to groups of atoms. The LDOS for such a group, which we will refer to as region I, is calculated by projecting each eigenstate onto the local orbitals of all the atoms within this region

$$\mathcal{N}_I(E) = \sum_{n} \delta(E - \epsilon_n) \langle \psi_n | \sum_{\alpha \in I} \Big(|\phi^{\alpha}\rangle \langle \phi_{\alpha}| \Big) |\psi_n\rangle. \tag{D.3}$$

The non-orthogonality of the NGWFs has been accounted for by introducing the duals of the NGWFs $|\phi^{\alpha}\rangle$ which are related to the NGWFs by $|\phi_{\alpha}\rangle = \sum_{\beta} S_{\alpha\beta} |\phi^{\beta}\rangle$ and together

with the NGWFs satisfy the bi-orthogonality relation $\langle\phi^\alpha|\phi_\beta\rangle = \delta^\alpha_\beta$. Using these results, Eqn. (D.3) can be rewritten as

$$\begin{aligned}\mathcal{N}_I(E) &= \sum_n \delta(E-\epsilon_n) \sum_{\beta\gamma,\alpha\in I} (M^\dagger)^\gamma_n \langle\phi_\gamma|\Big(|\phi^\alpha\rangle\langle\phi_\alpha|\Big)|\phi_\beta\rangle M^\beta_n, \\ &= \sum_n \delta(E-\epsilon_n) \sum_{\alpha\in I} (M^\dagger)^\alpha_n \Big(\sum_\beta S_{\alpha\beta} M^\beta_n\Big). \end{aligned} \tag{D.4}$$

A resulting series of functions $\mathcal{N}_I(E)$ are obtained for each of the chosen regions I.

BIBLIOGRAPHY

[1] S. Iijima, "Helical microtubules of graphitic carbon," *Nature*, vol. 354, pp. 56–58, Nov 1991.

[2] M. Monthioux and V. L. Kuznetsov, "Who should be given the credit for the discovery of carbon nanotubes?," *Carbon*, vol. 44, no. 9, pp. 1621–1623, 2006.

[3] L. V. Radushkevich and V. M. Lukyanovich, "O strukture ugleroda, obrazujucegosja pri termiceskom razlozenii okisi ugleroda na zeleznom kontakte (About the structure of carbon formed by thermal decomposition of carbon monoxide on iron substrate)," *Zurn. Fisic. Chim.*, vol. 1, p. 88, 1952.

[4] W. Bollmann and J. SpreadBorough, "Action of graphite as a lubricant," *Nature*, vol. 186, pp. 29–30, Apr 1960.

[5] A. Oberlin, M. Endo, and T. Koyama, "Filamentous growth of carbon through benzene decomposition," *Journal of Crystal Growth*, vol. 32, no. 3, pp. 335–349, 1976.

[6] M. Reibold, P. Paufler, A. A. Levin, W. Kochmann, N. Patzke, and D. C. Meyer, "Materials: Carbon nanotubes in an ancient Damascus sabre," *Nature*, vol. 444, pp. 286–286, Nov 2006.

[7] R. Zhang, Y. Zhang, Q. Zhang, H. Xie, W. Qian, and F. Wei, "Growth of half-meter long carbon nanotubes based on Schulz-Flory distribution," *ACS Nano*, vol. 7, no. 7, pp. 6156–6161, 2013. PMID: 23806050.

[8] R. M. Sundaram, K. K. K. Koziol, and A. H. Windle, "Continuous direct spinning of fibers of single-walled carbon nanotubes with metallic chirality," *Advanced Materials*, vol. 23, no. 43, pp. 5064–5068, 2011.

[9] N. Behabtu, C. C. Young, D. E. Tsentalovich, O. Kleinerman, X. Wang, A. W. K. Ma, E. A. Bengio, R. F. ter Waarbeek, J. J. de Jong, R. E. Hoogerwerf, S. B. Fairchild, J. B. Ferguson, B. Maruyama, J. Kono, Y. Talmon, Y. Cohen, M. J. Otto, and M. Pasquali, "Strong, light, multifunctional fibers of carbon nanotubes with ultrahigh conductivity," *Science*, vol. 339, no. 6116, pp. 182–186, 2013.

[10] N. Behabtu, M. J. Green, and M. Pasquali, "Carbon nanotube-based neat fibers," *Nano Today*, vol. 3, no. 5–6, pp. 24–34, 2008.

[11] K. S. Novoselov, A. K. Geim, S. V. Morozov, D. Jiang, Y. Zhang, S. V. Dubonos, I. V. Grigorieva, and A. A. Firsov, "Electric field effect in atomically thin carbon films," *Science*, vol. 306, no. 5696, pp. 666–669, 2004.

[12] A. H. Castro Neto, F. Guinea, N. M. R. Peres, K. S. Novoselov, and A. K. Geim, "The electronic properties of graphene," *Rev. Mod. Phys.*, vol. 81, pp. 109–162, Jan. 2009.

[13] H. W. Kroto, J. R. Heath, S. C. O'Brien, R. F. Curl, and R. E. Smalley, "C_{60}: Buckminsterfullerene," *Nature*, vol. 318, pp. 162–163, Nov 1985.

[14] R. Saito, G. Dresselhaus, and S. Dresselhaus, *Physical Properties of Carbon Nanotubes*. Imperial College Press, 1998.

[15] M.-F. Yu, O. Lourie, M. J. Dyer, K. Moloni, T. F. Kelly, and R. S. Ruoff, "Strength and breaking mechanism of multiwalled carbon nanotubes under tensile load," *Science*, vol. 287, no. 5453, pp. 637–640, 2000.

[16] E. Pop, D. Mann, Q. Wang, K. Goodson, and H. Dai, "Thermal conductance of an individual single-wall carbon nanotube above room temperature," *Nano Letters*, vol. 6, no. 1, pp. 96–100, 2006.

[17] C. Liao, K. Chen, W. Wu, and L. Chen, "In situ transmission electron microscope observations of electromigration in copper lines at room temperature," *Applied Physics Letters*, vol. 87, p. 141903, Oct 2005.

[18] D. Dew-Hughes, "The critical current of superconductors: an historical review," *Low Temperature Physics*, vol. 27, no. 9, pp. 713–722, 2001.

[19] H. Li and K. Banerjee, "High-frequency analysis of carbon nanotube interconnects and implications for on-chip inductor design," *Electron Devices, IEEE Transactions on*, vol. 56, pp. 2202–2214, Oct 2009.

[20] M. Meyyappan, ed., *Carbon nanotubes: Science and applications*. CRC Press, 2004.

[21] J. H. Lehman, M. Terrones, E. Mansfield, K. E. Hurst, and V. Meunier, "Evaluating the characteristics of multiwall carbon nanotubes," *Carbon*, vol. 49, no. 8, pp. 2581–2602, 2011.

[22] J.-C. Charlier, X. Blase, and S. Roche, "Electronic and transport properties of nanotubes," *Rev. Mod. Phys.*, vol. 79, pp. 677–732, May 2007.

[23] J.-F. Colomer, L. Henrard, G. Van Tendeloo, A. Lucas, and P. Lambin, "Study of the packing of double-walled carbon nanotubes into bundles by transmission electron microscopy and electron diffraction," *J. Mater. Chem.*, vol. 14, pp. 603–606, 2004.

[24] M. Motta, A. Moisala, I. A. Kinloch, and A. H. Windle, "High performance fibres from 'dog bone' carbon nanotubes," *Advanced Materials*, vol. 19, no. 21, pp. 3721–3726, 2007.

[25] Y. Zhao, J. Wei, R. Vajtai, P. M. Ajayan, and E. V. Barrera, "Iodine doped carbon nanotube cables exceeding specific electrical conductivity of metals," *Sci. Rep.*, vol. 1, Sep 2011.

[26] F. Bloch, "Über die quantenmechanik der elektronen in kristallgittern," *Zeitschrift für Physik*, vol. 52, no. 7-8, pp. 555–600, 1929.

[27] J. W. G. Wildöer, L. C. Venema, A. G. Rinzler, R. E. Smalley, and C. Dekker, "Electronic structure of atomically resolved carbon nanotubes," *Nature*, vol. 391, pp. 59–62, Jan 1998.

[28] H. Yorikawa and S. Muramatsu, "Energy gaps of semiconducting nanotubules," *Phys. Rev. B*, vol. 52, pp. 2723–2727, July 1995.

[29] X. Blase, L. X. Benedict, E. L. Shirley, and S. G. Louie, "Hybridization effects and metallicity in small radius carbon nanotubes," *Phys. Rev. Lett.*, vol. 72, pp. 1878–1881, Mar. 1994.

[30] H. J. Liu and C. T. Chan, "Properties of 4Å carbon nanotubes from first-principles calculations," *Phys. Rev. B*, vol. 66, p. 115416, Sept. 2002.

[31] J. Kürti, V. Zólyomi, M. Kertesz, G. Sun, R. Baughman, and H. Kuzmany, "Individualities and average behavior in the physical properties of small diameter single-walled

carbon nanotubes," *Carbon*, vol. 42, no. 5–6, pp. 971–978, 2004. European Materials Research Society 2003, Symposium B: Advanced Multifunctional Nanocarbon Materials and Nanosystems.

[32] V. Zólyomi and J. Kürti, "First-principles calculations for the electronic band structures of small diameter single-wall carbon nanotubes," *Phys. Rev. B*, vol. 70, p. 085403, Aug. 2004.

[33] C. L. Kane and E. J. Mele, "Size, shape, and low energy electronic structure of carbon nanotubes," *Phys. Rev. Lett.*, vol. 78, pp. 1932–1935, Mar. 1997.

[34] S. Reich, J. Maultzsch, C. Thomsen, and P. Ordejón, "Tight-binding description of graphene," *Phys. Rev. B*, vol. 66, p. 035412, July 2002.

[35] P. Delaney, H. J. Choi, J. Ihm, S. G. Louie, and M. L. Cohen, "Broken symmetry and pseudogaps in ropes of carbon nanotubes," *Nature*, vol. 391, pp. 466–468, Jan 1998.

[36] M. Ouyang, J.-L. Huang, C. L. Cheung, and C. M. Lieber, "Energy gaps in "metallic" single-walled carbon nanotubes," *Science*, vol. 292, no. 5517, pp. 702–705, 2001.

[37] J.-C. Charlier, X. Gonze, and J.-P. Michenaud, "First-principles study of carbon nanotube solid-state packings," *Europhysics Letters*, vol. 29, no. 1, p. 43, 1995.

[38] A. A. Maarouf, C. L. Kane, and E. J. Mele, "Electronic structure of carbon nanotube ropes," *Phys. Rev. B*, vol. 61, pp. 11156–11165, Apr. 2000.

[39] P. Lambin, V. Meunier, and A. Rubio, "Electronic structure of polychiral carbon nanotubes," *Phys. Rev. B*, vol. 62, pp. 5129–5135, Aug. 2000.

[40] S. Sanvito, Y.-K. Kwon, D. Tománek, and C. J. Lambert, "Fractional quantum conductance in carbon nanotubes," *Phys. Rev. Lett.*, vol. 84, pp. 1974–1977, Feb. 2000.

[41] Y.-K. Kwon, S. Saito, and D. Tománek, "Effect of intertube coupling on the electronic structure of carbon nanotube ropes," *Phys. Rev. B*, vol. 58, pp. R13314–R13317, Nov. 1998.

[42] B. J. van Wees, H. van Houten, C. W. J. Beenakker, J. G. Williamson, L. P. Kouwenhoven, D. van der Marel, and C. T. Foxon, "Quantized conductance of point contacts in a two-dimensional electron gas," *Phys. Rev. Lett.*, vol. 60, pp. 848–850, Feb. 1988.

[43] N. Agraït, A. L. Yeyati, and J. M. van Ruitenbeek, "Quantum properties of atomic-sized conductors," *Physics Reports*, vol. 377, no. 2, pp. 81–279, 2003.

[44] S. Frank, P. Poncharal, Z. L. Wang, and W. A. d. Heer, "Carbon nanotube quantum resistors," *Science*, vol. 280, no. 5370, pp. 1744–1746, 1998.

[45] S. Datta, *Electronic Transport in Mesoscopic Systems*. Cambridge University Press, 1995.

[46] Y. Zhou, S. Sreekala, P. M. Ajayan, and S. K. Nayak, "Resistance of copper nanowires and comparison with carbon nanotube bundles for interconnect applications using first principles calculations," *Journal of Physics: Condensed Matter*, vol. 20, no. 9, p. 095209, 2008.

[47] M. Kobylko, M. Kociak, Y. Sato, K. Urita, A. M. Bonnot, A. Kasumov, Y. Kasumov, K. Suenaga, and C. Colliex, "Ballistic- and quantum-conductor carbon nanotubes: A reference experiment put to the test," *Phys. Rev. B*, vol. 90, p. 195431, Nov 2014.

[48] T. Ando and T. Nakanishi, "Impurity scattering in carbon nanotubes – absence of back scattering," *Journal of the Physical Society of Japan*, vol. 67, no. 5, pp. 1704–1713, 1998.

[49] T. Ando, T. Nakanishi, and R. Saito, "Berry's phase and absence of back scattering in carbon nanotubes," *Journal of the Physical Society of Japan*, vol. 67, no. 8, pp. 2857–2862, 1998.

[50] S. Roche, G. Dresselhaus, M. S. Dresselhaus, and R. Saito, "Aharonov-bohm spectral features and coherence lengths in carbon nanotubes," *Phys. Rev. B*, vol. 62, pp. 16092–16099, Dec. 2000.

[51] Y. Fan, B. R. Goldsmith, and P. G. Collins, "Identifying and counting point defects in carbon nanotubes," *Nat Mater*, vol. 4, pp. 906–911, Dec 2005.

[52] C. L. Kane, E. J. Mele, R. S. Lee, J. E. Fischer, P. Petit, H. Dai, A. Thess, R. E. Smalley, A. R. M. Verschueren, S. J. Tans, and C. Dekker, "Temperature-dependent resistivity of single-wall carbon nanotubes," *Europhysics Letters*, vol. 41, no. 6, p. 683, 1998.

[53] H. Suzuura and T. Ando, "Phonons and electron-phonon scattering in carbon nanotubes," *Phys. Rev. B*, vol. 65, p. 235412, May 2002.

[54] J.-Y. Park, S. Rosenblatt, Y. Yaish, V. Sazonova, H. Üstünel, S. Braig, T. A. Arias, P. W. Brouwer, and P. L. McEuen, "Electron-phonon scattering in metallic single-walled carbon nanotubes," *Nano Letters*, vol. 4, no. 3, pp. 517–520, 2004.

[55] J. Appenzeller, R. Martel, P. Avouris, H. Stahl, and B. Lengeler, "Optimized contact configuration for the study of transport phenomena in ropes of single-wall carbon nanotubes," *Applied Physics Letters*, vol. 78, no. 21, pp. 3313–3315, 2001.

[56] S. J. Tans, M. H. Devoret, H. Dai, A. Thess, R. E. Smalley, L. J. Geerligs, and C. Dekker, "Individual single-wall carbon nanotubes as quantum wires," *Nature*, vol. 386, pp. 474–477, Apr 1997.

[57] H. T. Soh, C. F. Quate, A. F. Morpurgo, C. M. Marcus, J. Kong, and H. Dai, "Integrated nanotube circuits: Controlled growth and ohmic contacting of single-walled carbon nanotubes," *Applied Physics Letters*, vol. 75, no. 5, pp. 627–629, 1999.

[58] P. L. McEuen, M. Bockrath, D. H. Cobden, Y.-G. Yoon, and S. G. Louie, "Disorder, pseudospins, and backscattering in carbon nanotubes," *Phys. Rev. Lett.*, vol. 83, pp. 5098–5101, Dec. 1999.

[59] A. Javey, J. Guo, M. Paulsson, Q. Wang, D. Mann, M. Lundstrom, and H. Dai, "High-field quasiballistic transport in short carbon nanotubes," *Phys. Rev. Lett.*, vol. 92, p. 106804, Mar. 2004.

[60] B. Stojetz, C. Hagen, C. Hendlmeier, E. Ljubović, L. Forró, and C. Strunk, "Ensemble averaging of conductance fluctuations in multiwall carbon nanotubes," *New Journal of Physics*, vol. 6, no. 1, p. 27, 2004.

[61] S. J. Tans, A. R. M. Verschueren, and C. Dekker, "Room-temperature transistor based on a single carbon nanotube," *Nature*, vol. 393, pp. 49–52, May 1998.

[62] K. Liu, P. Avouris, R. Martel, and W. K. Hsu, "Electrical transport in doped multi-walled carbon nanotubes," *Phys. Rev. B*, vol. 63, p. 161404, Apr. 2001.

[63] M. Bockrath, D. H. Cobden, P. L. McEuen, N. G. Chopra, A. Zettl, A. Thess, and R. E. Smalley, "Single-electron transport in ropes of carbon nanotubes," *Science*, vol. 275, no. 5308, pp. 1922–1925, 1997.

[64] R. Kubo, "Statistical-mechanical theory of irreversible processes. I. General theory and simple applications to magnetic and conduction problems," *Journal of the Physical Society of Japan*, vol. 12, no. 6, pp. 570–586, 1957.

[65] D. A. Greenwood, "The Boltzmann equation in the theory of electrical conduction in metals," *Proceedings of the Physical Society*, vol. 71, no. 4, p. 585, 1958.

[66] R. Landauer, "Spatial variation of currents and fields due to localized scatterers in metallic conduction," *IBM Journal of Research and Development*, vol. 1, pp. 223–231, July 1957.

[67] R. Landauer, "Electrical resistance of disordered one-dimensional lattices," *Philosophical Magazine*, vol. 21, no. 172, pp. 863–867, 1970.

[68] M. Büttiker, "Four-terminal phase-coherent conductance," *Phys. Rev. Lett.*, vol. 57, pp. 1761–1764, Oct. 1986.

[69] S. D. Stone and A. Szafer, "What is measured when you measure a resistance? — the Landauer formula revisited," *IBM Journal of Research and Development*, vol. 32, pp. 384–413, May 1988.

[70] Y. Meir and N. S. Wingreen, "Landauer formula for the current through an interacting electron region," *Phys. Rev. Lett.*, vol. 68, pp. 2512–2515, Apr. 1992.

[71] C. Caroli, R. Combescot, P. Nozieres, and D. Saint-James, "Direct calculation of the tunneling current," *Journal of Physics C: Solid State Physics*, vol. 4, no. 8, p. 916, 1971.

[72] L. Keldysh, "Diagram technique for nonequilibrium processes," *Soviet Physics Journal of Experimental and Theoretical physics*, vol. 20, pp. 1018–1026, Apr. 1965.

[73] P. Drude, "Zur elektronentheorie der metalle," *Annalen der Physik*, vol. 306, no. 3, pp. 566–613, 1900.

[74] N. Ashcroft and N. Mermin, *Solid state physics*. Science: Physics, Brooks/Cole, Cengage Learning, 1976.

[75] D. S. Fisher and P. A. Lee, "Relation between conductivity and transmission matrix," *Phys. Rev. B*, vol. 23, pp. 6851–6854, June 1981.

[76] M. Di Ventra, *Electrical Transport in Nanoscale Systems*. Cambridge University Press, 2008.

[77] S.-I. Tomonaga, "Remarks on Bloch's method of sound waves applied to many-fermion problems," *Progress of Theoretical Physics*, vol. 5, no. 4, pp. 544–569, 1950.

[78] J. M. Luttinger, "An Exactly Soluble Model of a Many-Fermion System," *Journal of Mathematical Physics*, vol. 4, pp. 1154–1162, Sept. 1963.

[79] M. Bockrath, D. H. Cobden, J. Lu, A. G. Rinzler, R. E. Smalley, L. Balents, and P. L. McEuen, "Luttinger-liquid behaviour in carbon nanotubes," *Nature*, vol. 397, pp. 598–601, Feb 1999.

[80] H. Ishii, H. Kataura, H. Shiozawa, H. Yoshioka, H. Otsubo, Y. Takayama, T. Miyahara, S. Suzuki, Y. Achiba, M. Nakatake, T. Narimura, M. Higashiguchi, K. Shimada, H. Namatame, and M. Taniguchi, "Direct observation of Tomonaga-Luttinger-liquid state in carbon nanotubes at low temperatures," *Nature*, vol. 426, pp. 540–544, Dec. 2003.

[81] F. D. M. Haldane, "'Luttinger liquid theory' of one-dimensional quantum fluids. I. properties of the Luttinger model and their extension to the general 1D interacting spinless Fermi gas," *Journal of Physics C: Solid State Physics*, vol. 14, no. 19, p. 2585, 1981.

[82] R. Egger, A. Bachtold, M. Fuhrer, M. Bockrath, D. Cobden, and P. McEuen, "Luttinger liquid behavior in metallic carbon nanotubes," in *Interacting Electrons in Nanostructures* (R. Haug and H. Schoeller, eds.), vol. 579 of *Lecture Notes in Physics*, pp. 125–146, Springer Berlin Heidelberg, 2001.

[83] C. Møller and M. S. Plesset, "Note on an approximation treatment for many-electron systems," *Phys. Rev.*, vol. 46, pp. 618–622, Oct. 1934.

[84] A. Szabo and N. Ostlund, *Modern Quantum Chemistry: Introduction to Advanced Electronic Structure Theory*. Dover Books on Chemistry Series, Dover Publications, 1996.

[85] C. D. Sherrill and H. F. S. III, "The configuration interaction method: Advances in highly correlated approaches," in *Advances in Quantum Chemistry* (M. C. Z. Per-Olov Löwdin, John R. Sabin and E. Brändas, eds.), vol. 34, pp. 143–269, Academic Press, 1999.

[86] W. M. C. Foulkes, L. Mitas, R. J. Needs, and G. Rajagopal, "Quantum monte carlo simulations of solids," *Rev. Mod. Phys.*, vol. 73, pp. 33–83, Jan. 2001.

[87] P. Hohenberg and W. Kohn, "Inhomogeneous electron gas," *Phys. Rev.*, vol. 136, pp. B864–B871, Nov. 1964.

[88] M. Levy, "Universal variational functionals of electron densities, first-order density matrices, and natural spin-orbitals and solution of the v-representability problem," *Proceedings of the National Academy of Sciences*, vol. 76, no. 12, pp. 6062–6065, 1979.

[89] M. Levy, "Electron densities in search of Hamiltonians," *Phys. Rev. A*, vol. 26, pp. 1200–1208, Sept. 1982.

[90] H. Englisch and R. Englisch, "Exact density functionals for ground-state energies. I. general results," *Physica Status Solidi (b)*, vol. 123, no. 2, pp. 711–721, 1984.

[91] H. Englisch and R. Englisch, "Exact density functionals for ground-state energies II. details and remarks," *Physica Status Solidi (b)*, vol. 124, no. 1, pp. 373–379, 1984.

[92] L. H. Thomas, "The calculation of atomic fields," *Mathematical Proceedings of the Cambridge Philosophical Society*, vol. 23, pp. 542–548, Jan. 1927.

[93] E. Fermi, "Un metodo staistico per la determinazione di alcune proprietà dell'atome," *Rend. Accad. Naz. Lincei*, vol. 6, p. 602, 1927.

[94] P. A. M. Dirac, "Note on exchange phenomena in the Thomas atom," *Mathematical Proceedings of the Cambridge Philosophical Society*, vol. 26, pp. 376–385, July 1930.

[95] C. Weizsäcker, "Zur theorie der kernmassen," *Zeitschrift für Physik*, vol. 96, no. 7-8, pp. 431–458, 1935.

[96] E. Smargiassi and P. A. Madden, "Orbital-free kinetic-energy functionals for first-principles molecular dynamics," *Phys. Rev. B*, vol. 49, pp. 5220–5226, Feb. 1994.

[97] G. S. Ho, V. L. Lignères, and E. A. Carter, "Analytic form for a nonlocal kinetic energy functional with a density-dependent kernel for orbital-free density functional theory under periodic and dirichlet boundary conditions," *Phys. Rev. B*, vol. 78, p. 045105, July 2008.

[98] J.-D. Chai, V. L. Lignères, G. Ho, E. A. Carter, and J. D. Weeks, "Orbital-free density functional theory: Linear scaling methods for kinetic potentials, and applications to solid Al and Si," *Chemical Physics Letters*, vol. 473, no. 4–6, pp. 263–267, 2009.

[99] W. Kohn and L. J. Sham, "Self-consistent equations including exchange and correlation effects," *Phys. Rev.*, vol. 140, pp. A1133–A1138, Nov. 1965.

[100] M. C. Payne, M. P. Teter, D. C. Allan, T. A. Arias, and J. D. Joannopoulos, "Iterative minimization techniques for ab initio total-energy calculations: molecular dynamics and conjugate gradients," *Rev. Mod. Phys.*, vol. 64, pp. 1045–1097, Oct. 1992.

[101] M. Gell-Mann and K. A. Brueckner, "Correlation energy of an electron gas at high density," *Phys. Rev.*, vol. 106, pp. 364–368, Apr. 1957.

[102] D. M. Ceperley and B. J. Alder, "Ground state of the electron gas by a stochastic method," *Phys. Rev. Lett.*, vol. 45, pp. 566–569, Aug. 1980.

[103] J. P. Perdew and A. Zunger, "Self-interaction correction to density-functional approximations for many-electron systems," *Phys. Rev. B*, vol. 23, no. 10, pp. 5048–5079, 1981.

[104] N. H. March, "Asymptotic formula far from nucleus for exchange energy density in hartree-fock theory of closed-shell atoms," *Phys. Rev. A*, vol. 36, pp. 5077–5078, Nov. 1987.

[105] A. D. Becke, "Density-functional exchange-energy approximation with correct asymptotic behavior," *Phys. Rev. A*, vol. 38, pp. 3098–3100, Sept. 1988.

[106] J. P. Perdew, K. Burke, and M. Ernzerhof, "Generalized gradient approximation made simple," *Phys. Rev. Lett.*, vol. 77, pp. 3865–3868, Oct. 1996.

[107] R. Martin, *Electronic Structure: Basic Theory and Practical Methods*. Cambridge University Press, 2004.

[108] M. Dion, H. Rydberg, E. Schröder, D. C. Langreth, and B. I. Lundqvist, "Van der Waals density functional for general geometries," *Phys. Rev. Lett.*, vol. 92, p. 246401, June 2004.

[109] G. Román-Pérez and J. M. Soler, "Efficient implementation of a van der Waals density functional: Application to double-wall carbon nanotubes," *Phys. Rev. Lett.*, vol. 103, p. 096102, Aug. 2009.

[110] R. W. Godby, M. Schlüter, and L. J. Sham, "Accurate exchange-correlation potential for silicon and its discontinuity on addition of an electron," *Phys. Rev. Lett.*, vol. 56, pp. 2415–2418, June 1986.

[111] F. Gygi and A. Baldereschi, "Quasiparticle energies in semiconductors: Self-energy correction to the local-density approximation," *Phys. Rev. Lett.*, vol. 62, pp. 2160–2163, May 1989.

[112] R. W. Godby, M. Schlüter, and L. J. Sham, "Self-energy operators and exchange-correlation potentials in semiconductors," *Phys. Rev. B*, vol. 37, pp. 10159–10175, June 1988.

[113] A. G. Marinopoulos, L. Reining, V. Olevano, A. Rubio, T. Pichler, X. Liu, M. Knupfer, and J. Fink, "Anisotropy and interplane interactions in the dielectric response of graphite," *Phys. Rev. Lett.*, vol. 89, p. 076402, July 2002.

[114] J. R. Yates, C. J. Pickard, and F. Mauri, "Calculation of NMR chemical shifts for extended systems using ultrasoft pseudopotentials," *Phys. Rev. B*, vol. 76, p. 024401, July 2007.

[115] H.-S. Sim, H.-W. Lee, and K. J. Chang, "Even-odd behavior of conductance in monatomic sodium wires," *Phys. Rev. Lett.*, vol. 87, p. 096803, Aug. 2001.

[116] R. H. M. Smit, C. Untiedt, G. Rubio-Bollinger, R. C. Segers, and J. M. van Ruitenbeek, "Observation of a parity oscillation in the conductance of atomic wires," *Phys. Rev. Lett.*, vol. 91, p. 076805, Aug. 2003.

[117] J. P. Perdew, "Density functional theory and the band gap problem," *International Journal of Quantum Chemistry*, vol. 28, no. S19, pp. 497–523, 1985.

[118] Z. H. Levine and D. C. Allan, "Linear optical response in silicon and germanium including self-energy effects," *Phys. Rev. Lett.*, vol. 63, pp. 1719–1722, Oct. 1989.

[119] H.-J. Böhm and R. Ahlrichs, "A study of short-range repulsions," *The Journal of Chemical Physics*, vol. 77, no. 4, pp. 2028–2034, 1982.

[120] M. Elstner, P. Hobza, T. Frauenheim, S. Suhai, and E. Kaxiras, "Hydrogen bonding and stacking interactions of nucleic acid base pairs: A density-functional-theory based treatment," *The Journal of Chemical Physics*, vol. 114, no. 12, pp. 5149–5155, 2001.

[121] A. A. Mostofi, J. R. Yates, Y.-S. Lee, I. Souza, D. Vanderbilt, and N. Marzari, "wannier90: A tool for obtaining maximally-localised wannier functions," *Computer Physics Communications*, vol. 178, no. 9, pp. 685–699, 2008.

[122] N. Marzari and D. Vanderbilt, "Maximally localized generalized wannier functions for composite energy bands," *Phys. Rev. B*, vol. 56, pp. 12847–12865, Nov. 1997.

[123] S. J. Clark, M. D. Segall, C. J. Pickard, P. J. Hasnip, M. J. Probert, K. Refson, and M. C. Payne, "First principles methods using CASTEP," *Zeitschrift für Kristallographie*, vol. 220, no. 5-6-2005, pp. 567–570, 2005.

[124] P. Giannozzi, S. Baroni, N. Bonini, M. Calandra, R. Car, C. Cavazzoni, D. Ceresoli, G. L. Chiarotti, M. Cococcioni, I. Dabo, A. Dal Corso, S. de Gironcoli, S. Fabris, G. Fratesi, R. Gebauer, U. Gerstmann, C. Gougoussis, A. Kokalj, M. Lazzeri, L. Martin-Samos, N. Marzari, F. Mauri, R. Mazzarello, S. Paolini, A. Pasquarello, L. Paulatto, C. Sbraccia, S. Scandolo, G. Sclauzero, A. P. Seitsonen, A. Smogunov, P. Umari, and R. M. Wentzcovitch, "QUANTUM ESPRESSO: a modular and open-source software project for quantum simulations of materials," *Journal of Physics: Condensed Matter*, vol. 21, no. 39, p. 395502, 2009.

[125] J. M. Soler, E. Artacho, J. D. Gale, A. García, J. Junquera, P. Ordejón, and D. Sánchez-Portal, "The SIESTA method for ab initio order- n materials simulation," *Journal of Physics: Condensed Matter*, vol. 14, no. 11, p. 2745, 2002.

[126] J. Junquera, O. Paz, D. Sánchez-Portal, and E. Artacho, "Numerical atomic orbitals for linear-scaling calculations," *Phys. Rev. B*, vol. 64, p. 235111, Nov. 2001.

[127] C.-K. Skylaris, P. D. Haynes, A. A. Mostofi, and M. C. Payne, "Introducing ONETEP: linear-scaling density functional simulations on parallel computers.," *The Journal of Chemical Physics*, vol. 122, no. 8, p. 84119, 2005.

[128] A. A. Mostofi, C.-K. Skylaris, P. D. Haynes, and M. C. Payne, "Total-energy calculations on a real space grid with localized functions and a plane-wave basis," *Computer Physics Communications*, vol. 147, no. 3, pp. 788–802, 2002.

[129] X.-P. Li, R. W. Nunes, and D. Vanderbilt, "Density-matrix electronic-structure method with linear system-size scaling," *Phys. Rev. B*, vol. 47, pp. 10891–10894, Apr. 1993.

[130] N. Marzari, D. Vanderbilt, and M. C. Payne, "Ensemble density-functional theory for ab initio molecular dynamics of metals and finite-temperature insulators," *Phys. Rev. Lett.*, vol. 79, pp. 1337–1340, Aug. 1997.

[131] N. Hine, P. Haynes, A. Mostofi, C.-K. Skylaris, and M. Payne, "Linear-scaling density-functional theory with tens of thousands of atoms: Expanding the scope and scale of calculations with ONETEP," *Computer Physics Communications*, vol. 180, no. 7, pp. 1041–1053, 2009.

[132] A. Ruiz-Serrano and C.-K. Skylaris, "A variational method for density functional theory calculations on metallic systems with thousands of atoms," *The Journal of Chemical Physics*, vol. 139, no. 5, p. 054107, 2013.

[133] V. Heine, "The pseudopotential concept," vol. 24 of *Solid State Physics*, pp. 1–36, Academic Press, 1970.

[134] W. E. Pickett, "Pseudopotential methods in condensed matter applications," *Computer Physics Reports*, vol. 9, no. 3, pp. 115–197, 1989.

[135] D. R. Hamann, M. Schlüter, and C. Chiang, "Norm-conserving pseudopotentials," *Phys. Rev. Lett.*, vol. 43, pp. 1494–1497, Nov. 1979.

[136] L. Kleinman and D. M. Bylander, "Efficacious Form for Model Pseudopotentials," *Phys. Rev. Lett.*, vol. 48, no. 20, pp. 1425–1428, 1982.

[137] A. M. Rappe, K. M. Rabe, E. Kaxiras, and J. D. Joannopoulos, "Optimized pseudopotentials," *Phys. Rev. B*, vol. 41, pp. 1227–1230, Jan. 1990.

[138] M. Brandbyge, J.-L. Mozos, P. Ordejón, J. Taylor, and K. Stokbro, "Density-functional method for nonequilibrium electron transport," *Phys. Rev. B*, vol. 65, p. 165401, Mar. 2002.

[139] R. A. Bell, S. M.-M. Dubois, M. C. Payne, and A. A. Mostofi, "Electronic transport calculations in the ONETEP code: implementation and applications," *submitted*, 2014.

[140] M. Koentopp, C. Chang, K. Burke, and R. Car, "Density functional calculations of nanoscale conductance," *Journal of Physics: Condensed Matter*, vol. 20, no. 8, p. 083203, 2008.

[141] A. R. Rocha, M. Rossi, A. Fazzio, and A. J. R. da Silva, "Designing real nanotube-based gas sensors," *Phys. Rev. Lett.*, vol. 100, p. 176803, Apr. 2008.

[142] M. Strange, C. Rostgaard, H. Häkkinen, and K. S. Thygesen, "Self-consistent GW calculations of electronic transport in thiol- and amine-linked molecular junctions," *Phys. Rev. B*, vol. 83, p. 115108, Mar. 2011.

[143] C. M. Guedon, H. Valkenier, T. Markussen, K. S. Thygesen, J. C. Hummelen, and S. J. van der Molen, "Observation of quantum interference in molecular charge transport," *Nat Nano*, vol. 7, pp. 305–309, May 2012.

[144] A. R. Rocha, V. M. García-Suárez, S. Bailey, C. Lambert, J. Ferrer, and S. Sanvito, "Spin and molecular electronics in atomically generated orbital landscapes," *Phys. Rev. B*, vol. 73, p. 085414, Feb. 2006.

[145] O. Hod, J. E. Peralta, and G. E. Scuseria, "First-principles electronic transport calculations in finite elongated systems: A divide and conquer approach," *The Journal of Chemical Physics*, vol. 125, no. 11, p. 114704, 2006.

[146] M. Shelley, N. Poilvert, A. A. Mostofi, and N. Marzari, "Automated quantum conductance calculations using maximally-localised wannier functions," *Computer Physics Communications*, vol. 182, no. 10, pp. 2174–2183, 2011.

[147] M. B. Nardelli, J.-L. Fattebert, and J. Bernholc, "$O(N)$ real-space method for ab initio quantum transport calculations: Application to carbon nanotube–metal contacts," *Phys. Rev. B*, vol. 64, p. 245423, Dec. 2001.

[148] J. Taylor, H. Guo, and J. Wang, "Ab initio modeling of quantum transport properties of molecular electronic devices," *Phys. Rev. B*, vol. 63, p. 245407, June 2001.

[149] D. Wortmann, H. Ishida, and S. Blügel, "Embedded Green-function approach to the ballistic electron transport through an interface," *Phys. Rev. B*, vol. 66, p. 075113, Aug. 2002.

[150] P. Havu, V. Havu, M. J. Puska, M. H. Hakala, A. S. Foster, and R. M. Nieminen, "Finite-element implementation for electron transport in nanostructures," *The Journal of Chemical Physics*, vol. 124, no. 5, p. 054707, 2006.

[151] T. Ozaki, K. Nishio, and H. Kino, "Efficient implementation of the nonequilibrium Green function method for electronic transport calculations," *Phys. Rev. B*, vol. 81, p. 035116, Jan. 2010.

[152] A. Calzolari, N. Marzari, I. Souza, and M. Buongiorno Nardelli, "Ab initio," *Phys. Rev. B*, vol. 69, p. 035108, Jan. 2004.

[153] K. Thygesen and K. Jacobsen, "Molecular transport calculations with wannier functions," *Chemical Physics*, vol. 319, no. 1-3, pp. 111–125, 2005.

[154] N. Marzari, A. A. Mostofi, J. R. Yates, I. Souza, and D. Vanderbilt, "Maximally localized wannier functions: Theory and applications," *Rev. Mod. Phys.*, vol. 84, pp. 1419–1475, Oct. 2012.

[155] J. Li, T. Jayasekera, V. Meunier, and J. W. Mintmire, "Electronic transport of silicon nanowires with surface defects," *International Journal of Quantum Chemistry*, vol. 109, no. 15, pp. 3705–3710, 2009.

[156] C.-K. Skylaris, A. A. Mostofi, P. D. Haynes, O. Diéguez, and M. C. Payne, "Nonorthogonal generalized wannier function pseudopotential plane-wave method," *Phys. Rev. B*, vol. 66, p. 035119, July 2002.

[157] M. P. L. Sancho, J. M. L. Sancho, and J. Rubio, "Quick iterative scheme for the calculation of transfer matrices: application to Mo (100)," *Journal of Physics F: Metal Physics*, vol. 14, no. 5, p. 1205, 1984.

[158] E. M. Godfrin, "A method to compute the inverse of an n-block tridiagonal quasi-hermitian matrix," *Journal of Physics: Condensed Matter*, vol. 3, no. 40, p. 7843, 1991.

[159] D. E. Petersen, H. H. B. Sørensen, P. C. Hansen, S. Skelboe, and K. Stokbro, "Block tridiagonal matrix inversion and fast transmission calculations," *Journal of Computational Physics*, vol. 227, no. 6, pp. 3174–3190, 2008.

[160] E. Anderson, Z. Bai, C. Bischof, S. Blackford, J. Demmel, J. Dongarra, J. Du Croz, A. Greenbaum, S. Hammarling, A. McKenney, and D. Sorensen, *LAPACK Users' Guide*. Philadelphia, PA: Society for Industrial and Applied Mathematics, third ed., 1999.

[161] M. Paulsson and M. Brandbyge, "Transmission eigenchannels from nonequilibrium Green's functions," *Phys. Rev. B*, vol. 76, p. 115117, Sept. 2007.

[162] L. S. Blackford, J. Choi, A. Cleary, E. D'Azevedo, J. Demmel, I. Dhillon, J. Dongarra, S. Hammarling, G. Henry, A. Petitet, K. Stanley, D. Walker, and R. C. Whaley, *ScaLAPACK Users' Guide*. Philadelphia, PA: Society for Industrial and Applied Mathematics, 1997.

[163] I. Souza, N. Marzari, and D. Vanderbilt, "Maximally localized wannier functions for entangled energy bands," *Phys. Rev. B*, vol. 65, p. 035109, Dec. 2001.

[164] L. E. Ratcliff, N. D. M. Hine, and P. D. Haynes, "Calculating optical absorption spectra for large systems using linear-scaling density functional theory," *Phys. Rev. B*, vol. 84, p. 165131, Oct. 2011.

[165] E. Anglada and J. M. Soler, "Filtering a distribution simultaneously in real and fourier space," *Phys. Rev. B*, vol. 73, p. 115122, Mar. 2006.

[166] I. Rungger and S. Sanvito, "Algorithm for the construction of self-energies for electronic transport calculations based on singularity elimination and singular value decomposition," *Phys. Rev. B*, vol. 78, p. 035407, July 2008.

[167] R. A. Bell, M. C. Payne, and A. A. Mostofi, "Improving the conductance of carbon nanotube networks through resonant momentum exchange," *Phys. Rev. B*, vol. 89, p. 245426, Jun 2014.

[168] L. Hu, D. S. Hecht, and G. Grüner, "Percolation in transparent and conducting carbon nanotube networks," *Nano Letters*, vol. 4, no. 12, pp. 2513–2517, 2004.

[169] J. Alvarenga, P. R. Jarosz, C. M. Schauerman, B. T. Moses, B. J. Landi, C. D. Cress, and R. P. Raffaelle, "High conductivity carbon nanotube wires from radial densification and ionic doping," *Applied Physics Letters*, vol. 97, no. 18, p. 182106, 2010.

[170] S.-H. Ke, H. U. Baranger, and W. Yang, "Contact transparency of nanotube-molecule-nanotube junctions," *Phys. Rev. Lett.*, vol. 99, p. 146802, Oct. 2007.

[171] Z. Qian, S. Hou, J. Ning, R. Li, Z. Shen, X. Zhao, and Z. Xue, "First-principles calculation on the conductance of a single 1,4-diisocyanatobenzene molecule with single-walled carbon nanotubes as the electrodes," *The Journal of Chemical Physics*, vol. 126, no. 8, p. 084705, 2007.

[172] T. B. Martins, A. Fazzio, and A. J. R. da Silva, "Organic molecule assembled between carbon nanotubes: A highly efficient switch device," *Phys. Rev. B*, vol. 79, p. 115413, Mar. 2009.

[173] M. Ge and K. Sattler, "Bundles of carbon nanotubes generated by vapor-phase growth," *Applied Physics Letters*, vol. 64, no. 6, pp. 710–711, 1994.

[174] E. Y. Li and N. Marzari, "Improving the electrical conductivity of carbon nanotube networks: A first-principles study," *ACS Nano*, vol. 5, no. 12, pp. 9726–9736, 2011.

[175] M. A. Tunney and N. R. Cooper, "Effects of disorder and momentum relaxation on the intertube transport of incommensurate carbon nanotube ropes and multiwall nanotubes," *Phys. Rev. B*, vol. 74, p. 075406, Aug. 2006.

[176] Y.-S. Lee, M. B. Nardelli, and N. Marzari, "Band structure and quantum conductance of nanostructures from maximally localized wannier functions: The case of functionalized carbon nanotubes," *Phys. Rev. Lett.*, vol. 95, p. 076804, Aug. 2005.

[177] D. J. Mowbray, C. Morgan, and K. S. Thygesen, "Influence of O_2 and N_2 on the conductivity of carbon nanotube networks," *Phys. Rev. B*, vol. 79, p. 195431, May 2009.

[178] T. Ohta, J. T. Robinson, P. J. Feibelman, A. Bostwick, E. Rotenberg, and T. E. Beechem, "Evidence for interlayer coupling and moiré periodic potentials in twisted bilayer graphene," *Phys. Rev. Lett.*, vol. 109, p. 186807, Nov. 2012.

[179] Y.-G. Yoon, P. Delaney, and S. G. Louie, "Quantum conductance of multiwall carbon nanotubes," *Phys. Rev. B*, vol. 66, p. 073407, Aug. 2002.

[180] Y.-G. Yoon, M. S. C. Mazzoni, H. J. Choi, J. Ihm, and S. G. Louie, "Structural deformation and intertube conductance of crossed carbon nanotube junctions," *Phys. Rev. Lett.*, vol. 86, pp. 688–691, Jan. 2001.

[181] H. J. Choi, J. Ihm, S. G. Louie, and M. L. Cohen, "Defects, quasibound states, and quantum conductance in metallic carbon nanotubes," *Phys. Rev. Lett.*, vol. 84, pp. 2917–2920, Mar. 2000.

[182] K. K. K. Koziol, C. Ducati, and A. H. Windle, "Carbon nanotubes with catalyst controlled chiral angle," *Chemistry of Materials*, vol. 22, no. 17, pp. 4904–4911, 2010.

[183] N. Fukui, Y. Suwa, H. Yoshida, T. Sugai, S. Heike, M. Fujimori, Y. Terada, T. Hashizume, and H. Shinohara, "Moiré image patterns on double-walled carbon nanotubes observed by scanning tunneling microscopy," *Phys. Rev. B*, vol. 79, p. 125402, Mar. 2009.

[184] Y. Ma, W. Cheung, D. Wei, A. Bogozi, P. L. Chiu, L. Wang, F. Pontoriero, R. Mendelsohn, and H. He, "Improved conductivity of carbon nanotube networks by in situ

polymerization of a thin skin of conducting polymer," *ACS Nano*, vol. 2, no. 6, pp. 1197–1204, 2008.

[185] A. Buldum and J. P. Lu, "Contact resistance between carbon nanotubes," *Phys. Rev. B*, vol. 63, p. 161403, Apr. 2001.

[186] C. Buia, A. Buldum, and J. P. Lu, "Quantum interference effects in electronic transport through nanotube contacts," *Phys. Rev. B*, vol. 67, p. 113409, Mar. 2003.

[187] S. Uryu and T. Ando, "Electronic intertube transfer in double-wall carbon nanotubes," *Phys. Rev. B*, vol. 72, p. 245403, Dec. 2005.

[188] A. A. Maarouf and E. J. Mele, "Low-energy coherent transport in metallic carbon nanotube junctions," *Phys. Rev. B*, vol. 83, p. 045402, Jan. 2011.

[189] R. A. Bell, M. C. Payne, and A. A. Mostofi, "*In preparation*," 2014.

[190] Q. Hill and C.-K. Skylaris, "Including dispersion interactions in the onetep program for linear-scaling density functional theory calculations," *Proceedings of the Royal Society A: Mathematical, Physical and Engineering Science*, vol. 465, no. 2103, pp. 669–683, 2009.

[191] K. Sattler, "Scanning tunneling microscopy of carbon nanotubes and nanocones," *Carbon*, vol. 33, no. 7, pp. 915–920, 1995. Nanotubes.

[192] D. W. Brenner, "Empirical potential for hydrocarbons for use in simulating the chemical vapor deposition of diamond films," *Phys. Rev. B*, vol. 42, pp. 9458–9471, Nov. 1990.

[193] J. D. Gale, "GULP: a computer program for the symmetry-adapted simulation of solids," *J. Chem. Soc., Faraday Trans.*, vol. 93, pp. 629–637, 1997.

[194] J. D. Gale and A. L. Rohl, "The general utility lattice program (GULP)," *Molecular Simulation*, vol. 29, no. 5, pp. 291–341, 2003.

[195] S. Iijima, C. Brabec, A. Maiti, and J. Bernholc, "Structural flexibility of carbon nanotubes," *The Journal of Chemical Physics*, vol. 104, no. 5, pp. 2089–2092, 1996.

[196] D. A. Walters, L. M. Ericson, M. J. Casavant, J. Liu, D. T. Colbert, K. A. Smith, and R. E. Smalley, "Elastic strain of freely suspended single-wall carbon nanotube ropes," *Applied Physics Letters*, vol. 74, no. 25, pp. 3803–3805, 1999.

[197] M. B. Nardelli, "Electronic transport in extended systems: Application to carbon nanotubes," *Phys. Rev. B*, vol. 60, pp. 7828–7833, Sept. 1999.

[198] R. Tamura and M. Tsukada, "Electronic states of the cap structure in the carbon nanotube," *Phys. Rev. B*, vol. 52, pp. 6015–6026, Aug. 1995.

[199] J.-C. Charlier and G.-M. Rignanese, "Electronic structure of carbon nanocones," *Phys. Rev. Lett.*, vol. 86, pp. 5970–5973, June 2001.

[200] J. Wu and F. Hagelberg, "Magnetism in finite-sized single-walled carbon nanotubes of the zigzag type," *Phys. Rev. B*, vol. 79, p. 115436, Mar. 2009.

[201] U. Fano, "Effects of configuration interaction on intensities and phase shifts," *Phys. Rev.*, vol. 124, pp. 1866–1878, Dec. 1961.

[202] J. Kim, J.-R. Kim, J.-O. Lee, J. W. Park, H. M. So, N. Kim, K. Kang, K.-H. Yoo, and J.-J. Kim, "Fano resonance in crossed carbon nanotubes," *Phys. Rev. Lett.*, vol. 90, p. 166403, Apr. 2003.

[203] H. T. Yang, J. W. Chen, L. F. Yang, and J. Dong, "Electronic transport and fano resonance in crossed carbon nanotubes," *Phys. Rev. B*, vol. 71, p. 073401, Feb. 2005.

[204] F. Xu, A. Sadrzadeh, Z. Xu, and B. I. Yakobson, "Can carbon nanotube fibers achieve the ultimate conductivity?–coupled-mode analysis for electron transport through the carbon nanotube contact," *Journal of Applied Physics*, vol. 114, no. 6, p. 063714, 2013.

[205] C. Jin, M. Strange, T. Markussen, G. C. Solomon, and K. S. Thygesen, "Energy level alignment and quantum conductance of functionalized metal-molecule junctions: Density functional theory versus GW calculations," *The Journal of Chemical Physics*, vol. 139, no. 18, p. 184307, 2013.

[206] R. A. Bell, M. C. Payne, and A. A. Mostofi, "Does water dope carbon nanotubes?," *The Journal of Chemical Physics*, vol. 141, no. 16, p. 164703, 2014.

[207] A. L. Antaris, J.-W. T. Seo, A. A. Green, and M. C. Hersam, "Sorting single-walled carbon nanotubes by electronic type using nonionic, biocompatible block copolymers," *ACS Nano*, vol. 4, no. 8, pp. 4725–4732, 2010.

[208] A. A. Green and M. C. Hersam, "Nearly single-chirality single-walled carbon nanotubes produced via orthogonal iterative density gradient ultracentrifugation," *Advanced Materials*, vol. 23, no. 19, pp. 2185–2190, 2011.

[209] X. Tu, S. Manohar, A. Jagota, and M. Zheng, "DNA sequence motifs for structure-specific recognition and separation of carbon nanotubes," *Nature*, vol. 460, pp. 250–253, July 2009.

[210] H. W. Lee, Y. Yoon, S. Park, J. H. Oh, S. Hong, L. S. Liyanage, H. Wang, S. Morishita, N. Patil, Y. J. Park, J. J. Park, A. Spakowitz, G. Galli, F. Gygi, P. H. S. Wong, J. B. H. Tok, J. M. Kim, and Z. Bao, "Selective dispersion of high purity semiconducting single-walled carbon nanotubes with regioregular poly(3-alkylthiophene)s," *Nature Communications*, vol. 2, Nov. 2011.

[211] K. Moshammer, F. Hennrich, and M. Kappes, "Selective suspension in aqueous sodium dodecyl sulfate according to electronic structure type allows simple separation of metallic from semiconducting single-walled carbon nanotubes," *Nano Research*, vol. 2, no. 8, pp. 599–606, 2009.

[212] H. Liu, D. Nishide, T. Tanaka, and H. Kataura, "Large-scale single-chirality separation of single-wall carbon nanotubes by simple gel chromatography," *Nature Communications*, vol. 2, May 2011.

[213] M. Krüger, I. Widmer, T. Nussbaumer, M. Buitelaar, and C. Schönenberger, "Sensitivity of single multiwalled carbon nanotubes to the environment," *New Journal of Physics*, vol. 5, pp. 138–138, 2003.

[214] T. Someya, P. Kim, and C. Nuckolls, "Conductance measurement of single-walled carbon nanotubes in aqueous environment," *Applied Physics Letters*, vol. 82, no. 14, p. 2338, 2003.

[215] D. Tang, L. Ci, W. Zhou, and S. Xie, "Effect of H_2O adsorption on the electrical transport properties of double-walled carbon nanotubes," *Carbon*, vol. 44, no. 11, pp. 2155–2159, 2006.

[216] D. Kingrey, O. Khatib, and P. G. Collins, "Electronic fluctuations in nanotube circuits and their sensitivity to gases and liquids," *Nano Letters*, vol. 6, no. 7, pp. 1564–1568, 2006.

[217] A. Zahab, L. Spina, P. Poncharal, and C. Marlière, "Water-vapor effect on the electrical conductivity of a single-walled carbon nanotube mat," *Phys. Rev. B*, vol. 62, pp. 10000–10003, Oct. 2000.

[218] H. E. Romero, G. U. Sumanasekera, S. Kishore, and P. C. Eklund, "Effects of adsorption of alcohol and water on the electrical transport of carbon nanotube bundles," *Journal of Physics: Condensed Matter*, vol. 16, no. 12, p. 1939, 2004.

[219] P. S. Na, H. Kim, H.-M. So, K.-J. Kong, H. Chang, B. H. Ryu, Y. Choi, J.-O. Lee, B.-K. Kim, J.-J. Kim, and J. Kim, "Investigation of the humidity effect on the electrical properties of single-walled carbon nanotube transistors," *Applied Physics Letters*, vol. 87, no. 9, p. 093101, 2005.

[220] O. K. Varghese, P. D. Kichambre, D. Gong, K. G. Ong, E. C. Dickey, and C. A. Grimes, "Gas sensing characteristics of multi-wall carbon nanotubes," *Sensors and Actuators B: Chemical*, vol. 81, no. 1, pp. 32–41, 2001.

[221] J. Zhao, A. Buldum, J. Han, and J. P. Lu, "Gas molecule adsorption in carbon nanotubes and nanotube bundles," *Nanotechnology*, vol. 13, no. 2, p. 195, 2002.

[222] R. Pati, Y. Zhang, S. K. Nayak, and P. M. Ajayan, "Effect of H_2O adsorption on electron transport in a carbon nanotube," *Applied Physics Letters*, vol. 81, no. 14, p. 2638, 2002.

[223] D. Sung, S. Hong, Y.-H. Kim, N. Park, S. Kim, S. L. Maeng, and K.-C. Kim, "Ab initio study of the effect of water adsorption on the carbon nanotube field-effect transistor," *Applied Physics Letters*, vol. 89, no. 24, p. 243110, 2006.

[224] B. Agrawal, V. Singh, A. Pathak, and R. Srivastava, "*Ab initio* study of $\mathrm{h_2O}$ and water-chain-induced properties of carbon nanotubes," *Phys. Rev. B*, vol. 75, p. 195421, May 2007.

[225] I. Rungger, X. Chen, U. Schwingenschlögl, and S. Sanvito, "Finite-bias electronic transport of molecules in a water solution," *Phys. Rev. B*, vol. 81, p. 235407, June 2010.

[226] F. Labat, P. Baranek, C. Domain, C. Minot, and C. Adamo, "Density functional theory analysis of the structural and electronic properties of TiO_2 rutile and anatase polytypes: Performances of different exchange-correlation functionals," *The Journal of Chemical Physics*, vol. 126, no. 15, 2007.

[227] F. Jensen, *Introduction to Computational Chemistry*, ch. 9. Wiley, 2nd ed., 2006.

[228] M. D. Segall, C. J. Pickard, R. Shah, and M. C. Payne, "Population analysis in plane wave electronic structure calculations," *Molecular Physics*, vol. 89, no. 2, pp. 571–577, 1996.

[229] E. Davidson and S. Chakravorty, "A test of the Hirshfeld definition of atomic charges and moments," *Theoretica Chimica Acta*, vol. 83, no. 5-6, pp. 319–330, 1992.

[230] K. Bradley, S.-H. Jhi, P. G. Collins, J. Hone, M. L. Cohen, S. G. Louie, and A. Zettl, "Is the intrinsic thermoelectric power of carbon nanotubes positive?," *Phys. Rev. Lett.*, vol. 85, pp. 4361–4364, Nov. 2000.

[231] S. J. Fox, C. Pittock, T. Fox, C. S. Tautermann, N. Malcolm, and C.-K. Skylaris, "Electrostatic embedding in large-scale first principles quantum mechanical calculations on biomolecules," *The Journal of Chemical Physics*, vol. 135, no. 22, p. 224107, 2011.

[232] F. A. Momany, "Determination of partial atomic charges from ab initio molecular electrostatic potentials. application to formamide, methanol, and formic acid," *The Journal of Physical Chemistry*, vol. 82, no. 5, pp. 592–601, 1978.

[233] N. D. M. Hine, P. W. Avraam, P. Tangney, and P. D. Haynes, "Linear-scaling density functional theory simulations of polar semiconductor nanorods," *Journal of Physics: Conference Series*, vol. 367, no. 1, p. 012002, 2012.

[234] B. Hess, C. Kutzner, D. van der Spoel, and E. Lindahl, "GROMACS 4: Algorithms for highly efficient, load-balanced, and scalable molecular simulation," *Journal of Chemical Theory and Computation*, vol. 4, no. 3, pp. 435–447, 2008.

[235] D. Van Der Spoel, E. Lindahl, B. Hess, G. Groenhof, A. E. Mark, and H. J. C. Berendsen, "GROMACS: Fast, flexible, and free," *Journal of Computational Chemistry*, vol. 26, no. 16, pp. 1701–1718, 2005.

[236] E. Lindahl, B. Hess, and D. van der Spoel, "GROMACS 3.0: a package for molecular simulation and trajectory analysis," *Molecular modeling annual*, vol. 7, no. 8, pp. 306–317, 2001.

[237] H. Berendsen, D. van der Spoel, and R. van Drunen, "GROMACS: A message-passing parallel molecular dynamics implementation," *Computer Physics Communications*, vol. 91, no. 1–3, pp. 43–56, 1995.

[238] W. F. van Gunsteren, S. R. Billeter, A. A. Eising, P. H. Hünenberger, P. Krüger, A. E. Mark, W. R. P. Scott, and I. G. Tironi, *Biomolecular Simulation: The GROMOS96 manual and user guide*. Zürich, Switzerland: Hochschuleverlag AG an der ETH Zürich, 1996.

[239] H. Berendsen, J. Postma, W. van Gunsteren, and J. Hermans, "Interaction models for water in relation to protein hydration," in *Intermolecular Forces* (B. Pullman, ed.), p. 331, Reidel, Dordrecht, 1981.

[240] G. Bussi, D. Donadio, and M. Parrinello, "Canonical sampling through velocity rescaling," *The Journal of Chemical Physics*, vol. 126, no. 1, p. 014101, 2007.

[241] P. Giannozzi, R. Car, and G. Scoles, "Oxygen adsorption on graphite and nanotubes," *The Journal of Chemical Physics*, vol. 118, no. 3, pp. 1003–1006, 2003.

[242] P. G. Collins, K. Bradley, M. Ishigami, and A. Zettl, "Extreme oxygen sensitivity of electronic properties of carbon nanotubes," *Science*, vol. 287, no. 5459, pp. 1801–1804, 2000.

[243] A. B. Kaiser, "Electronic transport properties of conducting polymers and carbon nanotubes," *Reports on Progress in Physics*, vol. 64, no. 1, p. 1, 2001.

[244] P. Pipinys and A. Kiveris, "Variable range hopping and/or phonon-assisted tunneling mechanism of electronic transport in polymers and carbon nanotubes," *Central European Journal of Physics*, vol. 10, no. 2, pp. 271–281, 2012.

[245] T. L. Burnett, J. Patten, and O. Kazakova, "Water desorption and re-adsorption on epitaxial graphene studied by SPM," *arXiv:1204.3323 [cond-mat.mes-hall]*, 2012.

[246] J. Hernandes and A. Assis, "Electric potential due to an infinite conducting cylinder with internal or external point charge," *Journal of Electrostatics*, vol. 63, no. 12, pp. 1115–1131, 2005.